ICE RECRYSTALLIZATION INHIBITION OF ICE-BINDING PROTEINS AND

BIOINSPIRED SYNTHETIC MIMICS IN NON-PHYSIOLOGICAL ENVIRONMENTS

by

Elizabeth Anna Delesky

B.S., University of Florida, 2015

M.S., University of Colorado Boulder, 2018

A thesis submitted to the

Faculty of the Graduate School of the

University of Colorado in partial fulfillment

of the requirement for the degree of

Doctor of Philosophy

Materials Science and Engineering Program

2020

Committee Members:

Wil V. Srubar III

Stephanie Bryant

Virginia Ferguson

Yifu Ding

Garret Miyake

ABSTRACT

Delesky, Elizabeth Anna (Ph.D., Materials Science and Engineering)

Ice Recrystallization Inhibition of Ice-Binding Proteins and Bioinspired Synthetic Mimics in

Extreme Environments

Thesis directed by Associate Professor Wil V. Srubar III

While water offers many unique and beneficial properties, the formation of ice can be detrimental for a variety of applications, such infrastructure, organ transplantation, aviation and energy surfaces, food preservation, space exploration. However, current ice prevention methodologies often rely on large quantities of potentially toxic small molecules (e.g., glycerol or dimethyl sulfoxide) to take advantage of the colligative effects they provide. Materials that prevent ice formation at lower concentrations through more robust mechanisms offer a revolutionary advancement for long-term economic and environmental effects on a wide variety of industries that must think about ice prevention.

Ice-binding proteins (IBPs) are a unique subset of natural proteins with the ability to prevent ice growth by increasing the energy for expansion of ice at the water-ice interface through the kelvin effect at nanomolar concentrations. However, proteins are expensive to produce and are known to restructure in non-physiological environments. Thus understanding the limits of IBP applicability as well as the crucial components for maximum efficacy are necessary to move towards synthetic replicates for large-scale applications. To mimic IBPs, it's important to understand the functional and structural characteristics.

The main objectives of this research were (1) to use native IBPs as a biological template to create synthetic polymers that mimic ice prevention activities of IBPs, (2) to investigate homo-polypeptides of functional groups responsible for IBP ice prevention, and (3) to test a full synthetic replicate for performance and stability in non-physiological environments to act as an alternative to IBPs.

In the first study, the ability of a natural ice-binding protein from *Shewanella frigidimarina* (SfIBP) to inhibit ice crystal growth in highly alkaline solutions with increasing pH and ionic strength was investigated in this work. The purity of isolated SfIBP was first confirmed via sodium dodecyl sulfate polyacrylamide gel electrophoresis (SDS-PAGE) and size-exclusion chromatography with an ultraviolet detector (SEC-UV). Protein stability was evaluated in the alkaline solutions using circular dichroism spectroscopy, SEC-UV, and SDS-PAGE. SfIBP ice recrystallization inhibition (IRI) activity, a measure of ice crystal growth inhibition, was assessed using a modified splat assay. Statistical analysis of results substantiated that, despite partial denaturation and misfolding, SfIBP limited ice crystal growth in alkaline solutions (pH ≤ 12.7) with ionic strength I ≤ 0.05 mol/L, but did not exhibit IRI activity in alkaline solutions where pH ≥ 13.2 and I ≥ 0.16 mol/L. IRI activity of SfIBP in solutions with pH ≤ 12.7 and I ≤ 0.05 mol/L demonstrated up to ≈ 66% reduction in ice crystal size compared to neat solutions.

In the second study, the ability of an ice-binding protein (IBP) from *Marinomonas primoryensis* (MpIBP) to influence ice crystal growth and structure in non-physiological pH environments was investigated in this work. The ability for MpIBP to retain ice interactivity under stressed environmental conditions was determined *via* (1) a modified splat assay to determine ice recrystallization inhibition (IRI) of polycrystalline ice and (2) nanoliter osmometry to evaluate the ability of MpIBP to dynamically shape the morphology of a single ice crystal. Circular dichroism (CD) was used to relate the IRI and DIS activity of MpIBP to secondary structure. Results illustrate that MpIBP was stable between pH 6 – pH 10. It was found that MpIBP did not interact with ice at pH ≤ 4 or pH ≥ 13. At 6 ≤ pH ≥ 12 MpIBP exhibited a reduction in mean largest grain size (MLGS) of ice crystals up to ~ 70% compared to control solutions and demonstrated dynamic ice shaping at 6 ≤ pH ≥ 10. The results substantiate that MpIBP retains some secondary structure and function in non-neutral pH environments, thereby enabling its potential utility in non-physiological materials science and engineering applications.

In a third study, single amino acids and homo polypeptides based on IBP ice-binding residues were investigated for their ability to influence ice-crystal growth in phosphate buffered saline

(PBS) using a modified splat assay to assess ice recrystallization inhibition (IRI), a measure of ice crystal growth inhibition. In PBS, the IRI activity of poly(threonine) at concentrations between 0.1-10 mg/ml reduced the mean largest grain size by ~75%. Based on its performance, threonine was chosen as a template to create a synthetic polymer mimic, poly(2-hydroxypropyl methacrylamide) (*pHPMA*). Poly(threonine) and *pHPMA* were investigated for their ability to influence ice-crystal growth in phosphate buffered saline (PBS), PBS solutions with alkaline pH (8-13), and 151.5 mM salt solutions with divalent cations relevant to infrastructure ($CaCl_2$ and $MgCl_2$). Overall, *pHPMA* reduced the mean largest grain size by ~60-75% at concentrations from 0.01-10 mg/ml, as well as inhibited ice growth by 80% at 10 mg/ml in pH 13 solution, demonstrating a viable option for mitigating ice growth in highly alkaline cementitious environments.

Considering that IBPs are an exemplary class of proteins with an ability to prevent ice formation in physiological environments, they offer a potentially disruptive model for creating bioinspired synthetic alternatives for ice growth mitigation in non-physiological environments for a variety of applications. It was shown that not only are IBPs prohibited by cost for application in non-native environments, but also by longevity. The crucial aspects of IBPs for their effect on ice growth inhibition i.e., ice-binding residues, structure-function relationship, were investigated, and it has been demonstrated that primary structure combined with ice-interactive residues is a crucial factor when considering design for ice recrystallization inhibitory materials. These results demonstrate that the ice-inhibition capabilities of future innovative bioinspired materials can be improved through incorporating amphipathic pendant groups, as demonstrated by the performance of poly(threonine) and *pHPMA* in non-physiological alkaline environments.

DEDICATION

To Kyle, Nyx, and Nya. I couldn't have done it without you.

ACKNOWLEDGEMENTS

First and foremost, I would like to thank the members of my committee: Dr. Yifu Ding, Dr. Stephanie Bryant, Dr. Ginger Ferguson, and Dr. Garret Miyake. I am most grateful to Dr. Wil V. Srubar III, who not only served as my principal investigator, but as a professional mentor, personal advocate, and even an emotional teacher. Your patience and kindness showed me what true compassion is, and your knowledge and guidance allowed me to persevere. This was not an easy road, and the encouragement I received from my committee has been crucial for my success.

I want to thank peers who have learned with me through the course of my PhD, those who I have bounced ideas around with, discussed the ups and downs of the research process, and all together made each day a little better. Patrick Thomas, I cannot begin to express how much I appreciate the time we spent together in the lab. You taught me so many meaningful skills and your patience and good humor made those repetitive months purifying proteins more bearable. I cannot believe my good luck that you decided to help a random student from another lab with a project so unrelated to your own research. Shane Frazier, I have never met anyone more committed to the scientific process. I am so grateful that we were on the same research team. Your abundant enthusiasm towards your work has been inspiring. You always know the right questions to ask and are the first with a fresh idea to try. I could always depend on your help with troubleshooting equipment or brainstorming for experiments. I'm glad for the research we were able to share.

I would like to thank the exceptionally gifted and motivated undergraduates who have worked with me through these various projects. To Kendra Bannister – I have never met a more capable young woman. Your ability to manage and navigate multiple responsibilities is astounding. To Aparna Lobo – your dedication and vigor will let you go wherever you want to in life. Your adept mind and ability to learn literally anything will only lead to resounding success.

I am fortunate to have received several fellowships through this process. The financial support gave me one less thing to worry about in an already anxious time of my life. I am appreciative of the Dean's Graduate Assistantship I received for the 2015-2016 academic year, and the ACI Presidents' Fellowship Award for the 2017-2018 academic year. I am most honored to have

I am so thankful for the other graduate students that made the day-to-day more exciting and who could commiserate on the graduate student experience. To Jesse Butterfield, I appreciate our chats about music and want to thank you for reminding me to nourish my forgotten hobbies. To Jorge Osio-Norgaard, I have learned so much from you, grown so much because of you, and our time as friends will always hold a spot in my heart. To Rob Wagner, thanks for being the best cat-uncle, weight-lifting buddy, and the most hilarious D&D companion.

To my mother, Joan Delesky. I know that science is not your forte. I know that academia is not exciting to you. I know that I never called as much as I should, and that it was hard to make it home, even during the holidays. You are the best mother and such a wonderful person, and your unconditional love and support made everything so much easier. Thank you for encouraging me when I wanted to quit. Thank you for having faith in me. Thank you for raising me.

I want to thank all my friends for helping me stay down to earth. Brian Estey, you are a constant reminder that there is a light at the end of the tunnel. Jay Farrow, all I can say is I miss you, and I look forward to a lifetime of oddities, plants, and wooden spoons. Cayla Cothron, my dearest love, my closest friend, thank you for all the late nights and phone calls discussing love, life, happiness, our futures, our parents, our faults, our dreams. Kyle Foster, I could never in a thousand lifetimes thank you enough. I don't quite have the words to give to you, so I won't even try. Just know that you're the reason I get up in the morning. You inspire me to work harder, work smarter, and to live my best life.

I am so grateful that my doctorate brought me to Boulder and the wonderful state of Colorado. I have developed and grown more than I ever thought would be possible, both professionally and personally. Coming to Boulder helped me learn that I can choose my own path that my passions can fluctuate and change.

<div align="right">
Elle Delesky

December 2020
</div>

CONTENTS

LIST OF TABLES

LIST OF FIGURES

CHAPTER 1
Introduction

1.1   Purpose of the Research.

The main objectives of the work were (1) to understand the performance of ice-binding proteins (IBPs) in non-physiological environments, (2) to elucidate which functional groups inspired by ice-binding residues from IBPs offer the greatest potential for inhibiting ice growth, and (3) to investigate a synthetic molecule designed from insights gained from objectives 1 and 2 to create an IBP mimic with improved performance.

1.2   Overview of Work and Organization of Dissertation.

Chapter 2 is a review that compares the performance of IBPs and synthetic replicates under the influence of non-physiological environmental factors. This review examined the performance of IBPs and synthetic replicates by ice recrystallization inhibition, thermal hysteresis, ice nucleation, or rate of growth. Non-physiological environmental factors examined include pH, salinity, and added sugars or polyols. In addition to considerations of environment, the review looks as the performance with consideration to material properties such as molecular weight or concentration. This review demonstrated a clear need for investigating molecules for IRI activity in both alkaline and acidic environments. The review in Chapter 2 is currently in preparation.

Chapter 3 of this dissertation focuses on the performance of an ice-binding protein from the Antarctic organism *Shewanella frigidimarina* (SfIBP) to inhibit ice growth in increasingly alkaline and ionic environments. SfIBP was procured from a collaborator in the biological sciences, Peter L. Davies, at Queen's University in Canada, who produced SfIBP using recombinant techniques with E. coli as a host strain and was purified using Ni-NTA agarose and size-exclusion chromatography purification techniques.[1] The purpose of this work was to determine an upper threshold of SfIBP ice recrystallization inhibition (IRI) activity in alkaline solutions (pH > 12) with increasing ionic strength. In this work, the effect of non-physiological environments on the

structural stability and IRI performance of SfIBP was investigated using circular dichroism spectroscopy, sodium dodecyl sulfate polyacrylamide gel electrophoresis, size-exclusion chromatography with an ultraviolet detector, and a modified splat assay.[2] The results in Chapter 3 have been published in Polymers.[3]

Chapter 4 investigates the performance of an ice-binding protein from the Antarctic organism *Marinomonas primoryensis* (*Mp*IBP) to inhibit ice growth and interact with the ice lattice in solutions with varied pH, from 2 to 13. Positive clonal colonies of *E. coli* expressing the *Mp*IBP ice-binding region were procured from a collaborator in the biological sciences, Peter L. Davies, at Queen's University in Canada. MpIBP was produced using recombinant techniques and purified using Ni-NTA agarose, ion exchange chromatography, and size-exclusion chromatography. The purpose of this work was to investigate the ability of the ice-binding region from a protein from the bacterium *Marinomonas primoryensis* (MpIBP) to control the size and inhibit the growth of ice crystals in non-physiological pH solutions ($2 \leq pH \geq 13$). In this work the effect of non-physiological pH environments on the structural stability, IRI activity, and ice-lattice interaction capabilities of MpIBP was investigated using circular dichroism spectroscopy, sodium dodecyl sulfate polyacrylamide gel electrophoresis, blue native polyacrylamide gel electrophoresis, size-exclusion chromatography with a multi-angle light scattering detector, a modified splat assay,[2] and dynamic ice shaping of a single ice crystal using a nanoliter osmometer. The results in Chapter 4 have been accepted for publication in Extremophiles.

Using bioinspired activity from Chapters 3 and 4, Chapter 5 investigates amino acid residues and their homo-polypeptides based on ice-binding residues present in ice-binding proteins. Three different amino acids and their homo-polypeptides were investigated by assessing ice recrystallization inhibition in PBS: a neutral amphipathic polar amino acid (L-threonine), a cationic polar amino acid (L-arginine), and an anionic polar amino acid (L-glutamic acid). The residue that exhibited the best ice recrystallization inhibition activity, threonine, was used as a molecular model for investigating a synthetic replicate in a wider array of techniques for ice inhibition performance. Chapter 5 goes on to investigate the ability of a bioinspired synthetic mimic comprised of 2-

hydroxypropyl methacrylamide (*HPMA*) and its polymer (*pHPMA*) for ice inhibition activity in alkaline environments (pH 8-13) as well as for possible synergistic effects with cationic salts ($CaCl_2$, $MgCl_2$, $CuCl_2$, $AlCl_3$). Ice interactions were investigated using differential scanning calorimetry, a modified splat assay,[2] and dynamic ice shaping. The *HPMA* monomer was synthesized in-house, and the *pHPMA* polymer was purchased from Sigma-aldrich. The results in Chapter 5 are currently in preparation.

Finally, Chapter 6 presents a summary of scientific contributions that this dissertation makes to the field of ice-binding proteins and bioinspired synthetic replicates for the mitigation of ice growth, specifically focused on broadening the application field to non-physiological environments such as infrastructure applications. Additionally, suggestions for future directions are discussed.

CHAPTER 2
Background

2.1   Introduction

Water is a common and readily available solvent that is used in most industrial fields, from medicine to infrastructure.[4] However, water has unique chemical and physical properties, such as expanding by 9% upon crystallization.[5,6] While ice expansion is an important feature in Earth's biosphere, the expansion upon freezing can cause a multitude of issues for systems containing water. For example, during cryopreservation, ice expansion can damage proteins[7–10] or rupture cells.[11–13] In food preservation, the formation and growth of crystallites can alter the texture of foods, making them unpalatable.[14–16] In infrastructure, the cyclic freeze-thaw of ice within concrete can induce cracking and failure.[17–21] Preventing ice-induced damage can expand the service life of materials and systems, saving money, resources, and time in the process.

To develop targeted mitigation strategies that prevent damage from ice growth, it is important to understand the properties and physical characteristics of ice. While ice is able to take on a variety of phases,[5] the most common for standard temperatures and pressures is 1H hexagonal ice, which exhibits a hexagonal crystal with lattice constants of a = 4.52 Å along the basal plane and c = 7.37 Å along the prism plane.[5] A microscopic crystallographic representation of 1H hexagonal ice with prominent basal plane and prism face can be seen in **Figure 1a**, and a macroscopic representation of a hexagonal ice crystallite with prominent basal plane and prism face is shown in **Figure 1b**.

A facile way to assess the growth of ice is to monitor recrystallization. A single ice crystal in a polycrystalline solid melts based on the diameter of the ice grain, which can be given by the Gibbs-Thomson effect (equation 1):

$$T_m(D) = T_{m,bulk}\left(1 - \frac{4\sigma_{sl}}{DH_f\rho_s}\right)$$

(1)

where $T_{m,bulk}$ (°C) is the melting temperature of the bulk solid (including solutes), and $T_m(D)$ (°C) is the melting temperature of a finite sized solid particle with a diameter D (cm) (*e.g.*, an individual ice grain). σ_{sl} (J/cm^2) is the interfacial energy at the solid-liquid interface, ρ_s (g/cm^3) is the density of the solid phase, and H_f (J/g) is the enthalpy of fusion. When $T_m(D)$ of a given ice

grain is greater than the recrystallization annealing temperature, it can exist stably, *i.e.*, without melting. However, for ice grains where $T_m(D)$ is greater than the annealing temperature, melt will occur. Certain materials (*e.g.,* proteins or polymers) can stabilize small ice crystals by interacting with the ice-water interface, thus increasing the energy required for recrystallization and preventing disruptive expansion.
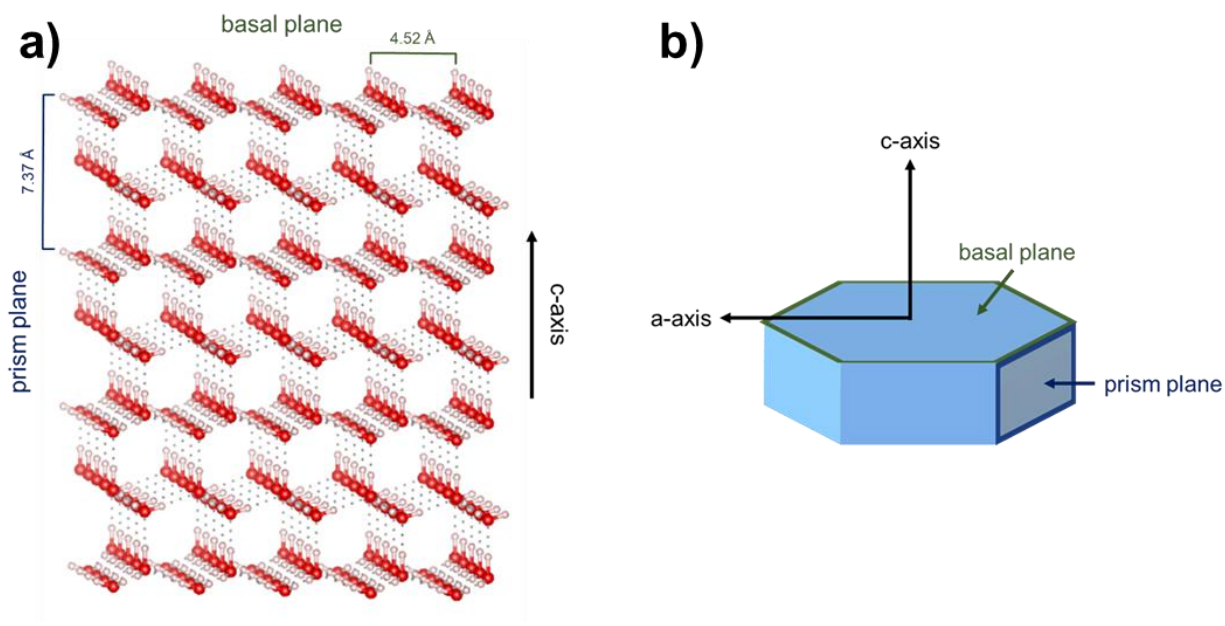
Figure 1. (a) Schematic demonstrating the microscopic hexagonal crystal of ice with prominent basal plane and prism face. Figure was made using VESTA software.[22] (b) Schematic representing a macroscopic hexagonal ice crystallite with prominent basal plane and prism face.

2.1.1   Ice-Binding Proteins

Ice-binding proteins (IBPs) are a robust series of proteins found in a wide array of organisms, ranging from plants,[23–26] fungi,[24,27,28] fish,[29–34] insects,[35–37] and microbes.[1,24,38,39] These proteins emerged through convergent evolution and thus display a variety of structures, amino acid sequences, and ice-interaction residues.[40,41] Most protein structures exhibit regular helices with spacing that matches the lattice structure of ice, while some proteins exhibit stabilized structures such as calcium ion (Ca^{2+}) coordination or disulfide bridges. Although different in structure, a subclass of IBPs called antifreeze proteins (AFPs) demonstrate similar ice interactions, namely:

(1) thermal hysteresis (TH) defined as a non-colligative depression of freezing-point while maintaining (or elevating) the melting point; (2) dynamic ice shaping (DIS) (*i.e.*, a reshaping of the 1H hexagonal ice crystal structure to form less disruptive ice geometries); and (3) ice recrystallization inhibition (IRI) (*i.e.*, a property that limits ice recrystallization through Ostwald ripening and reduces mean ice crystal size).[42] These ice interaction properties are more thoroughly described in **Section 2.2**. In parallel with IRI, the growth rate of ice crystals can be similarly affected by IBPs. Some IBPs exhibit a unique property, known as ice-nucleation, where ice formation is actually promoted due to the presence of the protein. This subclass of IBPs typically called ice-nucleating proteins (INPs) often work the same way as AFPs, but an increase in molecular size leads to a change in function.[41] For more information on IBP function, structure, and mechanism, comprehensive reviews have been published in the literature.[38,39]

The exact mechanism by which IBPs inhibit ice growth has not been fully explicated due to the sheer variety of IBPs. The prevailing mechanism that is widely agreed upon postulates that ice-interaction is facilitated by an array of quasi-liquid anchored clathrate-waters at the ice-IBP interface that aligns with the crystal lattice of ice.[40,43–45] Molecular dynamics has supported the importance of bound clathrate waters for ice interaction,[46–48] and genetic mutation studies have demonstrated that polar residues play a critical role.[49–54] Despite these advances, further fundamental understanding related to ice-IBP interactions is necessary to engineer effective bioinspired replicates.

Although not fully understood, the ice growth inhibition of IBPs is of interest for certain applications, such as cryopreservation. Traditional antifreeze agents (*e.g.*, ethylene glycol, dimethyl sulfoxide) for cryopreservation are known to be toxic to cells. In response, IBPs,[56] as well as chemical nucleation from crystalline cholesterol,[55] *Pseudomonas syringae*,[56] electro-freezing,[57] have been considered as potential alternatives to reduce cell toxicity. Cryogenic research indicates that IBPs may offer a new, biotechnological alternative to conventional antifreeze strategies for biological materials.[40,58] Previous research has shown that low concentrations of IBPs can be used to cryopreserve microorganisms, such as microalgae used to

6

produce insulin,[59] to improve the viability of rat kidneys post-thaw over conventional agents in media,[60] and to ameliorate follicular integrity of vitrified-warmed mouse ovaries.[61] Additionally, the efficacy of IBPs to reduce hemolysis of red blood cells upon thawing has previously been investigated. An IBP from the genus *Leucosporidium* significantly reduced hemolysis at concentrations of 0.4–0.8 mg/ml,[62] and three IBPs (AFPI, AFPII, and AFPIII) were shown to reduce hemolysis by 75% compared to controls.[63] The effects of IBPs on cryopreservation have been found to depend on IBP type and concentration, the preservation protocol, and biological material.[64] As an emerging biotechnology, IBPs have the potential to extend beyond biological applications to meet antifreeze needs of other industries in aerospace (*e.g.*, cryogenic fluids), civil engineering (*e.g.*, frost-resistant pavements), and energy infrastructure (*e.g.*, anti-icing coatings).

While IBPs have shown potential (*e.g.*, TH activity in micromolar concentrations and IRI activity in nanomolar concentrations),[40,41] widespread use of IBPs for large-scale applications may be limited due to (1) loss of functionality in different non-physiological environments, (2) limited yield for up-scaled IBP production, and (3) rapid expansion upon freezing. However, proteins are well known to restructure (*e.g.*, denature, aggregate, degrade) in non-physiological environments.[65] Changes in pH and ionic concentration may affect IRI activity of IBPs. Therefore, further investigation is needed to understanding the functionality IBPs in different non-physiological environments. Previous research has attempted to increase yield for IBP production (*e.g.*, 200 mg of IBP from a 5 L recombinant batch of yeast growth,[66] or 4.6 mg of IBP from 100 g of *Tenebrio molitor* larvae).[67] However, the quantity of protein produced (< 1 g) would be insufficient for large-scale applications. Finally, most IBPs demonstrate TH activity with a rapid and destructive ice 'burst' when reaching their new non-equilibrium freezing point temperature,[40] which poses a unique disadvantage for applications such as cell cryopreservation, as cells benefit from non-colligative freezing point depression but are susceptible to rapid ice expansion.[68] To address these limitations, further research is needed to characterize and modify IBPs as well as boost IBP production. Alternatively, IBP research can be used to inspire the development of synthetic IBP mimics that are easily produced in large quantities for a variety of commercial

industries (*e.g.*, cryogenics, aerospace, and infrastructure) while minimizing undesirable effects (e.g., restructuring and rapid expansion).

2.1.2 Ice Formation in Non-Physiological Environments

While IBPs offer a disruptive potential for physiological environments, ice can form in all systems where water is present, some of which contain constituents that are disruptive to proteins native folding structure, such as ions or pH. For example, AFPI found in winter flounder, *Pseudopleuronectes americanus*, prevents ice formation and growth within the organism at freezing sea temperatures reaching -1.9 °C.[69] For research purposes, IBPs are studied in solutions that mimic these natural environments (physiological) or simulate other environments (non-physiological). The physiological environments of most IBPs have a pH between ~6 and ~8, minimal concentrations of salts and sugars. As protein performance is dependent on properly folded secondary and tertiary structure,[65,70] having resilient alternatives that exhibit similar ice growth prevention activity to IBPs is a crucial step for materials that can better withstand non-physiological conditions. Many industry sectors, such as construction, renewable energy, and aviation, rely on antifreeze solutions, but ice formation in these applications occurs in non-physiological environments for IBPs.

Concrete is a material comprised of cement, water, and aggregate. Cement and water form a paste that binds aggregates together. The cement paste phase in concrete often has an water-cement ratio of 0.35-0.6,[71] and some of that water is present in a pore system.[72] In environments where concrete is exposed to subzero temperatures, ice expansion upon freezing of internal pore water produces pressure in the pores of concrete, which can lead to dilation and rupture.[17,18] Multiple and repetitive exposures to freezing and thawing, called freeze-thaw cycling, creates a cumulative effect that can ultimately lead to cracking, scaling, and crumbling of the concrete.[17,18] For more than 70 years, air entraining admixtures (AEAs) have been used to improve freeze-thaw resistance of concrete[73] through an air-void system that provides escape system pathways for the hydrostatic pressure created by ice crystal growth.[74] However, AEAs also reduce the strength and increase the

permeability of concrete proportionally to the amount of incorporated air.[17,75–79] The extreme chemical composition of concrete pore solution, which has a pH ~13 and a high ionic strength, makes it difficult to engineer new approaches and additives to prevent freeze-thaw damage.[80,81]

Alternative and efficient renewable energy technologies, such as wind and solar power, are of national and global importance, especially in lieu of the current climate crisis.[82–84] Novel energy technologies may be deployed around the world, from the tropics to the arctic, and the materials and devices must be able to withstand the environments in these extreme climates. In cold climates, ice can form on energy harvesting surfaces and can reduce efficiency,[85] such as ice formation on wind turbine blades can alter the aerodynamic profile and increase drag.[86] Additionally, ice formation on solar panel surfaces can reduce energy output due to obstruction.[87] Current methods to prevent ice formation on energy surfaces are energy intensive and require electronics to prevent the surface temperature from dropping below freezing,[85] and creating frost resistant surfaces could potentially improve the efficacy of renewable energy technologies in cold climates.

Aviation is effected during cold weather conditions due to ice formation on aircraft wings. Ice formation creates a rough surface that changes the airflow and can potentially lead to aerodynamic stall by increased drag and reduced lift force,[88] making it necessary to remove or prevent ice on wings. The most common plane deicer is ethylene glycol which can reduce the freezing point of water by up to ~50 °C,[89] a crucial temperature as the freezing point of ultrapure water found in clouds can be as low as -40 °C.[90] Ethylene glycol is sprayed onto aircraft wings, often with excess accumulating on the ground, which causes elevated environmental concerns for groundwater contamination as well as the death of nearby animals (mammalian and aquatic) that could potentially consume runoff.[91]

All of the proposed environments are non-physiological and could potentially disrupt protein folding, demonstrating a clear need for environmentally benign ice-growth prevention alternatives to address the demand for antifreeze solutions across industry sectors.

2.1.3 Synthetic IBP Mimics

Synthetic molecules present a unique advantage over IBPs as they offer tunable pendant moieties, architectures, and scalability for increasingly accessible ice-growth mitigation technologies and improved robustness in non-physiological environments. Identifying new materials that mimic IBP function, such as IRI activity, is crucial for targeting niche engineering applications in non-physiological environments. Antifreeze (glyco)proteins (AFGPs), a subset of IBPs, are among the most commonly mimicked IBPs as they demonstrate potent IRI activity at low concentraitons.[45,92–97] For example, poly(vinyl alcohol) (PVA) has exhibited notable biomimetic antifreeze behavior,[92–94,98] is easy to produce, and has shown promise for multiple cryopreservation applications.[68,99,100] One study demonstrated that 27 kDa PVA exhibited IRI behavior at concentrations as low as 0.05 mg/ml (1.6 μM),[98] which is comparable to the concentrations in which native IBPs are active. Other molecules, such as pigments,[101] polymer-modified nanoparticles,[102] polyampholytes,[103] quantum dots,[104] and nanocelluloses[105] also exhibit activity similar to IBPs. While certain synthetic molecules with varying chemistries have proven effective in terms of mimicking the antifreeze behavior of IBPs, further investigation and intentional design of synthetic molecules with exceptional biomimetic antifreeze behavior in non-physiological environments would broaden the application space in industry sectors that rely on antifreeze solutions.

2.2 Ice Interaction Properties and Characterization Techniques

Detailed below are methods used to investigate the influence of materials on ice formation and growth, many of which are employed in this work.

2.2.1 Thermal Hysteresis (TH)

Thermal hysteresis (TH) is the non-colligative depression of the freezing point of solution while maintaining or elevating the melting point, creating a temperature 'gap' between the freezing and melting temperatures. TH makes it more difficult for solution to freeze (when the temperature is being lowered) and more difficult for ice to melt (when the temperature is being elevated),

providing a stable temperature range. TH is one metric used to measure the efficacy of IBPs to prevent ice growth within organisms, and is typically characterized as moderate (~1 °C) or hyperactive (~5 °C or more).[40,106] TH was thought to be a unique property of IBPs until some synthetics were discovered to display marginal TH activity, such as zirconium acetate hydroxide (0.07 °C),[107] Safranine-O (0.6 °C),[101] and glucose carbon dots (0.02 °C),[108] although no synthetic has been able to match the TH activity of IBPs. TH can be measured through several means, and is often reported as ΔT (°C), taken as the difference between the non-colligative freezing point depression and the non-colligative melting point elevation induced by the material.

2.2.1.1 Using Osmometry to Measure TH Activity

The most common method for measuring TH is using a nanoliter osmometer. An aqueous sample is placed in immersion oil, frozen, and then slowly melted to achieve a single ice crystal, typically 10-50 µm in size. The temperature at which the single ice crystal is stable is taken as the melting point, and is often incubated at that temperature for 5-15 minutes to facilitate interaction of the material with the ice crystal. The temperature is then lowered at a slow rate (~0.01 C/min) until growth is observed. The difference between the melting point temperature and the temperature of growth is taken as the TH.[109] A microfluidic cold finger has been developed that observes TH similar to the osmometer, allowing precise nucleation and control of the single ice crystal.[110]

2.2.1.2 Using Other Methods to Measure TH Activity

While osmometry is the most commonly used method, other techniques have been developed to measure the TH activity of materials. In a study performed by Inada and Lu, a mm size ice crystal was grown, hollowed out, exposed to solution, and then monitored for ice growth, yielding a similar TH gap as osmometry.[111] Additionally, differential scanning calorimetry (DSC) has been used to observe TH by freezing the sample, then scanning for the melting point temperature. Once the melting point temperature is determined, the sample is frozen again, then heated until just

11

before the melting point, held for incubation, then frozen again to determine the TH based on the difference between the hold point temperature and the freezing point temperature.[112–114] However, DSC is not as frequently used because supercooling can occur in the DSC sample pan, leading to unpredictable and unreproducible freezing points.[115,116]

2.2.2 Dynamic Ice Shaping (DIS)

Dynamic ice shaping (DIS) is the reshaping of the 1H hexagonal ice structure by restricting growth in the plane of ice that the material is adsorbed to, and tends to be observed at concentrations lower than required for TH activity. For IBPs, the change in ice crystal geometry indicates that the growth of the crystalline plane of ice has been restricted, and is sometimes measured when TH activity is not available. Bipyramidal ice is seen when the prism plane of ice is restricted, and hexagonal ice is seen when both the prism and basal planes of ice are restrictred.[106] For materials other than IBPs, it has been shown that binding to the ice face is not required for ice growth inhibition, but changes in morphology are still seen. This is possibly due to material adsorption to the ice surface and preventing further ice growth through steric inhibition.[117] Often, DIS is observed through osmometry similar to TH although with the distinct lack of a TH gap.

2.2.3 Ice Recrystallization Inhibition (IRI)

Ice recrystallization is the process through which larger ice crystals expand at the expense of smaller ice crystals, a phenomenon known Ostwald ripening.[42] Ice recrystallization inhibition (IRI) is the limitation of ice recrystallization through the Gibbs-Thompson effect. Several methods have been established to determine the IRI activity of a material. The most common unit of reporting is percent mean largest grain size (%MLGS), which constitutes measuring ice grains along their longest axis and then normalizes the size by the blank solution tested, allowing a normalized comparison across solution type, and even test method. IRI activity ranges from negligible to moderate to potent. Negligible IRI activity is described by a large %MLGS (> ~80), whereas potent

IRI activity is described by a small %MLGS ($< \sim 30$), and moderate activity lies between negligible and potent. For preventing ice-induced damage, potent IRI activity is favored because it correlates to ice formation and growth inhibition.

2.2.3.1 Using Splat Assays to Measure IRI Activity

The splat assay was established in 1986 by Knight *et al.*[118] The splat assay creates a monolayer of polycrystalline ice by dropping a 10-20 µl droplet from ~2-3 m onto a chilled glass slide, typically resting on top of an aluminum block that is chilled by dry ice. The glass slide with the ice monolayer is then transferred to a cold stage on a microscope and annealed at a sub-melting point temperature (approx. -6 to -15 °C) to monitor ice recrystallization over time. Wu *et al.* determined that the sub-melting point or annealing temperature for the splat assay plays a more critical role in ice grain size than nucleation temperature, and that larger ice grains will be seen with warmer annealing temperatures.[119] Briefly, nucleation is the random formation of nascent crystals, and further described in **Section 2.2.5**. The sample is often incubated at the annealing temperature for time intervals ranging from 30 min to 18 hours, depending on the IRI activity of the molecule (e.g., more time is needed for stronger IRI activity). The data is reported either qualitatively by comparing micrographs at given time points, or quantitatively by reporting %MLGS. It has been shown that deionized or ultrapure water will provide false positives, as any molecule in pure water will accumulate at the ice grain boundaries and prevent ice recrystallization. [120] Thus, salt additives are necessary to keep the molecules at the solid-liquid interface, and active molecules will prevent ice recrystallization whereas inactive molecules will not.

2.2.3.2 Using Sucrose Sandwich Assays to Measure IRI Activity

The sucrose sandwich assay was developed by Worrall *et al.* in 1998[121] but only became widely used after method validation by Budke and Koop in 2006.[98] The sucrose sandwich assay is performed by adding the material of interest to a sucrose solution (20-40% sucrose) and sealing $\leq$

1 µl of solution between two pieces of coverslip glass using silicone grease. The sandwich is flash frozen by exposing it to a temperature of -50 °C or less to create a polycrystalline sample, then placed on a microscope cold stage (approx. -6 to -15 °C) and annealed between 1 and 18 hours with monitoring at one or more time intervals. The data is reported similar to the splat assay, as either qualitative micrographs or by quantitative %MLGS. The sucrose sandwich assay offers an advantage for monitoring solutions with insoluble components, because the high percentage of sucrose prevents interference from the insoluble particles. Additionally, quantitative analysis can be performed computationally due to the lack of grain impingement in the sucrose sandwich assay. However, the high percentage of sucrose in solution also slows the ice recrystallization process requiring longer annealing times to get an accurate comparison of material performance.

2.2.3.3 Using Other Assays to Measure IRI Activity

One of the drawbacks for both the splat and sucrose sandwich assays is the time required to monitor the IRI activity of a single sample. A few techniques have been developed to improve the throughput of IRI testing; however, they have yet to be widely adopted.

A capillary tube assay was developed by Tomczak *et al*. in 2003.[122] The capillary tube assay is performed by sealing samples in a 10 µl capillary tube (1 mm outer diameter) and snap freezing by placing into chilled 2,2,4-trimethylpentane (approx. -50 °C by dry ice). The samples are then transferred to a jacketed beaker filled with the same solvent cooled to the annealing temperature. The capillary tube assay allows for multiple samples (~15) to be viewed at once for side-by-side comparison and allows for long-term storage of the samples. However, the quality of image is reduced due to the curvature of the capillary tubes and direct grain counting is obscured. Thus, the capillary tube assay increases throughput but provides qualitative instead of quantitative measurements.

A high-throughput antifreeze protocol (HTAP) using a 96-well microtitre plate assay was developed by Gilbert *et al*. in 2004.[39] Samples are loaded into a 30% sucrose solution and compared to positive (IRI active) and negative (IRI inactive) controls. The plate is flash frozen at

-70 °C and held for 10 minutes, and then placed on a cold stage to anneal for 5 days. Samples that remain frozen after annealing are said to be IRI active, while samples that melt are inactive. The HTAP method allows for high throughput of samples with a qualitative comparison, however, the 5-day incubation period is long and the protocol can lead to false positives.

A high-capacity endpoint device was developed by Graham *et al*. in 2018 that allows up to 12 samples to be compared side-by-side.[123] The endpoint device consists of a sapphire slide with 8-12 sample wells of about 45 µm surrounded by a super-hydrophobic coating. Samples of approximately 1 µl are loaded into the sample wells, and a slide with a fluorinated surface coating of trichloro(1H,1H,2H, 2H-perfluorooctyl)silane is placed on top of the sample. The sample is then annealed and monitored for grain growth. The high-capacity device is able to produce high-quality images with a possibility for quantitative comparisons and can be washed with a detergent for repeated use. However, this method requires sapphire slides for high-quality images and a specially manufactured device making it potentially cost prohibitive compared to other IRI measurement methods. Finally, the super hydrophobic coating is sensitive to pH, so samples cannot be tested in some pH environments (*e.g.,* alkaline) using this method.

2.2.4 Ice Growth Rate

Rate of growth investigates the change in ice crystal size, often along a specified ice crystal axis (**Figure 1b**), over time at a set temperature below the freezing point of solution. Currently, there is no well-established method to measure rate of growth, but research has been completed to develop some experimental techniques.[107,124,125] Of note, the rates and units often differ based on the method employed, which makes it difficult to directly compare results across methodologies.

2.2.4.1 Using Osmometry to Measure Ice Growth Rate

Similar to measuring TH, osmometry can be used to determine ice growth by monitoring the growth of a singular ice crystal. A singular ice crystal is monitored for changes in diameter across either the a-axis or c-axis of ice, and reported as a unit of µm/sec or µm/ms. Typically multiple

holding temperatures below the freezing point of solution will be used and expressed as Δ°C below freezing, and often performed in increments of 0.01 or 0.02 °C. Rate determination using osmometry is sometimes used as a method to report TH activity for molecules with marginal TH, as rates less than 0.02 µm/sec are considered to be TH active.[107] Values are often reported as rate as a function of Δ°C, and tend to exhibit a sigmoidal shape.

2.2.4.2 Using Sucrose Sandwich Assay to Measure Ice Growth Rate

The sucrose sandwich assay described above in **Section 2.3.2** is sometimes used to determine the rate of growth. Since the ice grains are well defined and do not undergo impingement, the sample can be monitored using a camera at multiple pre-determined time intervals to observe and quantify ice grain diameter over time. Ice growth rate measurements are often reported as $µm^2$/min or $µm^3$/min. A circle Hough transform (CHT) algorithm has been developed to improve the processing and facilitate rapid analysis and material comparison.[124]

2.2.4.3 Using the Silicon Isolator Method to Measure Ice Growth Rate

The silicon isolator method was developed by Huang *et al*. and is performed by sealing ≤ 20 µl of sample in silicon isolator wells between two glass slides and placed on a room temperature thermal microscope stage. The sample is then cooled and monitored for ice growth using a camera. The rate of growth is quantified by measuring the advancement of the ice crystal front over time, and reported as µm/sec.[125]

2.2.5 Ice Nucleation

Some IBPs exhibit a property known as ice nucleation and readily enable the heterogeneous formation of ice crystals. Ice nucleation is useful for atmospheric science, specifically with regard to cloud formation.[126–128] At present, ice nucleation tends to be a less studied property of materials, thus a singular method for determining ice nucleation efficacy has not been well-established. However, two main methods of investigating ice nucleation have been reported, percentage of droplets frozen,[94,96,116] and time until nucleation.[129–131]

2.5.1 Using Percentage of Droplets Frozen to Measure Ice Nucleation

An array of ~1 µl sample droplets are placed in wells or separated by a hydrophobic surface. The surface is then placed on a microscope cold stage set to ambient temperature (15-20 °C) and monitored with a camera. The stage is cooled at a constant rate, normally from ambient to -40 °C to ensure a uniform and equilibrium cooling of the samples. Nucleation is reported as the percentage of droplets frozen at a given temperature, and most experiments are performed until 100% of samples have frozen.[94,96,116]

2.5.2 Using Time until Nucleation to Measure Ice Nucleation

A drop of solution is placed in an isolated sample cell, often composed of a hydrophobic sealant (*e.g.*, a silicon o-ring) that is then positioned between two cover glass slips. Ice nucleation is measured by monitoring the time it takes for ice formation after the substrate equilibrates at a specific temperature, and the time until nucleation is reported in milliseconds or seconds.[129,130]

An additional time until nucleation method was developed by Akhtar *et al*.,[131] where the ice prevention capabilities of hydrophobic surfaces was determined by dispensing ~4 µl of water onto the surface, lowering the temperature to a set holding temperature, and monitoring the time until freezing. Results are reported in milliseconds or seconds and describe the time until freezing at the holding temperature.

Table 1. Overview of experimental techniques as well as the information in the table. The filled and unfilled cells represent quantitative and qualitative measurements, respectively.

Experimental Technique	Measure of Performance				
	TH	DIS	IRI	Rate of Growth	Ice Nucleation
Osmometry	✔	✔		✔	
mm crystals	✔				
Differential Scanning Calorimetry	✔				
Splat Assays			✔		
Sucrose Sandwich Assays			✔	✔	✔
Capillary Tube Assay			✔		
HTAP Assay			✔		
High-Throughput Device Assay			✔		
Silicon Isolator Assay				✔	
%Droplets Frozen Assay					✔
Time until Nucleation Assay					✔

2.3 Effect of Environment on Ice Interactive Materials

Engineering applications tend to have varied, non-physiological environments that are system specific. However, the majority of research pertaining to TH and IRI is performed in natural, physiological environments of the ice interactive material (i.e., neutral pH and low salt). Herein is a review of material performance in physiological environments as well as literature tools to facilitate decisions for adding synergistic materials for the prevention of ice formation and growth in select engineering applications. The data available for some environments are limited, demonstrating a clear need for further research (**Section 2.4**).

2.3.1 Physiological Environments

For research purposes, physiological environments with a neutral (~7) pH and minimal solution additives (*e.g.*, salts, sugars, etc.) are the most common for investigating ice formation and growth. Controlling ice formation and growth in physiological environments is crucial for applications such as food storage and medical cryopreservation. Additionally, physiological environments provide a baseline for material performance to determine deviations in efficacy when compared to different non-physiological environments.

2.3.1.1 TH Activity of IBPs in Physiological Environments

IBPs are produced by biological organisms to regulate internal ice formation and growth, thus, IBPs evolved to function in physiological environments (*i.e.*, solutions with a pH ~6 to ~8 and low salt or sugar concentrations). IBPs that exhibit TH are often categorized as AFPs and subcategorized based on the upper limit of TH activity, most commonly as hyperactive or moderately active. However, some materials display lower limits than moderate, which are referred to herein as marginally active.

Figure 2 shows an overview of TH activity compared to molecular concentration (C) in physiological environments for different AFPs. **Table 2** demonstrates how to quantitatively determine molecule classification for TH activity (*e.g.*, when TH activity is presented as °C vs √C, if the slope > 0.8, the molecule is considered hyperactive). The data included in **Figure 2** is not exhaustive due to the sheer number of AFP TH studies, but uses a representative data set to demonstrate the range of TH activity. In general, TH is proportional to concentration, and often increases with the square root of the concentration of the active molecule.[41] As shown in **Figure 2a**, hyperactive AFPs tend to have a maximum TH activity of ≥ 5 °C and often originate from insects.[40] An exception is the hyperactive Maxi AFPI from the arctic winter flounder *Pseudopleuronectes americanus*.[29] Typically, fish AFPs (AFPI, AFPII, and AFPIII) are moderately active, with a TH ~1 °C. Antifreeze glycol proteins (AFGPs) exhibit TH activity between marginally active and moderately active, and more often are present in organisms for IRI activity as opposed to TH activity.[30,132] Most synthetics that exhibit TH activity are considered marginally active with TH activity < 0.5 °C. Notably, safranine-O has been shown to have a TH ~0.6 °C, making it a comparable replicate of AFGPs.[101]
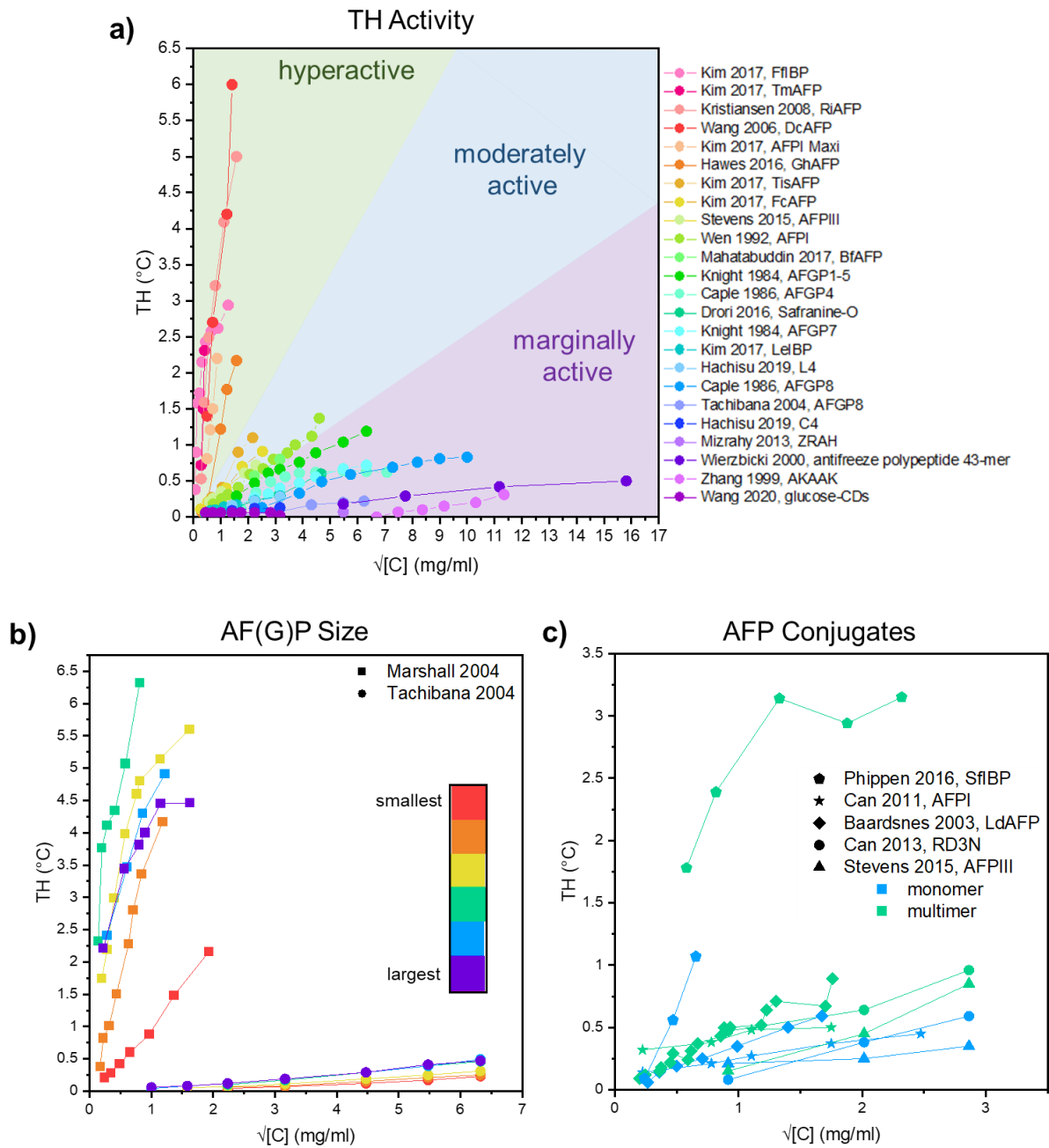
Figure 2. (a) Thermal hysteresis of select AFPs in physiological environments to show the range of TH activity. (b) Thermal hysteresis of genetically modified AFPs by increasing the size of the protein using repeating motifs within the AFP sequence. (c) TH activity by creating AFP multimers.[69,101,139–148,107,149,108,133–138]

Hyperactivity in AFPs is facilitated by an array of ice-binding residues that are able to bind to both the basal and prismatic faces of ice, inducing high thermal hysteresis activity. Ice-binding residues that occur across species are often threonine, asparagine, aspartic acid, and other polar,

slightly hydrophobic residues.[40] Wen *et al*. demonstrated the importance of neutral polar residues for TH activity.[69] Moderately active proteins tend to bind to only the prism face, resulting in lower TH activity. Marginally active materials, such as synthetics, are expected to adsorb to the ice surface instead of binding to the ice lattice,[117] which results in even lower TH activity, if any. However, further investigations are required to explicate the synthetic mechanism for TH activity.

Some research is dedicated to discovering the existence of IBPs in a diversity of organisms.[40,150] These investigations use site-specific mutagenesis to determine crucial amino acid residues for TH activity.[50,51,53,54] Additionally, improving TH activity of AFPs is investigated by size modifications through replicating motifs of ice-binding amino acid sequences[145,151] or by conjugation two or more AFPs to improve activity.[137,147–149,152] AFP size modifications, shown in **Figure 2b**, show that as size increases, activity increases. However, Marshall *et al.* determined that there are diminishing returns after a certain size.[145] It was hypothesized the optimum size for TH activity is limited by proper folding from structure alterations, as proteins that become too large no longer exhibit lattice matching due to misfolded structure. In **Figure 2c**, using a polymer or other linkage to create conjugated AFP multimers increases functionalization density and consequentially increased TH activity.

Table 2. Slopes for data in **Figure 2a** to demonstrate hyperactive (slope > 0.8), moderately active (0.8 > slope > 0.2), and marginally active (slope < 0.2) materials with TH activity.

Material	Slope	Classification	Reference
FfIBP	1.73	hyperactive	Kim *et al.*, 2017[150]
TmAFP	12.1	hyperactive	Kim *et al.*, 2017[150]
RiAFP	3.23	hyperactive	Kristiansen *et al.*, 2008[134]
DcAFP	4.5	hyperactive	Wang *et al.*, 2006[135]
AFPI Maxi	3.71	hyperactive	Kim *et al.*, 2017[150]
GhAFP	1.81	hyperactive	Hawes *et al.*, 2016
TisAFP	0.59	moderately active	Kim *et al.*, 2017[150]
FcAFP	0.36	moderately active	Kim *et al.*, 2017[150]
AFPIII	0.3	moderately active	Stevens *et al.*, 2015[137]
AFPI	0.28	moderately active	Wen *et al.*, 1992[69]
BfAFP	0.25	moderately active	Mahatabuddin *et al.*, 2017[138]
AFGP1-5	0.18	marginally active	Knight *et al.*, 1984[118]
AFGP4	0.07	marginally active	Caple *et al.*, 1986[140]
Safranine-O	0.14	marginally active	Drori *et al.*, 2016[101]
AFGP7	0.12	marginally active	Knight *et al.*, 1984[118]
LeIBP	0.09	marginally active	Kim *et al.*, 2017[150]
L4	0.07	marginally active	Hachisu *et al.*, 2019[142]
AFGP8	0.09	marginally active	Caple *et al.*, 1986[140]
AFGP8	0.05	marginally active	Tachibana *et al.*, 2004[153]
C4	0.02	marginally active	Hachisu *et al.*, 2019[142]
ZRAH	--	marginally active	Mizrahy *et al.*, 2013[107]
antifreeze polypeptide 43-mer	0.03	marginally active	Wierzbicki *et al.*, 2000[143]
AKAAK	0.06	marginally active	Zhang *et al.*, 1999[144]
glucose-CDs	0	marginally active	Wang *et al.*, 2020[108]

2.3.1.2 IRI Activity of Synthetic Materials in Physiological Environments.

IBPs that exhibit potent IRI activity are often produced by organisms that tolerate freezing as opposed to avoiding it, such as plants or fungi. Prioritizing IRI over TH activity ensures that sensitive internal structures, such as cell walls, are not ruptured during the freezing process. As the IRI activity of AFPs has been covered extensively,[133,154–156] the focus of this review will be how developed synthetic materials effect the recrystallization of ice. Accordingly, the IRI activity of various water soluble materials are shown in **Figure 3**, where IRI activity becomes more potent as %MLGS becomes bluer. Additionally, the IRI activity of materials that form suspensions or

complexes in solution be seen in **Figure 4**. For comparison to the synthetic materials shown **Figure 3** and **Figure 4**, some AFPs have been shown to exhibit potent IRI activity (< 15% MLGS) at nanomolar concentrations. For example, Capicciotti *et al*. reported %MLGS of 5.4%, 11.9%, 11.9%, and 13.4% in nanomolar concentrations of 0.0033 mg/ml, 0.0132 mg/ml, 0.00182 mg/ml, and 0.000743 mg/ml for AFPIII, AFGP-8, AFPI, and LpAFP, respectively.[157]

Figure 3a focuses on the molecular weight and concentration dependence of PVA on IRI activity, as PVA has been shown to be a readily accessible synthetic molecule that exhibits potent IRI activity. **Figure 3a** demonstrates that as PVA molecular weight increases, PVA continues to elicit IRI activity even at lower concentrations. In addition to the data presented in **Figure 3a**, Hedir *et al*. installed degradable ester linkages to form PVA-block-MDO (2-methylene-1,3-dioxepane) to investigate the retention of IRI activity post degradation and found that a 5% incorporation of degradable linkages led to marginal retained activity after decomposition.[158] Vail *et al*. investigated the effect of PVA polydispersity on IRI activity and found (a) PVA needs ~20 repeat units (MW ~1 kDa) before it becomes IRI active, and (b) polymers with larger polydispersity exhibit IRI activity due to the largest polymers in the dispersion.[159]

Figure 3b focuses on the IRI activity of polymers other than PVA. It is shown that most polymers elicit moderate IRI activity (~40-70%MLGS) at best, indicating the chemical structure of PVA plays a crucial role in eliciting IRI activity. In addition to the data in **Figure 3b**, Mitchell *et al*. investigated an array of polyampholytes for IRI activity and found that a 50:50 ratio of anionic to cationic charges demonstrated moderate IRI activity at best;[93] however, it has been shown that polyampholytes improve cell-viability post-thaw without potent IRI activity.[160,161] Stubbs *et al*. determined that increasing the hydrophobicity of a PVP pendant moiety increased the IRI activity,[97] which aligns with amino acid substitution studies demonstrating the importance of hydrophobicity for ice-binding residues. Thus, although the IRI activity is less potent compared to PVA, other polymers offer different properties than PVA.

Figure 3c presents the IRI activity of small molecules. In general, as solute concentration increases (> 100 mg/ml) IRI activity can be evoked, corroborating that the interruption of the ice hydrogen bonding network can reduce ice crystal size.
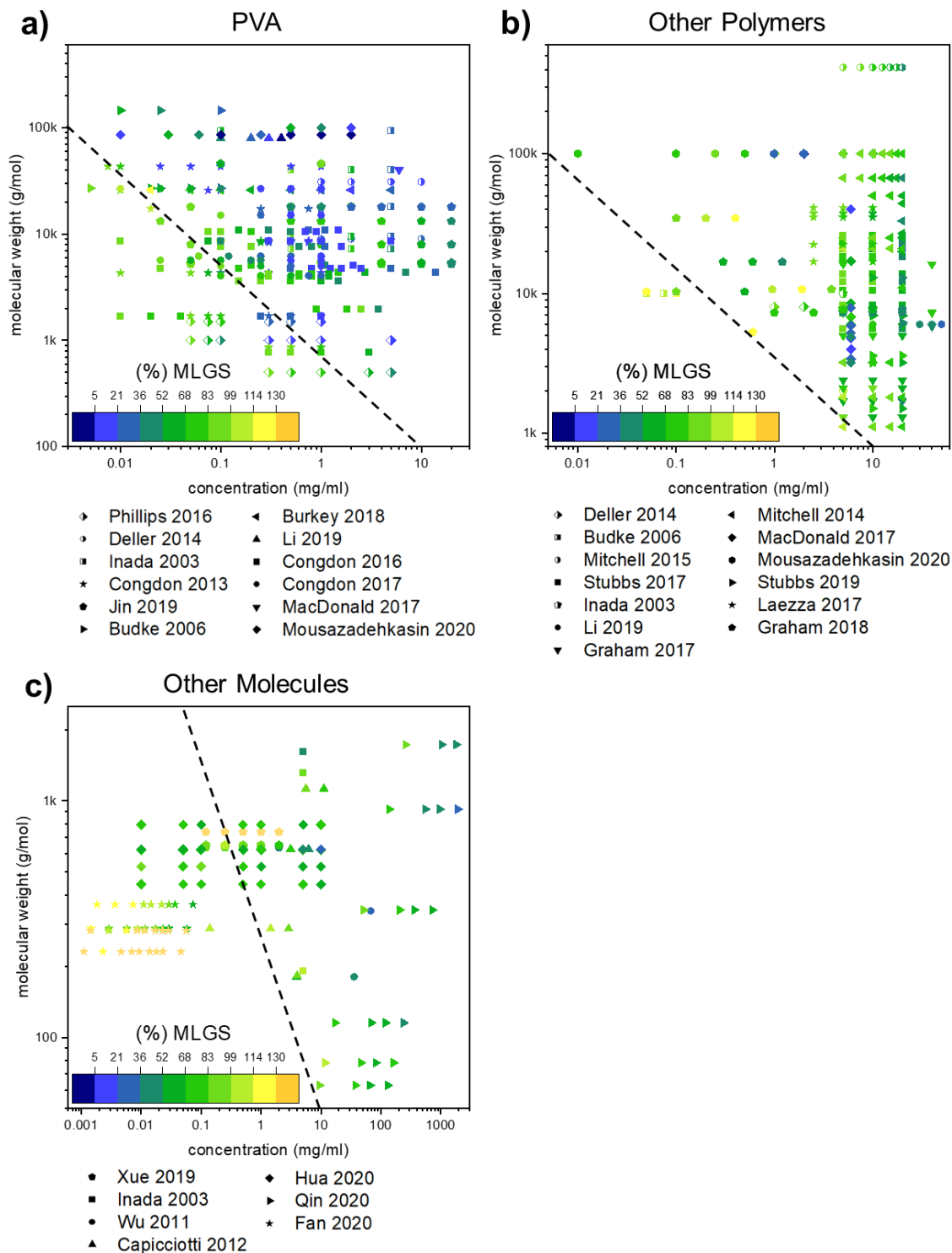
Figure 3. IRI performance of synthetic molecules where IRI activity increases as %MLGS becomes bluer compared to molecular weight and concentration for (a) PVA, (b) other polymers, and (c) other small molecules (e.g, surfactants, sugars and polyols). The lines on each graph indicate the upper limits for molecular weight and concentration for most materials to exhibit moderate IRI activity.[68,93,166–175,98,176,103,105,117,162–165]
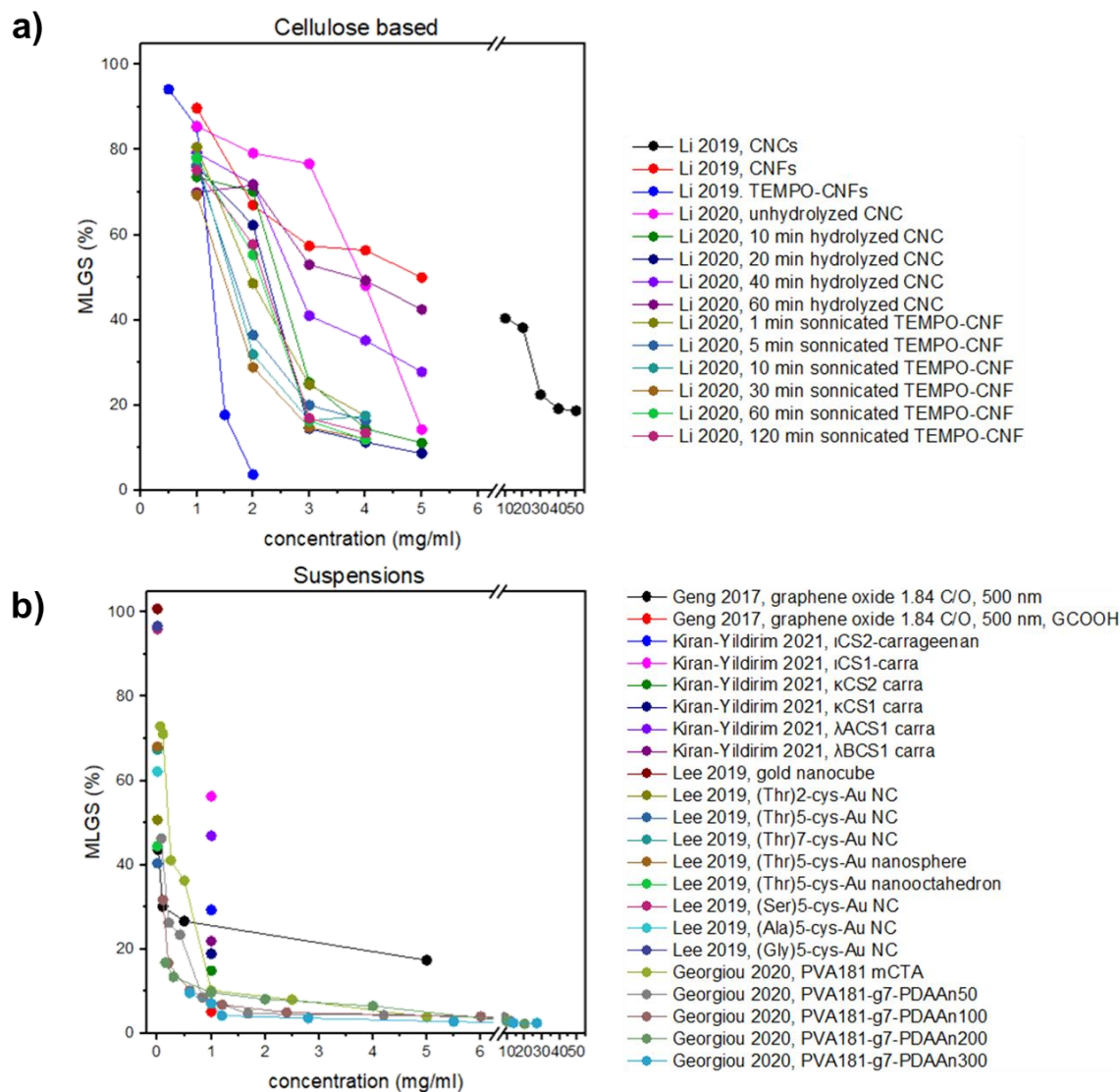
Figure 4. IRI activity shown in %MLGS compared to concentration for materials that form suspensions or complexes in solution. IRI activity for (a) insoluble cellulose-based molecules that form suspensions, and (b) other material suspensions.[105,177–182]

Figure 4a shows the concentration dependence of cellulose based materials on IRI activity, where a decrease in %MLGS corresponds to an increase in IRI activity. **Figure 4a** indicates that cellulose-based materials demonstrate moderate IRI activity (~30-50%MLGS). Of these materials, TEMPO cellulose nanofibers were shown to elicit the best IRI activity reaching 5%MLGS at a concentration of 2 mg/ml. **Figure 4b** demonstrates the effect of other material suspensions on IRI activity The best IRI performing material is a self-assembling PVA nano-sphere, which has a 5

%MLGS at a concentration of 1 mg/ml. This is expected since large PVA molecules exhibit potent IRI activity, as shown in **Figure 3a**. Graphene oxide, carrageenans, and conjugated gold nanoparticles exhibit moderate IRI activity with %MLGS of 27%, ~30%, and 40% at concentrations of 0.5 mg/ml, 1 mg/ml, and 0.2 nM, respectively. Thus, suspensions have potential for engineering applications that require solutions with low-solubility.

Additional studies have shown the importance of material synergy and the effect of high concentration ($\geq$ 20 mg/ml) on IRI activity (<50% MLGS). Gaukel *et al*. investigated the synergistic effect of hydrocolloids with AF(G)Ps to improve IRI activity and found that k-carrageenan improved the efficacy of AFPI, AFPIII, and AF(G)P.[183] Mitchell *et al*. determined that 20 mg/ml of various albumins (bovine, ovine, and human) demonstrated about 50% MLGS, indicating that at high concentrations, non-active materials can demonstrate moderate IRI activity by interrupting ice interactions.[184] Graham *et al*. reported that a 22-amino-acid truncated peptide with a photoreactive functionality (anthracene) could demonstrate photo-switchable IRI activity.[185] In general, the IRI efficacy of highly active synthetics, such as PVA, is dominated by molecular weight, whereas the efficacy of moderately active synthetics is dominated by concentration.

2.3.1.3 Ice Growth Rate of Synthetic Materials in Physiological Environments

Controlling the ice growth rate can be just as crucial as the final size of ice crystals. Since there is no established method for determining the ice growth rate (**Section 2.2.4**), there is no standard unit of measurement across studies or methodologies. However, an overview of experimental data for different synthetic materials is shown in **Table 3**. For reference to AFPs, the ice growth rate of AFGP1-5 and AFPIII in 30% sucrose solution has been reported as 0.67 um^3/min and 1.03 um^3/min in concentrations of 0.000012 mg/ml and 0.003 mg/ml.[186]

Olijve *et al*. demonstrated that PVA is effective at reducing the rate of growth of ice, further supporting PVA as a robust AFGP mimic.[124] Xue *et al*. and Drori *et al*. both demonstrated that self-assembling molecules facilitate ice growth retardation, indicating that ice lattice matching is

important for reducing the growth rate of ice.[101,171] However, the self-assembling molecules were not tested in non-physiological environments, and it is uncertain whether or not they would remain robust in the presence of external stressors such as high salt content or pH adjustors. Bai *et al*. and Geng *et al*. demonstrated that carbon based materials marginally slow the growth rate of ice.[104,179] Fan *et al*. determined that non-charged surfactants below their critical micelle concentration increase the growth rate of ice, contrary to some of the ice-binding residues found on IBPs.[175] The data presented in **Table 3** demonstrates that relatively high concentrations of synthetics (> 1 mg/ml) can mimic the rate growth reduction efficacy of AF(G)Ps.

Table 3. Overview of growth rates for synthetic materials in physiological environments.

Reference	Material	Environment	[C]	ΔT (°C)	Rate of Growth
Hua *et al*., 2020[176]	P-Nme	PBS	10 mg/ml	0.02	4.2 um/sec
	P-Net	PBS	10 mg/ml	0.02	1.2 um/sec
	P-Nae	PBS	10 mg/ml	0.02	5.8 um/sec
	P-Nce	PBS	10 mg/ml	0.02	4.8 um/sec
	P-Nhe	PBS	10 mg/ml	0.02	3.1 um/sec
Xue *et al*., 2019[171]	2-NapGFFT	PBS	1 mg/ml	0.12	2.0 um/sec
	2-NapGFFTT	PBS	1 mg/ml	0.12	1.2 um/sec
	2-NapGFFD	PBS	1 mg/ml	0.12	4.1 um/sec
Drori *et al*., 2016[101]	Safranine-O	water	14 mM	0.08	4.9 um/sec
		water	28 mM	0.08	3.8 um/sec
		water	62 mM	0.08	0.6 um/sec
Bai *et al*., 2017[104]	--	water	--	0.1	45.6 um/sec
	OCN	water	4 mg/ml	0.1	34.5 um/sec
	OQCN-180-3	water	4 mg/ml	0.1	26.8 um/sec
	OQCN-180-6	water	4 mg/ml	0.05	26.3 um/sec
	OQCN-200-1	water	4 mg/ml	0.07	22.3 um/sec
	OQCN-200-3	water	4 mg/ml	0.06	7.3 um/sec
	OQCN-200-6	water	4 mg/ml	0.05	14.1 um/sec
Fan *et al*., 2020[175]	--	water	--	--	2.7 um^2/min
	SDS	water	100 mM	--	1.8 um^2/min
	OA-12	water	100 mM	--	6.1 um^2/min
	DTAB	water	100 mM	--	2.0 um^2/min

	NA	water	100 mM	--	5.6 um^2/min
Huang _et al._, 2012[125]	--	water	--	--	1.7 um/sec
	Ac(Sar)$_3$	water	10 mg/ml	--	0.9 um/sec
	Ac(Nme)$_3$	water	10 mg/ml	--	0.8 um/sec
	Ac(Nser)$_3$	water	10 mg/ml	--	0.2 um/sec
	Ac(Ser)$_3$	water	10 mg/ml	--	0.8 um/sec
Geng _et al._, 2017[179]	--	0.14 M NaCl	--	0.04	3.7 um/sec
	C/O 1.84, 10 nm	0.14 M NaCl	1 mg/ml	0.04	0.3 um/sec
	C/O 1.84, 500 nm	0.14 M NaCl	1 mg/ml	0.04	2.4 um/sec
	C/O 1.84, 5000 nm	0.14 M NaCl	1 mg/ml	0.04	0.6 um/sec
	C/O 1.84, GCOOH, 500 nm	0.14 M NaCl	1 mg/ml	0.04	6.7 um/sec
	C/O 1.9, 500 nm	0.14 M NaCl	1 mg/ml	0.04	4.4 um/sec
	C/O 1.92, 500 nm	0.14 M NaCl	1 mg/ml	0.04	6.1 um/sec
	C/O 2.18, 500 nm	0.14 M NaCl	1 mg/ml	0.04	10.3 um/sec
Olijve _et al._, 2016[187]	PVA (~8kDa)	30% sucrose	0.2 mg/ml	--	0.03 um^3/min
		30% sucrose	2 mg/ml	--	0.001 um^3/min
	PVA bottle brush (~636 kDa)	30% sucrose	0.2 mg/ml	--	0.008 um^3/min
		30% sucrose	2 mg/ml	--	0.013 um^3/min

2.3.1.4 Ice Nucleation of Synthetic Materials in Physiological Environments.

Materials that promote ice nucleation could lend reproducibility to a typically random phenomenon that is often of interest for atmospheric science. As described in **Section 2.2.5**, ice nucleation tends to be determined two ways: _via_ percentage of droplets frozen (**Table 4**), or by time until nucleation (**Table 5**). In general, suspended materials such as carbon nanotubes and graphene oxide promote ice nucleation at temperatures above that of blank solution.[116,188] PVA was shown to prevent ice nucleation,[189] which is expected based on the IRI activity of PVA seen in **Figure 3a**. Ionic charged peptide surfaces exhibited tunable ice nucleation temperatures based on the number of peptide residues and the charge of the peptides.[129]

Table 4. Overview of materials that exhibit ice nucleation as determined by percentage of droplets frozen.

Reference	Material	Environment	[C]	T (°C)	Rate (°C/min)	Droplets Frozen
Congdon *et al.*, (2015)[94]	none	water	--	-20.7	2	100%
	PVA 13	water	1 mg/ml	-24.8	2	100%
	PVA 73	water	1 mg/ml	-29.2	2	100%
	PVA126	water	1 mg/ml	-27.9	2	100%
			10 mg/ml	-23.3	2	100%
	PVA 183	water	1 mg/ml	-25.4	2	100%
	PVA 322	water	1 mg/ml	-29.4	2	100%
	PVA 366	water	1 mg/ml	-25.6	2	100%
			10 mg/ml	-37.0	2	100%
	PVA 710	water	1 mg/ml	-26.3	2	100%
	pNIPAM67	water	10 mg/ml	-24.8	2	100%
	pNIPAM152	water	10 mg/ml	-29.7	2	100%
	pNIPAM452	water	10 mg/ml	-25.8	2	100%
	pOEGMA224	water	10 mg/ml	-26.0	2	100%
	Dextran	water	10 mg/ml	-25.4	2	100%
	pHEA	water	10 mg/ml	-23.5	2	100%
Whale *et al.*, (2015)[190]	none	water	--	-32.4	1	100%
	cx-GNF	water	0.1 wt%	-28.8	1	99.3%
			1 wt%	-24.8	1	100%
	mellitic acid	water	1 wt%	-30.8	1	100%
	GO	water	0.1 wt%	-25.0	1	100%
			1 wt%	-22.7	1	100%
	o-MWCNT	water	1 wt%	-18.2	1	100%
	o-SWCNT	water	0.07 wt%	-18.4	1	100%
Biggs *et al.*, (2017)[188]	none	MilliQ water	--	-29.3	2	96.4%
	bwGO	MilliQ water	2.5 mg/ml	-25.3	2	100%
	GO-cysteine	MilliQ water	2.5 mg/ml	-20.9	2	100%
	GO-HT	MilliQ water	2.5 mg/ml	-16.3	2	100%
	GO-DDT	MilliQ water	2.5 mg/ml	-17.8	2	100%
	GO-OcDT	MilliQ water	2.5 mg/ml	-15.0	2	100%
	GO-PNIPAM55	MilliQ water	2.5 mg/ml	-23.4	2	100%
	GO-PNIPAM140	MilliQ water	2.5 mg/ml	-23.0	2	100%
Yang *et al.*, (2016)[129]	K36	slide/air	n/a	-19.2	2	100%
	K18	slide/air	n/a	-19.2	2	100%
	K72	slide/air	n/a	-19.3	2	100%

	HC-K30	slide/air	n/a	-19.7	2	100%
	E36	slide/air	n/a	-22.8	2	100%
	E18	slide/air	n/a	-22.6	2	100%
	E72	slide/air	n/a	-22.9	2	100%
	HC-E35	slide/air	n/a	-22.2	2	100%
	KE16	slide/air	n/a	-20.1	2	100%
	ELP90	slide/air	n/a	-20.7	2	100%
	DOPA	slide/air	n/a	-21.0	2	100%

Table 5. Overview of materials that exhibit ice nucleation as determined by time until freezing.

Reference	Material	Environment	[C]	T (°C)	Time (sec)
Akhtar *et al*., (2019)[131]	sapphire	slide/air	n/a	-5.0	990
				-15.0	0
	graphene	slide/air	n/a	-5.0	1950
				-15.0	887
	graphene-30 sec XeF2 treatment	slide/air	n/a	-5.0	10745
				-15.0	3585
	graphene-1200 sec XeF2 treatment	slide/air	n/a	-5.0	24392
				-15.0	5401
He *et al*., (2016)[130]	PMETA	SO_4^{2-}	n/a	-23.9	6493
		Cl^-	n/a	-22.5	1659
		I^-	n/a	-18.7	122
		F^-	n/a	-23.6	5306
		Ac^-	n/a	-23.4	4913
		HPO_4^{2-}	n/a	-23.1	4048
		Br^-	n/a	-21.8	729
		SCN^-	n/a	-21.8	315
		NO_3^-	n/a	-20.4	157
	PSPMA	$Ca2+$	n/a	-24.5	7488
		Mg^{2+}	n/a	-24.1	6795
		Gdm^+	n/a	-23.8	6498
		K^+	n/a	-23.7	4501
		Na^+	n/a	-22.8	2190
		Cs^+	n/a	-22.6	1604
		TMA^+	n/a	-22.3	1307
		Li^+	n/a	-20.7	102
		NH^{4+}	n/a	-20.6	44

Yang *et al.*, (2016)[129]	K36	slide/air	n/a	-19.0	98
	HC-K30	slide/air	n/a	-19.0	686
	E36	slide/air	n/a	-19.0	1558
	HC-E35	slide/air	n/a	-19.0	946
Zhang *et al.*, (2019)[191]	none	60% glycerol	--	-72	94.2
	sucrose	60% glycerol	1 wt%	-72	155
			2 wt%	-72	154
			3 wt%	-72	153
			4 wt%	-72	94
	trehalose	60% glycerol	1 wt%	-72	124
			2 wt%	-72	126
			3 wt%	-72	124
			4 wt%	-72	125
	maltose	60% glycerol	1 wt%	-72	96
			2 wt%	-72	125
			3 wt%	-72	93
			4 wt%	-72	96
	lactose	60% glycerol	1 wt%	-72	94
			2 wt%	-72	95
			3 wt%	-72	95
			4 wt%	-72	95

Corroborating the importance of hydrophobic residues for IBP function, Akhtar *et al.* showed that increasing the hydrophobicity of graphene layers reduced time to nucleation.[131] He *et al.* determined that charged surfaces in the presence of counter ions behaved in accordance to the Hoffmeister series, similar to IBPs.[130] Zhang *et al.* showed the structure of disaccharide effects ice nucleation more so than molecular weight.[191]

2.3.2 Non-Physiological Environments

For research purposes, non-physiological environments include those with deviations from neutral pH (pH ≤ 6, pH ≥ 8) or those with of high concentrations of solution additives (e.g., salts, sugars, etc.). Controlling ice formation and growth in non-physiological environments is crucial for applications such as infrastructure, aviation, and renewable energy surfaces. Understanding

material performance in non-physiological environments will facilitate implementation to engineering applications for ice-growth prevention.

2.3.2.1 Ice Interaction Properties in Non-neutral pH Environments

Some applications, such as those found in civil engineering, would benefit from materials that prevent ice growth in highly alkaline environments, such as cement that has an internal pore solution pH of 13. **Figure 5a** and **Figure 5b** show the limited data that are available to describe the effect of pH and concentration on TH and IRI activity, respectively, of different materials. In general, previous studies have measured TH activity over a range of pH environments at a specific concentration. However, previous studies have generally measured IRI activity (%MLGS) over a range of concentrations in a specific pH environment.

Figure 5a shows TH activity as it relates to pH environment and concentration for different materials. For AFPs from the species *Barfin plaice* (BpAFP) and *Gomphiocephalus hodgsoni* (GhAFP) and the AFP synthetic mimic (AKAAK), the pH environment does not have an effect on the TH activity. More specifically, as the pH increased from 1 to 13, the TH activity of BpAFP, GhAFP, AKAAK remained relatively constant at 0.63 ± 0.10 °C, 0.06 ± 0.01 °C, and 0.24 ± 0.1 °C.[136,138,144] Finally, Mizrahy *et al*. investigated zirconium acetate (ZRA), which requires slightly acidic pH to function due to the oligomerization of the material, seen as a higher TH (0.07 °C) at a pH of 4.7.[107] **Figure 5b** shows IRI activity measured in %MLGS compared to the pH environment and concentration for different materials. At pH 6-7, 26 kDa PVA shows moderate IRI activity whereas 80 kDa PVA shows potent IRI activity at low (xx mg/ml) concentrations, corroborating the dependence molecular weight shown in **Figure 3**.[105,117] Additionally, 26 kDa PVA exhibits similar IRI activity at pH 1 and pH 13 when compared to pH 7, showing that PVA is resistant to changes in pH.[117] Other synthetics (CNCs and CNFs) exhibit negligible efficacy in all environments investigated.[105,178] AFPIII maintained potent IRI at both acidic and alkaline pH (pH 1 and 11), however, extreme alkaline environments like those seen in concrete (≥ pH 13) were not investigated.[192] These data demonstrate significant gaps for IRI efficacy in varied pH

environments, such as (1) IBP IRI activity between pH 1 and pH 6, between pH 8 and pH 11, and above pH 11, and (2) synthetic IRI activity between pH 7 and pH 13.
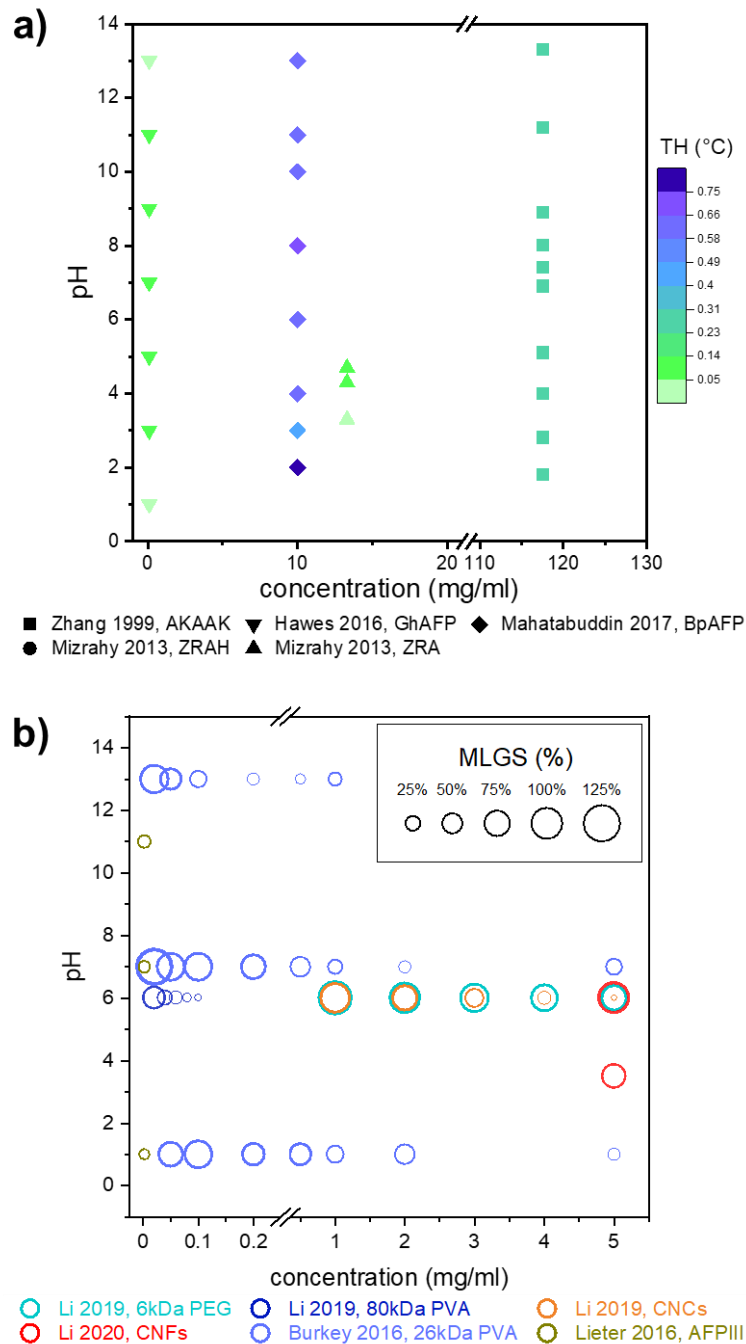
Figure 5. A review of material performance in pH adjusted environments, either for (a) TH activity or (b) IRI activity. The % MLGS is represented by circles, where a larger diameter indicates a larger % MLGS, or lower IRI activity. The legend presents example % MLGS and the corresponding circle size.[107,117,136,138,144,178,193,194]

A limited number of studies have investigated the effect of pH on the ice growth rate, and these data can be seen in **Table 6**. Additionally, the effect of non-neutral pH on ice nucleation has not been investigated to-date. Burkey *et al*. determined that acidic environments increased the rate of growth for PVA whereas basic environments reduced the rate of growth for PVA compared to pH 7 environments.[117] Additionally, the authors demonstrated that 1 M NaOH reduced the rate of growth for polymers without IRI activity (PEG, atactic PG, and isotactic PG) compared to 1 M NaCl. Mizrahy *et al*. looked at ZRA and ZRAH, small molecules that require acidic pH of ~4.7 for an increased number of active oligomeric species in solution, and determined that a pH of 4.7 resulted in the slowest ice growth rate.[107]

Table 6. The influence of pH on the rate of ice growth.

Paper	Environment	Material	[C]	ΔT (°C)	Rate
Mizrahy *et al*., 2013[107]	--	buffer	--	0.022	2.63 um/sec
	pH 3.3	ZRAH	150 mM	0.022	2.13 um/sec
		ZRA	150 mM	0.02	0.076 um/sec
	pH 4.2	ZRAH	150 mM	0.022	0.11 um/sec
		ZRA	150 mM	0.025	0.012 um/sec
	pH 4.7	ZRAH	150 mM	0.022	0.01 um/sec
		ZRA	150 mM	0.025	0.009 um/sec
Burkey *et al*., 2018[117]	0.1 M HCl (pH 1)	--	--	--	27.2 um^3/min
		26 kDa PVA	0.5 mg/ml	--	15.3 um^3/min
			5 mg/ml	--	0.6 um^3/min
	0.1 M NaCl (pH 7)	--	--	--	23.3 um^3/min
		26 kDa PVA	0.5 mg/ml	--	8.9 um^3/min
			5 mg/ml	--	0.3 um^3/min
	0.1 M NaOH (pH 13)	--	--	--	31.9 um^3/min
		26 kDa PVA	0.5 mg/ml	--	0.04 um^3/min
			5 mg/ml	--	0.1 um^3/min
	1 M NaOH	PEG	50 mg/ml	--	7.0 um^3/min
		PG - atactic	50 mg/ml	--	25.7 um^3/min
		PG - isotactic	50 mg/ml	--	29.8 um^3/min

2.3.2.2 Ice Interaction Properties in the Presence of Ionic Additives

In their physiological environments, IBPs are often not the only internal constituent responsible for preventing ice formation or for regulating ice growth and act synergistically with other solutes. For use in non-physiological environments, understanding the synergy between IBPs and controlled additives is important for tuning ice formation or ice growth within the engineered system. A common additive to enhance TH activity that is found in a menagerie of engineering applications is salt or other ionic solution constituents. An overview of the influence of salt additives on TH activity can be seen in **Figure 6**.
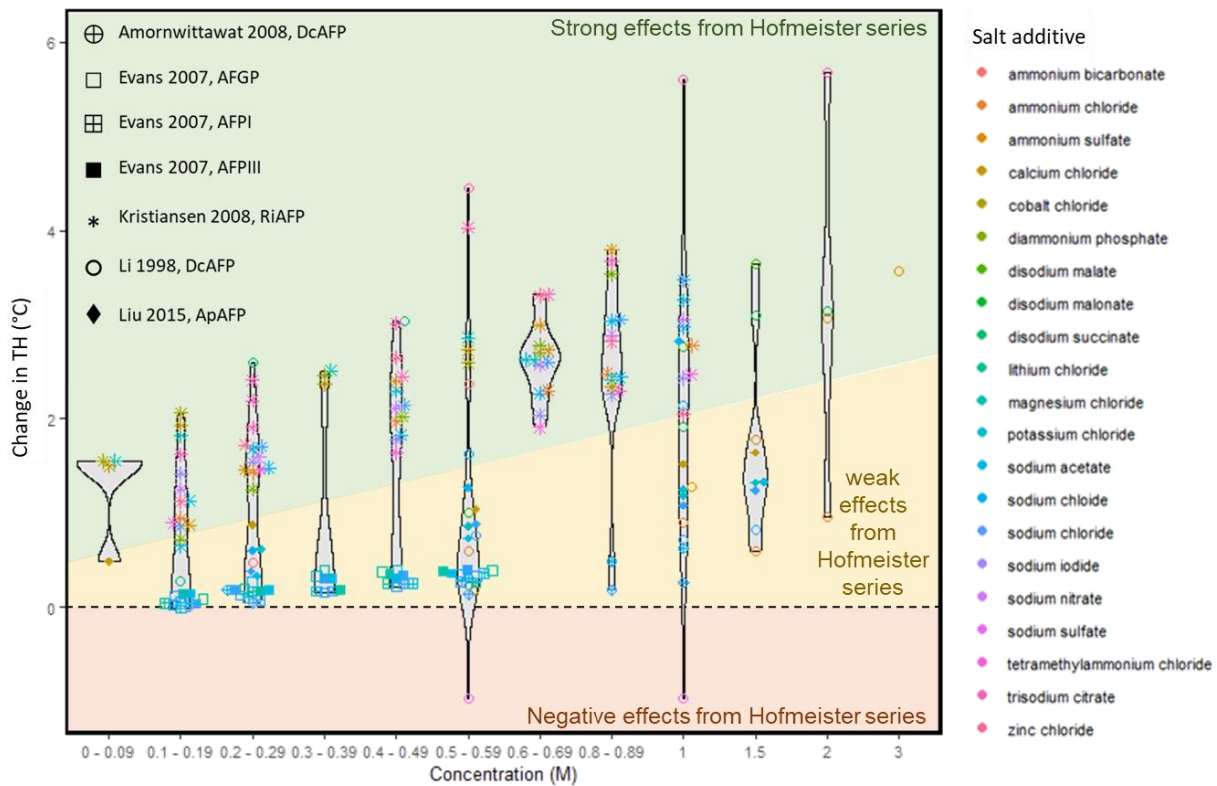
Figure 6. The effect of salt additives on TH activity, with synergistic contributions generally following the Hofmeister series.[112,134,195–197]

Salt additives appear to enhance the TH activity of hyperactive proteins[112,134,196,197] more than moderately active proteins.[195] In general, the synergy between salt additives and IBPs follows the Hofmiester series, but there are a few notable exceptions. First, the IBPs demonstrate a stronger

than anticipated synergy with zinc chloride, sodium nitrate, sodium iodide, and cobalt chloride. Second, the IBPs show a dependence on salt concentration for ammonium bicarbonate, which induced more synergy at high concentrations (0.5 M) than at low concentrations (0.2 M). Finally, there is a contradictory contribution by ammonium sulfate, seen as high synergy of the IBPs with RiAFP, but minimal synergy of the IBPs with DcAFP, possibly due to protein interactions.

Limited investigations have been completed on the synergistic effects of salt additives to enhance IRI activity. Leiter *et al*. investigated AFPIII under the influence of increasing concentrations of NaCl and found that IRI activity of AFPIII increased as the salt concentration increased.[192] Surís-Valls *et al*. also investigated the IRI activity of two types of AFGP under the influence of 0.1 M salt additives (NaCl, $Na_3C_6H_5O_7$, $Na_2[B_4O_5(OH)_4]$, $NaNO_3$, and Na_3PO_4) and found that all salt additives improved the IRI activity of the AFGPs.[186] Balcerzak *et al*. demonstrated that LiCl and KCl reduced the IRI activity of moderately active small molecule carbohydrates based on AFGP.[198] Wu *et al*. showed that salt additives effect the final crystal size for control salt solutions based on the Hofmeister series, although did not demonstrate synergistic effects with IRI active materials.[119] In general, the Hofmeister series seems to effect the recrystallization of ice, though further studies are required to fully elucidate potential synergistic effects for engineering applications.

A few studies have investigated the influence of ionic additives on the rate of ice growth, and these data can be seen in **Table 7**. To-date, the effect of salt additives on ice nucleation has not been investigated. Surís-Valls e*t al*. investigated the influence of 0.1 M salt additives (NaCl, $Na_3C_6H_5O_7$, $Na_2[B_4O_5(OH)_4]$, $NaNO_3$, and Na_3PO_4) on the rate of growth of two types of AFGPs and found that all salt additives reduced the rate of growth of the AFGPs by in accordance to the Hofmeister series.[186] Burkey *et al*. looked at 26 kDa PVA and how 0.1 M salts (NaCl, NaSCN, LiCl) effected the rate of growth, determining that both NaSCN and LiCl reducing the rate of growth by 64% and 97% compared to NaCl, respectively. More data is required to definitively determine the contribution of salt additives, although based on other literature it is possible that synergy may follow the Hofmeister series.

Table 7. Salt additive influenced rates.

Reference	Environment	Material	[C]	Rate (um^3/min)
Surís-Valls et al., 2019[186]	30 wt% sucrose	AFGP1-5	5 nM	0.67
		AFPIII rQAE	500 nM	1.03
	+0.1 M NaNO$_3$	AFGP1-5	5 nM	0.48
		AFPIII rQAE	500 nM	0.93
	+0.1 M NaCl	AFGP1-5	5 nM	0.45
		AFPIII rQAE	500 nM	0.42
	+0.1 M Na$_2$[B$_4$O$_5$(OH)$_4$]	AFGP1-5	5 nM	0.59
		AFPIII rQAE	500 nM	0.36
	+0.1 M Na$_3$PO$_4$	AFGP1-5	5 nM	0.26
		AFPIII rQAE	500 nM	0.29
	+0.1 M Na$_3$C$_6$H$_5$O$_7$	AFGP1-5	5 nM	0.01
		AFPIII rQAE	500 nM	0.24
Burkey et al., 2018[117]	0.1 M NaCl	--	--	23.3
		26 kDa PVA	0.5 mg/ml	8.9
			5 mg/ml	0.3
	1 M NaCl	PEG	50 mg/ml	49.2
		PG - atactic	50 mg/ml	71.9
		PG - isotactic	50 mg/ml	90
	0.1 M NaSCN	--	--	24.6
		26 kDa PVA	0.5 mg/ml	3.2
			5 mg/ml	0.2
	0.1 M LiCl	--	--	20
		26 kDa PVA	0.5 mg/ml	0.2
			5 mg/ml	0.1

2.3.2.3 Ice Interaction Properties in the Presence of Non-Ionic Additives

Similar to salt additives, non-ionic additives can behave synergistically with IBPs and synthetic materials to prevent or control ice formation and growth. As an example of non-ionic additives, small molecule polyols are often used as cryopreservation agents; however, they can be toxic to cells upon thawing. Additionally, polyols are often used for plane deicers, where excess contaminates water run-off and the nearby environment. Materials that are able to act

synergistically could reduce the amount of toxic polyols utilized while retaining ice-growth prevention.

The non-ionic additives considered herein fell into three main categories: sugars (or rings with pendant hydroxyls), linear hydroxyl-containing molecules, and carboxylated molecules. The effects of these additives on TH activity compared to concentration can be seen in **Figure 7**, **Figure 8**, and **Figure 9**, respectively.
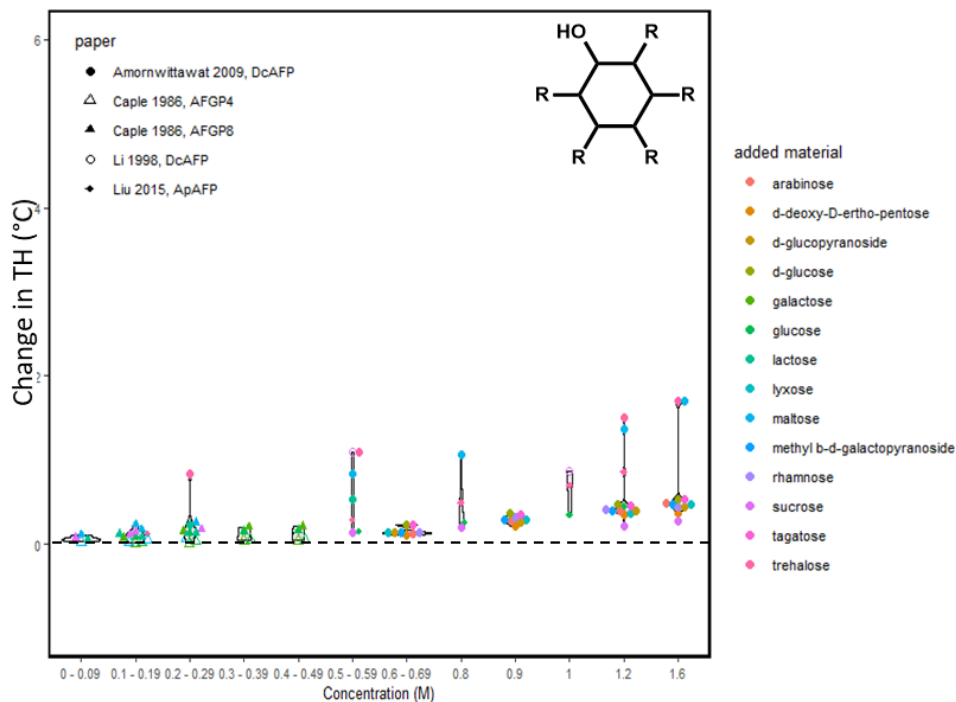
Figure 7. The effect of sugars as a non-ionic additive on the change in TH activity for different AFPs. Molecules included exhibited a sugar ring with at least one pendant –OH group. R groups on the schematic could be another ring, more –OH, or other pendant functionalities. [140,196,197,199]
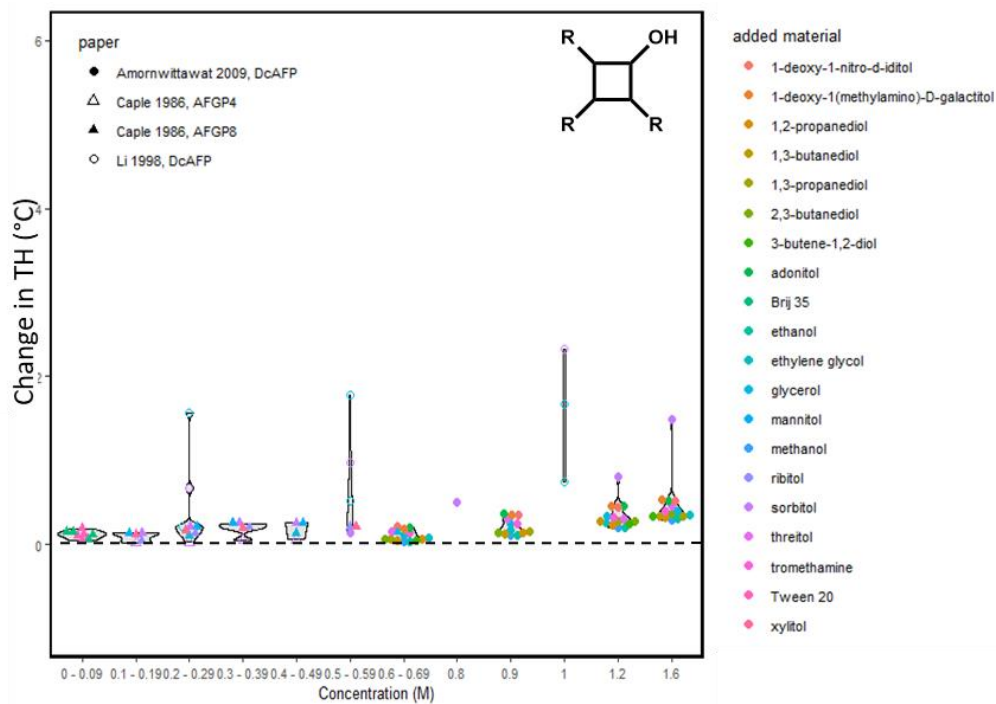
Figure 8. The effect of hydroxyl-containing molecules as a non-ionic additive on TH activity for different AFPs. Molecules included exhibited a linear or branched molecule (represented by a square) with at least one pendant –OH group. R groups on the schematic could be more –OH groups or other pendant functionalities.[140,196,199]
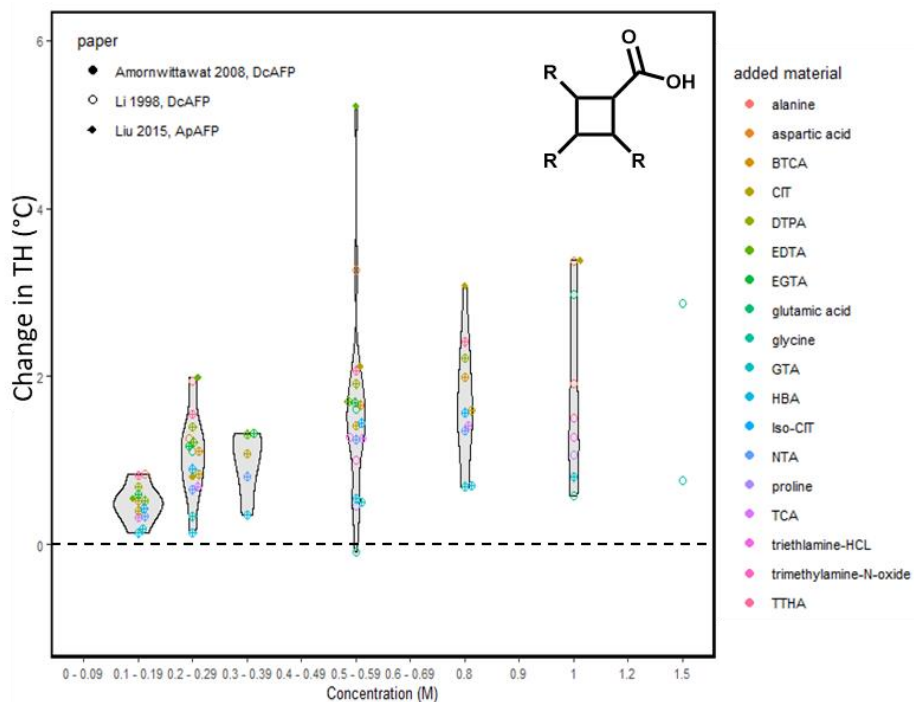
Figure 9. The effect of carboxyl-containing molecules as a non-ionic additive on TH activity for different AFPs. Molecules included exhibited a linear or branched molecule (represented by a square) with at least one pendant –COOH group. R groups on the schematic could be more – COOH groups or other pendant functionalities.[112,196,197]

As shown in **Figure 7**, **Figure 8**, and **Figure 9**, most non-ionic additives act synergistically to improve the TH activity of IBPs as indicated by the positive increase of TH activity with the increase of additive concentration. In general, as the concentration of non-ionic additive increased (≥ 1 M) there was a corresponding improvement in TH activity. Notably, carboxylated molecules as a non-ionic additive demonstrated the greatest synergy with respect to concentration as there was a greater increase of TH activity (**Figure 9**) at the same concentration of additive compared to sugars (**Figure 7**) and hydroxyl-containing molecules (**Figure 8**) as non-ionic additives. In addition, some studies have investigated the synergistic effect of larger molecules as non-ionic additives, such as proteins or polymers, on TH activity. For example, Funakoshi *et al*. examined the effect of adding a 10 kDa polymer, ammonium polyacrylate (NH$_4$PA), on the TH activity of AFPI and reported that 66 mg/ml NH$_4$PA increased TH by ~360%, and 167 mg/ml NH$_4$PA increased TH by ~460%.[200] Berger *et al*., demonstrated that a passive isoform of AFPIII (*i.e.*, no

TH activity), would enhance the TH activity of active isoforms.[201] Wu *et al*.[202] and Wang *et al*.[135] demonstrated that the introduction of other components of insect haemolymph increase TH activity, showing that adding synergistic components can drastically improve protein efficacy.

There have been limited studies that show the influence of non-ionic additives on IRI activity, and no studies to-date that have examined the effect on ice growth rate or ice nucleation. Ishibe *et al*. demonstrated the IRI activity of PVA could be improved by adding non-ionic molecules that do not demonstrate IRI activity. Molecules that worked were: 4kDa PEG, lactose (> 10 mg/ml), 12kDa poly acrylic acid, 7.7 kDa polymethacrylate, and 1.3 kDa poly vinyl prylodine 12. Molecules that did not work were: ethylene glycol, glucose, lactose (< 10 mg/ml), acrylic acid, methacrylate, and 15kDa PVP. The authors anticipated that the depletion forces incurred by additional soluble polymers were necessary to facilitate interactions between the IRI active PVA and ice.[203]

2.4 Prospects and Challenges

Data from the literature have shown that the performance of AFPs can be tuned to target specific TH activities. TH activity can be tuned by adding repeats of existing amino acid sequences to enlarge the AFP, creating larger AFP conjugates using a polymeric linker, or adding synergistic solution constituents to bolster protein performance. Solution constituents that have shown to exhibit synergism with AFPs are non-active proteins, salt additives that follow the Hofmeister series, or small hydrophilic molecules such as sugars, hydroxyl-containing molecules, or carboxyl-containing molecules. For AFPs, these trends appear true for IRI activity as well. However, AFPs can only be produced in limited yields, and production can be time and cost intensive.

To improve viability for large scale applications, synthetic IBP mimics have been developed. Most synthetic IBP mimics show limited TH activity, but have been shown to excel at exhibiting IRI activity. While the IRI activity of IBPs is still effective at concentrations several magnitudes lower than synthetic IBP mimics, the up-scalability and availability of synthetic production suggests promise and potential for engineering and other applications. Data from the literature

shows that the performance of synthetic IBP mimics can be tuned by molecular weight and pendant moieties, but there is limited data on the effects of solution composition.

2.5 Identified Gaps

Gap #1. IRI Activity of IBPs and Synthetic Mimics in Extreme pH Environments. While it has been shown that some IBPs are able to maintain TH and IRI activity in varied pH environments, the capabilities for IBPs to exhibit IRI activity in extreme pH solutions, such as those found in civil engineering concrete pore solutions (pH > 13) has yet to be investigated. While proteins have shown to be effective up to pH 11, synthetic materials could possibly offer better alternatives for engineering applications in aggressive environments, but to-date have not been investigated.

Gap #2. Synergy between Synthetic Mimics and Solution Additives. Research has shown that IBPs perform synergistically with non-active analogs to enhance TH and IRI activity. Additionally, PVA IRI performance was shown to improve in the presence of non-IRI active polymers. However, the extent to which non-active materials perform synergistically with synthetic analogs has yet to be explicated, yielding questions worth answering. For example, do salt additives perform synergistically to enhance PVA IRI activity? How do various moderately active synthetics, such as polyampholytes, work in synergy? Could a highly active, but expensive, material be enhanced by a cheap, easily accessible material?

Gap #3. Synthetic Mimic Alternatives to PVA. It was shown in this chapter that PVA is the only synthetic IBP mimic with potent IRI activity that is comparable to IBPs. However, PVA has some drawbacks, such as requiring mild heating and vigorous stirring to solubilize, and PVA can cryogelate upon repeated exposure to freeze-thaw conditions. These factors limit the viability of PVA to mitigate ice growth in applications with repeated or cyclic freeze-thaw temperature fluctuations, demonstrating a clear need for polymeric alternatives that exhibit potent IRI activity.

Gap #4. Resilience of Self-assembled Molecules. Self-assembled molecules, such as those shown by Drori *et al*. and Xue *et al*., demonstrated functional group spacing similar to IBPs,

lending to increased material performance.[101,171] However, self-assembling molecules have not been tested for resilience and activity retention in non-physiological environments with complex constituent composition.

Of most interest for this work is determining materials capable of exhibiting potent IRI activity in potential in civil engineering applications. Two specific applications are targeted: (a) to prevent freeze-thaw damage in concrete, which has a pore solution of pH 13; and (b) to act synergistically with deicing salts when applied to infrastructure surfaces. Performing investigations that fill Gap #1, Gap #2, and Gap #3 will address the above identified applications.

CHAPTER 3
Ice-Binding Protein from *Shewanella frigidimarina* Inhibits Ice Crystal Growth in Highly Alkaline Solutions

3.1   Introduction

Ice-binding proteins (IBPs) are a robust series of proteins found in a multitude of freeze-avoidant and freeze-tolerant organisms, including fish, fungi, plants, and bacteria, that are capable of surviving sub-zero temperatures by inhibiting ice crystal growth and controlling ice crystal morphology.[29,30,40,204,205] Some freeze-tolerant organisms produce IBPs that prevent the coalescence of small, nucleated ice crystals into larger, more destructive crystals through a mechanism known as ice recrystallization inhibition (IRI).[154] The growth of large ice crystals at the expense of smaller crystals is thermodynamically preferred to minimize interfacial energy at the grain boundaries.[206,207] Mechanistically, IBPs function in a non-colligative manner for IRI through lattice matching of the protein ice-binding face with the crystal lattice of ice, which induces a high local curvature and increases the energy required for further crystal growth.[40,49,208–210]

Previous cryogenic research indicates that IBPs may offer a new, biomimetic alternative to conventional frost-prevention strategies for biological materials[40,58] and, by extension, antifreeze applications in a host of other commercial industries (e.g., aerospace, infrastructure). Previous research indicates that low concentrations of IBPs can be used to cryopreserve microorganisms, such as microalgae used to produce insulin,[59] to improve the viability of rat kidneys post-thaw over conventional agents in media,[60] and to ameliorate follicular integrity of vitrified-warmed mouse ovaries.[61] Additionally, the efficacy of IBPs to reduce hemolysis of red blood cells upon thawing has previously been investigated: An IBP from the genus *Leucosporidium* significantly reduced hemolysis at concentrations of 0.4–0.8 mg/ml,[62] and three IBPS (AFPI, AFPII, and AFPIII) were shown to reduce hemolysis by 75% compared to controls.[63] The effects of IBPs on cryopreservation have been found to depend on IBP type and concentration, the preservation protocol, and biological material.[64] As an emerging biotechnology, IBPs have the potential to extend beyond biological applications to meet frost-prevention needs of other industries in

aerospace (e.g., cryogenic fluids), civil engineering (e.g., frost-resistant pavements), and energy infrastructure (e.g., anti-icing coatings). While IBPs offer a promising biological solution for these ice-prevention applications, proteins are well known to restructure (e.g., unfold, refold, denature, aggregate, degrade) in non-native environments.[65] Changes in pH and ionic concentration may affect IRI activity of IBPs and limit their applicability as a biotechnological frost-resistance solution in novel applications with more aggressive chemical environments.

IBPs have been shown to exhibit control of ice structures at nanomolar (nM) concentrations of IBPs in solution,[1,94] and a few studies have indicated that IBPs may perform similarly in ionic solutions.[134,192] While IRI was not reported, Kristainsen et al.[134] found that antifreeze activity as measured by thermal hysteresis using nanoliter osmometry for *Rhagium inquisitor* IBP was improved six-fold in 0.8 M monovalent ionic solutions of tri-sodium citrate, sodium chloride (NaCl), and sodium iodide. Leiter et al.[192] studied the performance of Type III fish antifreeze protein in low concentrations of NaCl (*i.e.*, 20–30 mM) and found a marginal increase in IRI activity compared to neat solutions. Leiter et al. also investigated the effect of 0.1 M NaOH (pH 11) on the IRI activity of Type III fish antifreeze protein and found that the elevated pH did not affect IRI activity.[192] Taken together, these studies indicate the potential for IBPs to maintain IRI activity in non-native ionic environments.

The purpose of this work was to investigate the ability of an ice-binding protein from the bacterium *Shewanella frigidimarinas* (SfIBP) to control the size and inhibit the growth of ice crystals in highly alkaline solutions (pH > 12) with increasing ionic strength. First, the structural stability of SfIBP was investigated using circular dichroism (CD) spectroscopy. Second, SfIBP stability, aggregation, and degradation were analyzed with two protein size-analysis techniques, sodium dodecyl sulfate polyacrylamide gel electrophoresis (SDS-PAGE) and size-exclusion chromatography with an ultraviolet detector (SEC-UV). Finally, SfIBP IRI activity was investigated using a modified splat assay and compared to controls of neat solutions. Similar to precedent research,[2,23,211,212] IRI activity was determined through direct measurement of the mean

size of ice crystals that formed in the alkaline solutions that contained SfIBP after incubation in freezing ($-4\ °C$) conditions compared to neat alkaline solutions.

3.2   Materials and Methods

3.2.1 Materials

Calcium hydroxide ($Ca(OH)_2$), potassium hydroxide (KOH), sodium hydroxide (NaOH), calcium sulfate ($CaSO_4$), 2-mercaptoethanol, and bovine serum albumin (BSA) were purchased from Sigma Aldrich without further purification. Tris(hydroxymethyl)aminomethane buffer (Tris) was purchased from Fisher Bioreagents without further purification. *Shewanella frigidimarina* IBP isoform 1 (SfIBP) at a concentration of 4 mg/ml in solution was obtained from Dr. Peter Davies at Queen's University in Kingston, Ontario, Canada[1] and was reconstituted using a centrifugal filter into 20 mM Tris solution. SfIBP concentration was verified at 4.4 mg/ml against BSA using UV-Vis.

Hydroxide salts were used to create alkaline solutions of increasing pH in ~0.5 pH increments from pH ~12.5 to 14.0. Solution formulations were adapted from studies performed by Ghods *et al.*,[81] and the supernatant decanted for use. The cation concentrations in the supernatant were verified using inductively coupled plasma mass spectrometry (ICP-MS), and hydroxide ion concentrations were determined from solution pH (**Table 8**). Tris buffer was included in all solutions to account for protein addition. Total ionic strength (*I*) for each solution was calculated according to Equation 1:

(1)
$$I = \frac{1}{2}\sum Z^2 C,$$

where *Z* is the valence of the ion and *C* is the ion concentration. As Tris has a pK_a of 8.1, solutions with pH > 12 were above Tris's buffer capacity. Therefore, Tris was determined to have dissociated completely to its conjugate base (deprotonated, uncharged) and conjugate acid (H^+), as per the Henderson-Hasselbach equation. Since Tris was in its deprotonated form, it was not included in the ionic strength calculations for solutions with pH > 12. The conjugate acid was

expected to neutralize through combination with hydroxide ions present in alkaline solutions to form water, which would have been reflected in measured solution pH used to determine hydroxide concentration. Samples for IRI characterization without or with 0.125 mg/ml SfIBP were prepared using stock solutions from **Table 8**. While SfIBP has been shown to exhibit activity in protein buffer conditions at concentrations as low as 50 nM (0.00125 mg/ml),[1] lower SfIBP concentrations tested did not exhibit inhibition in this study (data not shown) due to the ionic and alkaline nature of the solutions. Therefore, a concentration of 0.125 mg/ml was selected in this study to evaluate ice crystal nucleation and growth inhibition.

Table 8. Chemistry of alkaline solutions obtained *via* ICP-MS.

Solution	I (mol/L)	pH	OH (mM)	Tris (mM)	Ca (mM)	Na (mM)	K (mM)	S (mM)	Mg (mM)	Si (mM)
A	0.03	12.4 ± 0.1	26.71	20	0.003	6.1	9.85	5.02	0.001	0.005
A + 1/2 Tris*	0.03	12.4 ± 0.1	23.62	10	0.003	6.1	9.85	5.02	0.001	0.005
B	0.05	12.7 ± 0.1	48.60	20	0.003	9.7	15.5	8.08	0.001	0.005
C	0.16	13.2 ± 0.1	168.5	20	0.007	23.9	37.3	20.6	0.002	0.005
D	0.69	13.9 ± 0.2	857.7	20	0.761	90.5	132.0	76.4	-	0.008
Tris	0.01	8.90 ± 0.1	0.008	20	-	-	-	-	-	-
1/2 Tris*	0.005	8.40 ± 0.2	0.003	10	-	-	-	-	-	-

* Indicates samples that were used for SfIBP circular dichroism (CD) characterization.

3.2.2 Protein Structure

CD SPECTROSCOPY. SfIBP structure and stability were analyzed in two solutions (**Table 8**), namely 1/2 Tris and A + 1/2 Tris, *via* circular dichroism (CD) spectroscopy in the far UV range (190-260 nm) using a modular Applied Photophysics Chirascan Plus CD and Fluorescence Spectrometer at ambient temperature with 0.5 nm steps and 0.5 sec/step at a 0.5 mm path length. SfIBP was loaded at 0.5 mg/ml for CD analysis for improved protein signal. SfIBP could not be analyzed in all solutions, given the confluence of increasing alkalinity and ionic strength and the signal detection limits of the instrument. Secondary structure composition (% helix, sheet, turns,

etc.) was measured from the peptide bond region (<240 nm)[213] using BeStSel software.[214] SfIBP was allowed to incubate in solution for at least 24 hours to ensure equilibrium folding states,[215] as it was expected that the alkalinity and high ion concentrations would induce protein misfolding. All CD spectra were averaged over five runs on the same sample and the solution baseline was removed from the spectra. Curves were smoothed to remove noise using the Savitzky-Golay filter method in OriginPro 2016 using 5 points per window with a polynomial order of 2.

SEC-UV. SfIBP stability, aggregation, and degradation were analyzed using size-exclusion chromatography (SEC) equipped with an ultraviolet (UV) detector monitoring a wavelength of 220 nm. SEC was performed on an Agilent 1100 Series LC system with a UV detector and a Tosoh TSKgel G3000SWxl size exclusion column. For all experiments, the mobile phase was 100 mM potassium phosphate buffer (pH 7.4) at a flow rate of 0.4 mL/min. Solutions from **Table 8** were analyzed without and with a SfIBP concentration of 0.4 mg/mL for improved signal. For each injection, 50 µL of sample were analyzed, resulting in a final SfIBP content of 20 µg. Data were processed using Astra software 7.1.2 and plotted using GraphPad Prism software 7.04.

SDS-PAGE. Sodium-dodecyl sulfate polyacrylamide gel electrophoresis (SDS-PAGE) was performed on SfIBP loaded into solutions from **Table 8** at a concentration of 1 mg/ml to ensure visible bands in the gel. SfIBP samples were denatured prior to SDS-PAGE *via* the additional of 2-mercaptoethanol and subsequent heating at 95 °C for 5 minutes. Samples were loaded onto a 4–20% denaturing TGX gel from Bio-Rad (1.0 mm × 12 well; 35 min, 200 V, 1X Tris-Glycine-SDS PAGE running buffer, pH 8.8) and compared to a 10-250 kDa protein ladder (New England BioLabs) for estimation of molecular weight. The protein content within the gel was stained with Coomassie SimplyBlue SafeStain (Invitrogen) according to manufacturer specifications.

3.2.3 Protein Performance

IRI ACTIVITY. A splat ice recrystallization assay was adapted from Knight *et al.*[2] Solutions from **Table 8** were tested neat or with a 0.125 mg/ml loading of SfIBP. A 10–20 µL droplet of solution was dispensed from 1.7 m through a PVC pipe onto a microscope slide on top of an

aluminum block chilled with dry ice to obtain a monolayer of ice crystals. The slide was then transferred to an Otago nanoliter osmometer sample stage and annealed at −4 °C. The temperature was monitored using a bead-type thermocouple. Images were collected immediately after the splat was performed (t_0) and again at 30 minutes (t_{30}) to observe ice recrystallization. Images were obtained using a Zeiss Axio Imager M2m microscope with an EC Epiplan 5x/0.13 BD M27 objective and crossed polarizers, equipped with an Axiocam 506 color camera on a 1" 1.0x 60N C-mount adapter. ZENCore 2.4 image processing was used to measure individual grain sizes along the major axis. Data were taken from images from 2–3 different splat samples and used to determine an average grain size ($n = 150$) at $t = 30$ min.

3.2.4 Statistical Analyses

Grain sizes were first averaged for each of the replicate images. The effect of solution (*i.e.*, different ionic strength and pH per **Table 8**) and inclusion of protein on mean grain size, as well as the interaction between these factors, was then tested using two-factor ANOVA. Model assumptions of residual normality and homoscedascity were satisfied. For main effects, significance was set *a priori* to $p < 0.05$. Simple effects (*i.e.*, the effect of protein on grain size for a particular solution) were assessed with the Fisher Least Significant Difference test using a Bonferroni correction to account for family-wise error (critical $\alpha = 0.05/3 = 0.0167$). To determine if ionic strength and pH influenced mean grain size, these two solution chemistry metrics were first tested for intercorrelation using Pearson product-moment correlation. Since ionic strength and pH were found to be intercorrelated, no conclusions about the relative influence of pH versus ionic strength on mean grain size could be made. All statistical analyses were performed with Minitab (v18).

3.3   Experimental Results and Discussion

3.3.1. Protein Structure

CD SPECTROSCOPY. Results from protein stability and secondary structure determination using CD are shown in **Figure 10**. As expected, SfIBP exhibited an initially well-folded secondary structure in 1/2 Tris (**Figure 10**) that matches previously reported spectra for SfIBP.[1] As anticipated, proteins incubated in solution A + 1/2 Tris at ambient conditions exhibited partial misfolding (**Figure 10**).

Since CD uses plane polarized light absorbance to analyze protein composition, highly ionic solutions can saturate the absorbance detectors in CD. Therefore, ion concentrations in solution were increased (A→D) to find the maximum ionic strength that did not saturate the CD detector, which corresponded to solution A with Tris concentration reduced to 10 mM (A + 1/2 Tris). CD spectra could not be obtained for solutions B, C, or D, as the ion concentration of the solutions saturated CD absorption, preventing detection of SfIBP in the peptide bond region.

An analysis of secondary structure using CD data of SfIBP in 1/2 Tris and its associated changes when placed in A + 1/2 Tris is presented in **Table 9**. Data analysis using BeStSel software parsed secondary structure of SfIBP into 8 categories: Regular α-helix, distorted α-helix, left β-helix, relaxed β-helix, right β-helix, parallel β-strand, turn, and other (disordered). **Table 9** lists the relative percentages of each secondary structure identified for SfIBP in 1/2 Tris and the relative changes to those structures when placed in A + 1/2 Tris. Values are expressed as a positive or negative percent.
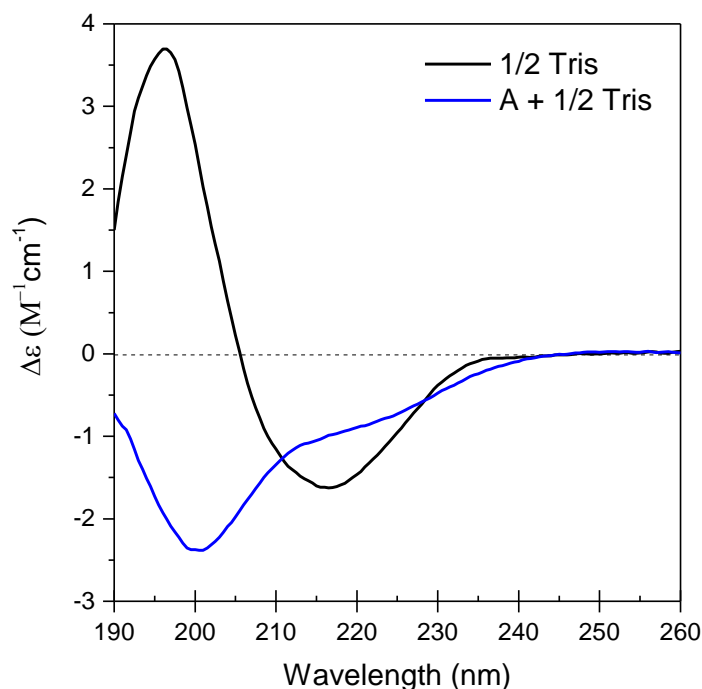
Figure 10. CD spectra showing SfIBP secondary structure at 0.5 mg/ml in 1/2 Tris (—) and A + 1/2 Tris (—). Spectra for B, C, and D were not attainable due to oversaturation of CD absorption.

Table 9. SfIBP CD structure analysis in 1/2 Tris and A + 1/2 Tris.

Secondary Structure	1/2 Tris	A + 1/2 Tris	Difference
Regular α-helix	3.8%	2.1%	-1.7%
Distorted α-helix	5.1%	2.3%	-2.8%
Left β-helix	7.5%	1.0%	-6.5%
Relaxed β-helix	18.3%	10.4%	-7.9%
Right β-helix	13.2%	21.1%	+7.9%
Parallel β-strand	0.1%	0.8%	+0.7%
Turn	10.3%	15.3%	+5.0%
Other	41.7%	46.9%	+5.2%

SEC-UV AND SDS-PAGE. SEC-UV and SDS-PAGE were used to analyze protein stability, aggregation, and degradation in the alkaline solutions investigated herein. SEC-UV data are presented in **Figure 11a**. The chromatograms show UV absorbance signals from SfIBP as a function of elution volume from the column. SfIBP in Tris exhibited a singular dominant peak around 10 mL, similar to the singular peak exhibited by Vance *et al.*[1] The SfIBP signal in alkaline solutions with $I \leq 0.05$ mol/L (solutions A and B) had a shape and elution volume similar to SfIBP

in Tris (**Figure 11a**). Additional UV signals appeared for SfIBP in all alkaline solutions at greater elution volumes with lower UV absorbance than the main protein elution at ~10 mL. In solution A, SfIBP exhibited a peak at the 10 mL mark, similar to Tris, along with other prominent peaks past 12.5 mL. Similarly, for solution B, SfIBP exhibited one prominent peak that matches SfIBP in Tris at 10 mL, but residual peaks were evident after 12.5 mL. SfIBP in solution C exhibited peaks after 12.5 mL—as do all other solutions—but manifests a peak around 6 mL and distinctly lacks a peak at 10 mL. SfIBP in solution D exhibited absorbance peaks that are shifted to greater elution volumes than SfIBP in Tris and exhibited peak broadening.

The SDS-PAGE results are presented in **Figure 11b**. The results for SfIBP in Tris and alkaline solutions are depicted with decreasing ionic concentrations (solution D→A). SfIBP in Tris exhibited a large, single band ≈ 25 kDa, matching the molecular weight of SfIBP as previously reported by Vance *et al.*[1] SfIBP incubated in solution D did not demonstrate any obvious bands for SDS-PAGE. However, in solutions where $I \leq 0.16$ mol/L (i.e., solutions A, B, C), bands corresponding to intact SfIBP protein ≈ 25 kDa are evident. SfIBP exhibited faint bands in lower molecular weight regions (≈ 10 kDa) for all alkaline solutions except for solution D.
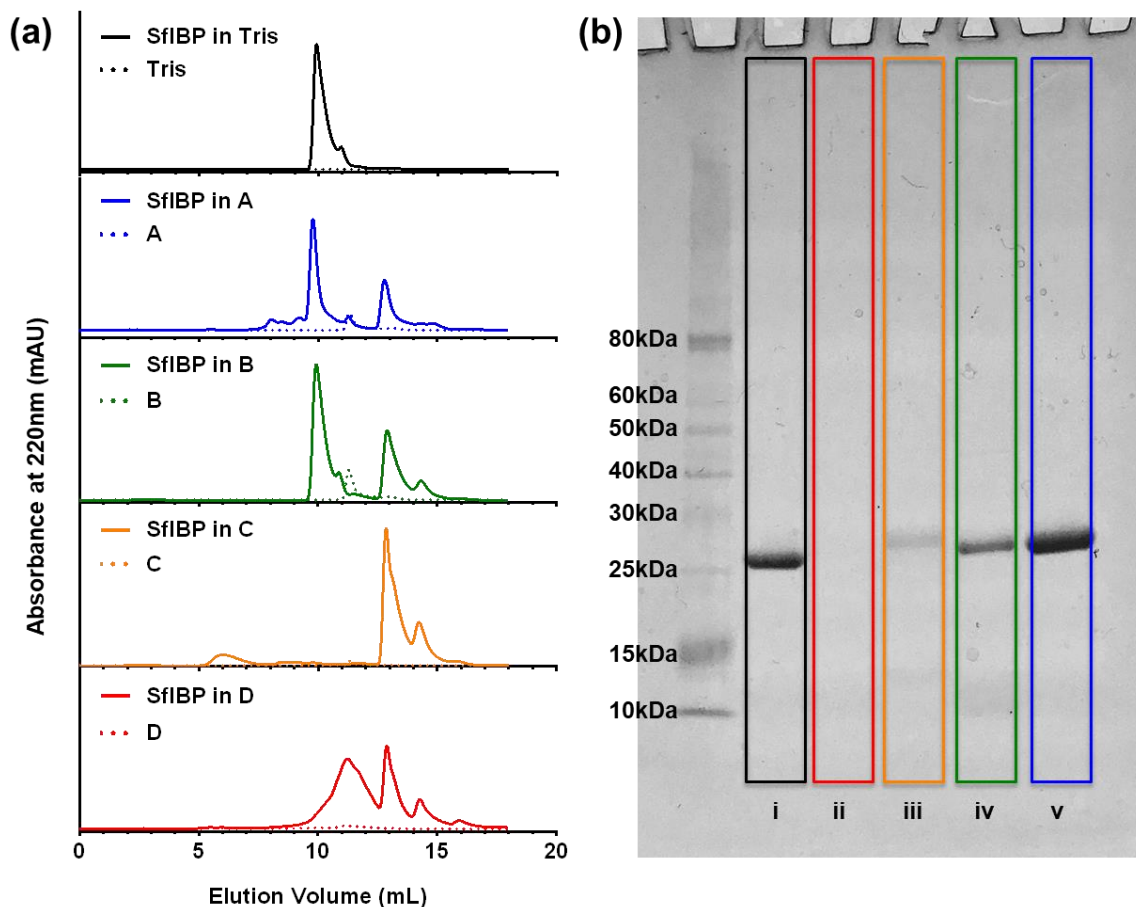
Figure 11. (**a**) SEC-UV absorbance at 220 nm as a function of elution volume for SfIBP in Tris and alkaline solutions with increasing ionic strength. (**b**) SDS-PAGE for SfIBP. Left to right, SfIBP in: (i) Tris; (ii) solution D; (iii) solution C; (iv) solution B; (v) solution A.

3.3.2. IRI activity

IRI activities of all solutions listed in **Table 8** without (0 mg/ml) and with (0.125 mg/ml) SfIBP protein are demonstrated in **Figure 12**. The average size of ice crystallites formed in each solution after incubation at -4 °C is summarized in **Table 10**. The average percent difference of mean ice crystal grain size relative to neat Tris after incubation without and with SfIBP is demonstrated in **Figure 13a**, and statistical relevance of results as determined by ANOVA is shown in **Figure 13b**.

As expected, all solutions without SfIBP exhibited ice nucleation and growth upon incubation at sub-freezing temperatures (−4 °C). Ice crystallites with an average grain size of 51±19 µm

formed in Tris without SfIBP, which were comparable in size to ice crystals formed in all alkaline solutions without SfIBP (**Table 10**).

SfIBP exhibited IRI activity in both Tris, as expected, and alkaline solutions (pH > 12) with $I \leq 0.05$ mol/L, (i.e., solutions A and B).
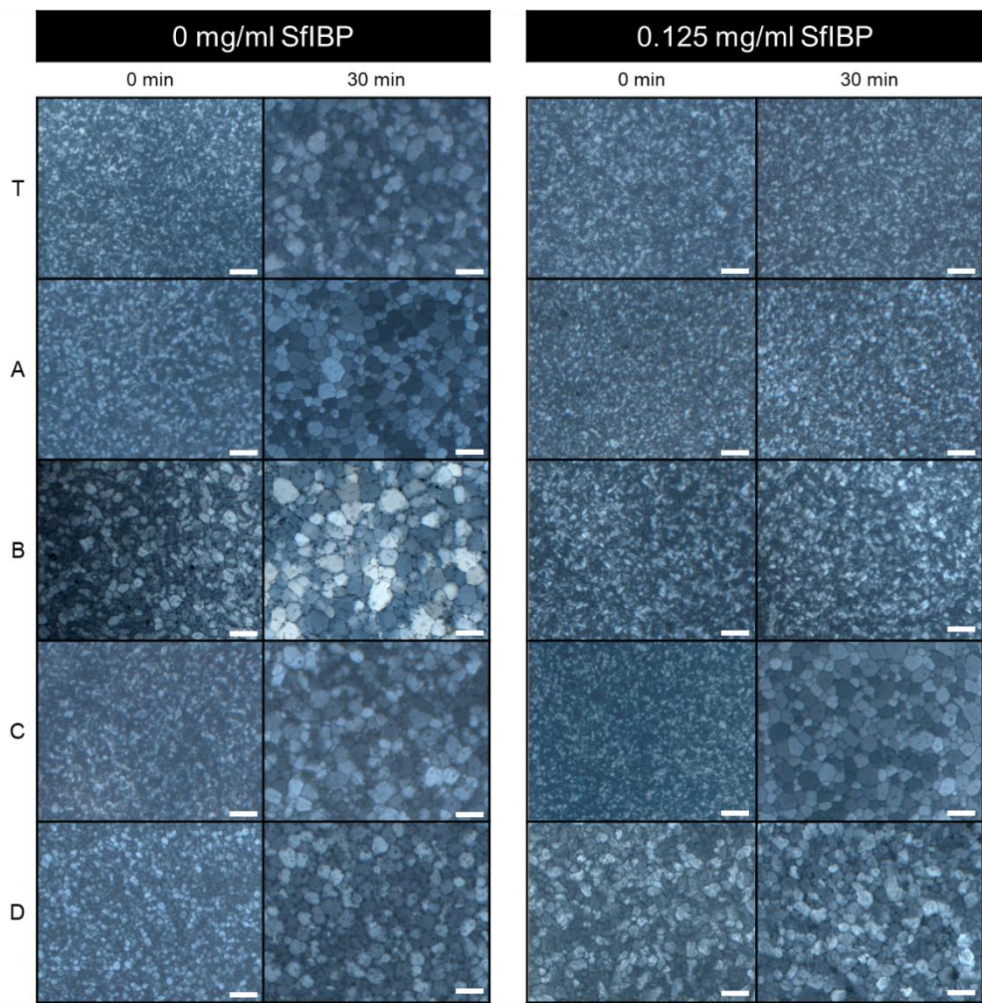
Figure 12. IRI activity of SfIBP in Tris buffer (**T**) and alkaline solutions (**A**, **B**, **C**, **D**) at 0 and 30 min. Scale bar = 100 μm.

Table 10. Average ice crystallite size of frozen solutions after incubation at −4 °C ($t = 30$ min).

Solution	SfIBP Loading (mg/ml)	Mean Crystal Size (µm)	% Change in Mean Crystal Size
Tris	0	51 ± 19	-
Tris	0.125	11 ± 4	−78%
A	0	51 ± 18	-
A	0.125	21 ± 5	−59%
B	0	68 ± 30	-
B	0.125	23 ± 6	−66%
C	0	61 ± 25	-
C	0.125	63 ± 27	+3%
D	0	54 ± 16	-
D	0.125	52 ± 14	+4%

3.3.3 Statistical Analysis

ANOVA determined that (i) solution, (ii) inclusion of protein, and (iii) the interaction between solution and protein all significantly affected mean grain size at $t = 30$ min. Simple effects testing revealed that for solutions A (−61.9%, p < 0.001), B (−66.3%, p < 0.001), and Tris (−76.9%, p < 0.001), including protein significantly reduced grain size (**Figure 13b**). SfIBP samples in Tris exhibited IRI activity, as evidenced by no noticeable ice growth beyond ice nucleation (**Figure 12**). When included in solution A, B, Tris, SfIBP inhibited the growth of ice crystals (p < 0.0167) (**Figure 13b**). As expected, however, the inhibition was less than SfIBP in pure Tris. The IRI activity of SfIBP was similar in both solutions A and B, which had comparable ionic strengths of 0.03 mol/L and 0.05 mol/L, respectively. As summarized in **Table 10,** SfIBP in solutions C and D exhibited no IRI activity, where $I \geq 0.16$ mol/L, as evidenced by final grain sizes that were not statistically different than their neat solutions (**Figure 13b**). The range of ionic strength in which SfIBP lost its ability to mitigate ice growth was 0.05 < I < 0.16 mol/L, and the range of pH for the loss of SfIBP function was 12.7 < pH < 13.2. Notably, in solutions where SfIBP exhibited ice growth inhibition (i.e., Tris, A, B), the distribution of crystal size was narrowed, as indicated by the smaller error bars.
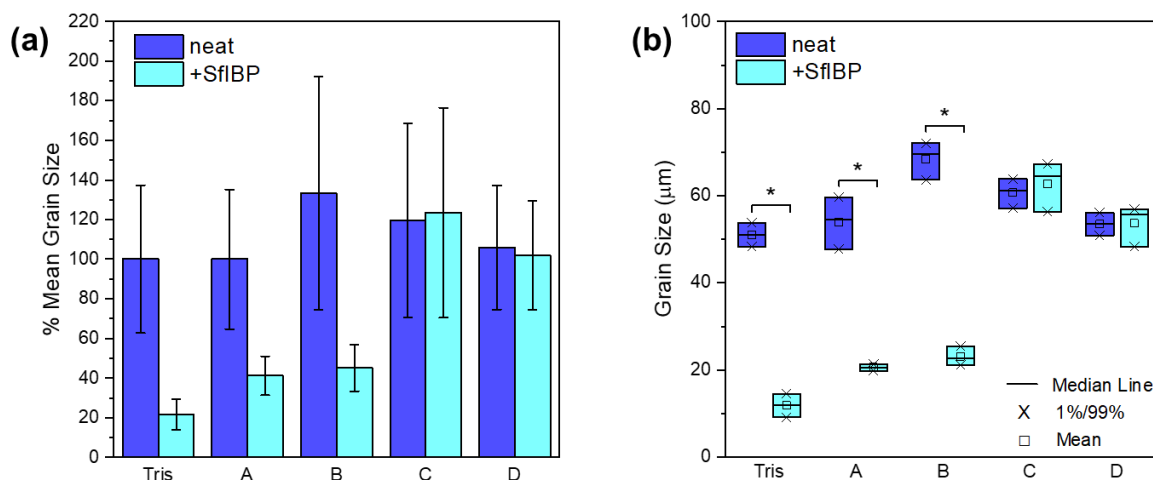
Figure 13. IRI activity of samples from **Table 8** after incubation at −4 °C ($t = 30$ min) without SfIBP (■) and with SfIBP (■). (**a**) Data represented as % Mean Grain Size of ice crystals relative to neat Tris. Error bars equal ± one standard deviation. (**b**) Data from two-factor ANOVA on the effect of solution and inclusion of protein. Asterisks indicate statistically significant differences in average grain size due to the addition of SfIBP ($p < 0.001$).

3.3.4 Discussion

The structure and activity of the ice-binding protein SfIBP was investigated in solutions with high alkalinity and increasing ionic strength. The reduction in average ice crystal size in solutions A and B with SfIBP was statistically significant compared to neat solutions. However, in more alkaline solutions C (pH = 13.2) and D (pH = 13.9) with higher ion content (0.16 mol/L and 0.69 mol/L, respectively), the protein stability and IRI efficacy decreased, which affected ice recrystallization inhibition.

Despite misfolding and partial degradation, SfIBP exhibited secondary structure and ice-inhibiting functionality in alkaline solutions (pH = 12.4 to 12.7) with ionic strength $I \leq 0.05$ mol/L. SfIBP degraded in solution D, as indicated by the lack of gel stain in SDS-PAGE (**Figure 11b**). Protein degradation is verified by the shifted peaks in SEC-UV (**Figure 11a**) to elution volumes greater than 12.5 mL in solution D. At $I \leq 0.16$ mol/L, bands in SDS-PAGE at ≈ 25 kDa mirror SfIBP in Tris, indicating that SfIBP likely retained some of its structure in these solutions. SDS-PAGE verifies that SfIBP did not aggregate in any of the tested solutions due to the lack of molecular weight bands above 25 kDa. The peak broadening observed in SEC-UV absorbance for

SfIBP in solution D (**Figure 11a**) corroborates the SDS-PAGE to indicate that protein secondary or tertiary structure was disrupted, likely due to changes in the proteins native charge, yielding chromatogram traces with peaks at larger volumes than the native protein due to ionic interactions with the column.[216,217] To this same end, the high alkalinity and ionic strength of the solutions likely facilitated covalent bond cleavage of the protein along the backbone through base-mediated hydrolysis,[218,219] as indicated by faint bands in SDS-PAGE for SfIBP in solutions A, B, and C in the ≈ 10 kDa molecular weight region, and the lack of bands for solution D (**Figure 11b**).

According to SDS-PAGE and SEC-UV, SfIBP exhibited some protein degradation in all solutions. Sample eluting at volumes of 12.5 mL and greater indicate that the high alkalinity and ion content of the solutions likely caused some degree of protein restructuring and degradation.[219,220] At ionic strengths $I \leq 0.05$ mol/L, chromatograms retained traces with absorbance peak shapes similar to SfIBP in Tris, along with evidence of some degradation. SfIBP in solutions A and B both exhibited UV absorbance peaks at 10 mL, similar to that of SfIBP in Tris, indicating retention of some protein. However, solutions C and D did not exhibit UV absorbance peaks at 10 mL, indicating degradation and, hence, a lack of protein structure that could exhibit IRI activity. The peak at 6 mL in solution C is decidedly an artifact due to the proportionally small signal, verified by the lack of higher molecular weight bands in SDS-PAGE.

Protein misfolding does not necessarily equate to loss of ice-binding functionality,[65] as some ice-binding protein faces may still have been exposed to the solution through the process of refolding, retaining—albeit reducing—IRI activity. Secondary structure analysis (**Table 9**) quantitatively approximates residual protein structure. The analysis of SfIBP structure following CD experiments indicated that in solution A + 1/2 Tris the amount of unstructured protein increased by 5.2%, although the overall change in protein structure (taken as the difference between each type of fold), was altered approximately 37.7%. The current hypothesis for SfIBP IRI activity is closely related to β-fold content in the DUF3494 domain (domain of undefined function).[1] The β-fold content in SfIBP secondary structure (left β-helix, relaxed β-helix, right β-helix, parallel β-strand) changed overall by ~ 23% when in A + 1/2 Tris compared to 1/2 Tris and

is hypothesized to be responsible for the change in IRI activity. Based on the changes observed in CD spectra (**Figure 10**) and peak broadening in SEC-UV (**Figure 11b**), it can be deduced that, while SfIBP is misfolding, it retains some ice-binding functionality in solutions with high alkalinity (pH 12.4 to 12.7), as seen *via* IRI activity that is comparable to SfIBP in Tris (**Figure 12**, **Figure 13a**).

Due to the high alkalinity and ionic nature of the solutions (**Table 8**), it was expected that the secondary structure of SfIBP would become disordered, leading to disruption of protein tertiary structure that would affect its ice-binding capabilities.[65] The induced conformational changes and refolding are likely due to the disruption of hydrogen bonds necessary for proper protein folding in the native state.[215] It is hypothesized that SfIBP is refolding in response to the alkalinity of solutions, with either the ionic strength, the high pH, or a combination of both ionic strength and pH acting as a denaturant.

Tris had a pH and ionic strength that promoted expected SfIBP conformation and function (**Table 8**, **Figure 10, Figure 12**) and corresponded to the slightly basic solution pH, as verified in Vance *et al*.[1] As Tris and solution A had comparable ionic strengths ($I = 0.01$ and $I = 0.03$ mol/L, respectively), the elevated pH of solution A likely caused SfIBP to misfold (**Table 9**). Despite the change in structure, however, SfIBP in solution A expressed a strong band at ≈ 25 kDa for SDS-PAGE (**Figure 11b**), a prominent absorbance peak at 10 mL for SEC-UV (**Figure 11a**), and IRI activity (**Figure 12**), indicating that SfIBP still maintained structure and functionality at elevated pH.

SfIBP in solution C did not evince IRI activity (**Figure 12**) and, as expected, showed clear signs of degradation, as seen in the lack of elution peak at 10 mL in SEC-UV (**Figure 11a**) and diminished intensity of the SDS-PAGE band at ≈ 25 kDa (**Figure 11b**). Solution D had the highest ionic strength ($I = 0.69$ mol/L) and highest alkalinity (pH = 13.9) of all tested solutions. Solution D was the only solution where SfIBP did not exhibit a band at ≈ 25 kDa in the SDS-PAGE gel (**Figure 11b**) and had a broadened peak in SEC-UV (**Figure 11a**), likely due to the extremely ionic and alkaline environment.

While the folded structure of SfIBP in solutions with higher ionic content (e.g., solutions B, C, and D) cannot be determined directly through CD, it is hypothesized that further denaturation and decomposition occurred that prevented inhibition of ice crystal growth, as determined by the lack of IRI behavior of SfIBP in solutions C and D (**Figure 12**). The mean ice crystal grain size SfIBP in solutions C and D (63 ± 27 µm and 52 ± 14 µm, respectively) are similar in size to ice grains of solutions C and D without SfIBP (61 ± 25 µm and 54 ± 16 µm), indicating that the ice-binding face of the protein was no longer interacting with ice crystals nucleating and recrystallizing in solution (**Table 10**). However, given the retention of some protein structure in solution A + 1/2 Tris (**Table 9**), it was expected that SfIBP would still exhibit some inhibition of ice crystal growth, as substantiated in **Figure 12**, which shows that SfIBP in solutions A and B exhibit IRI activity. SfIBP in solutions A and B exhibited grain sizes of 21 ± 5 µm and 23 ± 6 µm, respectively, indicating the likelihood of protein interaction with ice crystals despite protein misfolding. While IRI activity was not as potent as in Tris, SfIBP effectively reduced average grain sizes in solutions A and B by $\approx 59\%$ and $\approx 66\%$, respectively, compared to neat solutions (**Figure 13a**).

SfIBP exhibits IRI activity in alkaline solutions (pH > 12) with ionic strength $I \leq 0.05$ mol/L, indicating that SfIBP (and other IBPs) could be effective at mitigating frost-induced damage in applications that necessitate activity in non-native chemical environments. It is clear from these data in **Table 10** that solutions that exhibit IRI activity (*i.e.*, SfIBP in Tris, A, and B) also demonstrate much narrower crystal size distributions, indicating that SfIBP not only inhibits ice crystal coalescence in these solutions, but dictates its final size in equilibrium.

While SfIBP exhibits a potential to reduce frost-induced damage in select highly alkaline environments, other IBPs and new classes of biomimetic polymeric materials may prove more effective. Certain IBPs are well known to contain structures with a high density of stabilizing di-sulfide bonds, such as IBPs from *Tenebrio molitor*,[221] which offer the potential of maintaining increased tertiary structure, and, thus, performance, in extremely ionic and alkaline environments. Other IBPs, such as those from *Marinomonas primoryensis*,[222] require divalent calcium for proper folding and may be stabilized by calcium-rich environments with higher ionic strengths to maintain

activity. In addition to proteins, polymer architectures that mimic the ice-binding functionality of IBPs offer a unique avenue for mitigating and controlling ice nucleation and growth, as they may not only be more cost-effective, but also able to inhibit ice crystal recrystallization in solutions of higher alkalinity without relying on tertiary structure or reduced ionic strength to exhibit IRI activity.[42,92,93]

3.4   Conclusions

This study evaluated the potential of an ice-binding protein (IBP) from *Shewanella frigidimarinas* (SfIBP) to inhibit and control ice crystal nucleation and growth in highly alkaline solutions of increasing pH and ionic strength. While the folded structure of SfIBP in media with ionic strength $I > 0.03$ mol/L could not be determined directly through CD, based on evidence from SEC-UV and SDS-PAGE, it is assumed that a greater extent of denaturation and degradation occurred at higher ionic concentrations ($I \geq 0.16$ mol/L) that prevented the inhibition of ice crystal growth, as determined by the lack of IRI behavior. Despite protein misfolding, data indicate that SfIBP exhibits ice recrystallization inhibition (IRI) activity in solutions with high alkalinity (pH = 12.4 to 12.7) and low ionic strength ($I \leq 0.05$ mol/L) ($\approx 66\%$ reduction in ice crystal size compared to neat solutions). In conclusion, these results suggest that SfIBP (and other IBPs and their biomimetic synthetic replicates) could be effective at mitigating frost-induced damage in applications with chemically extreme non-native environments.

3.5   Authorship and Acknowledgements

AUTHORS: Elizabeth A. Delesky[1], Shane D. Frazier[1], Jaqueline D. Wallat[2], Kendra L. Bannister[3], Chelsea M. Heveran[2], and Wil V. Srubar III[1,2,*]

[1]Materials Science and Engineering Program, University of Colorado Boulder, Boulder, CO 80309, USA; elizabeth.delesky@colorado.edu (E.A.D.); shane.frazier@colorado.edu (S.D.F.)

[2]Department of Civil, Environmental, and Architectural Engineering, University of Colorado Boulder; Boulder, CO 80309, USA; jaqueline.wallat@colorado.edu (J.D.W.); chelsea.heveran@colorado.edu (C.M.H.)

[3]Department of Chemical and Biological Engineering, University of Colorado Boulder; Boulder, CO 80309, USA; kendra.bannister@colorado.edu

* Correspondence: wsrubar@colorado.edu (W.V.S.III); Tel.: +1-303-492-2621

CHAPTER 4
Effect of pH on the Activity of Ice-Binding Protein from *Marinomonas primoryensis*

4.1 Introduction

Previous research indicates that ice-binding proteins (IBPs) may offer an alternative to conventional frost-prevention strategies for biological cryopreservation[40,223] and, by extension, antifreeze applications in a host of other commercial industries such as coolants in aerospace engineering, frost-resistant pavements in civil engineering, and anti-icing coatings for energy infrastructure such as solar panels or wind turbines. While IBPs offer a promising biological solution for these ice-prevention applications, proteins are well known to unfold, refold, denature, aggregate, or degrade in non-physiological environments.[65] Applications with harsh chemical environments, such as concrete in civil engineering that has a pH of 12-13,[81] would benefit from a material that inhibits ice recrystallization. Freeze-thaw damage in concrete is due, in part, to the expansion of ice crystals[224] demonstrating a need for materials that inhibit ice growth in extreme pH environments. To the authors' knowledge, some studies have investigated the effect of pH on thermal hysteresis activity,[196,202,225–227] and a limited number of studies have indicated that IBPs may produce similar ice recrystallization inhibition (IRI) activity in non-physiological pH solutions[3,192] which necessitates pH studies for the IRI activity of IBPs in non-physiological environments.

IBPs are a diverse category of proteins that have evolved independently among many types of organisms, including plants,[24–26,228] fungi,[24,28,229] fish,[29–34] insects,[35–37] and microbes[1,24,38,39] to help them survive in freezing environments. As IBPs come from a wide range of organisms, they vary in molecular weight, structure, and activity.[41] X-ray crystallography and NMR studies have resolved IBP structures to include α-helices, β-solenoids, helix bundles, and small globular proteins.[41] Although all structures exhibit the ability to adsorb to ice, there are few trends among residues or sequences that lead to ice binding.[41] Mechanistically, the current hypothesis for IBP function is through adsorption-inhibition.[41] The ice-binding face of an IBP is composed of regularly spaced ice-binding residues that match the lattice spacing of one or more faces of the ice

crystal lattice. The lattice match allows the protein to adsorb to a nascent ice crystal and induce high local curvature on the ice crystal surface that makes further crystal growth energetically unfavorable, a process known as the Gibbs-Thomson effect.[41,49,209,210,230] All IBPs exhibit one or more phenomena that indicate their interaction with ice. These phenomena include: (1) thermal hysteresis (TH), a non-colligative depression of freezing-point temperature while maintaining (or raising) the melting point; (2) dynamic ice shaping (DIS), a reshaping of the 1H hexagonal ice structure to form less disruptive ice geometries; and (3) ice recrystallization inhibition (IRI), a property that limits ice recrystallization through Ostwald ripening and overall reduces mean crystal size.[42] *Marinomonas primoryensis* is an Antarctic bacterium that uses a 1.5 MDa extracellular protein to keep it in the oxygen and nutrient rich phototropic zone by binding to the surface of ice.[41,231] Of the 1.5 MDa protein, a 34 kDa region, dubbed region IV, is responsible for ice-binding.[231] The ice-binding region consists of mostly β-strands that form a calcium-stabilized β-solenoid.[38,232] The β-solenoid structure of the *Marinomonas primoryensis* IBP is similar to other hyperactive IBPs, though few IBPs have calcium stabilized structures. The calcium-stabilization offers a unique potential for a more robust structure in non-ideal environments.

The purpose of this work was to investigate the ability of the calcium-stabilized ice-binding region IV from the *Marinomonas primoryensis* extracellular adhesion protein (*Mp*IBP) to control the size and inhibit the growth of ice crystals in non-physiological pH solutions ($2 \leq \text{pH} \geq 13$). It is not known whether the calcium-stabilized *Mp*IBP is also pH tolerant, thus, we characterized its activity in non-physiological solutions.

4.2   Materials and Methods

4.2.1 Materials

All reagents were purchased from Fisher Bioreagents without further purification. Clonal cells with *Mp*IBP were obtained from Dr. Peter Davies at Queen's University in Kingston, Ontario, Canada and used for protein expression.[222] Solutions with a pH range from 2 to 13 were created at room temperature in increments of ~2 by adjusting with either HCl or NaOH, and pH was

measured again at 0 °C (**Table 11**). *Mp*IBP at each pH was compared to its respective blank solution so that all constituents were the same save for the addition of *Mp*IBP. pH 8 was used as the reference solution as it was close to the pH of purification solutions (~8.5). Tris(hydroxymethyl)aminomethane (Tris) was an artifact from protein purification and included in blank solutions to account for protein addition. Total ionic strength (*I*) for each solution was calculated according to Equation 1:

$$I = \frac{1}{2}\sum Z^2 C,$$
(1)

where Z is the valence of the ion and C is the concentration. Varied pH solutions were tested for IRI and DIS either blank or loaded with 0.1 mg/ml *Mp*IBP. A protein concentration of 0.1 mg/ml was used in this study as this was previously determined to be the level at which *Mp*IBP thermal hysteresis activity is at a maximum (Garnham 2008). It was anticipated for *Mp*IBP in pH 4 solution the concentration might have been less than 0.1 mg/ml as pH 4 is close to the isoelectric point of 4.11 (**Table 12**), which often reduces protein solubility (Xia 2018). The concentration of *Mp*IBP in pH 4 solution was lower than 0.1 mg/ml and measured using UV-Vis at 280 nm and was found to be ~0.04 mg/ml (**Table 13**). **Table 14** provides the composition for solutions used during *Mp*IBP production and purification procedures.

Table 11. Solutions for evaluating *Mp*IBP efficacy in different pH conditions

pH			Constituents (mM)					Total Ion Content		
Target	Ambient	0 °C	Tris	NaCl	CaCl$_2$	NaOH	HCl	Na$^+$ (mM)	Cl$^-$ (mM)	*I* (mol/L)
2	2.15	3.31	10	15	10	-	32	15	67	0.066
4	3.99	5.81	10	15	10	-	25	15	60	0.063
6	6.18	6.93	10	15	10	2.6	26	17.6	61	0.064
8	8.06	9.21	10	15	10	-	8.5	15	43.5	0.054
10	9.98	10.52	10	15	10	8.4	2.5	23.4	37.5	0.055
12	12.01	13.08	10	15	10	44	-	59	35	0.078
13	12.98	*14+	10	15	10	219	-	234	35	0.207

*Measured pH was above the threshold of the pH meter

Table 12. Breakdown of the structure and properties for region IV of the ice-binding protein from *Marinomonas primoryensis* (MpIBP) as determined by Expasy.

General Information		
Number of amino acids	331	
Molecular weight	34375.03	
Theoretical pI	4.11	
Amino Acid Composition		
Residue	#	%
Ala (A)	27	8.2
Arg (R)	5	1.5
Asn (N)	32	9.7
Asp (D)	39	11.8
Cys (C)	0	0
Gln (Q)	8	2.4
Glu (E)	13	3.9
Gly (G)	46	13.9
His (H)	12	3.6
Ile (I)	22	6.6
Leu (L)	21	6.3
Lys (K)	8	2.4
Met (M)	3	0.9
Phe (F)	8	2.4
Pro (P)	1	0.3
Ser (S)	22	6.6
Thr (T)	19	5.7
Trp (W)	2	0.6
Tyr (Y)	8	2.4
Val (V)	35	10.6
Pyl (O)	0	0
Sec (U)	0	0
Number of Charged Residues		
Positive (Asp + Glu)	52	
Negative (Arg + Lys)	13	
Atomic Composition		
Carbon	1473	
Hydrogen	2286	
Nitrogen	420	
Oxygen	525	
Sulfur	3	
Extinction Coefficient (M^{-1} cm^{-1}) at 280 nm in water		
Ext. coefficient	22920	
Abs 0.1% (=1 g/l)	0.667	

Table 13. Absorbance for *Mp*IBP in pH 4 solution. As the isoelectric point for *Mp*IBP is ~4.1, the actual concentration in solution was tested. The mixed solution was tested, as well as the top of a centrifuged solution. It was assumed that during testing the concentration would be between the two states, and this an average of all was used.

Solution	Trial	A_{280}	E/1000 $(M^{-1}cm^{-1})$	b (cm)	MW (kDa)	Protein (mg/mL)	Average (mg/ml)	Total Average (mg/ml)
mixed	1	0.047	22.9	1	33.5	0.071	0.0685	0.0415
	2	0.044	22.9	1	33.5	0.066		
centrifuged	3	0.014	22.9	1	33.5	0.021	0.0145	
	4	0.005	22.9	1	33.5	0.008		

The concentration of *Mp*IBP was calculated using Beer's law, as seen in Equation 2:

$$(2) \qquad\qquad A_{280} = EbC$$

where A_{280} is the absorbance measured at 280 nm using a UV-Vis, *E* is the extinction coefficient for the protein (**Table 12**), *b* is the path length of the UV-Vis, and *C* is the molar concentration.

4.2.2 Expression of MpIBP

Expression of *Mp*IBP was adapted from Garnham *et al.*[38] Briefly, a culture was used to inoculate 1.6 L of lysogeny broth (LB) medium with kanamycin (100 µg/mL) and grown until OD_{600} reached 0.5 (37 °C, 200 rpm). The temperature was lowered to 23 °C until cells reached $OD_{600} = 1$ (~2 hours). Then, isopropyl β-D-1-thiogalactopyranoside was added to a final concentration of 1 mM to induce expression overnight. Cells were recovered by centrifugation (30 min, 4,300 g, 4 °C), resuspended in Buffer A (**Table 14**), and lysed using a Qsonica Q55 Sonicator Ultrasonic Homogenizer with Probe 55W (5x, 45 seconds, 50% amplitude). Cellular debris was removed *via* centrifugation (1.5 hours, 4 °C, 4,300 g) on a Beckman Coulter Allegra X-14R Centrifuge with a SX4750A rotor.

4.2.3 Purification of MpIBP

The cellular supernatant was mixed with 16 mL of Ni-NTA (Ni^{2+}-nitriloacetate) resin (16 hr, 4 °C), loaded into a column, washed with Buffers A through C, and eluted with Buffers D and E (**Table 14**). Fractions were examined using SDS-PAGE, and samples displaying bands for *Mp*IBP

67

(~34kD) were pooled before running through a ThermoScientific Protein Biology 50 mL 30kD Pierce Protein Concentrator (2000g, 4 °C) in Buffer F (10-fold reduction, 3x). The concentrate was loaded onto a DEAE–Sepharose resin column equilibrated with Buffer F, washed with Buffers F through H, and protein was eluted using Buffers I through K (**Table 14**). Fractions displaying a band for *Mp*IBP *via* SDS-PAGE were pooled and concentrated, then run on a GE Healthcare AKTApurifier FPLC with a Frac 950 equipped with a HiLoad Superdex 75 PG preparative size exclusion chromatography column. Fractions that displayed a band for *Mp*IBP *via* SDS-PAGE were again pooled and concentrated. Concentrate purity was verified using SDS-PAGE (**Figure 14**), and absorbance at 280 nm. The final yield was 3 mg of pure *Mp*IBP.

Table 14. Solution recipes for buffers used during *Mp*IBP purification.

Buffer	Tris/HCl, pH 7.9	NaCl	CaCl₂	Glycerol	Imidazole
A	50 mM	0.5 M	2 mM	2% v/v	20 mM
B	50 mM	0.5 M	2 mM	2% v/v	40 mM
C	50 mM	0.5 M	2 mM	2% v/v	150 mM
D	50 mM	0.5 M	2 mM	2% v/v	200 mM
E	50 mM	50 mM	2 mM	-	-
F	50 mM	125 mM	2 mM	-	-
G	50 mM	250 mM	2 mM	-	-
H	50 mM	0.5 M	2 mM	-	-
I	50 mM	1 M	2 mM	-	-
J	50 mM	1.25 M	2 mM	-	-
K	50 mM	1.5 M	2 mM	-	-
L	50 mM	2.5 M	2 mM	-	-
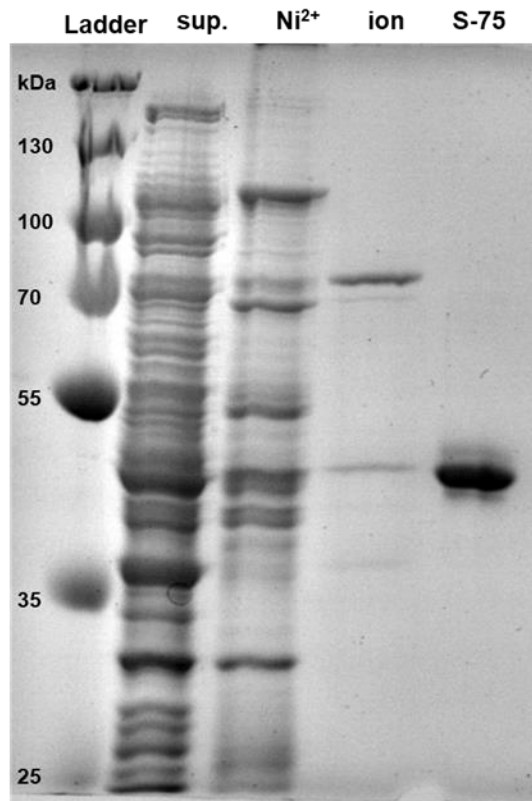
Figure 14. SDS-PAGE (10% w/v) analysis of the purification of *Mp*IBP. Lanes from left to right are identified as follows: Ladder, DNA-ladder; sup., E. coli supernatant lysate; Ni^{2+}, pooled fractions from the Ni-NTA agarose affinity chromatography; ion, pooled fractions from the DEAE sepharose ion-exchange chromatography; S-75, pooled fractions from the size-exclusion chromatography on a HiLoad Superdex 75.

4.2.4 Blue Native Polyacrylamide Gel Electrophoresis (BN-PAGE).

Blue-native polyacrylamide gel electrophoresis (BN-PAGE) was performed on *Mp*IBP in varied pH solutions at a concentration of 0.4 mg/ml to ensure visible bands in the gel. BN-PAGE procedures were adapted from Fiala *et al.*[233] and Krause *et al.*[234] Briefly, protein solutions were stained using sample buffer (50 mM bis-tris, 5% w/v Coomassie brilliant blue, 10% glycerol, pH 7). Samples were dry-loaded into a 10% denaturing acrylamide gel (1.75 mm x 10 well; 80 min, 300 mA; outer buffer 1X Tris-Glycine Native PAGE running buffer, pH 8.3) and run using a voltage of 100 V until the samples entered the separating gel, where the voltage was increased to 150 V. Samples were compared to a 10-250 kDa PageRuler Plus protein ladder (ThermoFisher

Scientific) to estimate molecular weight. *Mp*IBP content within the gel was stained using Coomassie SimplyBlue SafeStain (Invitrogen) according to manufacturer specifications.

4.2.5 Size-Exclusion Chromatography with Multi-Angle Light Scattering Detecor (SEC-MALS).

Varied pH solutions were analyzed blank or loaded with 1 mg/ml *Mp*IBP using size-exclusion chromatography (SEC) equipped with a multi-angle light scattering (MALS) detector. SEC was performed on an Agilent 1100 Series LC system and a Tosoh TSKgel G3000SWxl size exclusion column. MALS was performed using a Wyatt miniDAWN Treos II. The mobile phase was 30 mM tris, 150 mM NaCl, and 10 mM $CaCl_2$ at a flow rate of 0.4 mL/min. 50 µL of each sample were analyzed (50 µg *Mp*IBP/injection). Data were processed using Astra software 7.1.2 and were compared against a bovine serum albumin (BSA) standard to determine size. Data were smoothed using an FFT algorithm with a 15-point window and plotted using Origin 2019.

4.2.6 Circular Dichroism (CD) Spectroscopy.

Circular dichroism (CD) spectra were collected on a modular Applied Photophysics Chirascan Plus CD and Fluorescence Spectrometer in the far UV range (190-260 nm) at ambient temperature with 0.5 nm steps and 0.5 sec/step at a 0.5 mm path length. *Mp*IBP was loaded at 0.4 mg/ml to ensure adequate detection of the protein. The solutions were tested from 260 nm to a varied minimum wavelength. The final wavelength was altered to be as low as possible per sample before the signal detection limits of the instrument were saturated from the interference of the pH adjusters, namely HCl and NaOH, as they absorb in the peptide bond region.[235] *Mp*IBP was incubated in solutions for at least 24 hours before testing to ensure equilibrium folding states.[215]

Five repeat scans were averaged for each loading of *Mp*IBP in pH solutions and the corresponding baseline for the control pH solution. After removing the control solution baseline, noise was removed from the data in the Chirascan Software using the Savitzky-Golay smoothing filter using five points per window with a polynomial order of two. Protein conformation (% helix, strand, turns, etc.) was measured from the peptide bond region (<240 nm)[213] using BeStSel

software[214] with the exception of the pH 13 sample as the measured data set did not meet the minimum wavelength range for deconvolution.

4.2.7 Ice Recrystallization Inhibition (IRI).

Ice recrystallization inhibition of *Mp*IBP was investigated using a splat assay adapted from Knight et al.[2] Varied pH solutions were tested blank or with a 0.1 mg/ml loading of *Mp*IBP. Splats were performed in triplicate. A 10 µL droplet of sample was dispensed from 1.7 m through a PVC pipe onto a microscope slide on an aluminum block chilled with dry ice to obtain a single layer of ice crystals. The slide was rapidly transferred to an Otago nanoliter osmometer sample stage annealed at -4 °C for 30 min. The temperature was monitored using a bead-type thermocouple. Ice recrystallization was observed by collecting images immediately after the splat was performed (t_0) to ensure a polycrystalline sample had been obtained, and again at 30 minutes (t_{30}) to observe IRI activity. Images were taken using an Olympus BX41 microscope with an Olympus PLN 10X objective (NA = 0.25), equipped with an Axiocam 506 color camera on a 1" 1.0x 60N C-mount adapter. ImageJ 1.48v image processing software (National Institutes of Health, USA) was used to estimate the grain size along the major axis, which was taken as the longest dimension of the ice grain. Data were collected by manually counting 15 of the largest grains and then sorted to take the largest 10 grains of those counted. Analysis was performed from 3 different regions per splat to determine the mean largest grain size (MLGS) at t_{30} (n = 90). MLGS was normalized by the respective control pH solutions to elucidate the effect of *Mp*IBP. Standard deviations are the deviation between splats (n = 3).

4.2.8 Dynamic Ice Shaping (DIS).

*Mp*IBP was tested for dynamic ice shaping (DIS) in pH solutions by modifying a protocol established by Bar-Dolev et al.[236] using an Otago nanoliter osmometer sample stage mounted on an Olympus BX41 microscope with an Olympus LUCPlanFL N 20x /0.45 Ph1 microscope objective (NA = 0.45). *Mp*IBP pH solutions were tested for DIS at a solution concentration of 0.1

mg/ml. Approximately 1 μl sample was loaded into immersion oil in the sample holder for the osmometer, which was carefully placed onto the sample stage atop thermal paste to improve heat transfer. The sample was then frozen rapidly by lowering the temperature to -20 °C. The sample was slowly melted (~1 °C/min) until a single ice crystal (≤ 25 μm) remained. The sample was incubated for 15 min to ensure interaction of *Mp*IBP with the ice surface before the temperature was decreased at 0.01°C/min until ice growth occurred. Videos were recorded using Axiocam 506 color camera on a 1" 1.0x 60N C-mount adapter. VideoPad Video Editor (NCH Software) was used to isolate still images from video recordings.

4.3   Experimental Results

4.3.1 Primary structure of monomeric MpIBP is stable from pH 2 – pH 12

*Mp*IBP was tested for agglomeration and degradation of primary structure in varied pH solutions using SEC-MALS and BN-PAGE, which revealed that the expected protein molecular weight and monomeric state of *Mp*IBP in solution was maintained at pH 4 – pH 12, but that hydrolysis and significant degradation occurred at pH 13.

The elution time by SEC-MALS for *Mp*IBP can be related to molecular weight, indicating integrity of the primary structure. A distinct absorbance peak was observed at an elution time of 19.5 min for *Mp*IBP in pH 8 solution, the physiological control pH solution at which we expect *Mp*IBP to be intact (**Figure 15a**). *Mp*IBP in solutions at pH 4, 6, and 10 expressed a peak with shape and elution time similar to *Mp*IBP at pH 8 (**Figure 15a**). *Mp*IBP in pH 12 solution exhibited peak broadening, with the peak starting at ~14.5 min as opposed to 18.5 min. *Mp*IBP in pH 2 solution demonstrated a broad peak at an elution time of 20 min with a reduced intensity compared to *Mp*IBP in pH 8 solution. For *Mp*IBP in pH 2 and pH 12, it is likely that secondary or tertiary structure was disrupted[220] due to changes in the protein's native charge, yielding chromatogram traces with broadened peaks compared to the native protein due to ionic interactions with the column.[216,217] *Mp*IBP in pH 2 may have succumbed to acid mediated hydrolysis,[237] given the

reduced intensity and peak broadening observed in the MALS. MpIBP at pH 13 did not evince any peaks, indicating MpIBP did not retain primary structure in this condition.

To verify primary structure integrity, BN-PAGE was performed (**Figure 15b**). A clear band for MpIBP at the expected molecular weight was seen in solutions at pH 2 to pH 12, indicating intact primary protein structure. While the predicted molecular weight of MpIBP is 34 kDa, the observed band lies at a higher molecular weight. It is anticipated that the increase in observed molecular weight is likely due to a lack of complete denaturation of the protein, possibly due to calcium stabilization, and was observed in preceding literature.[222] BN-PAGE bands were distinctly absent for MpIBP at pH 13. As there was residual dye in the lanes from running the BN-PAGE, SDS-PAGE was run in addition to verify that there were no smaller protein fragments that may have been obscured by the lane run-off (**Figure 16**). Only MpIBP at pH 13 exhibited protein bands at lower molecular weights. The lack of a band near 34 kDa and presence of lower bands for MpIBP at pH 13 corroborates the SEC-MALS result, indicating that MpIBP degraded, likely due to hydrolysis of amino acids.[218,219,237]
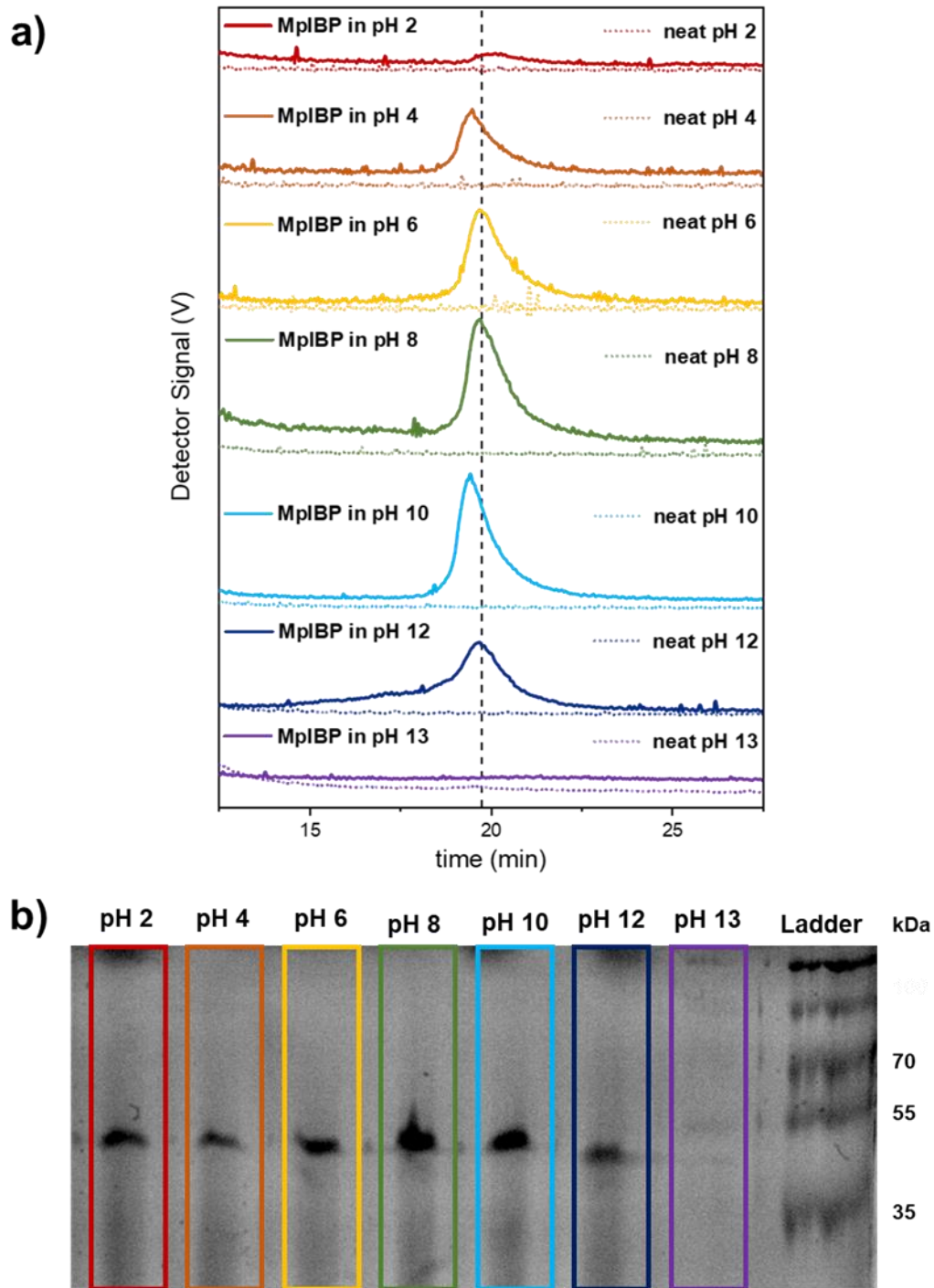
Figure 15. The stability of MpIBP in pH solutions. (a) SEC-MALS detector absorbance as a function of elution time for 1 mg/ml MpIBP in solutions with pH 2 – 13. (b) BN-PAGE (10% w/v) analysis of 0.4 mg/ml MpIBP stability in solutions with pH 2 – pH 13.
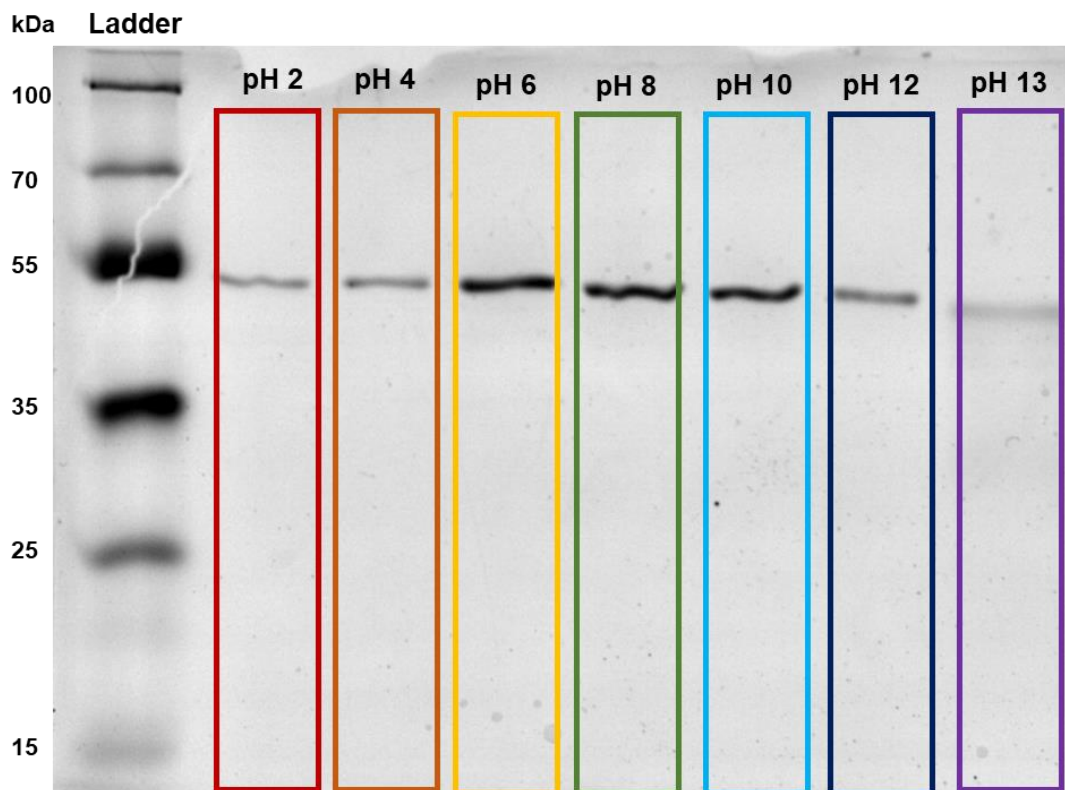
Figure 16. SDS-PAGE for *Mp*IBP in different pH solutions from **Table 11** to verify that *Mp*IBP did not degrade. As the BN-PAGE had dye runoff, SDS-PAGE was run to verify if any hydrolysis or degradation occurred. Lanes from left to right show 0.4 mg/ml *Mp*IBP in: pH 2, pH 4, pH 6, pH 8, pH 10, pH 12, and pH 13.

4.3.2. *MpIBP retains secondary structure between pH 6 and pH 10*

*Mp*IBP exhibits regularly spaced β-strands that form a β-solenoid. The spacing of the ice-binding residues on the regularly spaced β-strands is currently hypothesized to contribute to its ice-binding activity.[38,238] Therefore, *Mp*IBP was tested for retention of secondary structure in non-physiological pH solutions using CD (**Figure 17**). Data analysis using BeStSel software parsed secondary structure of *Mp*IBP into eight categories—regular α-helix, distorted α-helix, left β-strand, relaxed β-strand, right β-strand, parallel β-strand, turn, and other (disordered) (**Table 15**).

As expected, ellipticity for *Mp*IBP in the pH 8 control solution exhibited a secondary structure with two distinct peaks: a positive band at 194.5 nm, and a negative band at 218 nm, which matches the spectra previously reported by Garnham *et al.*[38] and are indicative of high β-strand content.

The CD spectra for *Mp*IBP at pH 10 shows bands in the same locations as pH 8 with a slightly larger magnitude. *Mp*IBP CD spectra in pH 12 solution shows two negative bands at 216.5 and 204 nm. *Mp*IBP CD spectra in pH 13 solution was not able to be measured to achieve a true minimum due to the interference of the pH adjustor with the CD detector. Similar absorbance saturation occurred when measuring the blank pH 13 solution due to the pH adjustors. Band shifts can be seen for *Mp*IBP in pH 2 (negative to 215 nm, positive to 190 nm), *Mp*IBP in pH 4 (negative to 221.5 nm, positive to ≤ 190 nm), and for *Mp*IBP in pH 6 (negative to 217 nm, positive to ≤ 195 nm).
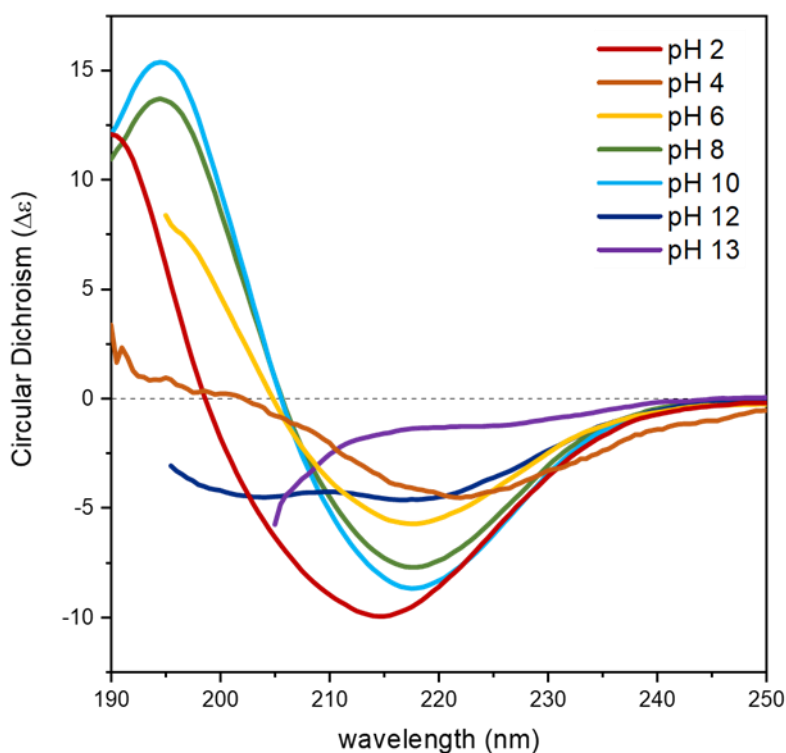
Figure 17. The far-UV CD spectra of *Mp*IBP in the presence of varied pH solutions (pH 2 (—), pH 4 (—), pH 6 (—), pH 8 (—), pH 10 (—), pH 12 (—), pH 13 (—)). The lowest wavelength was determined by the interference of the pH adjustors and instrument absorption limits

Table 15. Secondary structure of *Mp*IBP under the influence of different pH solutions as determined by BeStSel software.[214]

			*Mp*IBP Structure				
fold type	pH 2	pH 4	pH 6	pH 8	pH 10	pH 12	*pH 13
Regular α-helix	35.0%	0.0%	6.9%	20.9%	25.6%	5.8%	-
distorted α-helix	11.9%	0.0%	5.4%	1.3%	4.0%	3.1%	-
left-twisted antiparallel β-strand	0.0%	1.8%	3.5%	4.7%	3.2%	15.5%	-
relaxed antiparallel β-strand	0.0%	0%	0.0%	16.8%	12.7%	0.0%	-
right-twisted antiparallel β-strand	14.9%	16.9%	3.1%	3.9%	0.4%	0.0%	-
parallel β-strand	11.0%	10.4%	25.2%	26.6%	30.9%	17.1%	-
turn	0.0%	39.5%	5.1%	2.1%	1.5%	7.8%	-
other (irregular/loop)	27.1%	31.5%	50.7%	23.7%	21.6%	50.8%	-

*pH 13 was not able to be measured in the minimum range for BeStSel deconvolution.

4.3.3. MpIBP exhibits IRI activity between pH 6 and pH 12

IRI assays were implemented to determine the efficacy of *Mp*IBP to prevent ice growth in varied pH environments. As some salts have been shown to effect ice morphology,[119] control pH solutions without *Mp*IBP were compared to pH solutions with 0.1 mg/ml *Mp*IBP to rule out the influence of salt constituents. The pH of solutions changed upon temperature reduction due to the presence of Tris buffer. However, as all pH solutions with added MpIBP were compared to blank solutions of the same composition, the difference in behavior is still representative of *Mp*IBP ice reduction efficacy. As expected, all control pH solutions demonstrated ice recrystallization after incubating for 30 minutes, seen as larger ice grains compared to ice grains at t_0 (**Figure 18**). All control pH solutions exhibited varied ice recrystallization end points, which is expected due to the addition of pH adjusters (HCl or NaOH) that will affect the hydrogen bonding network of water based on ion interactions with the bulk, and thus affect the recrystallization process.[119,239] Control solutions at pH 4, pH 6, pH 10, and pH 12 have larger ice crystals at t_{30} compared to the blank pH 8 solution (**Figure 18**). The control pH 2 solution had the same ice recrystallization effect as the

blank pH 8 solution. Control pH 13 solution exhibits smaller ice crystals at t_{30} compared to control pH 8 solution, which is expected because an increase in ionic content has been shown to affect the ice recrystallization process and exhibit smaller ice grains.[119] However, the ionic strength does not inhibit or negate the effect added IBPs.[240]

MpIBP in pH 8 exhibited IRI activity, as evidenced by smaller ice grains than blank pH 8 solution at t_{30} (**Figure 18**). For pH 6, pH 8, pH 10, and pH 12 solutions, the addition of 0.1 mg/ml MpIBP reduced the growth of ice at t_{30} compared to control pH solutions (**Figure 18**, **Figure 19**). For the pH 4 solution, the addition of 0.1 mg/ml MpIBP did not evince IRI activity and ice grain sizes at t_{30} were the same as the control pH 4 solution. For pH 2 and pH 13 solutions, the addition of 0.1 mg/ml MpIBP resulted in larger ice crystals as compared to control solutions. To determine if pH or ionic strength influenced MpIBP activity more, ice grain sizes were estimated and normalized relative to each respective control solution. The mean largest grain size estimates were compared to pH and ionic strength (**Figure 19**). It was found that pH had a greater effect on IRI than ionic strength – for example, MpIBP exhibited IRI in pH 12 solution with an ionic strength of 0.078 mol/L, but did not exhibit IRI in pH 2 or pH 4 solutions, each with an ionic strength ≤ 0.066 mol/L.
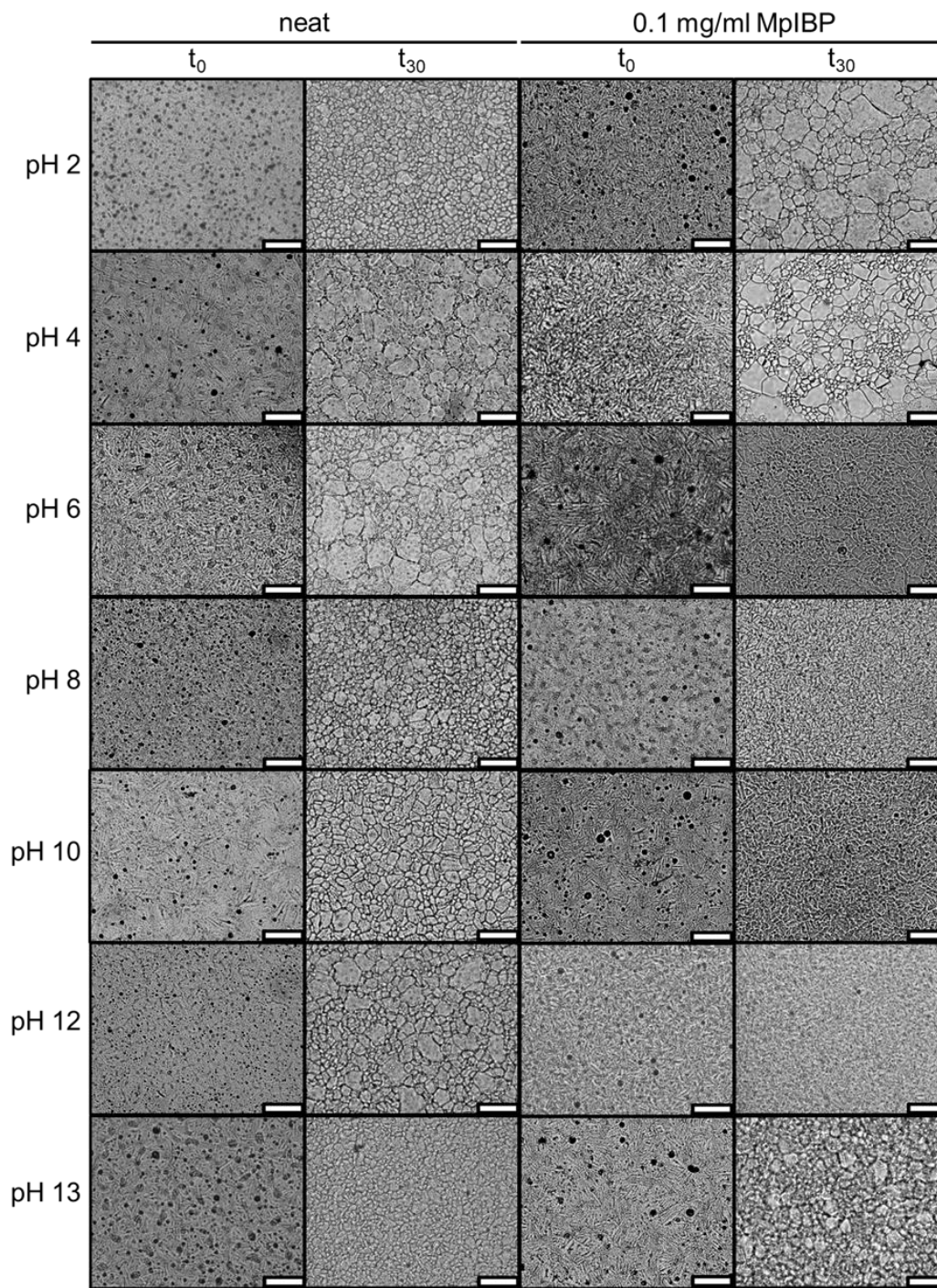
Figure 18. Ice recrystallization micrographs at t_0 and t_{30} of varied pH solutions either as a blank control or loaded with 0.1 mg/ml *Mp*IBP. Scale bar = 100 µm
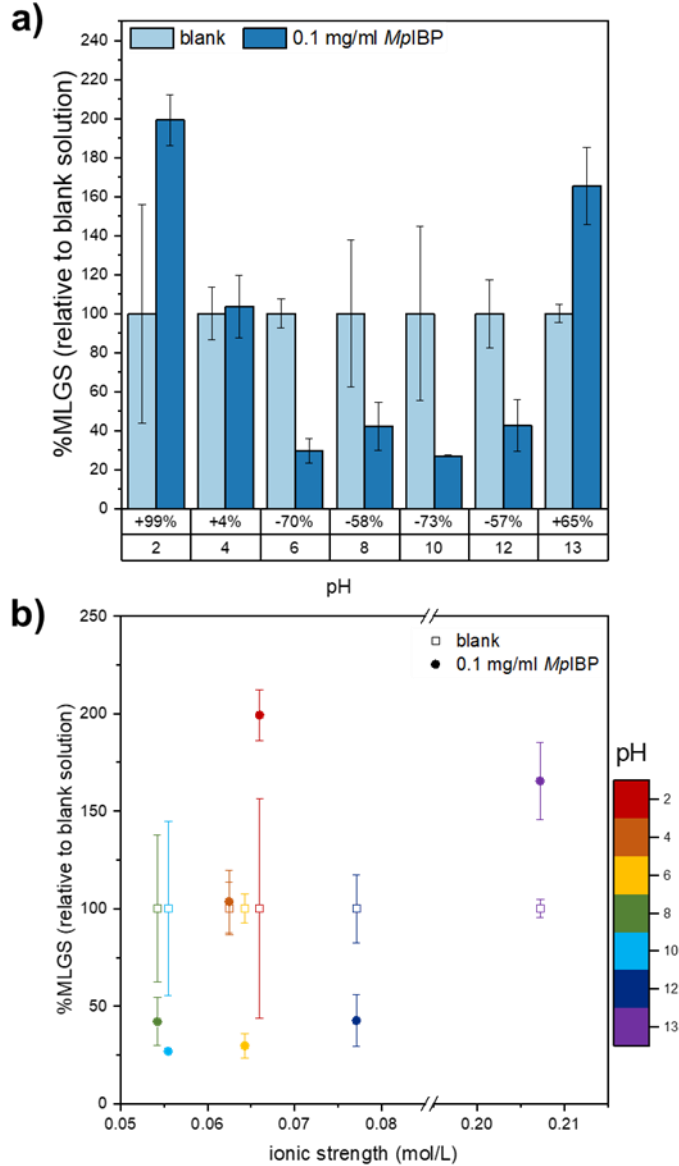
Figure 19. Quantitative analysis for IRI on the addition of 0.1 mg/ml *Mp*IBP at t_{30} to varied pH solutions. (a) Relative %MLGS as a function of pH for *Mp*IBP in non-physiological pH solutions compared to blank pH controls. Percentage indicates the change in ice crystal size compared to control solution by the addition of 0.1 mg/ml *Mp*IBP, with positive percentages indicating an increase in grain size (*Mp*IBP is not IRI active) and negative percentages indicating a decrease in grain size (*Mp*IBP is IRI active). (b) Relative %MLGS as a function of ionic strength. It was found that pH has a stronger influence on the IRI activity of *Mp*IBP than ionic strength.

4.3.4. MpIBP exhibits DIS between pH 6 and pH 10

DIS was implemented to determine if *Mp*IBP was adsorbing to the ice crystal surface (**Figure 20**). None of the control pH solutions elicited dynamic ice shaping, evidenced by spherical single crystals. DIS by *Mp*IBP was readily seen in pH 6, pH 8, and pH 10 solutions as a change to hexagonal ice crystals. At pH $\geq$ 12 or pH $\leq$ 4 *Mp*IBP did not demonstrate any DIS and behaved similarly to control solutions. In physiological solutions, when *Mp*IBP adsorbs to ice crystals it prevents expansion of the crystal in the basal and prism planes, creating a hexagonal ice crystal.[38]
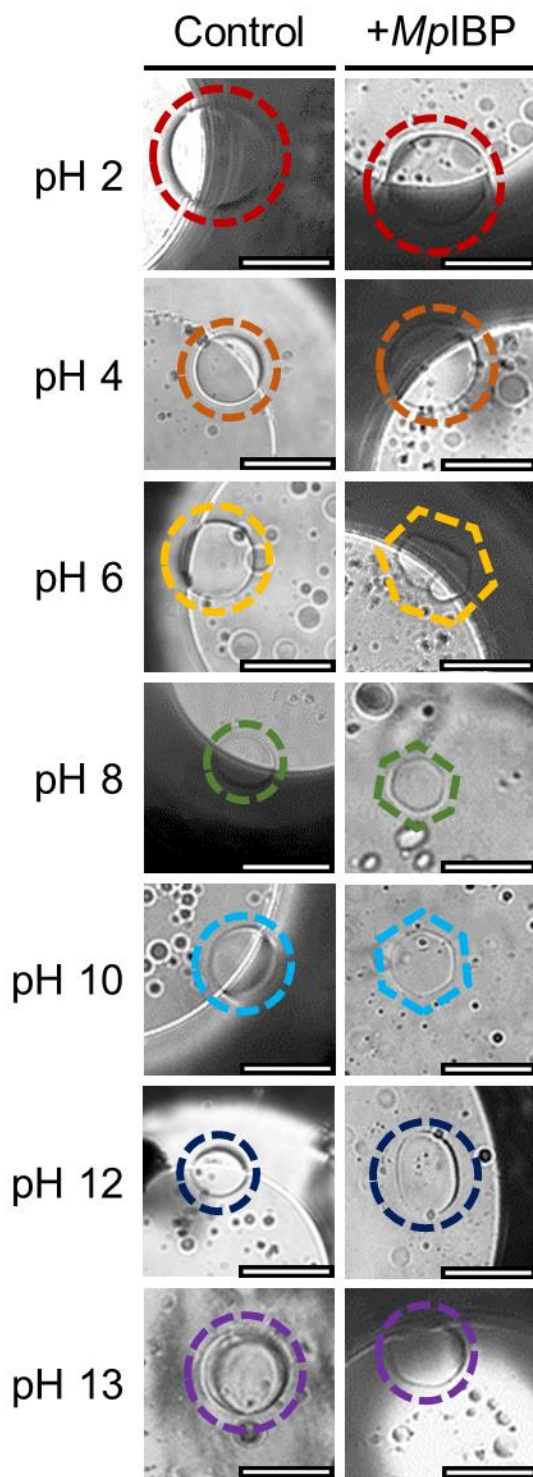
Figure 20. Dynamic ice shaping for (left) blank control pH solutions and (right) 0.1 mg/ml *Mp*IBP in pH solutions. Ice crystals outlined with a circle do not demonstrate DIS, and ice crystals outlined with a hexagon demonstrate DIS. Bubbles in the images are a result of the immersion oil. Black regions in the images are the sample holder. Scale bar = 50 µm.

4.4   Discussion

The results displayed here demonstrate that *Mp*IBP is able to elicit IRI activity between pH 6 – pH 12, as well as DIS between pH 6 – pH 10. This study investigated the ice-binding protein from *Marinomonas primoryensis* in various pH environments (pH 2 – pH 13). It was found that the primary structure of monomeric *Mp*IBP is stable from pH 4 – pH 12, and that secondary structure is retained between pH 6 – pH 10. *Mp*IBP was found to elicit IRI activity between pH 6 – pH 12 and DIS activity between pH 6 – pH 10. To the authors' knowledge, this is one of only a few studies that looks at the IRI activity of an IBP under the influence of pH adjusted ionic solutions. Most studies investigate IRI activity in neutral ionic solutions or with added polyols or investigate the change in thermal hysteresis activity.[3,112,134,140,192,195,196,199,240] This novel contribution of ice inhibition by proteinaceous materials in non-physiological environments could be applied to a variety of engineering applications.

Based on singular observable peaks in SEC-MALS and single bands at the expected molecular weight by BN-PAGE, *Mp*IBP does not aggregate or degrade in solutions between pH 4 to pH 12. *Mp*IBP only exhibits degradation in pH 13 solution, made apparent by a lack of elution peak in SEC-MALS and no prominent band at the expected molecular weight by BN-PAGE, as well as smaller molecular weight bands in SDS-PAGE. *Mp*IBP at pH 2 exhibits a broadened peak at the same elution time in SEC-MALS compared to pH 8 but exhibits a band at the expected molecular weight by BN-PAGE, suggesting intact protein with different charge interactions in the SEC-MALS column. The elution peaks for *Mp*IBP in solution with pH 4 – pH 12 are singular, and similar in size and elution time compared to *Mp*IBP in pH 8. Assuming that *Mp*IBP is monomeric at 0.1 mg/ml at pH 8 based on previous literature,[38,43] it can be assumed they *Mp*IBP is also monomeric in solutions at pH 4 – pH 12. The BN-PAGE showed that the protein was not aggregating due to a lack of upper molecular weight bands, nor was it degrading due to a lack of bands at lower molecular weights, thus the primary structure of the protein is stable and not aggregating.

Properly folded *Mp*IBP creates a calcium-stabilized β-solenoid tertiary structure that would have its ice-binding face exposed to solution, allowing interactions with ice crystals (**Figure 21**a). The β-solenoid consists of thirteen tandem repeats with the sequence -xGTGNDxuxuGGxuxGxux-, where x is any amino acid and u is a hydrophobic amino acid.[238] The current hypothesis for *Mp*IBP ice-binding activity is closely related to its regularly spaced parallel β-strands that promote a 7.4 Å spacing between ice-binding residues (threonine (T) and asparagine (N)) on the same coil of the β-solenoid, as well as 4.6 Å spacing between ice-binding resides on adjacent coils, as can be seen in **Figure 21b**.[38,43,238] Oxygen atoms in the ice crystal lattice repeat at 7.37 Å along the c-axis of the primary prism plane as well as repeat at 4.52 Å along the a-axis in the primary prism and basal planes, as can be seen in **Figure 21c**. The spacing of ice-binding residues along the coils of the *Mp*IBP β-solenoid allow it to match the ice lattice on the primary prism and basal planes of ice, resulting in IRI and hexagonal DIS.

A disruption of protein tertiary structure does not necessarily equate to loss of functionality.[65] Small molecule peptide analogs have shown activity, albeit reduced, when compared to their structured counterparts,[186] indicating that if a portion of the protein responsible for ice growth inhibition remains intact, then some activity may be seen. Herein, CD was utilized to hypothesize how changes in secondary structure influenced IRI and DIS activity. CD analysis revealed that *Mp*IBP exhibited relatively well folded structure between pH 8 and pH 10, consisting largely of β-strands, similar to literature precedence.[38,43,238] For *Mp*IBP in pH 10, a change of 23.5% secondary structure, taken as the absolute difference between fold types, is observed although no singular fold type changed by > 5% (Table 2), indicating *Mp*IBP stability at pH 10. Based on high IRI activity (**Figure 19**) and hexagonal DIS for *Mp*IBP in pH 8 and pH 10 solutions (**Figure 20**), we suggest that the β-helix region hypothesized to interact with ice is intact (**Figure 21a**) and can interact with ice crystals to reduce recrystallization (**Figure 19**) or alter ice morphology (**Figure 20**). Control pH 10 solution exhibited larger grain sizes than control pH 8 solution, demonstrating that for applications in pH 10 environments the crystal expansion would be more detrimental. As the blank solution grain size at t_{30} was larger than pH 8 blank solution, *Mp*IBP at pH 10 appeared

to have the greatest reduction of ice size. Since the grain size at t_{30} for *Mp*IBP at pH 10 was similar to *Mp*IBP in pH 8 solution, it could be concluded that *Mp*IBP was most effective in pH 10 solution.
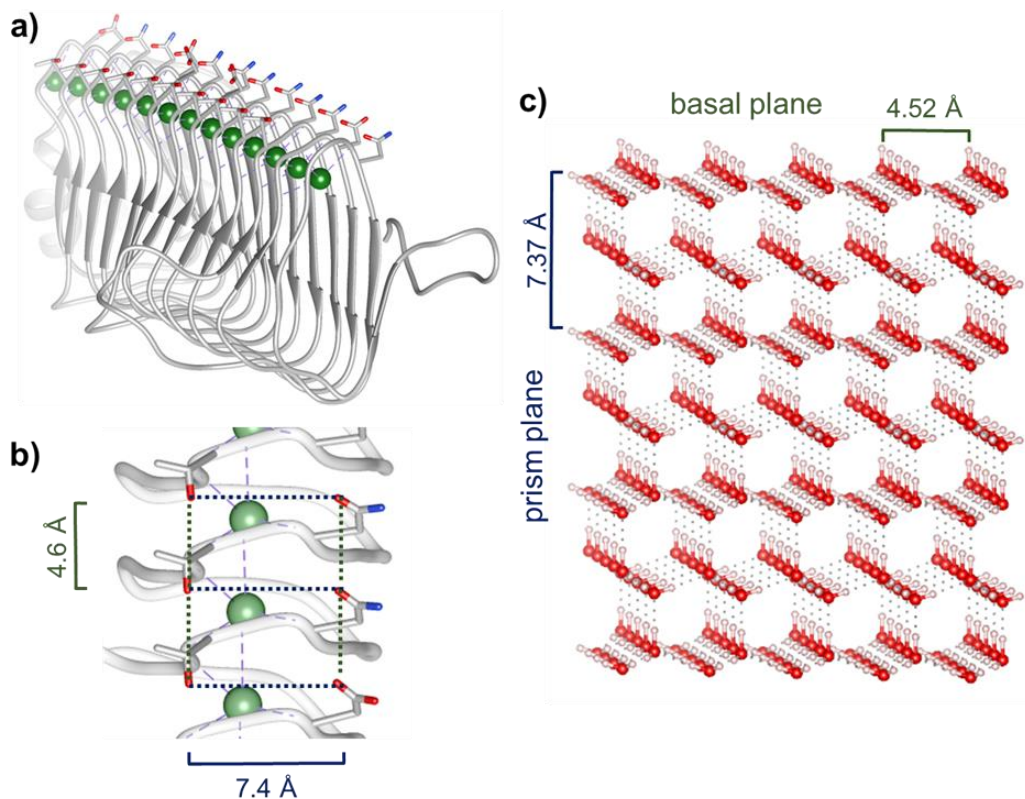
Figure 21. (a) The β-solenoid structure of properly folded *Mp*IBP in the presence of Ca^{2+} ions (green spheres). (b) Spacing of ice-binding residues of properly folded *Mp*IBP. The ice-binding face of *Mp*IBP exhibits ice-binding residues with 7.4 Å spacing on the same coil of the β-solenoid, as well as 4.6 Å spacing between ice-binding resides on adjacent coils. (c) Schematic of the hexagonal ice crystal lattice. Oxygen atoms in the ice crystal lattice repeat at 7.35 Å along the c-axis of the primary prism plane as well as repeat at 4.52 Å along the a-axis in the primary prism plane and basal plane. *Mp*IBP crystal structure was provided by Garnham et al. (PDB 3P4G).[43] *Mp*IBP molecular graphics performed with UCSF Chimera, developed by the Resource for Biocomputing, Visualization, and Informatics at the University of California, San Francisco, with support from NIH P41-GM103311.[241] Ice lattice schematic was made using VESTA software.[22]

*Mp*IBP exhibited promising activity for acidic (pH 6) and basic (pH 12) solutions as a reduction of grain size was observed compared to neat solutions, especially considering the final ice grain size for control solutions were larger than control pH 8 solution. *Mp*IBP in pH 6 had a

greater reduction of ice size compared to *Mp*IBP in pH 8 at t_{30}, and *Mp*IBP in pH 12 demonstrated a reduction of ice crystal size at t_{30} compared to neat pH 12 solution. However, the crystal size for *Mp*IBP in pH 6 and pH 12 at t_{30} was larger than pH 8, indicating decreased IRI activity. The CD spectra for *Mp*IBP in pH 6 demonstrates some folded structure (**Figure 17**); however, the BeStSel deconvolution (**Table 15**) resulted in 50% unfolded structure. *Mp*IBP exhibits a few α-helices and antiparallel β-strands that are not calcium stabilized (**Figure 21a**), and it is anticipated that at pH 6 the non-stabilized structures of the protein are beginning to denature while the calcium-stabilized parallel β-strands remain intact. Similar to *Mp*IBP in pH 6, *Mp*IBP in pH 12 solution shows a decrease in secondary structure that is not calcium stabilized while retaining some parallel β-strand structure. As the ice-binding residues of *Mp*IBP are regularly spaced between the calcium-stabilized parallel β-strands,[43] the retention of the β-strand structure could explain the of IRI activity despite the increase of irregular structure at pH 6. To further probe *Mp*IBP structure under the influence of external stressors such as pH, NMR could be implemented; however, NMR fell outside the scope of this research study.

DIS was only seen in pH 6 and pH 10 solutions where *Mp*IBP showed ≤ 5% change of parallel β-strand structure compared to pH 8, likely because the ice-binding residues still mimicked the distance of oxygen atoms in the ice lattice to facilitate adsorption (**Figure 21**). The tertiary structure of *Mp*IBP regularly aligns the ice-binding residues into a 7.4 Å by 4.6 Å motif that facilitates adsorption to hexagonal ice. The 7.4 Å by 4.6 Å motif is structured through the parallel β-strands, and it is anticipated that changes in the β-strand alignment would disrupt the spacing of the residues, reducing the match to the ice crystal lattice. *Mp*IBP in pH 12 retained a similar amount of overall β-strand structure as *Mp*IBP in pH 6. However, *Mp*IBP in pH 12 retained less parallel β-strand and exhibited more twisted β-strand structure. We hypothesize that the increase of twisted β-strand is responsible for the loss of DIS activity as there are no longer enough adjacent coils on the β-solenoid to align the ice-binding residues with an appropriate spacing to match the ice crystal lattice, but the overall retention of general β-strands resulted in IRI activity. As IRI is more reliant on the disruption of water molecules at the ice-water interface between ice grains, retention of any

β-strand structure could enable some short-range water ordering to inhibit ice growth. DIS appeared to be more reliant on tertiary structure than IRI, indicating that there is a minimum amount of native structure required to ensure interaction between the protein and ice.[40] To better understand how *Mp*IBP can elicit IRI but not DIS in pH 12 solution, it could be beneficial to observe *Mp*IBP in physiological and stressed environments using neutron reflection to observe interactions at the ice-water interface.[242]

Similar to *Mp*IBP in pH 12, the secondary structure of *Mp*IBP at pH 4 showed an increase in twisted antiparallel β-strands; although *Mp*IBP in pH 4 showed right twisted antiparallel β-strands as opposed to left twisted antiparallel β-strands. However, *Mp*IBP at pH 4 did not evince any IRI activity. It is possible that the difference in the twist direction impacts the difference in IRI activity. Since *Mp*IBP has an isoelectric point of 4.1 (**Table 12**), *Mp*IBP was expected to exhibit instability in pH 4 solution, which resulted in measurement fluctuations in the CD detector.[243] It is possible that in pH 4 solution *Mp*IBP is unable to interact with ice due to the net neutral charge of the protein. In the future, to better understand *Mp*IBPs activity around the isoelectric point, solutions with finer gradations of pH could be implemented to glean what might be happening.

Although *Mp*IBP exhibited larger ice crystals compared to control solutions for pH 2 and pH 13, an additional class of proteins, called ice nucleation proteins, can be useful for targeting specific ice crystal sizes in solution.[106] The shift of CD spectra to lower wavelengths for *Mp*IBP in pH 2 solution indicates some restructuring with an increase in regular and distorted α-helix structure at the expense of turns, antiparallel β-strands, and parallel β-strands. What β-strand structure that was preserved in *Mp*IBP at pH 2 is again possibly due to calcium-stabilization and likely allowed some ice-binding residues to remain exposed to solution. For *Mp*IBP at pH 13, the amount of NaOH necessary to create a pH 13 environment caused absorbance saturation in the CD detector, preventing enough data to be collected for BeStSel deconvolution; however, the spectra that was able to be collected is reminiscent of a typical denatured protein, which is further supported by the lack of elution peak in SEC-MALS and the lack of band at the expected molecular weight by BN-PAGE, indicating protein degradation. It is possible that despite degradation some

of the ice-binding residues remained intact on one or more of the sequence repeats (-xGTGNDxuxuGGxuxGxux-). Therefore, it is possible that there were enough ice-binding residues exposed to solution at pH 2 and pH 13 to interact with ice; however, without a regular structure to promote ice growth inhibition, they could facilitate ice nucleation. Ice nucleation proteins typically exhibit a common contiguous octapeptide repeat composed of mainly hydrophilic residues (-AGYGSTLT-).[244] While *Mp*IPBP does not exhibit more than two adjacent residues from this octapeptide (**Figure 22**), there is a -GTG- repeat close to the -GYG- repeat, as well as a high percentage of the hydrophilic residues present in the *Mp*IBP sequence, e.g., 8.2% A, 13.9% G, and 5.7% T (**Table 12**). To further probe this phenomenon, it would be beneficial to investigate *Mp*IBP in pH 2 and pH 13 as a possible ice nucleator using an ice nucleation assay as described by Congdon et al.[94] Additionally, the sequence of the protein fragments observed at pH 13 could be investigated through mass spectrometry, facilitating understanding of retained amino acid sequences capable of ice nucleation.

*Mp*IBP Sequence

```
       10        20        30        40        50        60
MNVSQSNSFG FWDGTSTQAE ITHSFDHYIG SAFDASNNNV AVTGNVSATL NVLAGDDKVS

       70        80        90       100       110       120
IDGNVEDVLV AANVAVLDMG TGNDQLYVAG DVLGKIDAGT GNDEIYIKGD VSAAVDAGTG

      130       140       150       160       170       180
NDEVYIGGNL SGDLDAGTDN DNIQIGGDVN AALNAGTGND NLIIGHDVSG IVNMGTDNDT

      190       200       210       220       230       240
VEVGRTINAS GKVLLDTGDD SLLVSGDLFG EVDGGTGNDT IIIAGKVSGN IQGGTGNDIV

      250       260       270       280       290       300
RVQSQVWAEA NISLGTGDDV LIVEHELHGT VAGNEGDDSI YLKFYAKEQY NNNSDLRNRV

      310       320       330
ANFEHIRVSD GVVKGSPADF ADYLEHHHHH H
```

Ice Nucleating Octapeptide

AGYGSTLT

Figure 22. Amino acid sequence for the ice-binding region IV from the *Marinomonas primoryensis* protein and the octapeptide repeat for ice nucleating proteins. Accession number WP_112138148.1 in NCBI

To contextualize the importance of investigating ice growth in extreme pH environments, previous research has shown that IRI active materials can decrease freeze-thaw damage in cement due to, in part, to prevention of ice crystal expansion.[245,246] Cementitious materials have a pH of 12-13 due to the presence of $Ca(OH)_2$ that creates a calcium-silicate-hydrate gel, giving concrete its strength[81] which necessitates pH compatible IRI additives. As Ca^{2+} plays an important role in *Mp*IBP structure, the calcium present in cementitious environments could be advantageous for an *Mp*IBP additive. Additionally, since *Mp*IBP prevents ice growth *via* IRI at pH 12, it could be a beneficial additive to cementitious environments to prevent freeze-thaw damage.

*Mp*IBP exhibits IRI activity in solutions $6 \leq pH \leq 12$, indicating that *Mp*IBP (and other IBPs) could be effective at mitigating frost-induced damage in applications that necessitate activity in somewhat non-physiological chemical environments. Although the presence of Na^+ and Ca^{2+} have been shown to effect ice crystal shape and recrystallization,[119] no shaping or significant inhibition of ice recrystallization was seen in control solutions pH 6 – 10, indication that the addition of 0.1

mg/ml *Mp*IBP affected both crystal size (**Figure 19**) and shape (**Figure 20**). *Mp*IBP is more resistant to the presence of OH⁻ compared to H_3O^+, which is substantiated by the isoelectric point of the protein (pI ≈ 4.1). Given that *Mp*IBP is only effective at preventing ice growth in solutions $6 \leq pH \leq 12$, alternative materials for controlling ice morphology in environments beyond these pH bounds must be considered. To further improve pH stability, synthetic biology approaches could be utilized to engineer a more stable protein that retains activity and mitigates ice growth in environments with a pH < 6 or a pH > 12.[247–250] Additionally, synthetic polymer architectures that mimic the ice-binding functionality of IBPs offer a unique avenue for mitigating and controlling ice nucleation and growth, as they may be not only more cost-effective, but also more able to inhibit ice crystal recrystallization in aggressive chemical solutions without relying on tertiary structure to elicit ice interaction activity.[45,92–96,251]

4.5   Conclusions

This study evaluated the potential of a calcium dependent ice-binding protein (IBP) from *Marinomonas primoryensis* (*Mp*IBP) to inhibit and control ice crystal nucleation and growth in non-physiological environments, and changes in activity were found to be a function of protein structure. *Mp*IBP showed the ability to retain its primary and secondary structure in the pH range of 6 – 10 as indicated by similar CD spectra, a single elution peak in SEC-MALS, and a single band at the expected molecular weight by BN-PAGE. DIS and IRI were observed between pH 6 and pH 10. *Mp*IBP lost parallel β-strand structure at solutions of pH < 6 or pH > 10, as well as the ability to inhibit ice crystal growth and exhibit dynamic ice shaping (DIS). *Mp*IBP at pH 12 was an exception, as it misfolded but still retained IRI activity, though it did not elicit DIS. In the most extreme environments (pH 2 and pH 13), the addition of *Mp*IBP resulted in larger ice crystals after 30 min compared to control solutions. Some applications, such as preventing freeze-thaw damage in cement, require pH resilience for IRI active materials due to a highly alkaline environment (pH 12 – 13). In conclusion, these results suggest that *Mp*IBP has some applications in non-physiological environments as frost-prevention materials.

4.6   Authorship and Acknowledgments

AUTHORS: Elizabeth A. Delesky [1], Patrick E. Thomas [2,3], Marimikel Charrier [4], Jeffrey C. Cameron [2,3,5], and Wil V. Srubar III [1,4,*]

[1]Materials Science and Engineering Program, University of Colorado Boulder, Boulder, CO 80309, USA; elizabeth.delesky@colorado.edu (E.A.D.)

[2]Department of Biochemistry, University of Colorado Boulder; Boulder, CO 80303, USA; patrick.thomas@colorado.edu (P.E.T.)

[3]Renewable and Sustainable Energy Institute, University of Colorado, Boulder, CO 80309, USA; jeffrey.c.cameron@colorado.edu (J.C.C.)

[4]Department of Civil, Environmental, and Architectural Engineering, University of Colorado Boulder, Boulder, CO 80309; mmcharrier@colorado.edu (M.C.)

[5]National Renewable Energy Laboratory, Golden, CO 80401, USA

*Correspondence: wsrubar@colorado.edu (W.V.S.III); Tel.: +1-303-492-2621

CHAPTER 5
Ice Recrystallization Inhibition by Single Amino Acid Peptides, Polypeptides, and Threonine-based Polymer Mimics

5.1 Introduction

5.1.1 Ice in Infrastructure

Concrete is prevalent in infrastructure and is one of the most widely consumed materials on Earth.[252] In 2012, it accounted for 9% of global industrial water withdrawals in 2012.[253] Improving the sustainability and long-term resilience of cementitious materials is important worldwide for minimizing material and economic costs.[252] One way to improve sustainability is to prevent or reduce deterioration and consequently increase the lifetime of concrete. A common deterioration pathway for cementitious materials is through the formation and growth of ice, either on the surface or within the concrete itself. To prevent formation of ice on concrete surfaces, deicing salts, such as $CaCl_2$ or $MgCl_2$ are applied; however, the salts can lead to salt scaling and surface degradation and lead to oxidative corrosion of embedded steel reinforcement.[254,255] Within concrete, ice nucleates and grows within pores to generate hydraulic, osmotic, and crystallization pressures that induce cracking—known as freeze-thaw damage.[17,78] Traditionally, internal freeze-thaw damage is mitigated through the addition of surfactant air-entraining admixtures, which stabilize permanent air voids that relieve internal pressures caused by ice nucleation and growth. Mitigation with air entrainment comes with the expense of a reduction in concrete compressive strength and increased permeability.[74,256] New materials that mitigate damages due to or associated with ice in infrastructure could improve concrete sustainability by minimizing environmental and economic costs. For example, a material that performs synergistically with salt deicers may slow the process of salt scaling, improving the lifetime of concrete. Additionally, materials that prevent freeze-thaw damage without the introduction of air voids could extend the lifetime of concrete without compromising strength.

5.1.2 Ice-binding proteins.

Ice-binding proteins (IBPs) are a diverse category of proteins that have evolved independently among many different types of organisms, including plants,[24–26,228] fungi,[24,27,28] fish,[29–34] insects,[36,37,209] and microorganisms.[1,24,38,39] IBPs emerged through convergent evolution and thus display a variety of structures, amino acid sequences, and ice-binding residues.[40,106] Although different in structure, all IBPs demonstrate similar ice-interactions, namely: (1) thermal hysteresis (TH) (*i.e.*, a non-colligative depression of freezing-point temperature while maintaining (or elevating) the melting point); (2) dynamic ice shaping (DIS) (*i.e.*, a reshaping of the 1H hexagonal ice structure to form less disruptive ice geometries); and (3) ice recrystallization inhibition (IRI) (*i.e.*, a property that limits ice recrystallization through Ostwald ripening and overall reduces mean crystal size).[42]

The exact mechanism by which IBPs inhibit ice growth has not been fully explicated due to the sheer variety of IBPs and their different genomic sequences. The prevailing mechanism that is widely agreed upon postulates that ice-interaction is facilitated by an array of quasi-liquid anchored clathrate-waters at the ice-IBP interface that aligns with the ice-lattice of nascent crystals.[43–45,106] Molecular dynamics has supported the importance of bound clathrate waters on IBPs ice-interaction mechanism,[47,48,257] and genetic mutation studies have demonstrated that polar residues play a critical role.[49–54] Despite these advances, further fundamental understanding related to the interactions between ice and the residues of IBPs is an important step toward engineering effective bioinspired replicates.

5.1.3 Bioinspiration

While IBPs have displayed IRI activity in nanomolar concentrations,[40,106] using IBPs in large-scale applications may be limited, since (1) IBPs lose function in non-physiological environments and (2) up-scaled IBP productions to-date have produced limited yields. In a previous study by the authors, an IBP from the microorganism *Shewanella frigidimarina* demonstrated IRI activity in alkaline solutions (pH ≤ 12.7);[3] however, in solutions with higher alkalinity (pH > 12.7) IRI

activity was lost due to degradation of the primary structure of the protein. These results demonstrated limited applicability for IBPs in environments such as concrete, in which the pore solution pH can exceed 13.5.[81] While researchers have attempted to increase yield for IBP production, currently attainable quantities of protein (< 1 g) would be insufficient for large-scale applications. In a study conducted by Tab *et al.*, a 5 L recombinant batch of yeast growth only produced 200 mg of *Glaciozyma Antarctica* IBP.[66] Tomalty *et al.* performed an IBP isolation from *Tenebrio molitar* larvae and only obtained 4.6 mg of protein from 100 g of larvae.[67] Additionally, most IBPs demonstrate TH activity with a rapid and destructive ice 'burst' when reaching their new non-equilibrium freezing point temperature,[40] which poses a unique disadvantage for applications such as freeze-thaw mitigation. These factors create a niche application space for synthetic IBP mimics that are readily produced in large quantities for a variety of commercial industries (e.g., cryogenics, aerospace, infrastructure) and that help mitigate destructive ice bursts typical of native IBPs.

Polymers exhibit a unique advantage over IBPs as they offer tunable pendant moieties, architectures, and scalability for increasingly accessible ice mitigation technologies. Identifying new materials capable of inhibiting ice growth is crucial for targeting niche engineering applications. A recent study performed by Frazier *et al.* proved that using a polymer mimic of natural ice-binding proteins[245] is a viable, alternative strategy for preventing freeze-thaw damage in cement paste and concrete. This approach differs from conventional air entrainment by targeting the source of internal pressures – ice crystal growth – rather than the symptom of internal pressurization. Poly(vinyl alcohol) (PVA) has exhibited promising biomimetic antifreeze behavior,[92–94,98] is easy to produce, and has been shown to mitigate ice growth in a pH 13 environment.[117] One study demonstrated that 27 kDa PVA exhibited moderate IRI behavior at concentrations as low as 0.05 mg/ml (1.6 µM),[98] which is comparable to the concentrations in which biological IBPs are IRI active. However, PVA has shown a propensity to cryogelate upon exposure to freeze-thaw cycles.[258–260] Other molecules, such as pigments,[101] polymer-modified nanoparticles,[102] polyampholytes,[103] quantum dots,[104] and nanocelluloses[105] also exhibit IRI

activity similar to IBPs, however, these molecules do not exhibit the tunability offered by polymers. While certain synthetic molecules with varying chemistries have proven effective in terms of mimicking the IRI behavior of IBPs, the use of commercially available synthetic mimics that mitigate ice growth would be further enabled by understanding the contribution of pendent functional groups found on amino acid residues responsible for ice-binding in IBPs.

5.1.4 Scope of Work

The purpose of this work was (a) to determine which peptides and polypeptides best mitigate ice growth in environments reminiscent of infrastructure applications, i.e., deicing salts or within high pH concrete, and (b) to design and test a robust IBP that mimicked the most effective amino acid structure and function. First, a molecular model was determined by studying three different amino acids based on IBP ice-binding residues and their homo-polypeptides: a neutral amphipathic polar amino acid (l-threonine), a cationic polar amino acid (l-arginine), and an anionic polar amino acid (l-glutamic acid). More specifically, the molecular model was determined by assessing ice formation and ice recrystallization in PBS (pH 7.19). The polypeptide that exhibited the best inhibition of ice growth in PBS, as well as a full synthetic replicate, were then investigated for performance in environments relevant to infrastructure – i.e., alkaline pH and divalent salt solutions. To probe ice interactions, the onset of melting and enthalpy of crystallization were determined by differential scanning calorimetry (DSC). The efficacy of ice recrystallization inhibition (IRI) activity was investigated using a modified splat assay. Dynamic ice shaping (DIS) was determined using a nanoliter osmometer. Similar to precedent research,[2,3,98,211,212,228] IRI activity was determined through direct measurement of the mean largest grain size (MLGS) of ice crystals that formed in the solutions that contained ice mitigation materials after incubation in freezing (-4 °C) conditions compared to blank control solutions.

5.2   Materials

L-threonine (*Thr*), L-arginine (*Arg*), L-glutamic acid (*Glu*), 7.6 kDa poly(L-threonine) (*pThr*), 15 kDa poly(L-arginine) (*pArg*), 12.1 kDa poly(L-glutamic acid) (*pGlu*), calcium chloride, magnesium chloride, copper chloride, aluminum chloride, sodium carbonate, 2,2'-azobis(2-methopropionitrile), 2-cyano-2-propyl dodecyl trithiocarbonate, methanol, methacryloyl chloride, D-L-1-amino-2-propanol, dichloromethane, sodium hydroxide (NaOH), hydrogen chloride (HCl), and poly(2-hydroxypropyl methacrylamide) (*pHPMA*) were purchased from Sigma Aldrich without further purification. Molecular weights of the polypeptides and *pHPMA* were provided by Sigma Aldrich and can be seen in **Table 16**. Phosphate buffered saline (PBS) was purchased from Fisher Scientific without further modification. NaOH was utilized to create PBS solutions with a pH of 8, 10, 12, or 13.

Table 16. Polymer Properties as given by Sigma Aldrich.

Polymer Properties							
Material	Product No.	Batch No.	[a]MW Range (kDa)	[b]DP	[c]MW$_v$ (kDa)	[d]MW$_{GPC}$ (kDa)	[e]PDI
Poly(threonine) (*pThr*)	P8077	018H5900	5-15	75	7.6	-	-
Poly(arginine) (*pArg*)	P4663	SLBF2407V	5-15	78	15	-	-
Poly(glutamic acid) (*pGlu*)	P4636	SLBR1777V	3-15	80	12.1	-	-
Poly(2-hydroxypropyl methacrylamide) (*pHPMA*)	804746	MKCF7844	30-50	290	-	41.4	1.2

[a]The molecular weight (MW) range.
[b]The degree of polymerization (DP).
[c]The molecular weight of the product as determined by viscosity.
[d]The molecular weight of the product as determined by gel permeation chromatography.
[e]The polydispersity index (PDI) of the product. Note: *pThr*, *pArg*, and *pGlu* were not given PDI due to the method used to determine molecular weight.

5.3   Determining a Molecular Model

To determine the best amino acid residue to model for full synthetic mimics, select amino acids inspired IBP ice-binding residues were examined for interaction with ice in a variety of solutions through several characterization techniques described below.

5.3.1 Amino Acids and homo-polypeptides

Amino acids (*Thr, Arg, Glu*) and homo-polypeptides (*pThr, pArg, pGlu*) were loaded into PBS at a concentration of 10 mg/ml unless otherwise stated. The only exception was *Glu*, which had a maximum concentration of 8.6 mg/ml due to solubility limitations. For the sake of comparison, the maximum concentration of *Glu* was compared to 10 mg/ml concentrations. The chemical structure for amino acids and homo-polypeptides used in this study can be seen in **Figure 23**. The pendant functional group for *Thr* and *pThr* is a neutral polar structure, while *Arg* and *pArg* exhibit a protonated cationic structure due to a pK_a of 12.5, and *Glu* and *pGlu* exhibit a deprotonated anionic structure due to a pK_a of 4.25.[261] To ensure the best amino acid residue was chosen for replication, properties such as structure, melting point depression, enthalpy of crystallization, and IRI activity were investigated and compared. However, as the target application depends on IRI, the material with the best IRI activity in PBS was used to determine the molecular model.
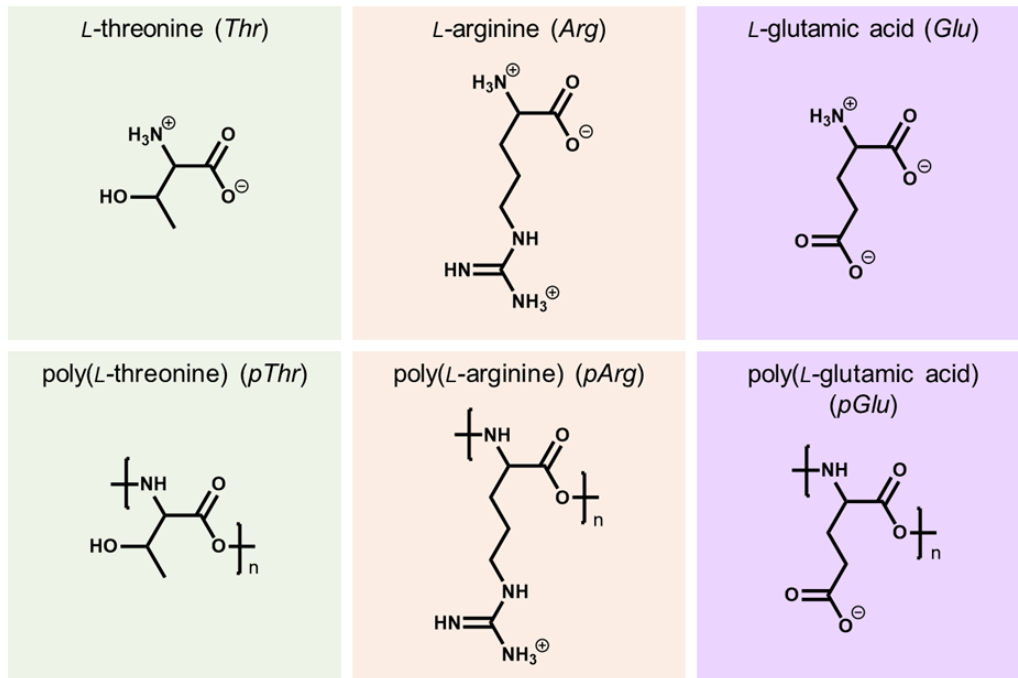
Figure 23. Chemical structure of amino acids (*Thr*, *Arg*, *Glu*) and polypeptides (*pThr*, *pArg*, *pGlu*) used in this study.

5.3.2 Secondary Structure using Circular Dichroism Spectroscopy

Homo-polypeptides were tested for secondary structure in PBS *via* CD spectroscopy in the far UV range (190-260 nm) using a modular Applied Photophysics Chirascan Plus CD and Fluorescence Spectrometer at ambient temperature with 0.5 nm steps and 0.5 sec/step at a 0.5 mm path length. Homo-polypeptides were loaded at 1 mg/ml for CD analysis for improved absorption without exceeding the absorption limits. It should be noted that *pArg* absorbance could not be measured below 197 nm due to the confluence of molecule absorbance interfering with the signal detection limits of the instrument. Similarly, scattering artifacts induced distortions in the PBS scans below 195 nm due to insufficient intensity absorption limits commonly encountered on conventional CD instruments for saline solutions.

Five repeat scans were averaged for each homo-polypeptide and the corresponding baseline for blank solution. After removing the blank solution baseline, data were processed in the Chirascan Software using the Savitzky-Golay smoothing filter using 5 points per window with a polynomial order of 2. Secondary structure composition (i.e., % helix, sheet, turns, etc.) was measured from the peptide bond region (< 240 nm)[213] using BeStSel analysis software.[214]

5.3.3 Determining Solution Constituents

As the splat assay described in **Section 5.3.5** can yield false positives for IRI activity at low salt concentrations,[120] calcium chloride solutions were made from 10 mM to 151 mM (1) to determine if activity changed with salt concentration, and (2) to find a salt concentration where material performance was constant. Once salt concentration was determined, salt solutions with different cations but the same anion were used to determine the effect of cations on material efficacy, as **Chapter 2** showed that some salt constituents can improve IRI activity. Salts chosen for this study were $CaCl_2$, $MgCl_2$, $CuCl_2$, and $AlCl_3$. $CaCl_2$ and $MgCl_2$ were chosen as they are relevant to infrastructure as deicing salts.[255] $CuCl_2$ was chosen as it is relevant to the cryopreservation of red blood cells, and $AlCl_3$ was chosen to compare the effects of a trivalent

cation. To elucidate the effect of salt concentration and salt type on the performance of the molecules, all molecules were loaded at 10 mg/ml.

5.3.4 Melting Point and Crystallization Enthalpy using Differential Scanning Calorimetry

An assessment of ice formation was performed with amino acids (*Thr*, *Arg*, *Glu*) and homopolypeptides (*pThr*, *pArg*, *pGlu*) loaded in PBS at concentrations of 0.001, 0.01, 0.1, 1, or 10 mg/ml. Samples were run in duplicate. 10 µl of sample was loaded into a Tzero hermetic aluminum pan from TA Instruments and hermetically sealed. Both the weight of the pan and the weight of the sample were recorded. The sample was transferred to a TA DSC Q2000 stage with an attached refrigerated cooling system (RCS 90). Heat flow (mW/g) was measured and recorded against an empty, pre-weighed Tzero hermetic aluminum reference pan to detect any exothermic or endothermic transitions. Each individual DSC sample was cycled from 10 °C to -30 °C to 10 °C at 2 °C/min (3x), with an exothermic loop indicating freezing and an endothermic peak demonstrating ice melting.

The enthalpy of crystallization and melting point were determined using TA Universal Analysis Software 2000 Version 4.5A. The enthalpy of crystallization was taken as the integration of the melting peak and the melting point was defined as the onset of the melting peak.[115] Both enthalpy of crystallization and melting point averages were determined from six melting cycles. The melting curve was used instead of the freezing point as DSC does not allow for facile determination of ice nucleation[116] due to supercooling within the DSC pan, which can cause varied, irregular freezing points.

5.3.5 Ice Recrystallization Inhibition Activity

To determine ice recrystallization inhibition activity, a splat assay was adapted from Knight *et al.* [2] Briefly, amino acids (*Thr*, *Arg*, *Glu*) and homo-polypeptides (*pThr*, *pArg*, *pGlu*) were loaded in PBS at a concentration of 10 mg/ml and diluted to 0.01 mg/ml using 10-fold dilutions. Materials were additionally loaded at 10 mg/ml into 151.5 mM $CaCl_2$, 151.5 mM $MgCl_2$, 151.5

mM $CuCl_2$, and 151.5 mM $AlCl_3$ solutions to investigate the effect of multivalent cations on IRI. Splats were performed in triplicate. 10 µL samples were dispensed onto a microscope slide on top of an aluminum block chilled with dry ice from 1.7 m through a PVC pipe to obtain a monolayer of ice crystals. The slide was then transferred to an Otago nanoliter osmometer sample stage and annealed at -4 °C. The temperature was monitored using a bead-type thermocouple. Images were collected immediately after the splat was performed (t_0) to verify polycrystalline ice formation and again at 30 minutes (t_{30}) to observe ice recrystallization. Images were obtained using an Olympus BX41 microscope with an Olympus PLN 10X objective, equipped with an Axiocam 506 color camera on a 1" 1.0x 60N C-mount adapter. ImageJ image processing software version 1.48v (National Institutes of Health, USA) was used to measure the mean largest grain size along the major axis. Data were collected by counting the 10 largest grains from 3 different regions per splat to determine an average grain size ($n = 90$) at t_{30} for each sample type.

5.4   Bioinspired Synthetic Mimics

Based on IRI in PBS, *pThr* was determined to be the best performing homo-polypeptide, and the chemical structure for the threonine residue and was used as a molecular model to choose a synthetic replicate, 2-hydroxypropyl methacrylamide (*HPMA*) and its respective polymer, *pHPMA*.

5.4.1 Synthesis of 2-hydroxypropyl methacrylamide.

The molecule 2-hydroxypropyl methacrylamide (*HPMA*) and its respective polymer were chosen as a synthetic mimic for threonine, and their chemical structures can be seen in **Figure 24**. While this study used a *HPMA* molecule that was synthesized in house, it is a commercially available material to keep in line with the nature of this study. *HPMA* was synthesized following a previously published protocol,[262] and the schematic can be seen in **Figure 25**. In brief, dichloromethane was placed in a round bottom flask and dried with sodium carbonate as well as a nitrogen purge. The flask was cooled to -10 °C using an acetone-ice bath. D-L-1-amino-2-propanol

was added to the flask followed by a nitrogen purge. Methacryloyl chloride was loaded into dichloromethane and added dropwise to the D-L-1-amino-2-propanol mixture until a 1:1 molar ratio has been achieved. After the methacryloyl chloride was added, the reaction was allowed to proceed for 45 minutes at -10 °C. The reaction was then removed from the acetone-ice bath and stirred as it warmed to room temperature (~1 hour). The solution was then filtered to remove the sodium bicarbonate, crystallized in DCM at -20 °C overnight and the off-white crystals collected, then recrystallized in acetone at -20 °C overnight, filtered again to collect the pure white crystals. The final product was dried and verified using ^{1}H NMR (**Figure 26**).
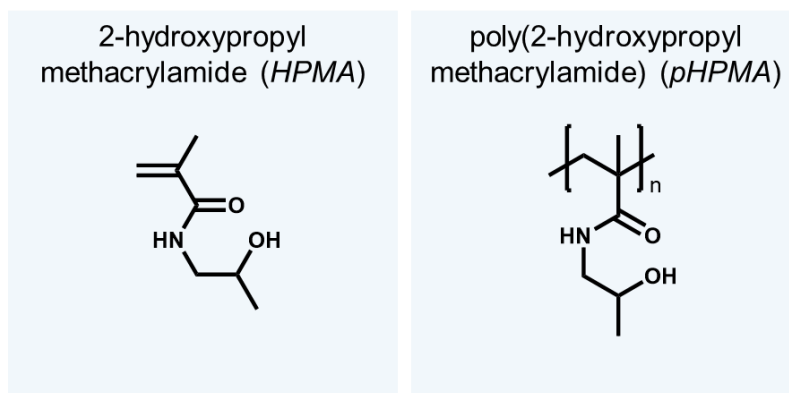
Figure 24. Chemical Structure of 2-hydroxypropyl methacrylamide (*HPMA*) and poly(2-hydroxypropyl methacrylamide) (*pHPMA*) synthetic threonine mimics.
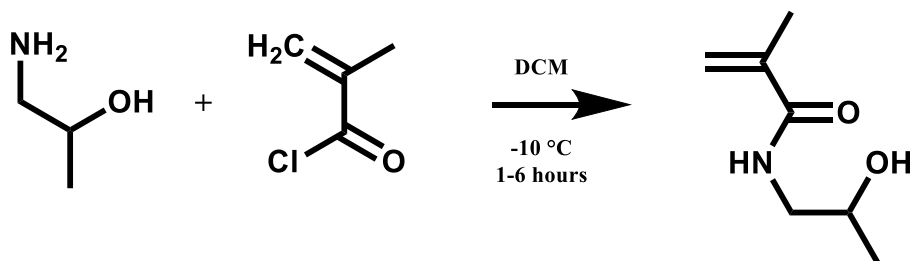
Figure 25. Synthesis of *HPMA* monomer by combining amino-2-propanol and methacryloyl chloride.
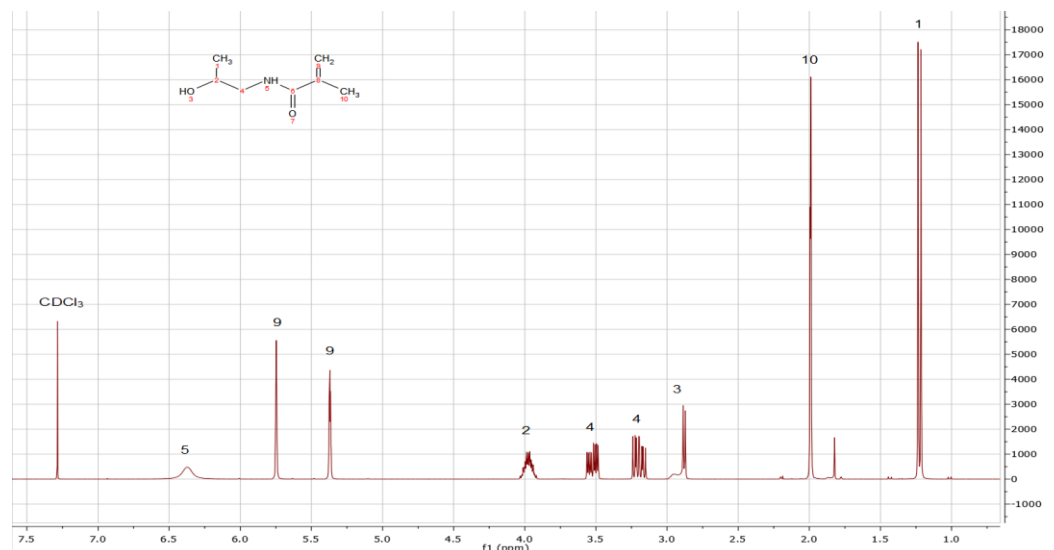
Figure 26. 1H NMR spectra verifying pure HPMA. ^{1}H NMR (400 MHz) for N-(2-hydroxypropyl)methacrylamide in CDCl$_3$: δH (ppm) = 1.22 (dd, 3H, CH(OH)-C$\underline{H_3}$), 1.99 (dd, 3H, C(CH$_2$)C$\underline{H_3}$)), 2.88 (dd, 1H, O$\underline{H}$), 3.20 (ddd, 1H, NH-C$\underline{H_2}$), 3.52 (ddd, 1H, NH-C$\underline{H_2}$), 3.97 (m, 1H, C(OH)$\underline{H}$), 5.37 (dq, 1H, CC$\underline{H_2}$), 5.75 (dq, 1H, CC$\underline{H_2}$), 6.37 (br s, 1H, N$\underline{H}$).

5.4.2 Synthesis of poly(2-hydroxypropyl methacrylamide)

To determine the efficacy of *pHPMA*, four target *pHPMA* molecular weights were synthesized, and the details for the polymers are listed in **Table 17**. To polymerize *HPMA*, a protocol was adapted from previously published research.[262] Briefly, RAFT polymerization was performed using the chain transfer agent 4-Cyano-4-[(dodecylsulfanylthiocarbonyl)sulfanyl] pentanoic acid. A dry reaction vessel was loaded with dry dimethyl formamide (DMF) and purged with nitrogen. The chain transfer agent, monomer, and initiator were loaded into the reaction vessel which was subsequently purged with nitrogen for 45 minutes to ensure that there was no oxygen in the vessel. Once purged, the vessel was placed in a hot oil bath heated to 70 °C under continuous nitrogen flow. The reaction proceeded for 24 hours and was stopped by exposing it to air. Solvent was evaporated the crude product was examined using 1H NMR to determine monomer conversion. The product was purified by precipitation into a cold ACETONE vortex, filtered, and then freeze-dried. The final product was confirmed using 1H NMR.

Table 17. *pHPMA* synthesis details and results.

Target MW (g/mol)	25,000[a]	10,000[a]	5,000[b]	2,500[b]
HPMA Molarity (Solvent MeOH)	2M	2M	2M	2M
Equivalence (HPMA:CTA:AIBN)	246:1:0.6	95.2:1:0.6	39.4:1:0.6	18:1:0.6
Conversion	76.8%	85.5%	85.3%	90.5%
MW (g/mol)	28,176	11,160	5,225	2,729
Yield	67.5%	81.4%	78.9%	67.4%

[a]MW @ 70% conversion
[b]MW @ 80% conversion

5.4.3 Melting Point and Crystallization Entropy using Differential Scanning Calorimetry

DSC assessment of ice formation was performed with *Thr*, *pThr*, *HPMA*, and *pHPMA*, which were loaded into PBS, 151.5 mM $CaCl_2$, 151.5 $MgCl_2$, 151.5 mM $CuCl_2$, 151.5 mM $AlCl_3$, or pH varied PBS solutions at a concentration of 10 mg/ml. DSC was performed as described in **Section 5.3.4**.

To compare the effect of *Thr*, *pThr*, *HPMA*, and *pHPMA* on the observed melting point of solutions ($T_{m,(observed)}$), the theoretical melting point ($T_{m,(theoretical)}$) was calculated assuming an ideal solution using Equation 1:

(1) $$T_{m,(theoretical)} = 0°C - (\Delta T_{s,(ideal)} + \Delta T_{a,(ideal)})$$

Where $\Delta T_{s,(ideal)}$ is the ideal contribution of the solution salts to the expected melting temperature and $\Delta T_{a,(ideal)}$ is the ideal contribution of *Thr*, *pThr*, *HPMA*, or *pHPMA* to the change in meting temperature, and 0 °C is the melting point of water in Celsius. $\Delta T_{s,ideal}$ and $\Delta T_{a,ideal}$ were determined using Blagden's law (Equation 2):

(2) $$\Delta T_{s,(ideal)} \ or \ \Delta T_{a,(ideal)} = K_f * b * i$$

Where K_f is the cryoscopic constant of water (1.853 K·kg/mol), *b* is the molality of solute, and *i* is the van't Hoff factor of solute. To quantify how well the predicted behavior reflects the experimental behavior, data were plotted as observed vs. theoretical with a y = x line demonstrating the fit to predicted behavior. The curated data were then compared to the y = x line using the coefficient of determination, R^2 (Equation 3):

$$R^2 = 1 - \frac{SQR}{SE_{\bar{y}}}$$

(3)

Where SQR determines the squares of the residual, and $SE\bar{y}$ is the total variation in y. As Blagden's law assumes ideal behavior, the model was adjusted using blank solution data to account for non-ideal contributions of the solution on the theoretical melting point, and subsequently the non-ideal effect of solute on the melting point. Non-ideal contributions were determined by fitting $T_{m,(theoretical)}$ to the y = x line, resulting in an empirically derived constant, $\Delta T_{s,(non\text{-}ideal)}$, which, in this case was found to be 1.28 °C. The same determination was done for the non-ideal contributions of molecules, which resulted in a $\Delta T_{a,(non\text{-}ideal)}$ for each molecule. After adjusting data to account for non-ideal contributions to the melting point data were evaluated for a slope of best fit. The new $T^*_{m,(theoretical)}$ that accounts for non-ideal contributions can be seen in Equation 4:

(4) $$T^*_{m,(theoretical)} = 0°C - (\Delta T_{s,(ideal)} + \Delta T_{a,(ideal)} + \Delta T_{s,(non-ideal)} + \Delta T_{a,(non-ideal)})$$

$T_{m,(observed)}$ data sets were then compared to adjusted $T^*_{m,(theoretical)}$ to determine contributions of molecules beyond colligative, represented by the slope (M) of the line of best fit for each individual data set.

As the enthalpy of crystallization (ΔH_{melt}) is directly proportional to the amount of crystalline ice formed in solution, ΔH_{melt} was used to determine how much crystalline ice was forming. However, since ΔH_{melt} can be affected by the concentration of solute when compared to blank solution, ΔH_{melt} and $T_{m,(observed)}$ were used to calculate the entropy of crystallization (ΔS_{melt}) per Equation 5:

(5) $$\Delta S_{melt} = \frac{\Delta H_{melt}}{T_{m,(observed)}}$$

Since both ΔH_{melt} and $T_{m,(observed)}$ are affected by solute concentration, ΔS_{melt} will demonstrate any effects in solution not expected from the concentration of added solute.

5.4.4 IRI activity in Infrastructure Relevant Environments.

To further probe ice inhibition in infrastructure relevant environments, *Thr, pThr, HPMA,* and *pHPMA* were loaded at 10 mg/ml into salt solutions (151.5 mM $CaCl_2$, 151.5 mM $MgCl_2$, 151.5

mM $CuCl_2$, or 151.5 mM $AlCl_3$) or into pH adjusted PBS solutions (PBS pH 8, PBS pH 10, PBS pH 12, PBS pH 13). Salt solutions were chosen to investigate possible synergistic effects with various cations as possibly additives to deicing salts, or for other applications in the presence of salts. pH solutions were varied through the alkaline region to determine molecular viability as an additive to cement or concrete, which exhibits a highly alkaline pore solution (pH ~13). To determine the potency of *pThr* and *pHPMA*, IRI was performed with 10-fold dilutions until the molecules no longer demonstrated IRI in PBS. IRI efficacy was performed using a splat assay, as described above.

5.4.5 Dynamic Ice Shaping.

Thr, *pThr*, *HPMA*, and *pHPMA* were loaded into PBS at a concentration of 10 mg/ml and tested for dynamic ice shaping (DIS) using an Otago nanoliter osmometer sample stage mounted on an Olympus BX41 microscope with an Olympus LUCPlanFL N 20x /0.45 Ph1 Microscope Objective. Immersion oil was used to fill the holes of the sample holder of the osmometer and 1 µl of sample was loaded into the oil. The sample was frozen rapidly by lowering the temperature to -20 °C. The sample was then slowly melted (~1 °C/min) until a single ice crystal ($\leq$ 25 µm) remained and the temperature was recorded. The sample was incubated for 5 min to ensure interaction between the molecule and a single ice crystal. The temperature was then decreased at 0.01°C/min until ice expansion occurred. Videos were recorded using Axiocam 506 color camera on a 1" 1.0x 60N C-mount adapter. The Microsoft Photos app was used to isolate still images from video recordings. If a molecule demonstrated DIS in PBS, it was further investigated for DIS in salt solutions (151.5 mM $CaCl_2$, 151.5 mM $MgCl_2$, 151.5 mM $CuCl_2$, or 151.5 mM $AlCl_3$) or into pH adjusted PBS solutions (PBS pH 8, PBS pH 10, PBS pH 12, PBS pH 13).

5.5   Threonine as a Molecular Model

5.5.1 Secondary Structure

CD was utilized to examine secondary structure in homo-polypeptides. CD absorbance spectra for homo-polypeptides in PBS and can be seen in **Figure 27**. Content of secondary structure determined by BeStSel is summarized in **Table 18**. *pThr* exhibited negative peaks at 200 nm and 221 nm in PBS. *pArg* exhibited a negative peak at 200.5 nm and a positive peak at 217 nm in PBS. *pGlu* exhibited a negative peak at 198.5 nm, a positive peak at 217 nm in PBS. The negative peak for *pGlu* was 10 nm at half-max in PBS. The 10 nm half-max for the negative peak for pGlu in PBS indicates a misfolded structure (Table 18).[213]
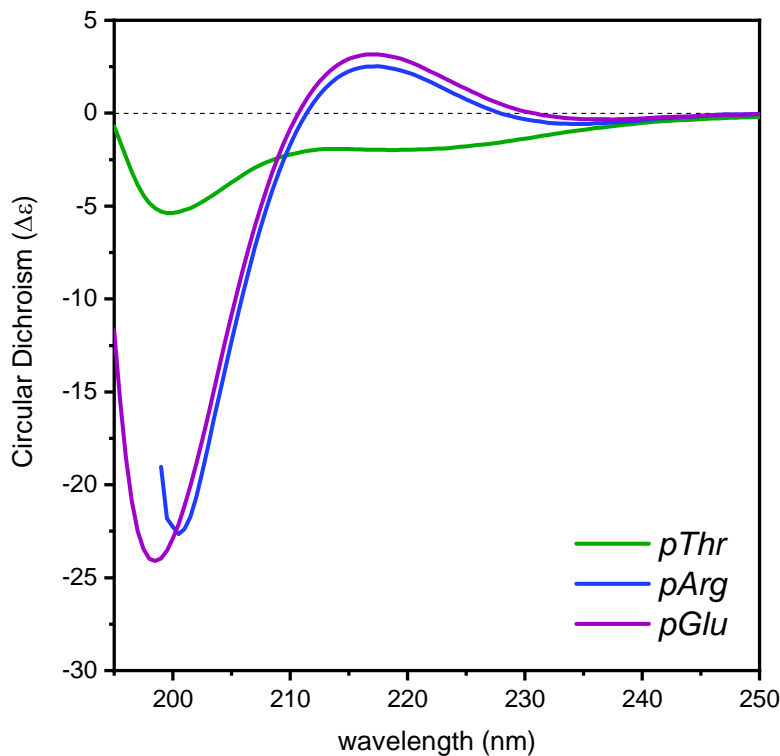
Figure 27. Circular Dichroism absorbance spectra for homo-polypeptides in PBS. *pArg* stops before *pThr* and *pGlu* in PBS due to absorbance saturation in the CD detector.

Table 18. Secondary structure of 1 mg/ml homo-polypeptides in PBS.

Homo-polypeptide Structure			
PBS			
Fold Type	*pThr*	*pArg*	*pGlu*
Regular α-helix	0.0%	0.0%	0.0%
distorted α-helix	2.0%	0.0%	0.0%
left-twisted antiparallel β-strand	0.0%	0.0%	0.0%
relaxed antiparallel β-strand	0.0%	0.0%	0.0%
right-twisted antiparallel β-strand	18.7%	0.0%	0.0%
parallel β-strand	0.0%	0.0%	0.0%
turn	15.6%	7.6%	12.6%
other (irregular/loop)	63.7%	92.4%	87.4%

pThr exhibited ordered structure in PBS, namely 18.7% right-twisted antiparallel β-strand. The β-strand structure likely formed due to dipolar forces and hydrogen bonding between the threonine residues, which lead to absorbance similar to denatured proteins.[263,264] β-sheets are thought responsible, in part, for spacing ice-binding residues at regular intervals to facilitate ice interactions of some IBPs[40,41] and could play a role in polypeptide-ice interactions. It was anticipated that homo-polypeptides would exhibit residual structures similar to denatured proteins[263,264] though with some behavior similar to a random coil akin to typical homo-polymers.[265] Results suggest the unique compositions of homopolymerized amino acid residues created molecular structures somewhere between a denatured protein (polymerized amino acid residues) and a homopolymer (polymerized monomer units); however, the structure determined by CD indicated that the homo-polypeptides were more similar to homopolymers than proteins. Further tests are required to more thoroughly understand the minimal structure of *pThr*, including temperature and time denaturation tests, however, these fell beyond the scope of this dissertation.

5.5.2 Solution Composition and molecular model determined via IRI

A representative splat endpoint (t_{30}) for each amino acid (*Thr*, *Arg*, *Glu*) and homo-polypeptide (*pThr*, *pArg*, *pGlu*) in PBS is shown in **Figure 28**. The concentrations 0.001 mg/ml, 0.1 mg/ml, and 10 mg/ml were chosen to represent the effect of changing concentration. Splat

images for the initial time (t_0) compared to the endpoint (t_{30}) for all concentrations (0.001, 0.01, 0.1, 1, and 10 mg/ml) are shown in **Appendix B**. The relative activity of each amino acid or homo-polypeptide compared to blank solutions is shown in **Figure 29**, and matches literature precedence for expected growth.[34,73,74]

In PBS, *pThr* exhibited significant IRI activity compared to blank solution at 0.1, 1, and 10 mg/ml with reductions of 71.9%, 60.9%, and 65.2%, respectively. *pThr* exhibited no activity at lower concentrations. At 0.001 mg/ml in PBS, *Thr* exhibited ice crystal sizes 51.9% larger than blank solution and was insignificant at higher concentrations. Neither *pArg* nor *Arg* exhibited any effect on ice growth in PBS. *pGlu* was IRI active at 10 mg/ml in PBS, seen as a reduction of 59.3%, and did not affect ice growth at concentrations ≤ 1 mg/ml, and *Glu* IRI activity in PBS was insignificant.
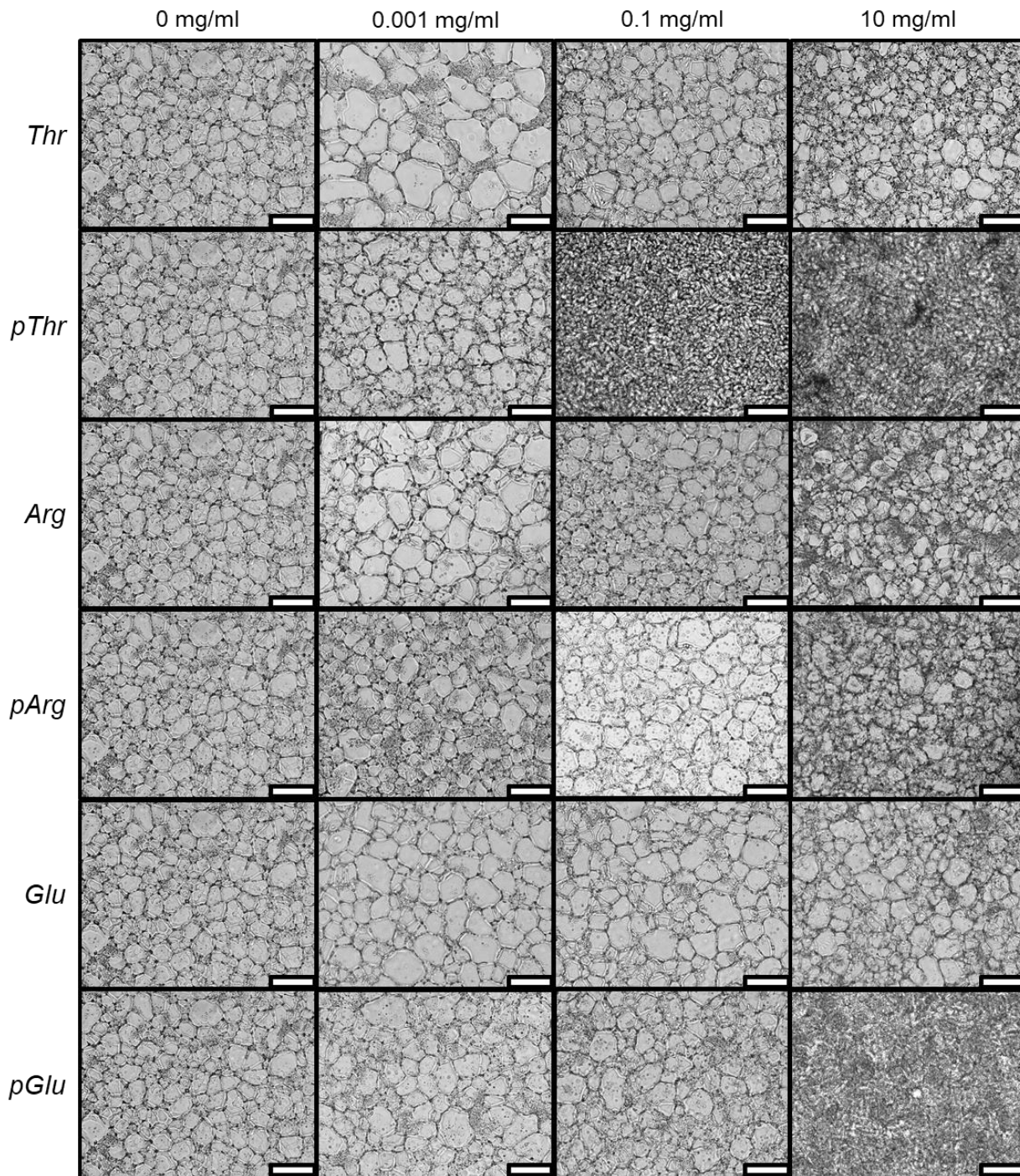
Figure 28. Representative endpoint IRI activities of each amino acid (*Thr*, *Arg*, *Glu*) and homo-polypeptide (*pThr*, *pArg*, *pGlu*) at concentrations of 0.001, 0.1, and 10 mg/ml in PBS. Scale bar = 100 μm.
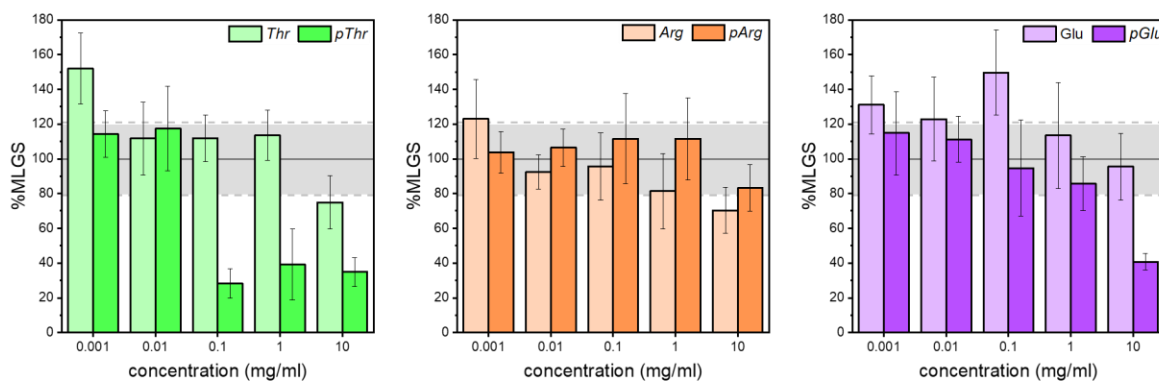
Figure 29. Percent mean largest grain size relative to blank solutions for amino acids and homo-polypeptide at concentrations from 0.001-10 mg/ml in PBS. The gray bands indicate the range of ice crystal mean largest grain size for blank solutions.

As anticipated, *pThr* was shown to exhibit the highest IRI activity in PBS, as threonine has been shown to be a common residue in IBPs to organize semi-liquid waters that facilitate interactions with ice.[49,54] *Thr* was expected to interact with ice; however, at low concentrations, *Thr* exhibited larger ice grains than blank solution. While the amphipathic moiety was perhaps interacting with ice at a low concentration, *Thr* possibly acted as a seeding agent as opposed to an ice growth inhibitor. *pGlu* demonstrated IRI activity at 10 mg/ml in PBS, which was expected, due to the hydrophilicity of carboxylic acids facilitating interactions with ice.

A representative splat endpoint (t_{30}) for each amino acid (*Thr*, *Arg*, *Glu*) and homo-polypeptide (*pThr*, *pArg*, *pGlu*) at 10 mg/ml in varied concentration $CaCl_2$ solutions is shown in **Figure 30**. The $CaCl_2$ concentrations of 10 mM, 50 mM, and 151.5 mM were chosen to represent the effect of changing solution constituent concentration. Splat images for the initial time (t_0) compared to the endpoint (t_{30}) for all concentrations (10, 25, 50, 100, 151.5 mM) are shown in **Appendix B**. The %MLGS for amino acid and homo-polypeptides in varied concentration $CaCl_2$ solutions can be seen in **Figure 31**.

For blank solutions, $CaCl_2$ concentrations between 10 mM and 100 mM had smaller ice crystals at t_{30} compared to PBS. At 151.5 mM $CaCl_2$, ice grain sizes were comparable to PBS grain sizes. In 10 mM $CaCl_2$, 10 mg/ml of any solute resulted in IRI activity, seen as a reduction of grain

size between 30-60%. As the concentration of $CaCl_2$ increased, the reduction of average grain size by each added molecule appeared to approach a plateau (**Figure 31**).
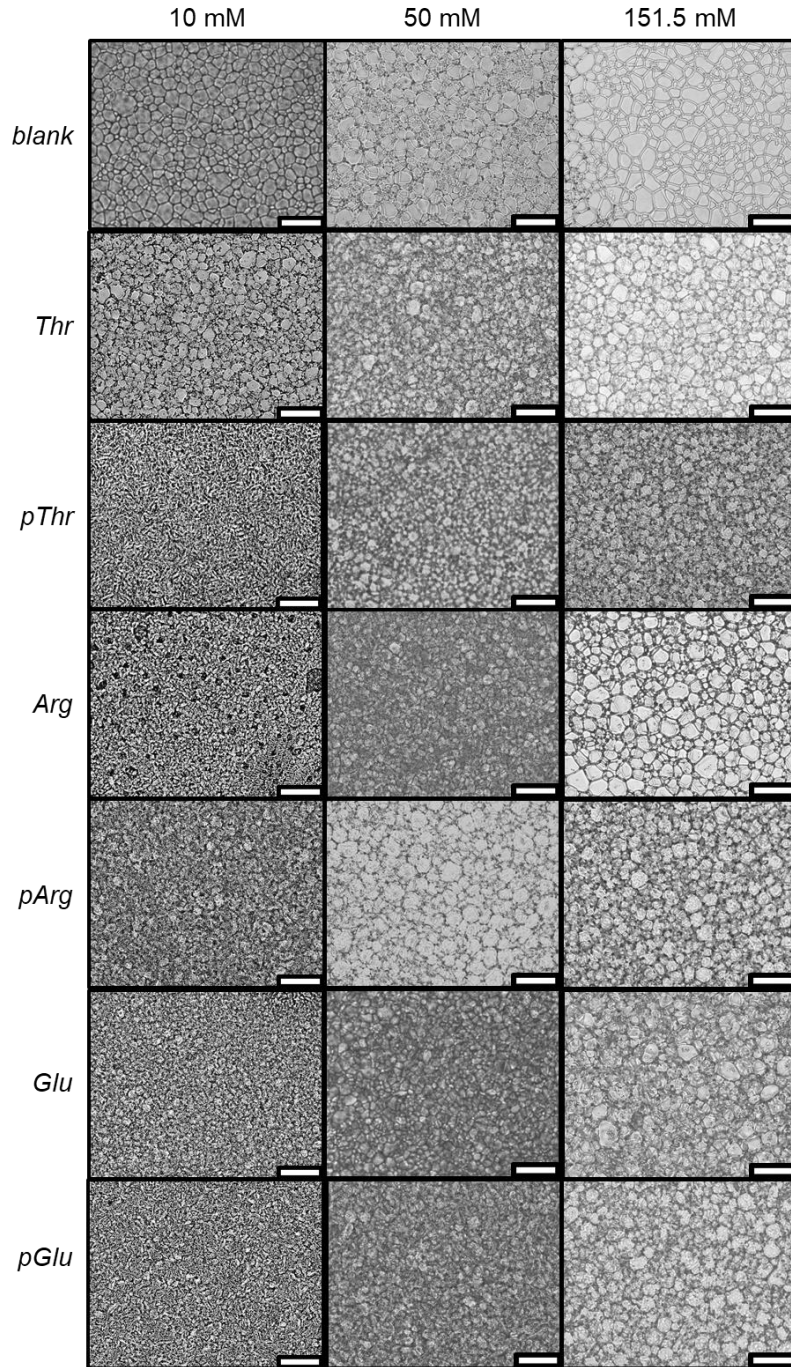
Figure 30. Representative endpoint IRI activities of each amino acid (*Thr*, *Arg*, *Glu*) and homo-polypeptide (*pThr*, *pArg*, *pGlu*) at 10 mg/ml in 10 mM $CaCl_2$, 50 mM $CaCl_2$, and 151.5 mM $CaCl_2$. Scale bar = 100 µm.
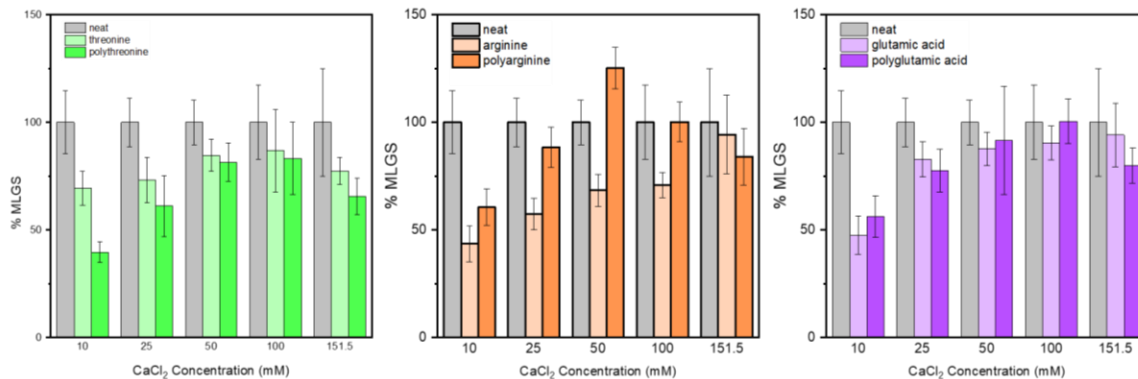
Figure 31. Percent mean largest grain size relative to blank solutions for amino acids and homo-polypeptides at 10 mg/ml in $CaCl_2$ solutions with increasing $CaCl_2$ concentration. The data are normalized to each blank solution, represented as a gray bar. This ensures that the graphs only show the effect of the added molecules.

It was originally shown by Knight *et al.*[120] that there is a minimum amount of salt that must be incorporated in solution to elucidate IRI activity. For a solution to be effective at determining the IRI activity of a material, the eutectic point of the solution needs to be below the annealing temperature of the splat assay to ensure liquid phases between the ice grain boundaries. A schematic illustrating this point can be seen in **Figure 32**. When the solution eutectic point is below the annealing temperature, the material of interest will accumulate in the liquid phase between the ice grain boundaries, and if it has IRI activity, it will interact at the ice-solution interface, whereas no interaction will occur if it is not IRI active. When an IRI active material interacts at the ice-solution interface, it immobilizes the liquid inclusions at the grain boundaries and prevents recrystallization. Conversely, when the salt concentration is too low, the solution is above its eutectic point and all molecules, even IRI inactive molecules, can act as inclusions at the ice grain boundary and prevent ice recrystallization by increasing the amount of energy required for molecular movement. Due to this effect, the increase in salt concentration results in an eventual plateau of IRI activity or lack thereof. As seen in **Figure 31**, the molecular activity approaches a plateau starting around 100 mM $CaCl_2$. 151,5 mM was chosen to investigate other salts to ensure the salts should be above the their eutectic point during IRI investigations. Additionally, 151.5

mM matches the molarity of PBS, which will facilitate direct comparison of molecule activities across solution types.
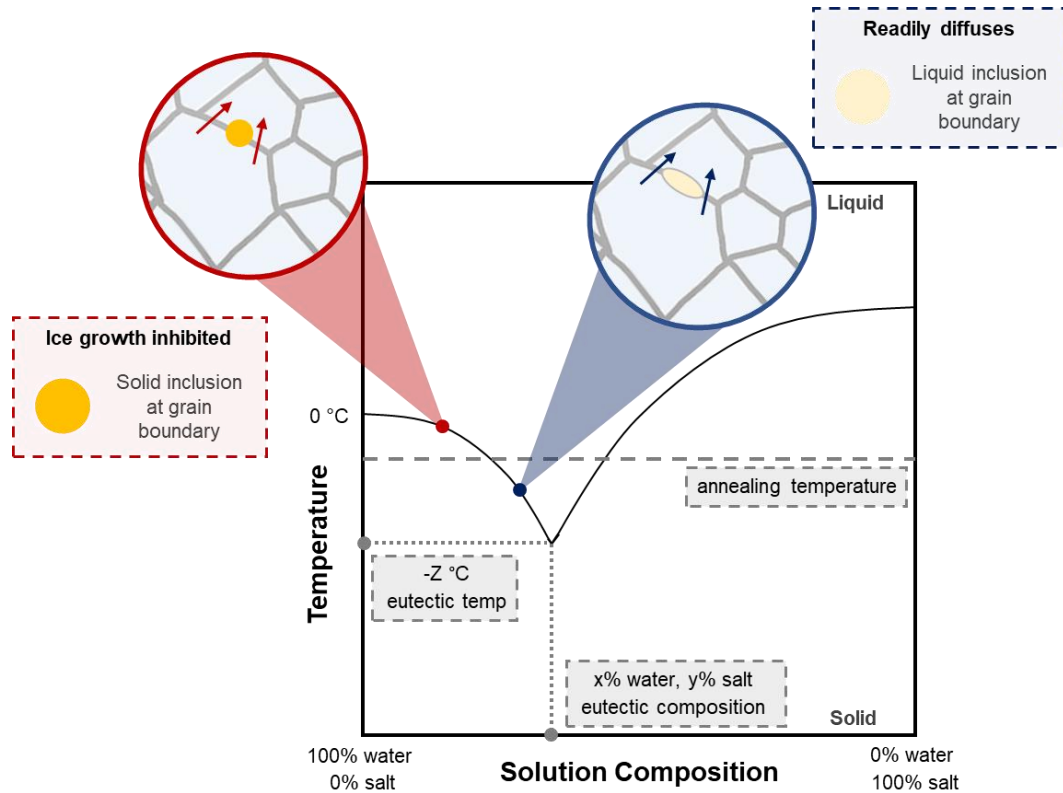
Figure 32. Schematic demonstrating the effect of solution composition on ice recrystallization through the migration of ice grain boundaries. For salt solutions with a freezing point above the annealing temperature, solutes will act as solid inclusions at the grain boundaries, preventing migration. For salt solutions with a freezing point below the annealing temperature, solutes will act as liquid inclusions at the grain boundaries that readily diffuse, preventing false positives. Arrows in the schematic indicate the direction of grain migration.

A representative splat endpoint (t_{30}) in 151.5 mM $CaCl_2$, 151.5 mM $MgCl_2$, 151.5 mM $CuCl_2$, and 151.5 mM $AlCl_3$ for each amino acid (*Thr*, *Arg*, *Glu*) and homo-polypeptide (*pThr*, *pArg*, *pGlu*) at 10 mg/ml can be seen in **Figure 33** and **Figure 34**, respectively. The %MLGS for amino acids and homo-polypeptides for varied salt solutions can be seen in **Figure 35**.

For blank salt solutions, all grain sizes at t_{30} were smaller than PBS, which was expected due to the effect of salts on ice recrystallization based on the Hofmeister series.[119] In 151.5 mM $CaCl_2$, 10 mg/ml *pThr* demonstrated reduced IRI activity compared to PBS (34.4% vs. 65.2% grain size

reduction, respectively). In 151.5 mM $MgCl_2$, 151.5 mM $CuCl_2$, and 151.5 mM $AlCl_3$ solutions, both *Thr* and *pThr* were insignificant at reducing ice grain size. For the most part, *Arg*, *Glu*, *pArg* and *pGlu* all did not demonstrate IRI for all salt solutions tested. However, *Arg* in 151.5 $CuCl_2$, exhibited a 35.7% reduction of ice grain size compared to blank solution.
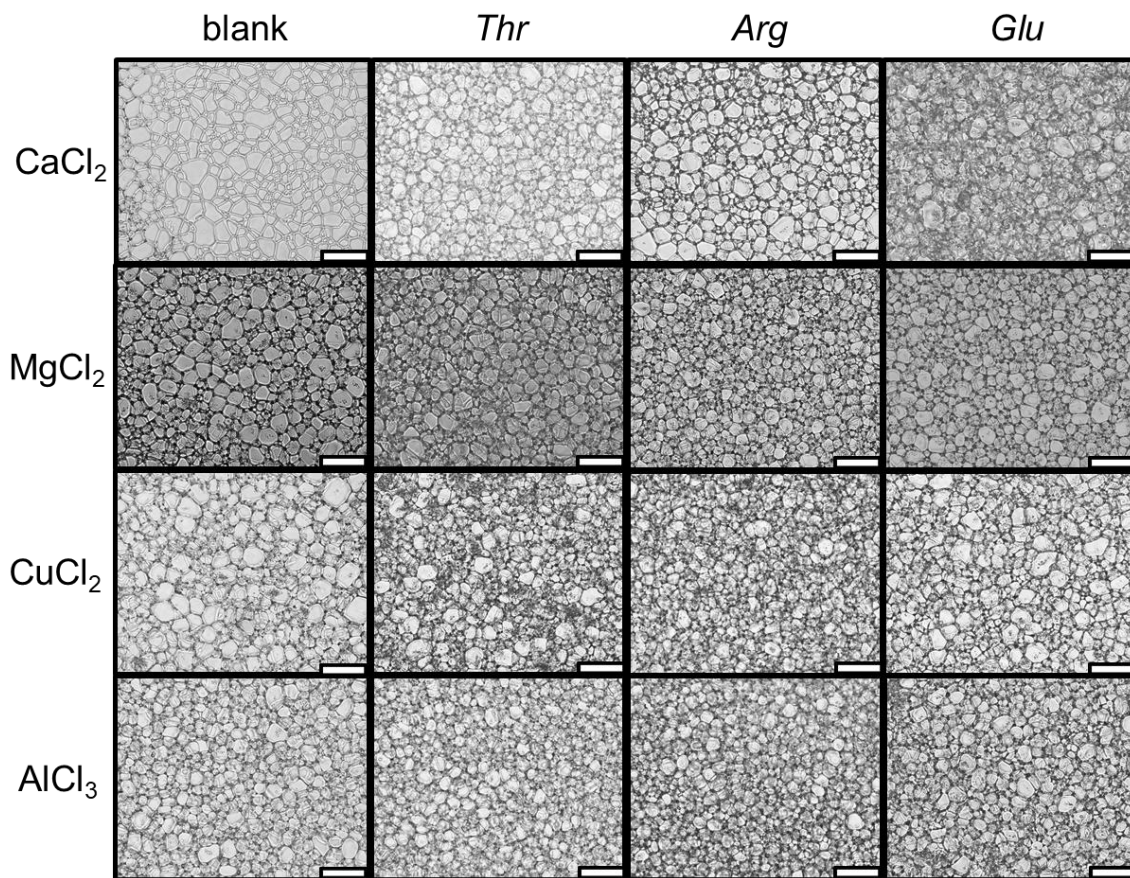
Figure 33. Representative endpoint IRI activities of *Thr*, *Arg*, and *Glu* at 10 mg/ml in 151.5 mM $CaCl_2$, 151.5 mM $MgCl_2$, 151.5 mM $CuCl_2$, and 151.5 mM $AlCl_3$. Scale bar = 100 µm.
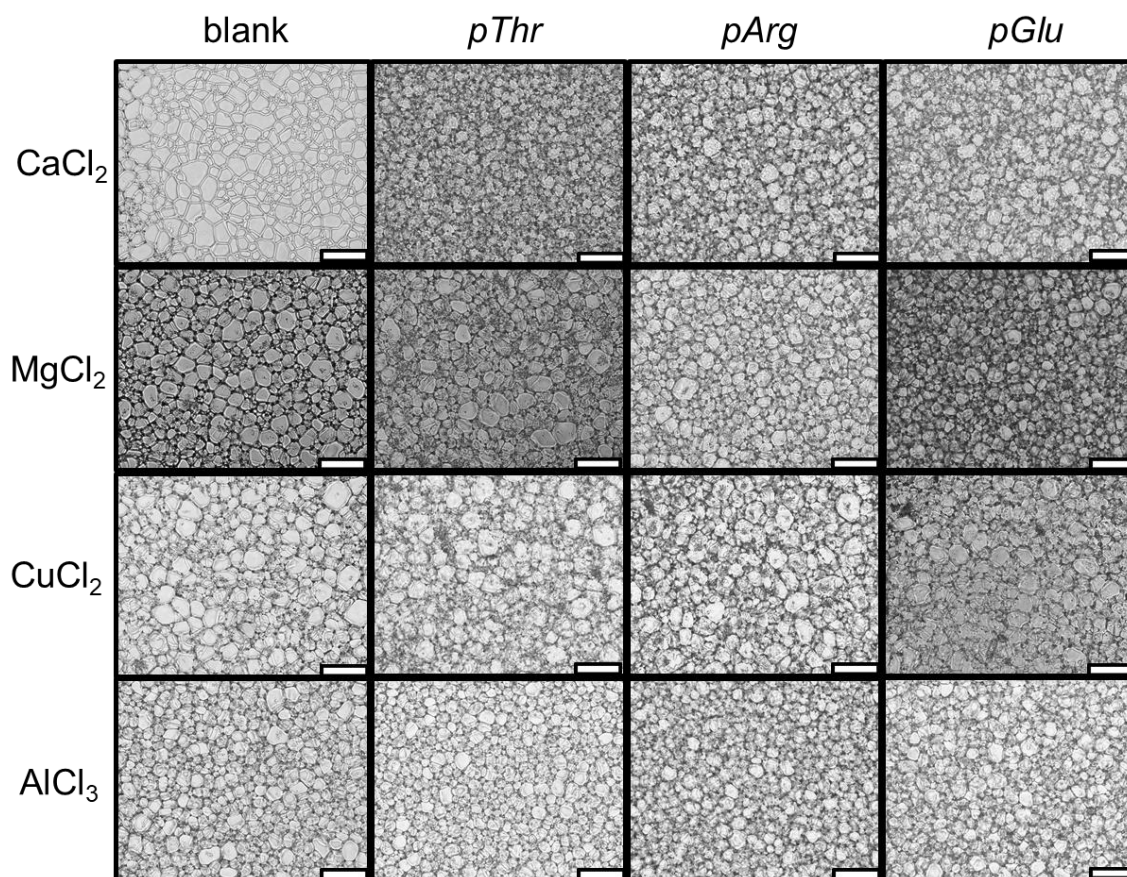
Figure 34. Representative endpoint IRI activities *pThr*, *pArg*, and *pGlu* at 10 mg/ml in 151.5 mM CaCl₂, 151.5 mM MgCl₂, 151.5 mM CuCl₂, and 151.5 mM AlCl₃. Scale bar = 100 µm.
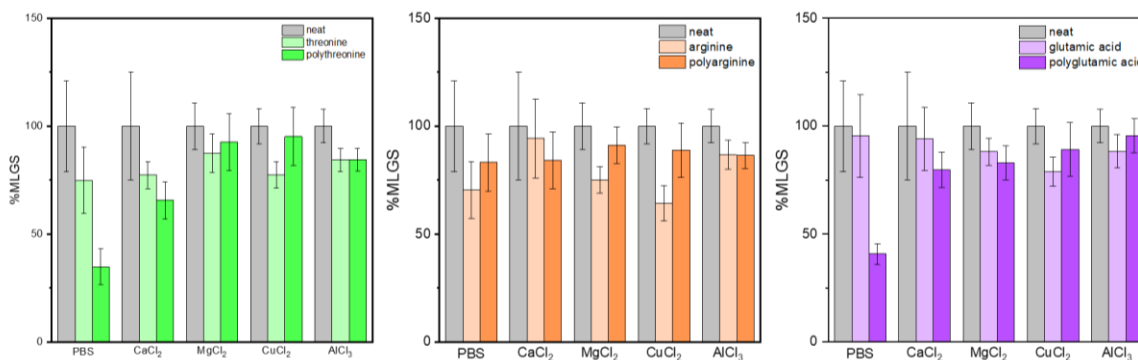
Figure 35. Percent mean largest grain size relative to blank solutions for amino acids and homo-polypeptides at 10 mg/ml in PBS and salt solutions (151.5 mM CaCl₂, 151.5 mM MgCl₂, 151.5 mM CuCl₂, and 151.5 mM AlCl₃). The data are normalized to each blank solution, represented as a gray bar.

In a nanodrop study investigating the impact of cations on the hydrogen bonding network of water, O'Brian et al.[266] showed that monovalent ions have little effect on the majority of water molecules, whereas multivalent ions induce some change in bulk water, indicating that the multivalent cations could have played a role in the bulk organization of charged or polar molecules in solutions. Multivalent cations are more likely to interact with water or other molecules due to a larger charge density based on the Hofmeister series,[239] which may have led to ion interactions of the solution cations with the polar *pThr* and charged *pGlu* functional groups.[267] It is hypothesized that the decrease in IRI activity for *pThr* and *pGlu* could be due to disruption of H-bonding between the homo-polypeptides and either liquid water or solid ice caused by the multivalent cations in solution. The difference in *pThr* and *pGlu* activity the $CaCl_2$, $MgCl_2$, $CuCl_2$, and $AlCl_3$ salt solutions tested compared to PBS could potentially be related to the Hofmeister series, where Na^+ and K^+, the cations present in PBS, are less disruptive than Ca^{2+} and Mg^{2+}.

5.5.3 Enthalpy of Crystallization

All amino acids and homo-polypeptides in PBS demonstrated an enthalpy of crystallization similar to that of blank solution, which can be seen in **Figure 36**. For all amino acids and homo-polypeptides in PBS, no discernable effect on melting point was observed as summarized in

Table 19. Raw DSC melting curves used to determine melting point and enthalpy of crystallization can be seen in **Appendix A**.

The small changes in crystallization enthalpy seen in **Figure 36** were expected from the low concentration of amino acids and homo-polypeptides, which would have minimal colligative effects on solution crystallization energy. As the enthalpy of crystallization is proportionally related to the amount of crystalline ice formed in solution, a reduction in enthalpy of crystallization would indicate the formation of a glassy state instead of polycrystalline ice.[96,268–271] Since the enthalpy of crystallization for all amino acids and homo-polypeptides are similar to that of blank solution, it can be concluded that all ice formed was polycrystalline, and therefore all interactions were mechanistically colligative.
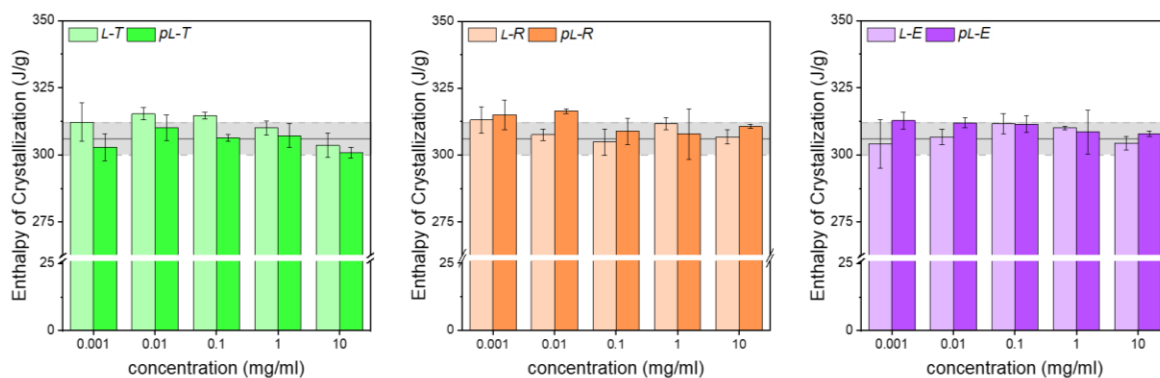
Figure 36. Enthalpy of crystallization for amino acids (*Thr*, *Arg*, *Glu*) and homo-polypeptides (*pThr*, *pArg*, *pGlu*) at concentrations from 0.001-10 mg/ml in PBS. The gray bar indicates the enthalpy of crystallization of blank solution (306 ± 6 J/g).

Table 19. Melting point of amino acids and homo-polypeptides at concentrations from 0.001-10 mg/ml in in PBS.

Melting Point (°C)					
PBS (-1.81 ± 0.10)					
[C] (mg/ml)	*Thr*	*pThr*	*Arg*	*pArg*	*Glu*	*pGlu*
0.001	-1.56 ± 0.08	-2.18 ± 0.13	-1.81 ± 0.15	-1.72 ± 0.25	-2.12 ± 0.27	-1.54 ± 0.12
0.01	-1.66 ± 0.20	-1.88 ± 0.07	-2.15 ± 0.07	-1.81 ± 0.13	-1.75 ± 0.17	-1.99 ± 0.07
0.1	-1.70 ± 0.05	-1.84 ± 0.08	-1.97 ± 0.04	-2.01 ± 0.05	-1.34 ± 0.22	-1.59 ± 0.12
1	-1.66 ± 0.17	-1.99 ± 0.12	-1.75 ± 0.12	-1.78 ± 0.07	-1.58 ± 0.13	-1.46 ± 0.09
10	-1.98 ± 0.23	-1.72 ± 0.07	-1.78 ± 0.03	-1.90 ± 0.05	-1.92 ± 0.07	-1.80 ± 0.10

In PBS, the melting point depression matches what is expected due to colligative contributions, suggests no interactions between the amino acids or homo-polypeptides with solution constituents.[272] The change in melting point for amino acids or homo-polypeptides in PBS solutions can be attributed solely to colligative interactions due to the lack of variation from the blank solution melting point relative to the solute concentration.

5.6   Threonine and Synthetic Mimics

As determined in **Section 5.5.2**, *pThr* exhibited the best IRI performance to the lowest concentration in PBS, as well as exhibited promising performance in varied salt solutions. Based

on melting point depression and the enthalpy of crystallization, the other homo-polypeptides investigated did not have other competing properties that would make them better candidates for synthetic replication. Thus, to investigate the efficacy of a full synthetic mimic compared to the homo-polypeptide of threonine, the effect on the growth of ice of *pThr* and *pHPMA* in different solutions was investigated.

5.6.1 Melting Point Depression

$T_{m,(observed)}$ of each material was compared to $T^*_{m,(theoretical)}$ for all solutions used, with the expectation that materials with purely colligative contributions to the melting point would exhibit a $T_{m,(observed)}$ equal to $T^*_{m,(theoretical)}$, seen as a 1:1 line through the (0,0) intercept in **Figure 37**. The results seen in **Figure 37a** show that the model determined by Blagden's Law is not a good fit, which is expected as the solutions are not ideal. The fit of all data with $\Delta T_{s,(non-ideal)}$ added can be seen **Figure 37c**. $\Delta T_{a,(non-ideal)}$ for each molecule and can be seen as a better fit in **Figure 37d**.

The slope of the data sets for *Thr*, *pThr*, *HPMA*, and *pHPMA* were taken as a measure of colligativity, with values closer to 1 indicating solely colligative contributions and values greater than 1 indicating effects beyond colligative contributing to the melting point depression of solution. A summary of ideal and non-ideal contributions to the melting point temperature of solution can be seen in **Table 20**, and the determination of those values can be seen in **Figure 37** and **Figure 38**. Additionally, the effect of *Arg*, *pArg*, *Glu*, and *pGlu* were examined to determine their effect on the melting point of solution, which can be seen in **Figure 39**.
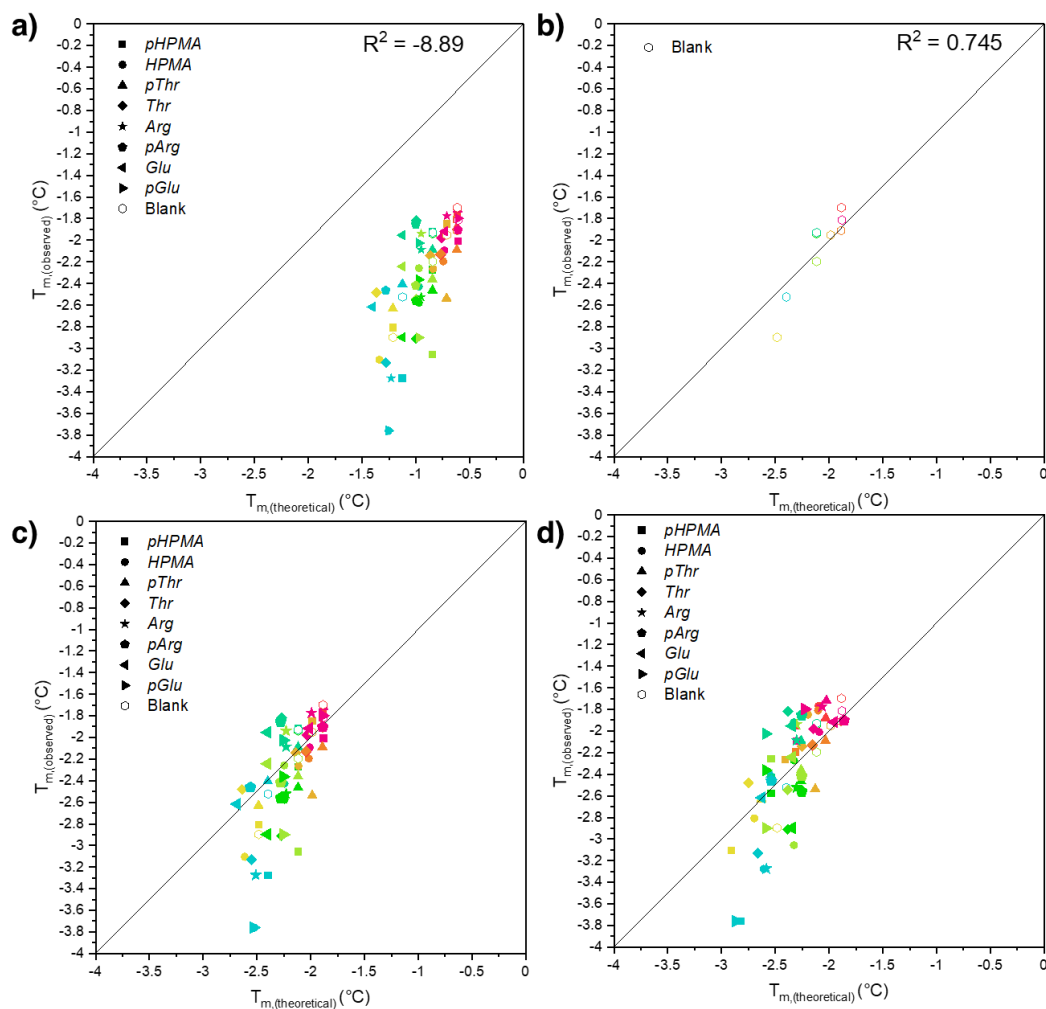
Figure 37. (a) Observed vs. theoretical T_m using Blagden's law. As the solutions are non-ideal, the model is not a good fit to the data, seen as a negative R^2 value. (b) Fit of blank solutions to the 1:1 line to yield $\Delta T_{s,(non-ideal)}$. (b) Observed vs. theoretical T_m using Blagden's law with theoretical data corrected with $\Delta T_{s,(non-ideal)}$. (d) Observed vs. theoretical T_m with molecule data sets fit to the 1:1 to yield $\Delta T_{a,(non-ideal)}$. Solutions are indicated by color: PBS (●); PBS pH 8 (●); PBS pH 10 (●); PBS pH 12 (●); PBS pH 13 (●); 151.5 mM CaCl$_2$ (●); 151.5 mM MgCl$_2$ (●); 151.5 mM CuCl$_2$ (●); and 151.5 mM AlCl$_3$ (●).
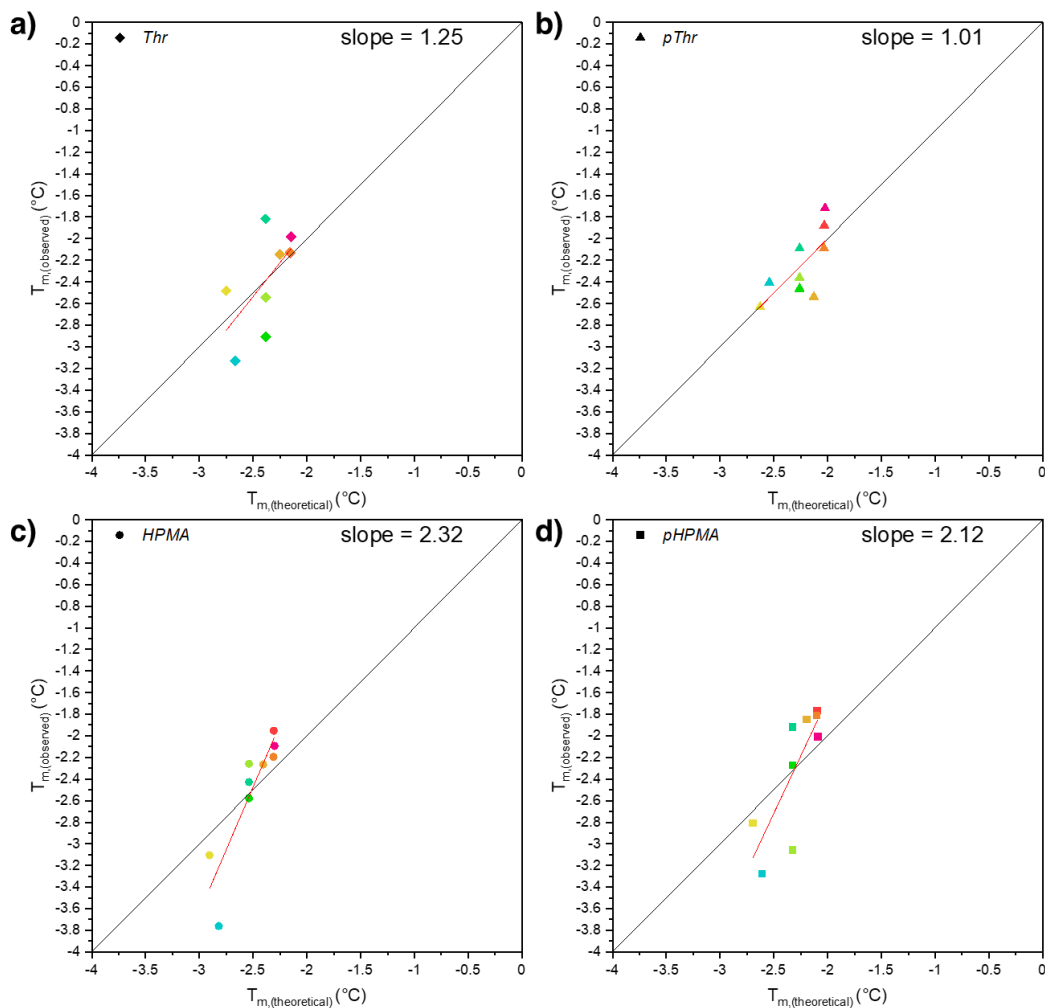
Figure 38. Slope of best fit for (a) *Thr*, (b) *pThr*, (c) *HPMA*, and (d) *pHPMA*. Solutions are indicated by color: PBS (●); PBS pH 8 (●); PBS pH 10 (●); PBS pH 12 (●); PBS pH 13 (●); 151.5 mM $CaCl_2$ (●); 151.5 mM $MgCl_2$ (●); 151.5 mM $CuCl_2$ (●); and 151.5 mM $AlCl_3$ (●).
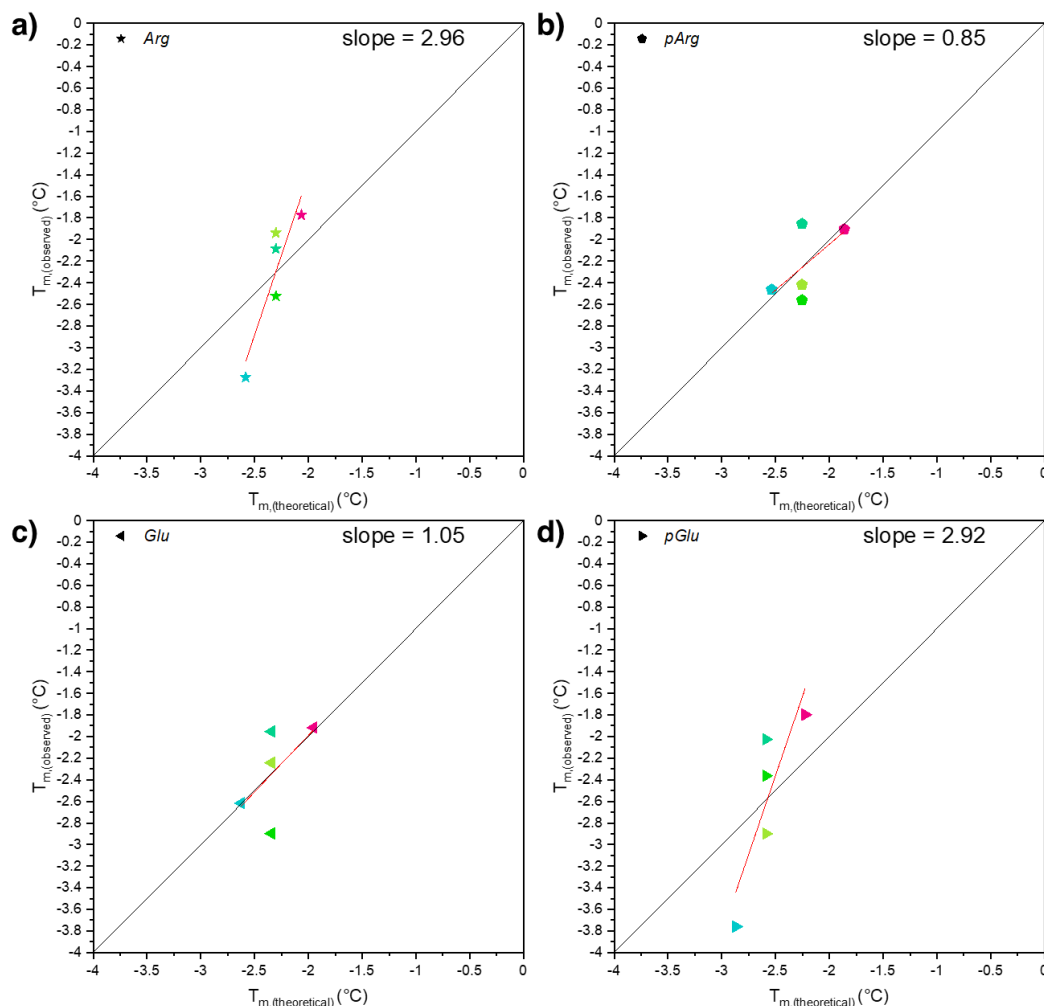
Figure 39. Slope of best fit for (a) *Arg*, (b) *pArg*, (c) *Glu*, and (d) *pGlu*. Solutions are indicated by color: PBS (●); PBS pH 8 (●); PBS pH 10 (●); PBS pH 12 (●); PBS pH 13 (●); 151.5 mM CaCl$_2$ (●); 151.5 mM MgCl$_2$ (●); 151.5 mM CuCl$_2$ (●); and 151.5 mM AlCl$_3$ (●).

For *Thr* and *pThr*, the slope of the data sets is 0.9 and 1.2, respectively, which suggests the change in melting point temperature can be solely attributed to colligative interactions. For *HPMA* and *pHPMA*, the slope of the data sets is 1.6 and 1.8, respectively, which suggests that there is some effect beyond colligative that is contributing to the melting point depression, resulting in a greater reduction of T_m than expected. For other amino acids and homo-polypeptides investigated, *pArg* and *Glu* exhibited slopes of 0.85 and 1.05, respectively, indicating colligative interactions. However, *Arg* and pGlu demonstrate effects beyond colligative, seen as slopes of 2.96 and 2.92,

respectively. The melting point depression lower than expected shows each molecules effect on the formation of crystals in solution, and not necessary the effect on growth. *Arg* and *pGlu* show no or weak IRI activity, indicating that there are multiple modes of interaction with ice and those modes of interaction are not necessarily correlated.

Table 20. Ideal and non-ideal contributions to the reductions in $T^*_{m,(theoretical)}$ of ice in the presence of different additives at 10 mg/ml.

Material	[a]MW (Da)	[b]$\Delta T_{a,(ideal)}$ (°C)	[c]$\Delta T_{a,(non-ideal)}$ (°C)	[d]M
Threonine (*Thr*)	119.1	0.1600	0.11	1.25
Poly(threonine) (*pThr*)	7,600	0.0024	0.14	1.01
Arginine (*Arg*)	174.2	0.1100	0.07	2.96
Poly(arginine) (*pArg*)	15,000	0.0012	0.03	0.85
Glutamic acid (*Glu*)	147.1	0.1300	0.06	1.05
Poly(glutamic acid) (*pGlu*)	12,100	0.0015	0.34	2.92
2-hydroxypropyl methacrylamide (HPMA)	143.2	0.1300	0.29	2.32
Poly(2-hydroxypropyl methacrylamide) (*pHPMA*)	41,400	0.0005	0.21	2.12

[a]molecular weight of molecule as provided by manufacturer (Table SX)
[b]ideal contribution of molecule to T_m as determined by Blagden's Law
[c]empirically derived non-ideal contribution of molecule to T_m
[d]M is the slope of line of best fit for each molecule, indicating the effects beyond colligative to T_m

Huang *et al*. investigated oligomeric peptoids using DSC to determine contributions beyond colligative.[125] The authors tested a known purely colligative substance, glycerol, which was used to adjust the theoretical T_m for the oligomeric peptoids (**Figure 40**). After accounting for non-ideal contributions, glycerol was found to lie on the 1:1 line, validating the adjustment of the model. After adjustment, it was found that the oligomeric peptoids were solely colligative in nature (**Figure 40**). In comparison, the performance of *HPMA* and *pHPMA* to were able to depress the melting point of solution beyond expected by colligative effects alone at the same concentration as the oligomeric peptoids.
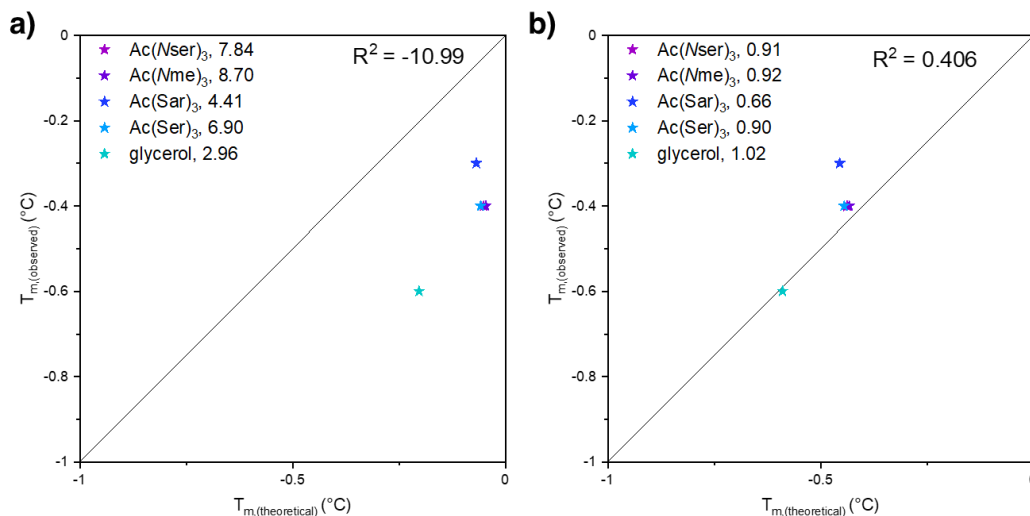
Figure 40. Data taken from Huang et al.[125] for melting point depression of peptoids and glycerol. The number next to the molecule name is the ratio of $T_{m,(observed)}/T_{m,(theoretical)}$, which is essentially equivalent to the slope of data sets determined in Figure SX. a) observed data plotted against ideal melting point. b) data adjusted to account for non-ideal behavior of materials in solution.

The behavior of *HPMA* and *pHPMA* is distinctly different from IBPs. IBPs exhibit TH, a non-colligative phenomenon that lowers the freezing point of solution while either maintaining or elevating T_m. However, the TH typically results in rapid, and potentially detrimental, expansion of ice crystals.[273,274] It has been shown that disrupting the interaction of water molecules can delay ice formation and growth.[129,275] It is possible that *HPMA* and *pHPMA* are disrupting the interaction of water molecules, lower the melting point beyond expected for the loaded concentration by changing the chemical potential of water. *HPMA* and *pHPMA* are more effective at lower concentrations and can further depress the melting point compared to materials that only exhibit colligative contributions. *HPMA* and *pHPMA* could prove to be a synergistic additive to deicing salts, which rely on melting point depression to remove ice on pavements. Similarly, *HPMA* and *pHPMA* could work as an additive in cement and concrete, as they could prevent ice formation at lower temperatures compared to other additives, reducing the number of freeze-thaw cycles that result in deleterious damage from ice nucleation and growth.

5.6.2 Effects on Crystallization

ΔH_{melt} for *Thr*, *pThr*, *HPMA* and *pHPMA* in PBS, PBS pH solutions, or salt solutions can be seen in **Figure 41**. As ΔH_{melt} is proportionally related to the amount of crystalline ice formed in solution, a reduction in ΔH_{melt} would indicate formation of a glassy state instead of polycrystalline ice, a process called vitrification.[96,268–271] However, ΔH_{melt} can be affected by the concentration of solute when compared to blank solution, so ΔS_{melt} was used to determine concentration independent influences on solution crystallization. If ΔS_{melt} for an added solute was similar to the ΔS_{melt} of blank solution, only crystalline ice was formed. If ΔS_{melt} was less than blank solution, it is expected that some vitrification occurred. ΔS_{melt} for *Thr*, *pThr*, *HPMA*, and *pHPMA* in all solutions with respect to pH can be seen in **Figure 42**.

When the pH of the solutions range from 8 –12, the added solutes induced some formation of glassy ice, albeit in small quantities, seen as < 5% change in ΔS_{melt} from blank solution. When pH < 8 or pH > 12, solutes exhibited the formation of crystalline ice, seen in **Figure 42**, where ΔS_{melt} is similar to that of the blank solution. Notably, HPMA exhibited some vitrification in PBS (pH 7.2) and in PBS pH 13. It is expected that between pH 8 – 12, the addition of solutes resulted in a disordered state. It is hypothesized that there is some disruption of H-bonding in this pH range that prevents crystallization, leading to more amorphous, glassy structure formation.

Although the formation of glassy ice has not been proven beneficial to infrastructure applications, cryopreservation of biological materials sometimes necessitates the formation of glassy ice.[276–278] Vitrification for cryopreservation is often performed with rapid cooling, or by including materials that encourage glassy ice formation and prevent crystalline ice formation. The results seen in **Figure 42** indicate that *Thr*, *pThr*, *HPMA*, and *pHPMA* could potentially be used as preservation agents for materials in alkaline environments, such as those used for some proteins.[279] *HPMA* is notably different as it induces glassy ice formation both above and below the pH range identified. *HPMA* could be inducing the formation of more glassy ice than its polymer counterpart, *pHPMA*. At the same concentration, there are more *HPMA* molecules than *pHPMA* molecules, which has been shown to impact vitrification due to an increase in osmolality.[280]

Although *Thr* has a similar number of molecules to *HPMA* at 10 mg/ml, it is possible the difference in structure and greater hydrophobicity of *HPMA* plays a role in its ability to induce vitrification. Overall, *HPMA* could be a potential additive for cryopreservation at physiological pH, but vitrification benefits for infrastructure-relevant applications have yet to be determined.
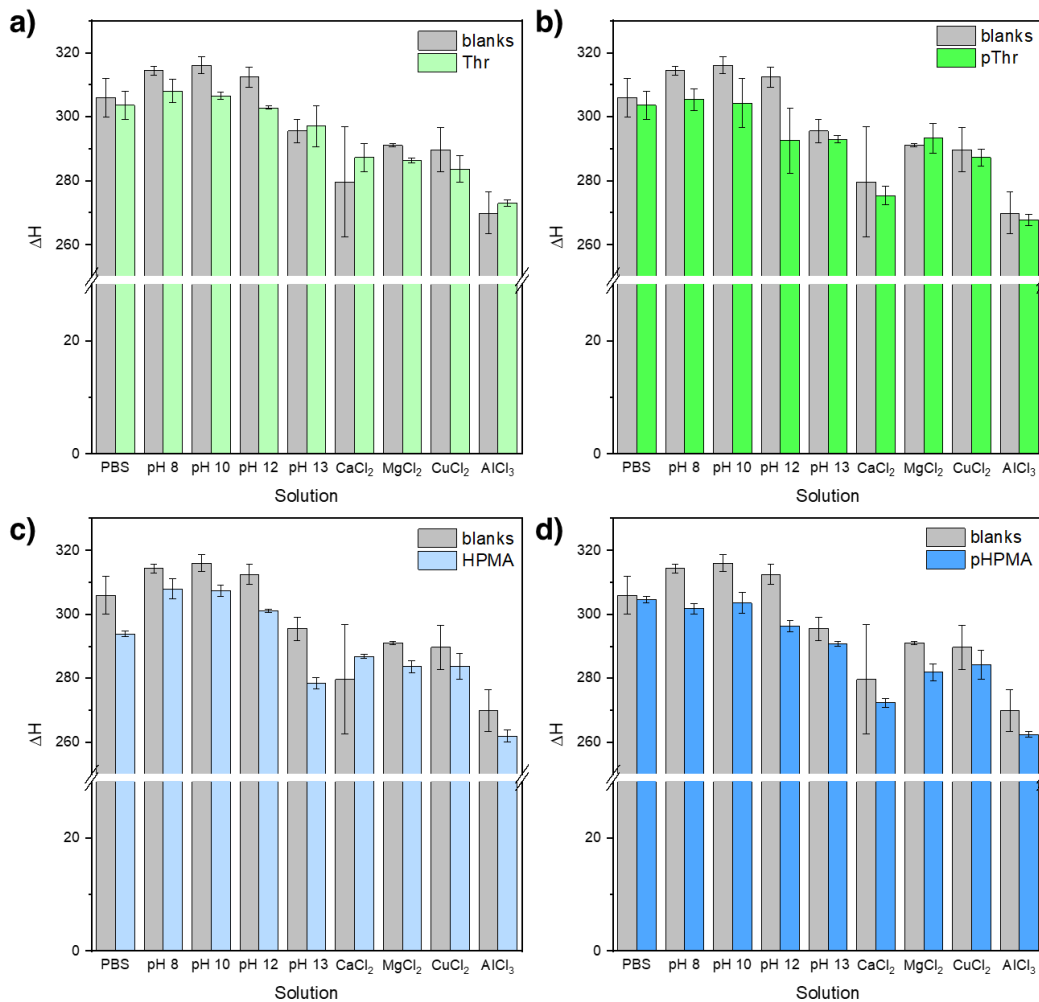
Figure 41. Enthalpy of crystallization of (a) *Thr*, (b) *pThr*, (c) *HPMA*, and (d) *pHPMA* at 10 mg/ml in each solution. The gray bar indicates the enthalpy of freezing for blank solution.
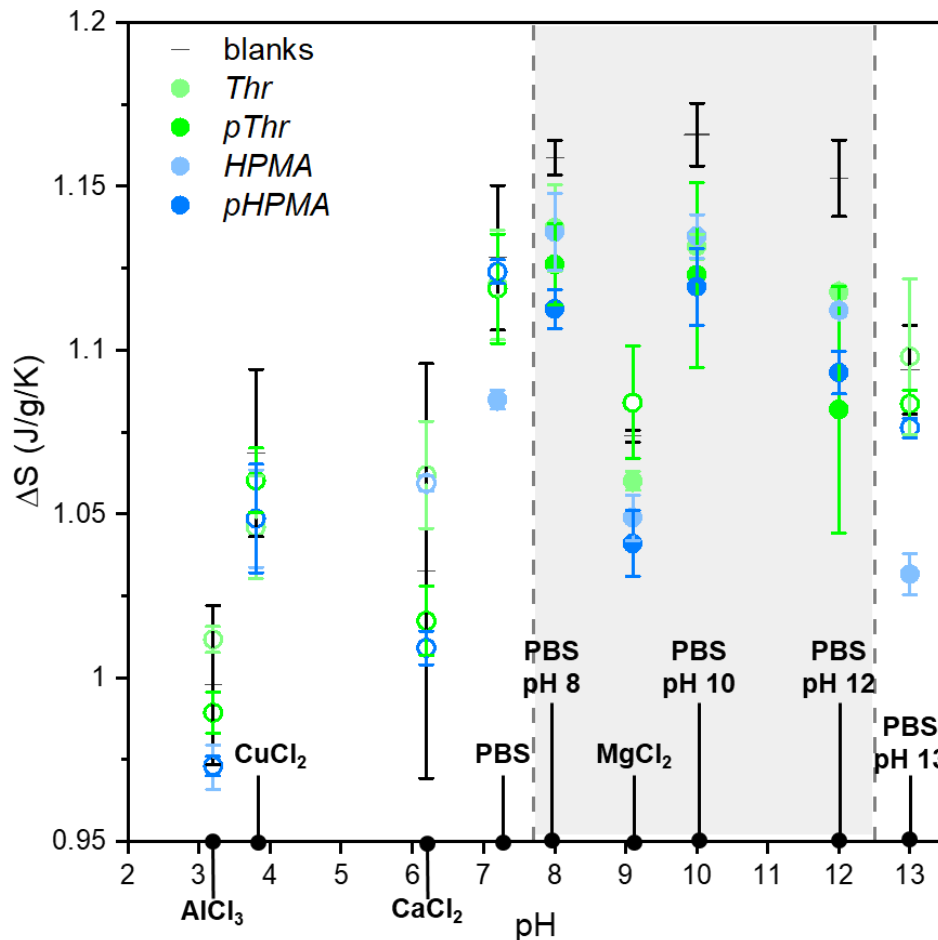
Figure 42. Entropy of crystallization for *Thr*, *pThr*, *HPMA*, and *pHPMA* in PBS (pH 7.2), PBS pH 8, PBS pH 10, PBS pH 12, PBS pH 13, 151.5 mM $CaCl_2$ (pH 6.2), 151.5 mM $MgCl_2$ (pH 9.1), 151.5 mM $CuCl_2$ (pH 3.8), and 151.5 mM $AlCl_3$ (pH 3.2). Hollow data points indicate the formation of only crystalline ice. Solid data points indicate the formation of some glassy (in lieu of crystalline) ice. The gray region indicates the range of pH where added solutes alone promote glassy ice formation.

5.6.3 IRI for Threonine and Synthetic Mimics

    pThr and *pHPMA* were tested for a minimum concentration needed to exhibit IRI activity. Micrographs can be seen in **Figure 43**, and dilution micrographs for *Thr* and *HPMA* can be seen in **Figure 44**. The relative activity for *pThr* and *pHPMA* compared to blank PBS solution can be seen in **Figure 45**. As neither *Thr* nor *HPMA* exhibited IRI activity, values were not reported. Micrographs for *Thr*, *pThr*, *HPMA*, *pHPMA* in PBS pH solutions are in **Figure 46**, and in varied salt solutions are in **Figure 47**. Micrographs for t_0 compared to t_{30} for all molecules in PBS pH

solutions and salt solutions can be found in **Appendix B**. The %MLGS for *Thr*, *pThr*, *HPMA*, *pHPMA* in PBS pH solutions can be seen in **Figure 48**, and in varied salt solutions are in **Figure 49**. The relative activity compared to blank solution for *Thr*, *pThr*, *HPMA*, and *pHPMA* matches literature precedence for expected growth.[163,281] Blank control solutions demonstrated varied crystal sizes at t_{30} compared to PBS due to contributions of solution constituents that effect the recrystallization process.[119,239] However, as the estimated grain size of *Thr*, *pThr*, *HPMA*, and *pHPMA* was normalized to each respective blank solution, the reported %MLGS demonstrates the efficacy of each molecule to inhibit growth in each environment.

pHPMA demonstrated IRI activity an order of magnitude lower than *pThr*, seen as a 61% reduction of ice crystal size compared to blank solution at 0.01 mg/ml in PBS (**Figure 45**). Both *pThr* and *pHPMA* exhibited IRI activity at 10 mg/ml in all PBS pH solutions. Most notably, *pThr* and *pHPMA* exhibited IRI activity in pH 13 solution, seen as a 70.9% and a 79.6% reduction in ice crystal size, respectively (**Figure 48**). Interestingly, both *pThr* and *pHPMA* demonstrated reduced activity in 151.5 mM $CaCl_2$ and 151.5 mM $MgCl_2$ environments (**Figure 49**). *pThr* only exhibited a 34.4% reduction in 151.5 mM $CaCl_2$, and did not exhibit IRI in 151.5 mM $MgCl_2$. While *pHPMA* did not inhibit ice as strongly in 151.5 mM $CaCl_2$ or 151.5 mM $MgCl_2$ solutions (seen as a 56.8% and 41.6% reduction, respectively), there was still some inhibition of ice growth, demonstrating stronger IRI activity than *pThr* in infrastructure relevant salt environments. In all environments except 151.5 mM $MgCl_2$, both *Thr* and *HPMA* demonstrated an average ice crystal size smaller than blank solution; however, the reduction in ice crystal size was within error and *Thr* and *HPMA* cannot be stated to have IRI activity. A previous study by Congdon *et al.* demonstrated that IRI activity can be improved by ensuring IRI active moieties are proximal to each other,[163] which corroborates the results seen herein where *Thr* and *HPMA* do not exhibit IRI activity, but their respective polymers do.
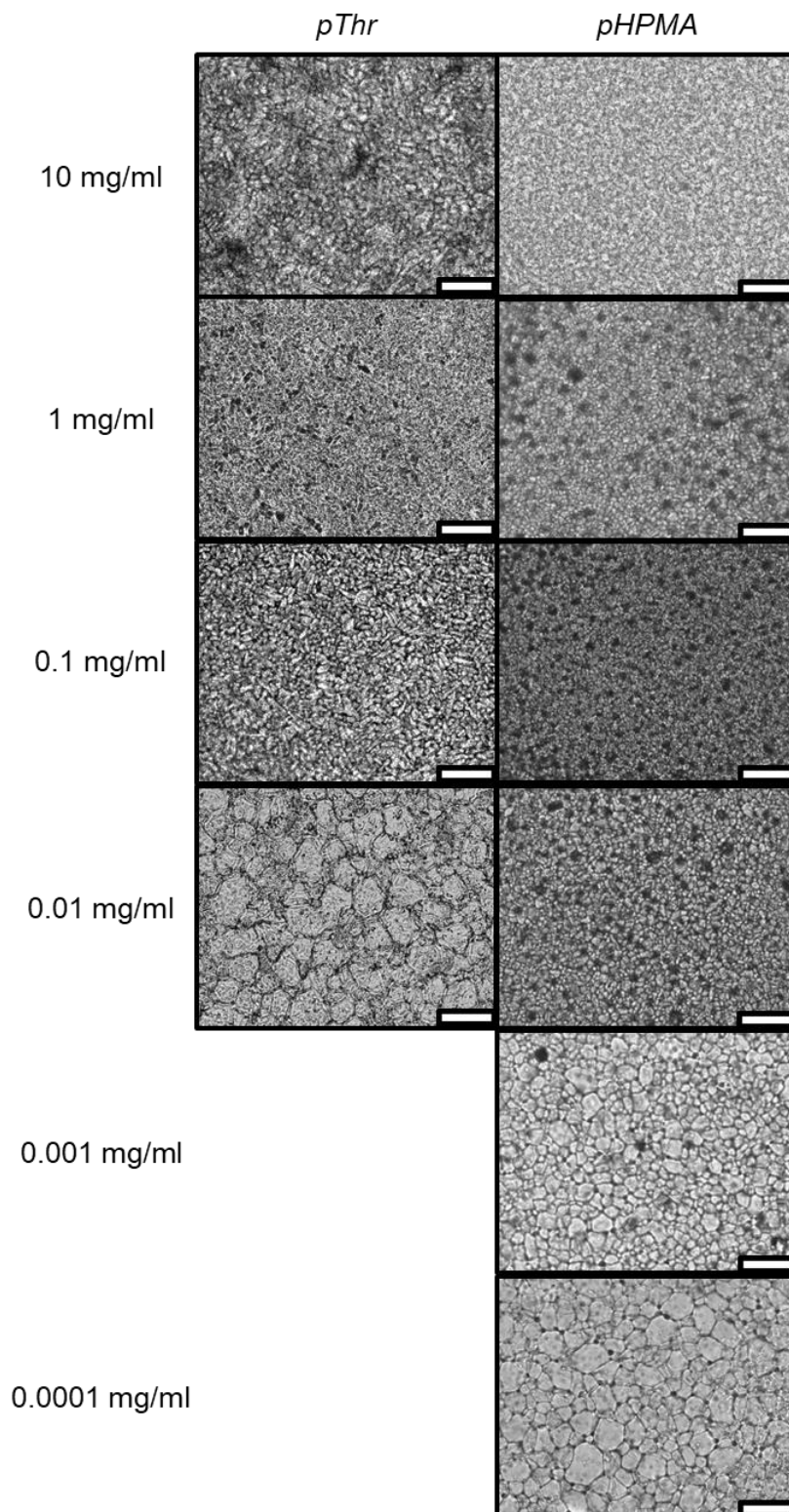
Figure 43. Representative micrographs for the concentration dependence of *Thr*, *pThr*, *HPMA*, and *pHPMA* in PBS. Images are from the end point of the IRI splat assay at t_{30}. Scale bar is 100 µm.
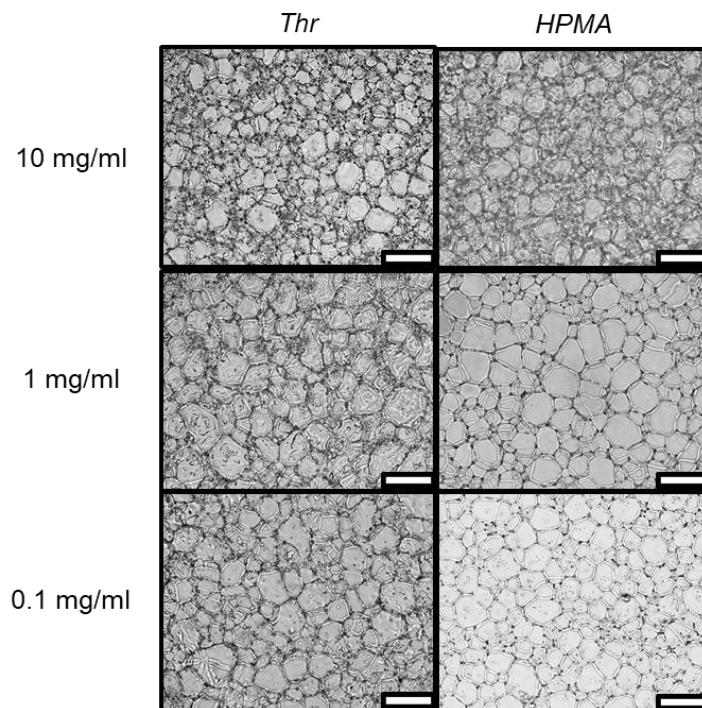
Figure 44. Representative micrographs for the concentration dependence of *Thr* and *HPMA* in PBS. Images are from the end point of the IRI splat assay at t_{30}. Scale bar is 100 µm.
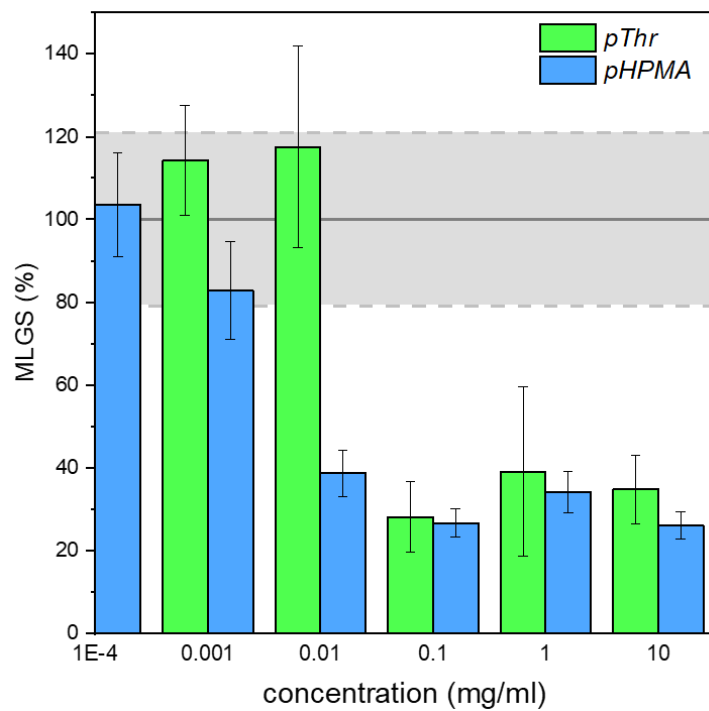
Figure 45. MLGS relative to blank solution for *pThr* and *pHPMA* at 0.0001, 0.001, 0.01, 0.1, 1, and 10 mg/ml in PBS. The gray band indicates the range of ice crystal mean largest grain size for blank PBS.
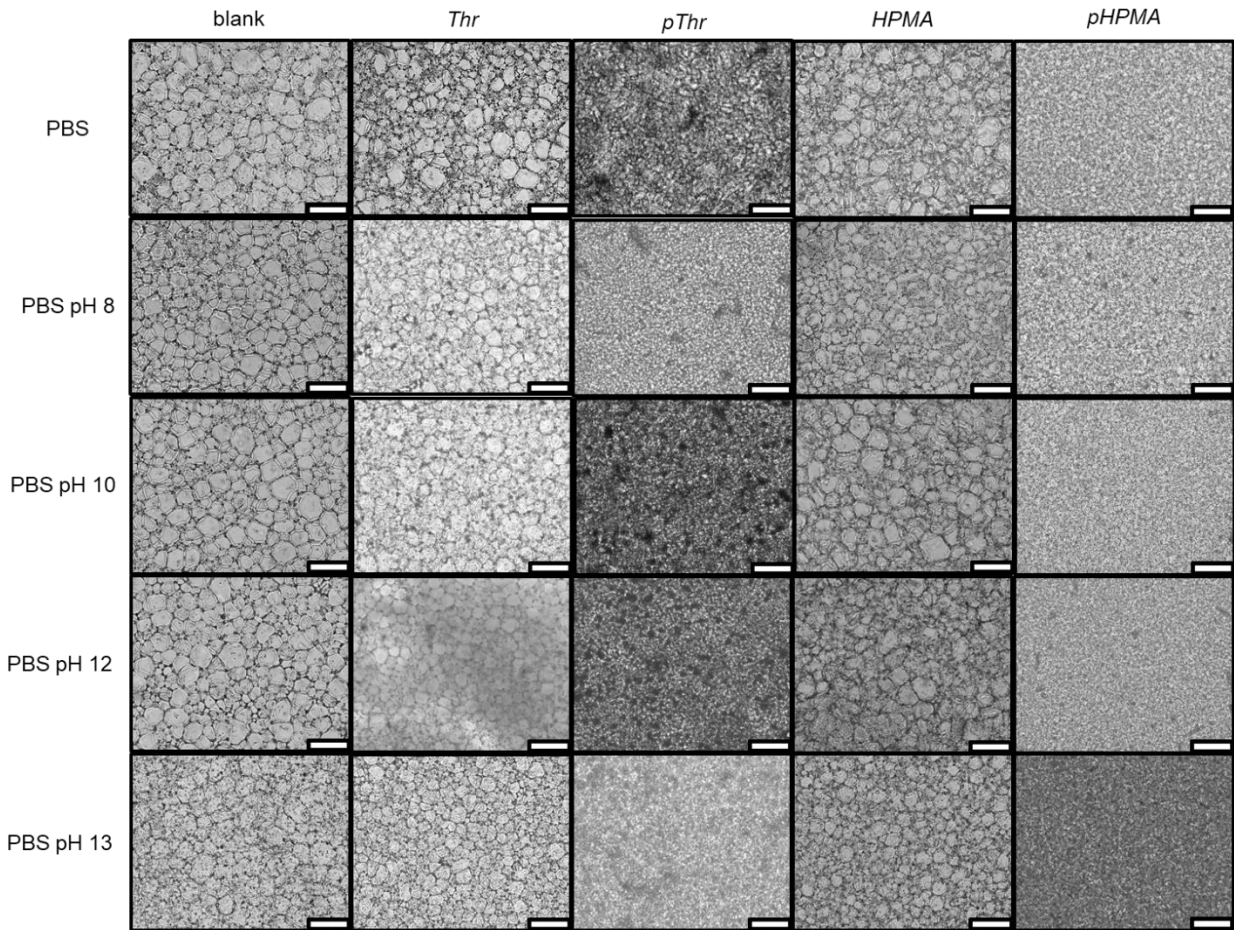
Figure 46. Representative micrographs for *Thr*, *pThr*, *HPMA*, and *pHPMA* at 10 mg/ml in PBS at various pH. Images are from the end point of the IRI splat assay at t_{30}. Scale bar is 100 µm.
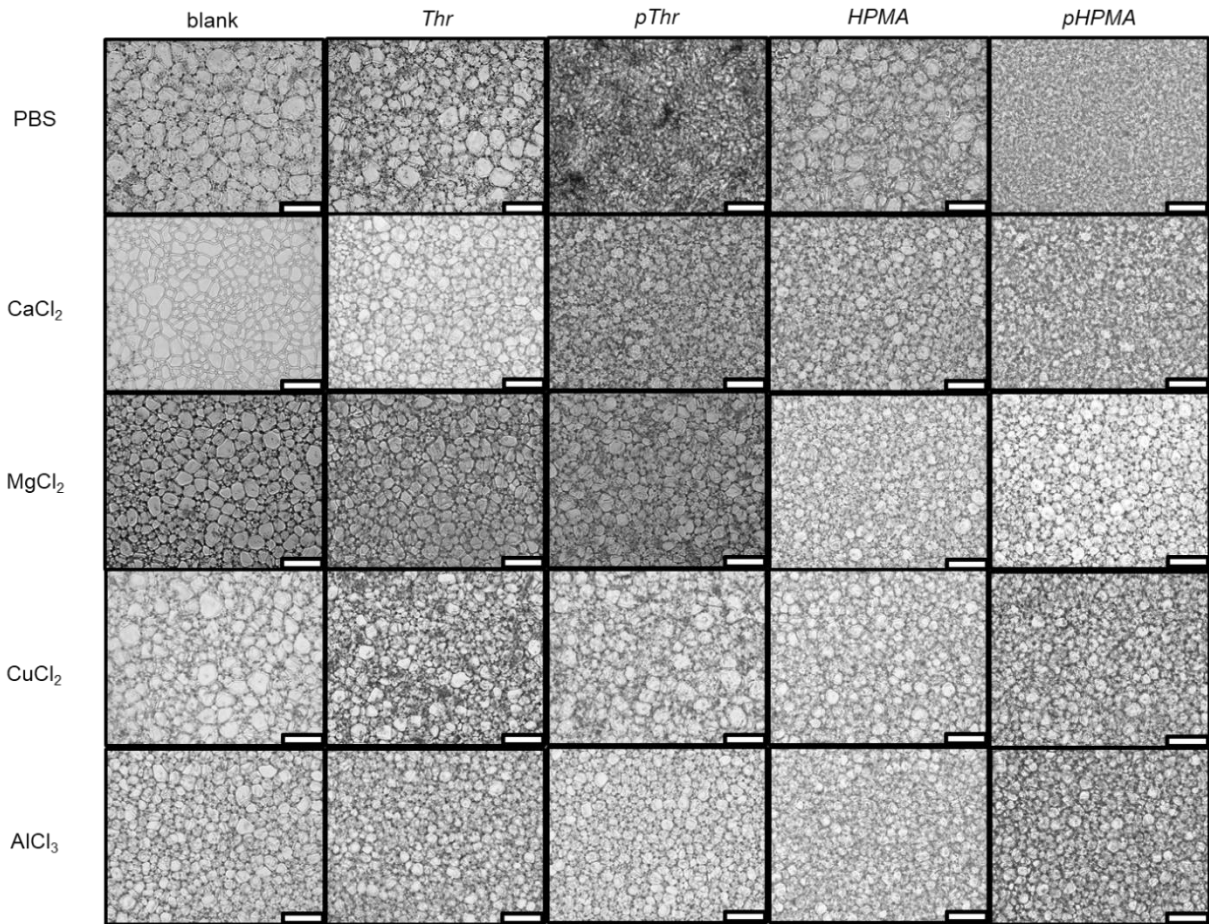
Figure 47. Representative micrographs for *Thr*, *pThr*, *HPMA*, and *pHPMA* at 10 mg/ml in various 151.5 mM salt solutions. Images are from the end point of the IRI splat assay at t_{30}. Scale bar is 100 μm.
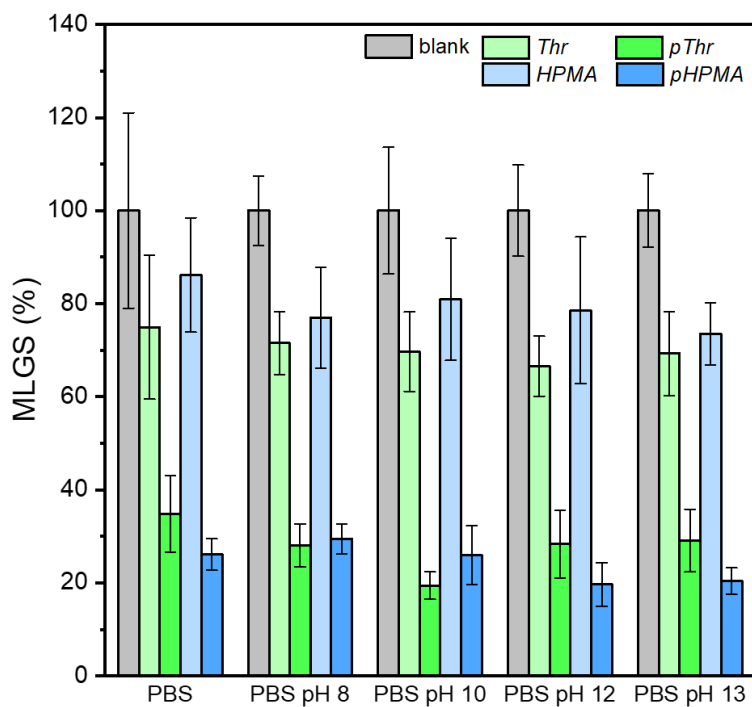
Figure 48. %MLGS relative to blank solution for *Thr*, *pThr*, *HPMA*, and *pHPMA* at 10 mg/ml in PBS at physiological pH, pH 8, pH 10, pH 12, and pH 13.
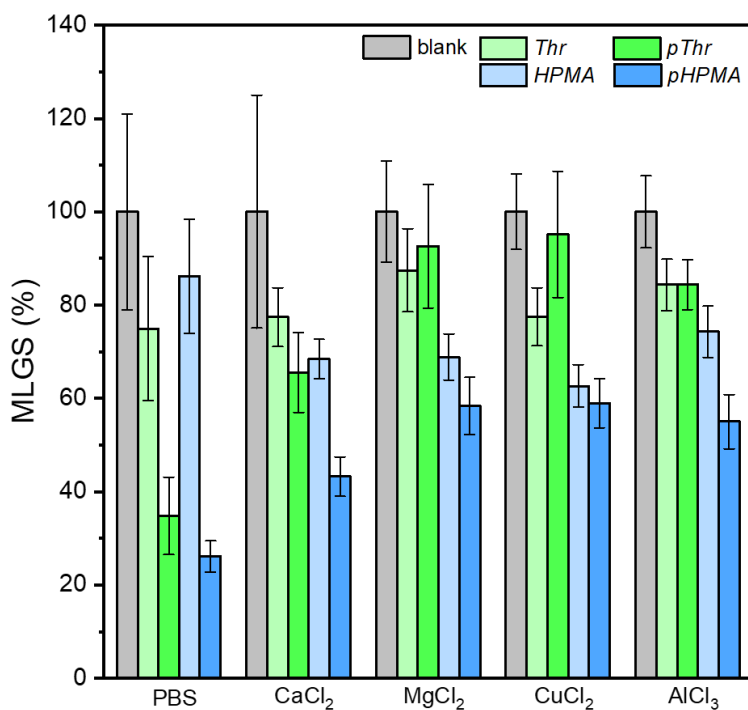
Figure 49. %MLGS relative to blank solution for *Thr*, *pThr*, *HPMA*, and *pHPMA* at 10 mg/ml in various 151.5 mM salt solutions.

To examine the potency of *pHPMA*, a sweep of molecular weights was synthesized and investigated for IRI activity. Micrographs for the molecular weight sweep and dilution series can be seen in **Figure 50**, and the relative activity reported as MLGS compared to blank PBS solution can be seen in **Figure 51**. All molecular weights of *pHPMA* demonstrated IRI activity to concentrations as low as 0.01 mg/ml in PBS, with reductions ranging between 50-70% MLGS compared to blank solution.
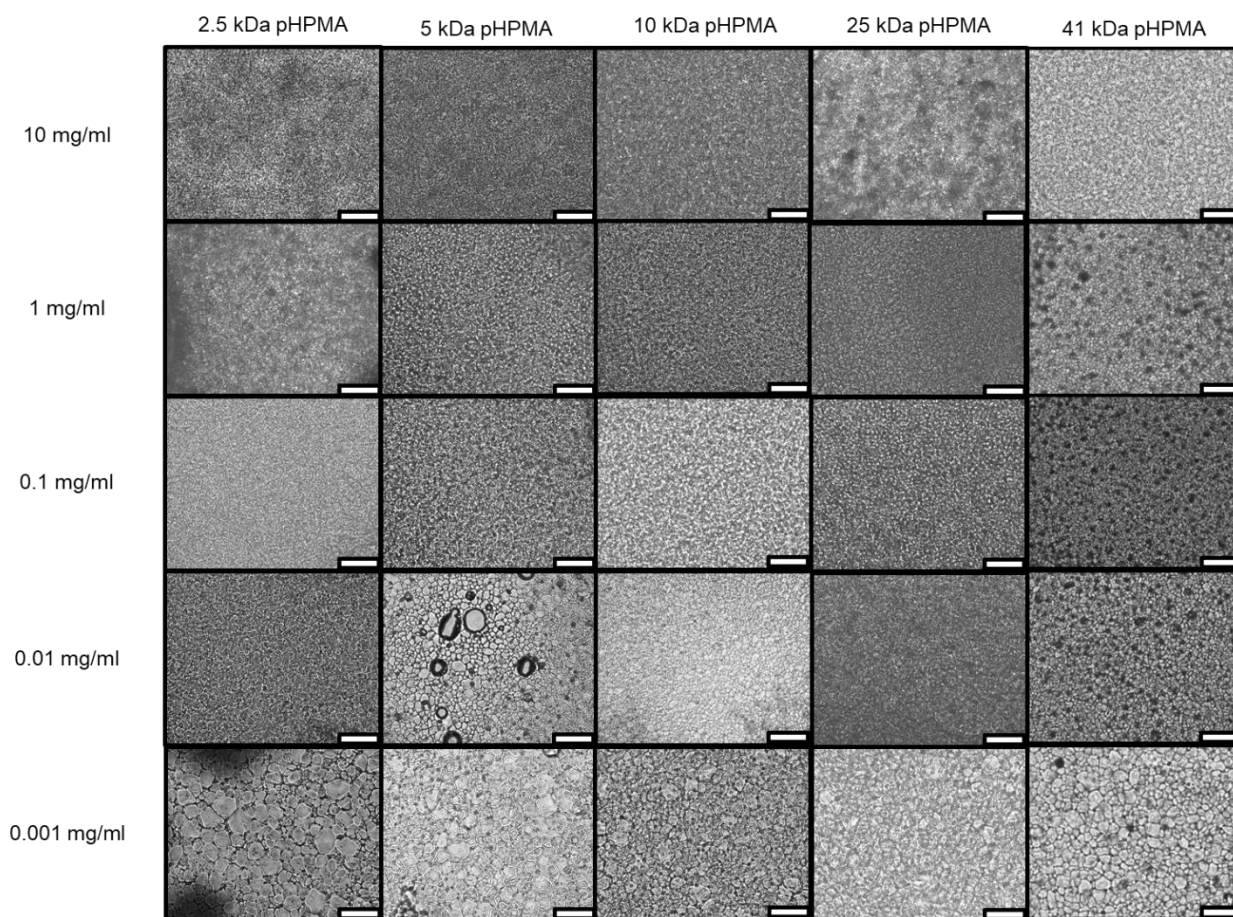
Figure 50. Representative micrographs for the concentration dependence of 2.5 kDa *pHPMA*, 5 kDa *pHPMA*, 10 kDa *pHPMA*, and 25 kDa *pHPMA* in PBS at concentrations of 0.001, 0.01, 0.1, 1, and 10 mg/ml in PBS. Images are from the end point of the IRI splat assay at t_{30}. Scale bar is 100 μm.
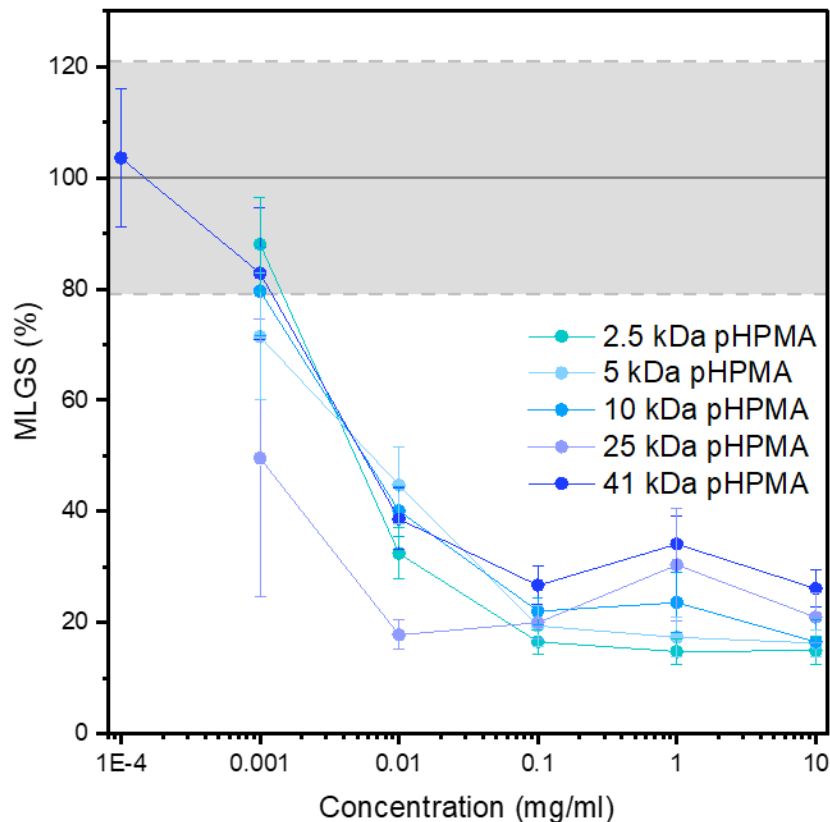
Figure 51. MLGS relative to blank solution for 2.5 kDa *pHPMA*, 5 kDa *pHPMA*, 10 kDa *pHPMA*, and 25 kDa *pHPMA* at 0.001, 0.01, 0.1, 1, and 10 mg/ml in PBS. The gray band indicates the range of ice crystal mean largest grain size for blank PBS.

Previous studies that have looked at IBPs in pH 13 solution found that the alkaline environment disrupted the proteins ability to prevent ice crystal growth, such as **Chapter 3** that demonstrated an IBP from the Antarctic bacterium *Shewanella frigidimarina* increased grain size in pH 13.2 solution.[3] As the ice inhibition activity imparted by *pThr* and *pHPMA* is not reliant on secondary structure like IBPs, they offer a distinct advantage at preventing ice growth in non-physiological environments compared to their biological counterparts. A previous study performed by Burkey et al.[117] investigated the performance of PVA with a molecular weight of 27 kDa at 1 mg/ml in pH 13 solution and found that the reduction in crystal size was ~80%, further corroborating that synthetics perform better in non-physiological environments than IBPs, offering potential ice inhibition strategies in engineering applications, such as freeze-thaw mitigation in cement and concrete.

Other studies have looked at the effect of homo-polypeptides on ice recrystallization inhibition. Graham *et al*. found similar results for a 16.2 kDa poly(glutamic acid) and a 7.3 kDa poly(lysine) at 5 mg/ml in PBS, which exhibited a ~22% and a ~21% reduction, respectively. In the study performed by Graham *et al*., the best performing molecule they tested was a 1.7 kDa poly(D-proline), which exhibited a ~42% reduction of ice crystal size at 10 mg/ml compared to blank PBS.[170] A qualitative study performed by Knight *et al*. investigated homo-polypeptides in spired by IBP ice-binding residues and found the best performing was a 15 kDa poly-L-hydroxyproline, which exhibited 'a lot' of IRI activity from 0.1-1 mg/ml in saline, and 'some' at 0.01 mg/ml.[120] These literature results corroborate that *pThr* and *pHPMA* are competitive bioinspired mimics for their molecular weights and concentrations.

PVA is a potent IRI active molecule with a pendant hydroxyl moiety on each repeat unit and currently remains one of the most widely studied synthetics that display IRI activity. An 8.6 kDa PVA has been shown to exhibit a grain size reduction of ~88% at 1 mg/ml and no reduction at 0.1 mg/ml respective to blank PBS.[92] *pThr*, which has a similar molecular weight of 7.6 kDa, comparatively exhibits a grain size reduction of ~61% at 1 mg/ml and a ~72% reduction at 0.1 mg/ml respective to blank PBS. Similarly, a 43 kDa PVA exhibited a grain size reduction of ~95% at 1 mg/ml, ~91% at 0.1 mg/ml, and ~19% at 0.01 mg/ml respective to blank PBS.[92] *pHPMA*, which has a similar molecular weight of 41.4 kDa, exhibited a grain size reduction of ~66% at 1 mg/ml, ~73% at 0.1 mg/ml, and ~61% at 0.01 mg/ml respective to blank PBS. A visual comparison between *pThr* and *pHPMA* to PVA of similar molecular weights can be seen in **Figure 52**, and these results lend to the hypothesis that the threonine pendant moiety, a hydroxyl adjacent to a methyl, may exhibit more potent IRI activity than PVA at similar molecular weights. IBPs have been shown to demonstrate IRI down to nanomolar concentrations,[39,41] and *pHPMA* exhibited IRI activity at 0.01 mg/ml (242 nM), demonstrating IRI efficacy approaching that of IBPs.

While PVA exhibits potent IRI activity at low concentrations and in elevated pH environments, it has been shown to cryogelate upon exposure to repetitive freeze-thaw cycling.[258–260] Additionally, *pHPMA* exhibits potent IRI activity at low molecular weights (2.5 kDa) and low

concentrations (0.01 mg/ml), demonstrating potency similar to native IBPs. This quality of PVA creates a unique advantage for *pThr* and *pHPMA* to supersede PVA as a novel, low-concentration additive to mitigate ice crystal growth.
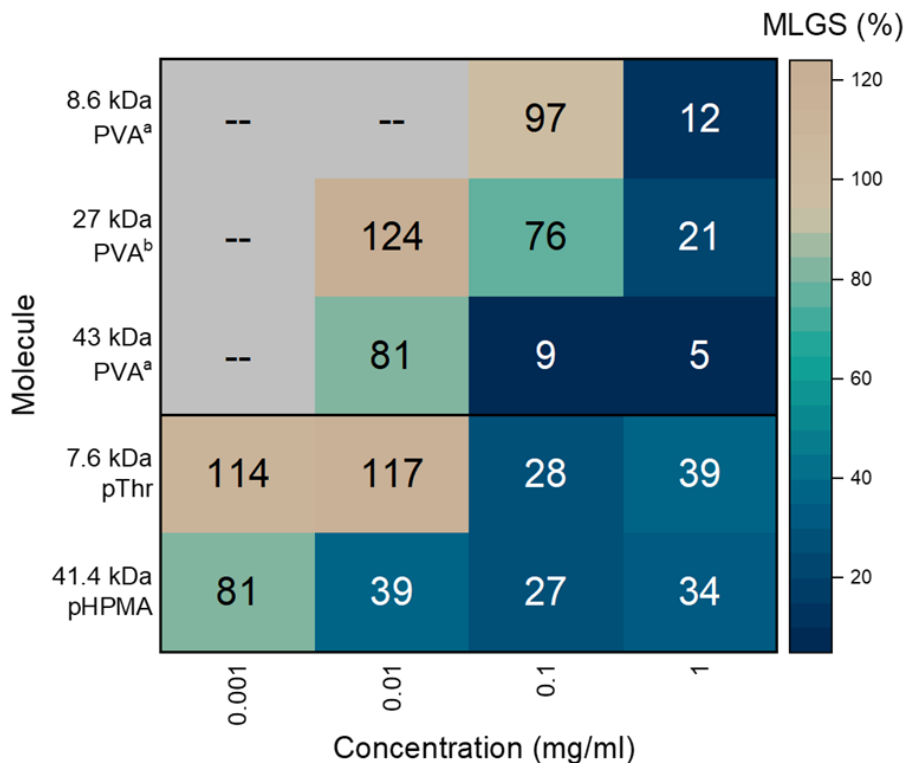
Figure 52. Comparison of IRI activity in PBS for *pThr* and *pHPMA* to PVA, where darker squares indicate higher IRI activity. [a]Data pulled from Congdon et al.[167] [b]Data pulled from Burkey et al.[117]

Multivalent cations, such as Ca^{2+} and Mg^{2+}, are more likely to interact with water or other polar molecules due to a larger charge density based on the Hofmeister series,[239] which may have led to ion interactions of the solution cations with *pThr* and *pHPMA*.[267] In a nanodrop study investigating the impact of cations on the hydrogen bonding network of water, O'Brian *et al.*[266] showed that monovalent ions have little effect on the majority of water molecules, whereas multivalent ions induce some change in bulk water, indicating that Ca^{2+} and Mg^{2+} could have played a role in the bulk organization of polar molecules in the solutions. It is hypothesized that the drop off in IRI activity in the Ca^{2+} and Mg^{2+} solutions could be due the divalent cations disrupting necessary interactions of *pThr* and *pHPMA* with either liquid water or solid ice. The

difference in *pThr* and *pHPMA* activity the salt solutions tested compared to the varied pH PBS environments could potentially be related to the Hofmeister series, where Na^+ and K^+, the cations present in PBS, are less disruptive than Ca^{2+}, Mg^{2+}, Cu^{2+}, and Al^{3+}.

5.6.4 DIS

The shape of single ice crystals under the influence of *Thr*, *pThr*, *HPMA*, and *pHPMA* in PBS can be seen in **Figure 53**. As expected, blank PBS did not exhibit any DIS, as seen by an ovular ice crystal. *Thr*, *pThr*, and *HPMA* did not exhibit any DIS, either, seen as round ice crystals. *pHPMA* exhibited DIS as evidenced by a hexagonal ice crystal. Once *pHPMA* was determined to shape ice in neutral PBS, it was tested for DIS in multivalent salt solutions and varied pH PBS solutions to determine if further ice shaping would be evinced. It was found that *pHPMA* did not induce any DIS in solutions other than neutral PBS (**Figure 54**).
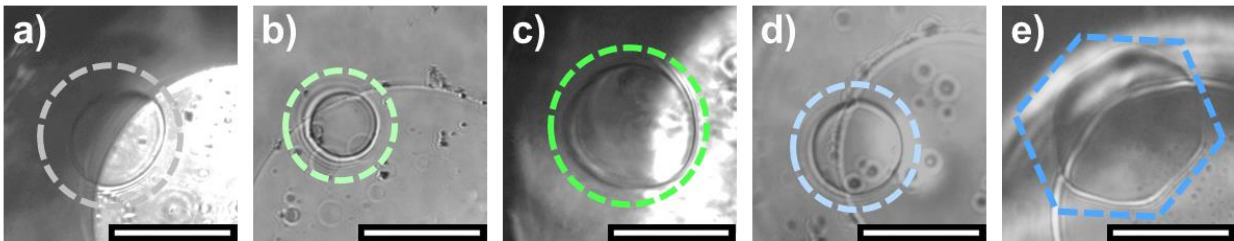
Figure 53. Dynamic ice shaping shown for a) PBS, b) 10 mg/ml *Thr* in PBS, c) 10 mg/ml *pThr* in PBS, d) 10 mg/ml *HPMA* in PBS, and e) 10 mg/ml *pHPMA* in PBS. Single ice crystals that did not demonstrate DIS are outlined with a circle. Single ice crystals that did demonstrate DIS are outlined with a hexagon. Scale bar = 50 um.
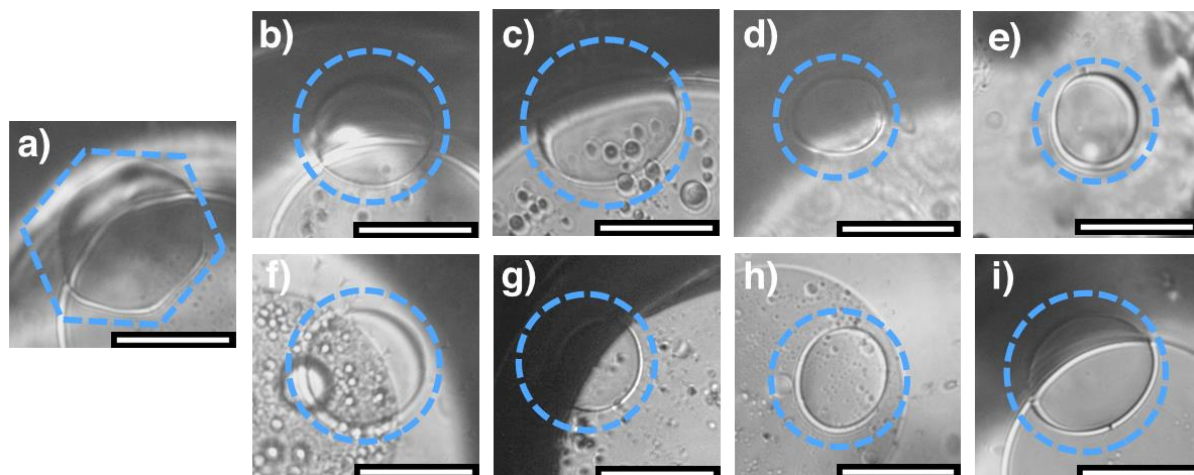
Figure 54. Representative DIS micrographs for *pHPMA* at 10 mg/ml in a) PBS, b) PBS pH 8, c) PBS pH 10, d) PBS pH 12, e) PBS pH 12, f) 151 mM $CaCl_2$, g) 151 mM $MgCl_2$, h) 151 mM $CuCl_2$, i) 151 mM $AlCl_3$. Scale bar is 50 µm.

pHPMA exhibits DIS of singular ice crystals without disruptive ice expansion upon additional cooling, further separating its performance from IBPs. DIS without disruption indicates it is able to interact at the ice-water interface but without the drawbacks of explosive growth. *pHPMA* exhibits DIS of singular ice crystals similar to other synthetic IRI active molecules, including PVA and PEG-PVA,[245] graphene oxide,[179] safranine-O,[101] and quantum dots.[104] Interestingly, *pHPMA* induced a hexagonal shape whereas *pThr* did not, indicating that the pendant functional group is not the only contributing factor to DIS. It has been hypothesized that PVA adsorbs to the ice crystal surface, and the steric hindrance of the polymer bulk prevents ice growth.[117] It is possible that the molecular weight of *pHPMA* (41.4 kDa) encouraged DIS. To further elucidate why *pHPMA* elicits DIS but *pThr* does not, testing a ~40 kDa *pThr* and a ~8 kDa *pHPMA* would be illuminating. Additionally, to further understand how the *pHPMA* was interacting at the ice crystal surface, it would be beneficial to attach a fluorescent tag to the terminus of the polymer and investigate polymer accumulation at the ice-water interface,[236] as well as determining polymer adsorption through an ice slurry assay.[117] However, as 40 kDa *pThr* and 8 kDa *pHPMA* are not readily commercially available, and neither is fluorescently tagged *pHPMA*, these tests fell outside the

scope of this study. Since *pHPMA* only exhibited DIS in neutral PBS, the addition of pH adjustors or divalent cations might have disrupted its ability to adsorb to ice.

pHPMA exhibits higher IRI activity than *pThr* in alkaline pH solutions and at lower concentrations in neutral PBS. As it has been shown that addressing the source of ice expansion is beneficial to preventing freeze-thaw damage in concrete,[245] *pHPMA* would likely be a promising additive to cement paste or concrete to prevent freeze-thaw damage. Since *pHPMA* shows some IRI activity in $CaCl_2$ or $MgCl_2$ salt solutions as well as some contributions beyond colligative to the melting point of solutions, it has some potential to work with currently existing deicers to reduce overall added salt concentration as a more eco-friendly option.[282]

5.7 Conclusions

This study investigated three amino acids (*Thr*, *Arg*, *Glu*) and their respective homo-polypeptides (*pThr*, *pArg*, *pGlu*) to inhibit and control ice crystal nucleation and growth in a PBS. The materials were tested by looking at their IRI activity and the amino acids and homo-polypeptides were used to elucidate the optimal concentration of multivalent cationic salts for further testing, and a concentration of 151.5 mM was determined to be optimal. IRI activity in multivalent cationic salt solutions was investigated, and it was found that activity was lost upon the addition of larger valences. Neither melting point depression nor enthalpy of crystallization gave indication of potential IRI activity, as exemplified by *pThr*, which exhibited IRI activity but no change in melting point or crystallization enthalpy compared to blank solutions. Ultimately, *pThr* was determined to be the best homo-polypeptide for synthetic replication. 2-hydroxypropyl methacrylamide (*HPMA*) and its respective polymer, *pHPMA* were chosen as they exhibit a pendant functional group similar to threonine. *Thr*, *pThr*, *HPMA*, and *pHPMA* were investigated for multiple modes of interaction with ice, namely: melting point depression, entropy of crystallization, IRI activity, and DIS. It was found that the modes of interaction are not interdependent and molecules can exhibit one mode without demonstrating another, showing versatility and tunability with respect to modes of interaction. *HPMA* and *pHPMA* both exhibited

some interactions beyond colligative to lower the melting point of solution. *pHPMA* was shown to have IRI activity at ultra-low concentrations (0.01 mg/ml) in PBS and demonstrated an ~80% reduction in ice crystal size in pH 13 solution, which is comparable to PVA, another well-studied synthetic that is often used.[117,167] *pHPMA* was the only molecule investigated herein to exhibit DIS in PBS, though upon introduction of external stressors (salts, pH) it no longer exhibited DIS.

In conclusion, these results suggest that the chemical structure of threonine (and polymers thereof) is an important amino acid residue to mimic in the design of biologically inspired macromolecules that exhibit ice interaction. Molecules based on its chemical structure, such as *pHPMA*, may exhibit more potent IRI activity than PVA at similar molecular weights. Additionally, peptidic or synthetic polymers with pendant functional groups like threonine are a promising potential additive for mitigating ice growth in infrastructure relevant environments, such as cementitious materials with highly alkaline pH or deicing salt solutions containing high concentrations of divalent cations.

5.8   Authorship and Acknowledgements

AUTHORS: Elizabeth A. Delesky[1], Felipe Garcia-Alzate[2], Aparna J. Lobo[3], Jaqueline D. Wallat[4], Garret Miyake[2], and Wil V. Srubar III[1,4,*]

[1]Materials Science and Engineering Program, University of Colorado Boulder, Boulder, CO 80309, USA; elizabeth.delesky@colorado.edu (E.A.D.);

[2]Deparment of Chemistry, Colorado State University, Fort Collins, CO 80523, USA; Felipe.Garcia_Alzate@colostate.edu (F.G.A), Garret.Miyake@colostate.edu (G.M.);

[3]Department of Chemical Engineering, University of Colorado Boulder; Boulder, CO 80309, USA; aparna.lobo@colorado.edu (A.J.L)

[4]Department of Civil, Environmental, and Architectural Engineering, University of Colorado Boulder; Boulder, CO 80309, USA; jaqueline.wallat@colorado.edu (J.D.W.);

* Correspondence: wsrubar@colorado.edu (W.V.S.III); Tel.: +1-303-492-2621

CHAPTER 6
Concluding Remarks

6.1   Summary of Contributions

IBPs and synthetic mimics have gained interest due to their potential application to a wide variety of fields, such as cryopreservation, transgenics, food storage, and even energy materials. While IBPs show extraordinary abilities to prevent ice growth, they are limited by denaturation and loss of activity in non-physiological environments, as well as are expensive to produce large quantities. Synthetic materials, such as PVA, have shown promising ice mitigation activities, however, have also been shown to cryogelate.

The research presented herein advances scientific understanding of ice inhibition in non-physiological environments using naturally occurring materials or bioinspired synthetic replicates. The following demonstrates a brief summary of the significant scientific contributions to this field of work.

- The review of recent literature has provided an overview of ice mitigation for a variety of materials, facilitating material choice for targeted ice control in various environments with concentration constraints.

- An ice-binding protein from *Shewanella frigidimarina* retains primary structure when pH ≤ 12.7 and ionic strength is ≤ 0.05 mol/L, and loses secondary structure when pH ≥ 12.4 and ionic strength is ≥ 0.03 mol/L.

- SfIBP exhibits IRI activity when primary structure is retained, demonstrating secondary structure is not as important as primary structure for eliciting IRI activity.

- *Mp*IBP retains primary structure in solutions with pH 2 – 12, and retains secondary structure in solutions with pH 6 – 10.

- *Mp*IBP exhibits IRI activity in solutions with pH 6 – 12, demonstrating that primary structure is required for IRI activity, but does not guarantee IRI activity.

- *Mp*IBP only demonstrates DIS in solutions with pH 6 – 10, suggesting that secondary structure is important for DIS.

- The amphipathic residue threonine exhibited potent IRI activity as a homo-polypeptide, demonstrating a ~75% reduction in mean largest grain size at concentrations of 0.1 mg/ml.

- The synthetic replicate of threonine, *pHPMA*, reduced the mean largest grain size by ~60-75% at concentrations from 0.01-10 mg/ml, demonstrating a synthetic polymer with potent IRI activity, active at lower concentrations than the leading synthetic contender, PVA.

- *pHPMA* inhibited ice growth by 80% at 10 mg/ml in pH 13 solution, demonstrating a viable option for mitigating ice growth in highly alkaline cementitious environments.

- Low molecular weight pHPMA oligomers (2.5 kDa) demonstrated IRI activity at 10 mg/ml in PBS, indicating a potent new polymer for ice growth mitigation.

Investigating materials with IRI activity in non-physiological pH adjusted environments with the potential of mitigating freeze-thaw damage in alkaline cementitious materials was the primary thrust of research. From the identified gaps in **Chapter 2**, a visual representation of the contributions of this work is shown below in **Figure 55**.
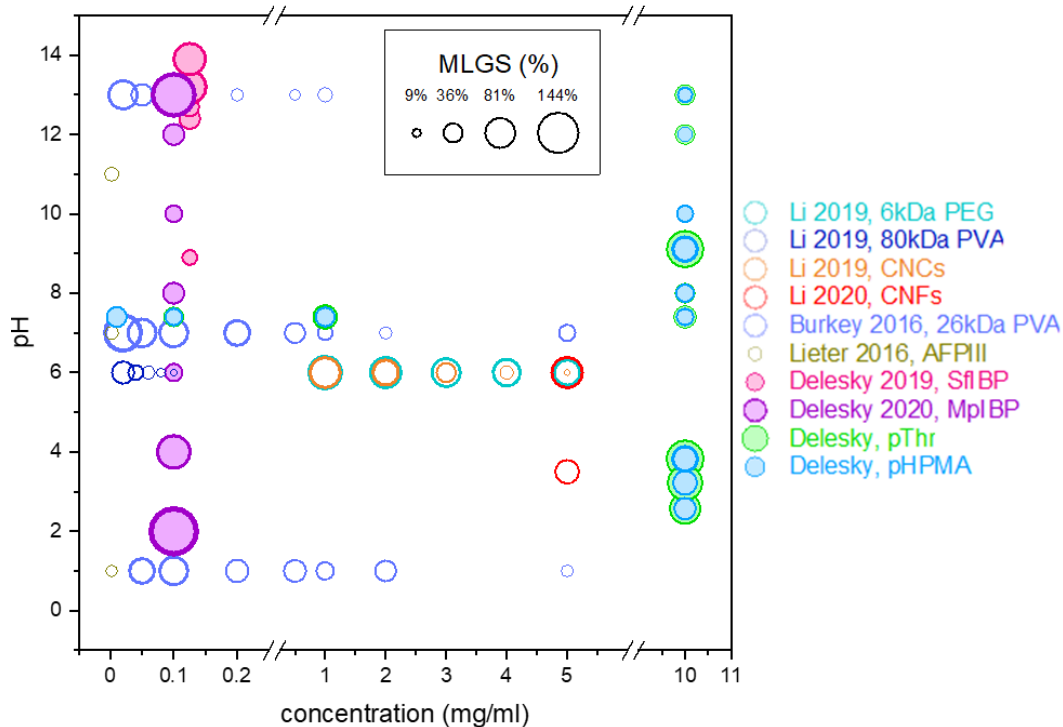
Figure 55. Bubble plot showing the contributions of this work to the knowledge of the field for materials that effectively mitigate ice recrystallization in varied pH environments. Contributions made by this work are filled in, whereas previous data from the field are hollow.

6.2   Future Research Directions

In this work, key contributions were made to understand the viability and limitations of applying ice-binding proteins to non-physiological environments, as well as determine a synthetic alternative that exhibits IRI activity at low concentrations as well as potent activity in alkaline environments. However, further research is required qualify performance in both physiological and non-physiological environments to potentially execute these technologies in commercial applications.

Future Research Direction #1. *pHPMA* Degradation Pathways. First, the degradation and long-term viability for IBPs, homo-polypeptides, and synthetic replicates, i.e., *pHPMA*, have not been fully explicated for applications in non-physiological environments. Experiments that look at the time of degradation, byproducts of degradation, and activity during degradation is an important next step to determine viability in industrial applications. Additionally, understanding

byproducts and intermediates for materials and their impact on health and the environment are important to consider before upscaling material production.

Future Research Direction #2. Determining the *pHPMA*-ice Interaction Mechanism. Second, the interaction of *pHPMA* with ice has not been determined. For IBPs, the proteins have been shown to directly adsorb to nascent ice crystals, which was determined using a fluorescent tag and imaging single ice crystals in contact with the proteins. For synthetic molecules, such as PVA, the molecules were tagged and placed in an ice slurry bath and tested for concentration after equilibrating for an hour. For small molecules, the surface tension of solution was tested before and after ice affinity purification to determine adsorption to the growing ice front. Performing all of these experiments could be valuable to elucidate how *pHPMA* is interacting with ice.

Future Research Direction #3. *pHPMA* Application Testing. Third, small-scale application testing is required to determine viability for *pThr* and *pHPMA* to mitigate ice in physiological and non-physiological environments. For physiological applications, such as cryopreservation, cell compatibility should be determined. Determining cell viability in the presence of these materials in ambient living conditions, as well as survivability post-thaw, is a crucial step for implementation for cryopreservation applications. Additionally, comparing these materials to current cryopreservation materials, such as glycerol or DMSO, would be important to determine if the post-thaw mortality is low enough to offer a competitive material for cryopreservation technologies. Investigating the freeze-thaw durability of cementitious materials should be considered for non-physiological applications. Considerations for additives in cement or concrete requires testing these materials for fresh- and hardened-state properties, as well as determining the reduction of damage caused by freeze-thaw cycling. Additives would need to be tested for workability, set-time, and shrinkage. Hardened state properties, such as strength and porosity, under the influence of the additive would also have to be examined. Most importantly, the freeze-thaw durability of the IRI-active additive would have to be compared to traditional freeze-thaw mitigation agents, air-entraining admixtures, to determine viability for infrastructure applications.

Future Research Direction #4. Large Scale *pHPMA* Production. Finally, the cost of materials and validity of synthesis needs to be considered. For most applications, upscaling requires cheap materials that are stable in large batches. Precursors for *HPMA* are volatile and toxic, although RAFT mechanisms are already well implemented for a variety of complex architectures available for industrial applications, such as lubricants, foam-control agents, elastomers, and more.[283] For proteins and polypeptides, upscaling is a rather difficult and expensive issue that has been tackled for decades with only marginal success. To fully implement these materials for commercial practices, viability would need to be considered or cheaper and more reliable precursors would have to be considered.

REFERENCES

1. Vance, T. D. R. R., Graham, L. A. & Davies, P. L. An ice-binding and tandem beta-sandwich domain-containing protein in *Shewanella frigidimarina* is a potential new type of ice adhesin. *FEBS J.* **285**, 1511–1527 (2018).

2. Knight, C. A., Hallett, J. & Devriess, A. L. Solute Effects on Ice Recrystallization: An Assessment Technique. *Cryobiology* **25**, 55–60 (1988).

3. Delesky, E. A. E. A. *et al.* Ice-binding protein from Shewanella frigidimarinas inhibits ice crystal growth in highly alkaline solutions. *Polymers (Basel).* **11**, 9–12 (2019).

4. Industrial Water Use. Available at: https://www.usgs.gov/mission-areas/water-resources/science/industrial-water-use?qt-science_center_objects=0#qt-science_center_objects.

5. Eisenberg, D. & Kauzmann, W. *The structure and properties of water*. (Oxford University Press on Demand., 2005).

6. Voitkovskii, K. F. Translation of The Mechanical Properties of Ice. (1960).

7. Kasper, J. C. & Friess, W. The freezing step in lyophilization: Physico-chemical fundamentals, freezing methods and consequences on process performance and quality attributes of biopharmaceuticals. *Eur. J. Pharm. Biopharm.* **78**, 248–263 (2011).

8. Arakawa, T., Prestrelski, S. J., Kenney, W. C. & Carpenter, J. F. Estabilidad de proteínas. *Adv. Drug Deliv. Rev.* **46**, 1–8 (2001).

9. Jiang, S. & Nail, S. L. Effect of process conditions on recovery of protein activity after freezing and freeze-drying. *Eur. J. Pharm. Biopharm.* **45**, 249–257 (1998).

10. Costantino, H. R. & Pikal, M. J. *Lyophilization of biopharmaceuticals*. (Springer Science & Business Media, 2004).

11. Gao, D. & Critser, J. K. Mechanisms of cryoinjury in living cells. *ILAR J.* **41**, 187–196 (2000).

12. Harding, K. Genetic integrity of cryopreserved plant cells: A review. *Cryo-Letters* **25**, 3–22 (2004).

13. John Morris, G. & Acton, E. Controlled ice nucleation in cryopreservation - A review. *Cryobiology* **66**, 85–92 (2013).

14. Kaleda, A., Tsanev, R., Klesment, T., Vilu, R. & Laos, K. Ice cream structure modification by ice-binding proteins. *Food Chem.* **246**, 164–171 (2018).

15. Soukoulis, C. & Fisk, I. Innovative ingredients and emerging technologies for controlling ice recrystallization, texture, and structure stability in frozen dairy desserts: A review. *Critical Reviews in Food Science and Nutrition* **56**, 2543–2559 (2016).

16. Kiani, H. & Sun, D. W. Water crystallization and its importance to freezing of foods: A review. *Trends Food Sci. Technol.* **22**, 407–426 (2011).

17.   Scherer, G. W. & Valenza, J. J. Mechanisms of Frost Damage. *Mater. Sci. Concr.* **7**, 209–246 (2005).

18.   Scherer, G. W. Crystallization in pores. *Cem. Concr. Res.* **29**, 1347–1358 (1999).

19.   Liu, L. *et al.* Analysis of damage development in cement paste due to ice nucleation at different temperatures. *Cem. Concr. Compos.* **53**, 1–9 (2014).

20.   Rahman, S. & Grasley, Z. A poromechanical model of freezing concrete to elucidate damage mechanisms associated with substandard aggregates. *Cem. Concr. Res.* **55**, 88–101 (2014).

21.   Yang, R., Lemarchand, E., Fen-Chong, T. & Azouni, A. A micromechanics model for partial freezing in porous media. *Int. J. Solids Struct.* **75–76**, 109–121 (2015).

22.   Momma, K. & Izumi, F. VESTA 3 for three-dimensional visualization of crystal, volumetric and morphology data. *J. Appl. Crystallogr.* **44**, 1272–1276 (2011).

23.   Hincha, D. K. & Zuther Editors, E. *Plant Cold Acclimation Methods and Protocols Methods in Molecular Biology 1166*.

24.   Duman, J. G. & Olsen, T. M. Thermal hysteresis protein activity in bacteria, fungi, and phylogenetically diverse plants. *Cryobiology* **30**, 322–328 (1993).

25.   Griffith, M., Ala, P., Yang, D. S. C., Hon, W. C. & Moffatt, B. A. Antifreeze protein produced endogenously in winter rye leaves. *Plant Physiol.* **100**, 593–596 (1992).

26.   Moffatt, B., Ewart, V. & Eastman, A. Cold comfort: Plant antifreeze proteins. *Physiol. Plant.* **126**, 5–16 (2006).

27.   Hoshino, T. *et al.* Antifreeze proteins from snow mold fungi 1. doi:10.1139/b03-116

28.   Xiao, N. *et al.* Comparison of functional properties of two fungal antifreeze proteins from Antarctomyces psychrotrophicus and Typhula ishikariensis. *FEBS J.* **277**, 394–403 (2010).

29.   Marshall, C. B., Fletcher, G. L. & Davies, P. L. Hyperactive antifreeze protein in a fish. *Nature* **429**, 153 (2004).

30.   DeVries, A. L. The role of antifreeze glycopeptides and peptides in the freezing avoidance of antarctic fishes. *Comp. Biochem. Physiol. -- Part B Biochem.* **90**, 611–621 (1988).

31.   Fletcher, G. L., King, M. J. & Kao, M. H. Low temperature regulation of antifreeze glycopeptide levels in Atlantic cod (Gadus morhua) . *Can. J. Zool.* **65**, 227–233 (1987).

32.   Hew, C. L., Slaughter, D., Fletcher, G. L. & Joshi, S. B. Antifreeze glycoproteins in the plasma of Newfoundland Atlantic cod (Gadus morhua) . *Can. J. Zool.* **59**, 2186–2192 (1981).

33.   Slaughter, D., Fletcher, G. L., Ananthanarayanan, V. S. & Hew, C. L. Antifreeze proteins from the sea raven, Hemitripterus americanus. Further evidence for diversity among fish polypeptide antifreezes. *J. Biol. Chem.* **256**, 2022–2026 (1981).

34.   Davies, P. L., Hew, C. L. & Fletcher, G. L. Fish antifreeze proteins: physiology and

evolutionary biology. *Can. J. Zool.* **66**, 2611–2617 (1988).

35. Graethert, S. P. *et al.* β-Helix structure and ice-binding properties of a hyperactive antifreeze protein from an insect. *Nature* **406**, 325–328 (2000).

36. Liou, Y. C., Thibault, P., Walker, V. K., Davies, P. L. & Graham, L. A. A complex family of highly heterogeneous and internally repetitive hyperactive antifreeze proteins from the beetle Tenebrio molitor. *Biochemistry* **38**, 11415–11424 (1999).

37. Graham, L. A. & Davies, P. L. Biochemistry: Glycine-rich antifreeze proteins from snow fleas. *Science (80-.).* **310**, 461 (2005).

38. Garnham, C. P. *et al.* A Ca2+-dependent bacterial antifreeze protein domain has a novel β-helical ice-binding fold. *Biochem. J.* **411**, 171–180 (2008).

39. Gilbert, J. A., Hill, P. J., Dodd, C. E. R. & Laybourn-Parry, J. Demonstration of antifreeze protein activity in Antarctic lake bacteria. *Microbiology* **150**, 171–180 (2004).

40. Davies, P. L. Ice-binding proteins: A remarkable diversity of structures for stopping and starting ice growth. *Trends Biochem. Sci.* **39**, 548–555 (2014).

41. Dolev, M. B., Braslavsky, I. & Davies, P. L. Ice-Binding Proteins and Their Function. (2016). doi:10.1146/annurev-biochem-060815-014546

42. Voets, I. K. From ice-binding proteins to bio-inspired antifreeze materials. *Soft Matter* **13**, 4808–4823 (2017).

43. Garnham, C. P., Campbell, R. L. & Davies, P. L. Anchored clathrate waters bind antifreeze proteins to ice. *Proc. Natl. Acad. Sci. U. S. A.* **108**, 7363–7367 (2011).

44. Chakraborty, S. & Jana, B. Optimum Number of Anchored Clathrate Water and Its Instantaneous Fluctuations Dictate Ice Plane Recognition Specificities of Insect Antifreeze Protein. *J. Phys. Chem. B* **122**, 3056–3067 (2018).

45. He, Z., Liu, K. & Wang, J. Bioinspired Materials for Controlling Ice Nucleation, Growth, and Recrystallization. *Acc. Chem. Res.* **51**, 1082–1091 (2018).

46. Hudait, A. *et al.* Preordering of water is not needed for ice recognition by hyperactive antifreeze proteins. *Proc. Natl. Acad. Sci. U. S. A.* **115**, 8266–8271 (2018).

47. Zanetti-Polzi, L., Biswas, A. D., Del Galdo, S., Barone, V. & Daidone, I. Hydration Shell of Antifreeze Proteins: Unveiling the Role of Non-Ice-Binding Surfaces. *J. Phys. Chem. B* **123**, 6474–6480 (2019).

48. Grabowska, J., Kuffel, A. & Zielkiewicz, J. Molecular dynamics study on the role of solvation water in the adsorption of hyperactive AFP to the ice surface. *Phys. Chem. Chem. Phys.* (2018). doi:10.1039/C8CP05027A

49. Jia, Z., DeLuca, C., Chao, H. & Davies, P. L. Structural basis for the binding of a globular antifreeze protein to ice. *Chemtracts* **11**, 229–232 (1998).

50. Zhang, D. Q., Liu, B., Feng, D. R., He, Y. M. & Wang, J. F. Expression, purification, and antifreeze activity of carrot antifreeze protein and its mutants. *Protein Expr. Purif.* **35**,

257–263 (2004).

51.	Deluca, C. I., Davies, P. L., Ye, Q. & Jia, Z. The Effects of Steric Mutations on the Structure of Type III Antifreeze Protein and its Interaction with Ice. (1998).

52.	Baardsnes, J. *et al.* New ice-binding face for type I antifreeze protein. *FEBS Lett.* **463**, 87–91 (1999).

53.	Baardsnes, J. & Davies, P. L. Contribution of hydrophobic residues to ice binding by fish type III antifreeze protein. *Biochim. Biophys. Acta - Proteins Proteomics* **1601**, 49–54 (2002).

54.	Haymet, A. D. J., Ward, L. G., Harding, M. M. & Knight, C. A. Valine substituted winter flounder 'antifreeze': Preservation of ice growth hysteresis. *FEBS Lett.* **430**, 301–306 (1998).

55.	Massie, I., Selden, C., Hodgson, H. & Fuller, B. Cryopreservation of encapsulated liver spheroids for a bioartificial liver: Reducing latent cryoinjury using an ice nucleating agent. *Tissue Eng. - Part C Methods* **17**, 765–774 (2011).

56.	Mazur, P., Seki, S., Pinn, I. L., Kleinhans, F. W. & Edashige, K. Extra- and intracellular ice formation in mouse oocytes. *Cryobiology* (2005). doi:10.1016/j.cryobiol.2005.04.008

57.	Petersen, A., Schneider, H., Rau, G. & Glasmacher, B. A new approach for freezing of aqueous solutions under active control of the nucleation temperature. *Cryobiology* (2006). doi:10.1016/j.cryobiol.2006.06.005

58.	Liang, S. *et al.* Effect of antifreeze glycoprotein 8 supplementation during vitrification on the developmental competence of bovine oocytes. *Theriogenology* (2016). doi:10.1016/j.theriogenology.2016.01.032

59.	Kim, H. J., Koo, B.-W., Kim, D., Seo, Y. S. & Nam, Y. K. Effect of Marine-Derived Ice-Binding Proteins on the Cryopreservation of Marine Microalgae. doi:10.3390/md15120372

60.	Tomalty, H. E. *et al.* Kidney preservation at subzero temperatures using a novel storage solution and insect ice-binding proteins. *Cryo-Letters* **38**, 100–107 (2017).

61.	Kim, M. K., Kong, H. S., Youm, H. W. & Jee, B. C. Effects of supplementation with antifreeze proteins on the follicular integrity of vitrified-warmed mouse ovaries: Comparison of two types of antifreeze proteins alone and in combination. *Clin. Exp. Reprod. Med.* (2017). doi:10.5653/cerm.2017.44.1.8

62.	Lee, S. G., Koh, H. Y., Lee, J. H., Kang, S. H. & Kim, H. J. Cryopreservative effects of the recombinant ice-binding protein from the arctic yeast leucosporidium sp. on red blood cells. *Appl. Biochem. Biotechnol.* **167**, 824–834 (2012).

63.	Chao, H., Davies, P. L. & Carpenter, J. F. Effects of antifreeze proteins on red blood cell survival during cryopreservation. *J. Exp. Biol.* **199**, 2071–2076 (1996).

64.	WAng, J.-H. A Comprehensive Evaluation of the Effects and Mechanisms of Antifreeze Proteins during Low-Temperature Preservation. *Cryobiology* **41**, 1–9 (2000).

65.   Ptitsyn, O. B. Protein folding: Hypotheses and experiments. *J. Protein Chem.* **6**, 273–293 (1987).

66.   Tab, M. M. *et al.* Large-Scale Production of Glaciozyma antarctica Antifreeze Protein 1 (Afp1) by Fed-Batch Fermentation of Pichia pastoris. *Arab. J. Sci. Eng.* **43**, 133–141 (2018).

67.   Tomalty, H. E., Graham, L. A., Eves, R., Gruneberg, A. K. & Davies, P. L. Laboratory-Scale Isolation of Insect Antifreeze Protein for Cryobiology. (2019).

68.   Deller, R. C., Vatish, M., Mitchell, D. A. & Gibson, M. I. Synthetic polymers enable non-vitreous cellular cryopreservation by reducing ice crystal growth during thawing. *Nat. Commun.* **5**, 1–7 (2014).

69.   Wen, D. & Laursens, R. A. Structure-Function Relationships in an Antifreeze Polypeptide. *J. Biol. Chem.* **267**, 14102–14108 (1992).

70.   Berg, J. M. *Biochemistry.* (2002).

71.   Hughes, B. P. RATIONAL CONCRETE MIX DESIGN. *Proc. Inst. Civ. Eng.* **17**, 315–332 (1960).

72.   Gambhir, M. L. *Concrete technology: theory and practice.* (Tata McGraw-Hill Education, 2013).

73.   Jackson, F. H. Concretes Containing Air-Entraining Agents. *J. Am. Concr. Inst.* **40**, 509–515 (1944).

74.   Du, L. & Folliard, K. J. Mechanisms of air entrainment in concrete. *Cem. Concr. Res.* **35**, 1463–1471 (2005).

75.   Xu, S., Scherer, G. W., Mahadevan, T. S. & Garofalini, S. H. Thermal expansion of confined water. *Langmuir* **25**, 5076–5083 (2009).

76.   Xu, S. *et al.* Transport of water in small pores. *Langmuir* **25**, 5084–5090 (2009).

77.   Sun, Z. & Scherer, G. W. Effect of air voids on salt scaling and internal freezing. *Cem. Concr. Res.* **40**, 260–270 (2010).

78.   Espinosa-Marzal, R. M. & Scherer, G. W. Crystallization pressure exerted by in-pore confined crystals. *Poromechanics IV - 4th Biot Conf. Poromechanics* 1013–1018 (2009).

79.   Klieger, P. Effect of entrained air on strength and durability of concrete made with various maximum sizes of sizes of aggregate. in *Highway Research Board Proceedings* 31 (1955).

80.   Pu, Q. *et al.* Evolution of pH and chemical composition of pore solution in carbonated concrete. *Constr. Build. Mater.* **28**, 519–524 (2012).

81.   Ghods, P., Isgor, O. B., McRae, G. & Miller, T. The effect of concrete pore solution composition on the quality of passive oxide films on black steel reinforcement. *Cem. Concr. Compos.* **31**, 2–11 (2009).

82.   Parry, M. L. *Climate change and world agriculture.* (Routledge, 2019).

83.   Crate, S. A. & Nuttal, M. *Anthropology and climate change: from encounters to actions*. (Routledge, 2016).

84.   Seinfeld, J. H. & Pandis, S. N. *Atmospheric chemistry and physics: from air pollution to climate change.* (John Wiley & Sons, 2016).

85.   The Ice Issue. *Winterwind. International Wind Energy Conference* (2014). Available at: http://winterwind.se/the-ice-issu.

86.   Lacroix, A. & Manwell, J. F. Wind energy: cold weather issues. *Univ. Massachusetts Amherst, Renew. Energy Lab.* (2000).

87.   McNeill, R. Winter Blasts Affecting Energy Output and Maintenance of Solar Panels. (2014). Available at: https://eponline.com/articles/2014/03/06/2014-winter-blasts.aspx.

88.   Cao, Y., Tan, W. & Wu, Z. Aircraft icing: An ongoing threat to aviation safety. *Aerosp. Sci. Technol.* **75**, 353–385 (2018).

89.   Ritter, S. What's that stuff?: Aircraft Deicers. *Chem. Eng. News* **79**, 30 (2001).

90.   Borrell, B. How does ice cause a plane to crash? (2009). Available at: https://www.scientificamerican.com/article/ice-flight-3407/.

91.   Kent, R. A., Andersen, D., Caux, P. Y. & Teed, S. Canadian water quality guidelines for glycols - An ecotoxicological review of glycols and associated aircraft anti-icing and deicing fluids. *Environ. Toxicol.* **14**, 481–522 (1999).

92.   Congdon, T., Notman, R. & Gibson, M. Antifreeze (Glyco)protein Mimetic Behavior of Poly(vinyl alcohol): Detailed Structure Ice Recrystallization Inhibition Activity Study. *Biomacromolecules* (2013). doi:dx.doi.org/10.1021/bm400217j

93.   Mitchell, D. E., Lilliman, M., Spain, S. G. & Gibson, M. I. Quantitative study on the antifreeze protein mimetic ice growth inhibition properties of poly(ampholytes) derived from vinyl-based polymers. *Biomater. Sci.* **2**, 1787–1795 (2014).

94.   Congdon, T. *et al.* Probing the Biomimetic Ice Nucleation Inhibition Activity of Poly(vinyl alcohol) and Comparison to Synthetic and Biological Polymers. *Biomacromolecules* **16**, 2820–2826 (2015).

95.   Mitchell, D. E., Cameron, N. R. & Gibson, M. I. Rational, yet simple, design and synthesis of an antifreeze-protein inspired polymer for cellular cryopreservation. *Chem. Commun.* **51**, 12977–12980 (2015).

96.   Biggs, C. I. *et al.* Polymer mimics of biomacromolecular antifreezes. *Nat. Commun.* **8**, 1–11 (2017).

97.   Stubbs, C., Congdon, T. R. & Gibson, M. I. Photo-polymerisation and study of the ice recrystallisation inhibition of hydrophobically modified poly(vinyl pyrrolidone) co-polymers. *Eur. Polym. J.* **110**, 330–336 (2019).

98.   Budke, C. & Koop, T. Ice recrystallization inhibition and molecular recognition of ice faces by poly(vinyl alcohol). *ChemPhysChem* **7**, 2601–2606 (2006).

99. Society, A. C. *et al.* Ice Recrystallization Inhibiting Polymers Enable Glycerol-Free Cryopreservation of Microorganisms. *Biomacromolecules* **19**, 3371–3376 (2018).

100. Mitchell, D. E. *et al.* Ice-recrystallization inhibiting polymers protect proteins against freeze-stress and enable glycerol-free cryostorage. *Mater. Horizons* **6**, 364–368 (2019).

101. Drori, R. *et al.* A Supramolecular Ice Growth Inhibitor. *J. Am. Chem. Soc.* **138**, 13396–13401 (2016).

102. Stubbs, C., Wilkins, L. E., Fayter, A. E. R., Walker, M. & Gibson, M. I. Multivalent Presentation of Ice Recrystallization Inhibiting Polymers on Nanoparticles Retains Activity. *Langmuir* acs.langmuir.8b01952 (2018). doi:10.1021/acs.langmuir.8b01952

103. Stubbs, C., Lipecki, J. & Gibson, M. I. Regioregular Alternating Polyampholytes Have Enhanced Biomimetic Ice Recrystallization Activity Compared to Random Copolymers and the Role of Side Chain versus Main Chain Hydrophobicity. *Biomacromolecules* **18**, 295–302 (2017).

104. Bai, G. *et al.* Oxidized Quasi-Carbon Nitride Quantum Dots Inhibit Ice Growth. *Adv. Mater.* **29**, (2017).

105. Li, T., Zhao, Y., Zhong, Q. & Wu, T. Inhibiting Ice Recrystallization by Nanocelluloses. *Biomacromolecules* **20**, acs.biomac.9b00027 (2019).

106. Dolev, M. B. *et al.* Ice-Binding Proteins and Their Function. *Annu. Rev. Biochem.* **85**, 515–542 (2016).

107. Mizrahy, O., Bar-Dolev, M., Guy, S. & Braslavsky, I. Inhibition of Ice Growth and Recrystallization by Zirconium Acetate and Zirconium Acetate Hydroxide. *PLoS One* **8**, (2013).

108. Wang, Z. *et al.* Bioinspired Cryoprotectants of Glucose-Based Carbon Dots. *ACS Appl. Bio Mater.* **3**, 3785–3791 (2020).

109. Braslavsky, I. & Drori, R. LabVIEW-operated Novel Nanoliter Osmometer for Ice Binding Protein Investigations. 1–6 (2013). doi:10.3791/4189

110. Haleva, L. *et al.* Microfluidic Cold-Finger Device for the Investigation of Ice-Binding Proteins. *Biophys. J.* (2016). doi:10.1016/j.bpj.2016.08.003

111. Inada, T. & Lu, S. Thermal hysteresis caused by non-equilibrium antifreeze activity of poly (vinyl alcohol). **394**, 361–365 (2004).

112. Amornwittawat, N., Wang, S., Duman, J. G. & Wen, X. Polycarboxylates enhance beetle antifreeze protein activity. *Biochim. Biophys. Acta - Proteins Proteomics* **1784**, 1942–1948 (2008).

113. Devries, A. L., Wilson, P. W. & Champaign, U. ANTIFREEZE GLYCOPROTEINS FROM THE ANTARCTIC FISH Dissostichus mawsoni STUDIED BY DIFFERENTIAL SCANNING CALORIMETRY (DSC) IN COMBINATION WITH NANOLITRE. **26**, 73–84 (2005).

114. Lu, M. *et al.* Differential scanning calorimetric and circular dichroistic studies on plant

antifreeze proteins. *J. Therm. Anal. Calorim.* (2002). doi:10.1023/A:1014369208229

115. Hill, J. O. *For Better Thermal Analysis and Calorimetry*. (1991).

116. Whale, T. F. *et al.* A technique for quantifying heterogeneous ice nucleation in microlitre supercooled water droplets. *Atmos. Meas. Tech.* **8**, 2437–2447 (2015).

117. Burkey, A. A., Riley, C. L., Wang, L. K., Hatridge, T. A. & Lynd, N. A. Understanding Poly(vinyl alcohol)-Mediated Ice Recrystallization Inhibition through Ice Adsorption Measurement and pH Effects. *Biomacromolecules* **19**, 248–255 (2018).

118. Knight, C. A. & Dumani, J. G. Inhibition of Recrystallization of Ice by Insect Thermal Hysteresis Proteins: A Possible Cryoprotective Role'. *Cryobiology* **23**, 256–262 (1986).

119. Wu, S. *et al.* Ion-specific ice recrystallization provides a facile approach for the fabrication of porous materials. *Nat. Commun.* **8**, 1–8 (2017).

120. Knight, C. A., Wen, D. & Laursen, R. A. Nonequilibrium antifreeze peptides and the recrystallization of ice. *Cryobiology* **32**, 23–34 (1995).

121. Worrall, D. *et al.* A carrot leucine-rich-repeat protein that inhibits ice recrystallization. *Science (80-.).* **282**, 115–117 (1998).

122. Tomczak, M. M., Marshall, C. B., Gilbert, J. A. & Davies, P. L. A facile method for determining ice recrystallization inhibition by antifreeze proteins. *Biochem. Biophys. Res. Commun.* **311**, 1041–1046 (2003).

123. Graham, L. A., Agrawal, P., Oleschuk, R. D. & Davies, P. L. High-capacity ice-recrystallization endpoint assay employing superhydrophobic coatings that is equivalent to the 'splat' assay. *Cryobiology* **81**, 138–144 (2018).

124. Olijve, L. L. C. C., Oude Vrielink, A. S. & Voets, I. K. A simple and quantitative method to evaluate ice recrystallization kinetics using the circle hough transform algorithm. *Cryst. Growth Des.* **16**, 4190–4195 (2016).

125. Huang, M. L. *et al.* Biomimetic peptoid oligomers as dual-action antifreeze agents. *Proc. Natl. Acad. Sci. U. S. A.* **109**, 19922–19927 (2012).

126. O'Sullivan, D. *et al.* The relevance of nanoscale biological fragments for ice nucleation in clouds. *Sci. Rep.* **5**, 1–7 (2015).

127. Hiranuma, N. *et al.* A comprehensive characterization of ice nucleation by three different types of cellulose particles immersed in water. *Atmos. Chem. Phys.* **19**, 4823–4849 (2019).

128. Murray, B. J., Ross, J. F., Webb, M. E., to, C. & dosullivan, S. The adsorption of fungal ice-nucleating proteins on mineral dusts: a terrestrial reservoir of atmospheric ice-nucleating particles. *Atmos. Chem. Phys* **16**, 7879–7887 (2016).

129. Yang, H. G. *et al.* Tuning ice nucleation with supercharged polypeptides. *Adv. Mater.* **28**, 5008–5012 (2016).

130. He, Z. *et al.* Tuning ice nucleation with counterions on polyelectrolyte brush surfaces. *Sci. Adv.* **2**, (2016).

131. Akhtar, N., Anemone, G., Farias, D. & Holst, B. Fluorinated graphene provides long lasting ice inhibition in high humidity. *Carbon N. Y.* **141**, 451–456 (2019).

132. Olijve, L. L. C. *et al.* Blocking rapid ice crystal growth through nonbasal plane adsorption of antifreeze proteins. *Proc. Natl. Acad. Sci. U. S. A.* **113**, 3740–3745 (2016).

133. Kim, H. J. *et al.* Marine Antifreeze Proteins: Structure, Function, and Application to Cryopreservation as a Potential Cryoprotectant. doi:10.3390/md15020027

134. Kristiansen, E., Pedersen, S. A. & Zachariassen, K. E. Salt-induced enhancement of antifreeze protein activity: A salting-out effect. *Cryobiology* (2008). doi:10.1016/j.cryobiol.2008.07.001

135. Wang, L. & Duman, J. G. A thaumatin-like protein from larvae of the beetle Dendroides canadensis enhances the activity of antifreeze proteins. *Biochemistry* **45**, 1278–1284 (2006).

136. Hawes, T. C. A root bond between ice and antifreeze protein. *Cryobiology* **73**, 147–151 (2016).

137. Stevens, C. A., Drori, R., Zalis, S., Braslavsky, I. & Davies, P. L. Dendrimer-linked antifreeze proteins have superior activity and thermal recovery. *Bioconjug. Chem.* **26**, 1908–1915 (2015).

138. Mahatabuddin, S. *et al.* Concentration-dependent oligomerization of an alpha-helical antifreeze polypeptide makes it hyperactive. *Sci. Rep.* **7**, 1–9 (2017).

139. Oolman, L. D. Freezing and Recrystallization of Ice. **308**, 1983–1984 (1984).

140. Caple, G. *et al.* Superadditive effects in mixtures of fish antifreeze glycoproteins and polyalcohols or surfactants. *J. Colloid Interface Sci.* **111**, 299–304 (1986).

141. Kametani, S., Tasei, Y., Nishimura, A. & Asakura, T. Distinct solvent-and temperature-dependent packing arrangements of anti-parallel b-sheet polyalanines studied with solid-state 13 C NMR and MD simulation. *Phys. Chem. Chem. Phys* doi:10.1039/c7cp03693k

142. Hachisu, M. *et al.* One-pot synthesis of cyclic antifreeze glycopeptides. *Chem. Commun.* 1641–1643 (2009). doi:10.1039/b815917c

143. Wierzbicki, A. *et al.* Structure - Function relationship in the antifreeze activity of synthetic alanine - Lysine antifreeze polypeptides. *Biomacromolecules* **1**, 268–274 (2000).

144. Zhang, W. & Laursen, R. A. Artificial antifreeze polypeptides: α-Helical peptides with KAAK motifs have antifreeze and ice crystal morphology modifying properties. *FEBS Lett.* **455**, 372–376 (1999).

145. Marshall, C. B., Daley, M. E., Sykes, B. D. & Davies, P. L. Enhancing the activity of a β-helical antifreeze protein by the engineered addition of coils. *Biochemistry* **43**, 11637–11646 (2004).

146. Phippen, S. W. ENGINEERING ANTIFREEZE PROTEIN MULTIMERS THROUGH GENETIC FUSION TO SELF-ASSEMBLING PROTEIN OLIGOMERS. (2017).

147. Can, Ö. & Holland, N. B. Conjugation of type i antifreeze protein to polyallylamine increases thermal hysteresis activity. *Bioconjug. Chem.* **22**, 2166–2171 (2011).

148. Can, Ö. & Holland, N. B. Utilizing avidity to improve antifreeze protein activity: A type III antifreeze protein trimer exhibits increased thermal hysteresis activity. *Biochemistry* **52**, 8745–8752 (2013).

149. Baardsnes, J., Kuiper, M. J. & Davies, P. L. Antifreeze protein dimer. When two ice-binding faces are better than one. *J. Biol. Chem.* **278**, 38942–38947 (2003).

150. Kim, M., Gwak, Y., Jung, W. & Jin, E. Identification and Characterization of an Isoform Antifreeze Protein from the Antarctic Marine Diatom, Chaetoceros neogracile and Suggestion of the Core Region. 82–32 (2017). doi:10.3390/md15100318

151. Tachibana, Y. *et al.* Antifreeze glycoproteins: Elucidation of the structural motifs that are essential for antifreeze activity. *Angew. Chemie - Int. Ed.* **43**, 856–862 (2004).

152. Phippen, S. W. *et al.* Multivalent Display of Antifreeze Proteins by Fusion to Self-Assembling Protein Cages Enhances Ice-Binding Activities. *Biochemistry* **55**, 6811–6820 (2016).

153. Tachibana, Y. *et al.* Antifreeze Glycoproteins: Elucidation of the Structural Motifs That Are Essential for Antifreeze Activity. *Angew. Chemie* **116**, 874–880 (2004).

154. Yu, S. O. *et al.* Ice restructuring inhibition activities in antifreeze proteins with distinct differences in thermal hysteresis. *Cryobiology* **61**, 327–334 (2010).

155. Mz, S., Am, F., Ia, N., Ali Q & Husnain T. COLD TOLERANCE OF PLANT ANTIFREEZE PROTEINS: A REVIEW. **6**, 1262–1275 (2017).

156. Ustun, N. S. & Turhan, S. ANTIFREEZE PROTEINS: CHARACTERISTICS, FUNCTION, MECHANISM OF ACTION, SOURCES AND APPLICATION TO FOODS. *J. Food Process. Preserv.* (2015). doi:10.1111/jfpp.12476

157. Capicciotti, C. J. *et al.* Small molecule ice recrystallization inhibitors enable freezing of human red blood cells with reduced glycerol concentrations. *Sci. Rep.* **5**, 1–10 (2015).

158. Hedir, G., Stubbs, C., Aston, P., Dove, A. P. & Gibson, M. I. Synthesis of Degradable Poly(vinyl alcohol) by Radical Ring-Opening Copolymerization and Ice Recrystallization Inhibition Activity. *ACS Macro Lett.* **6**, 1404–1408 (2017).

159. Vail, N. S., Stubbs, C., Biggs, C. I. & Gibson, M. I. Ultralow Dispersity Poly(vinyl alcohol) Reveals Significant Dispersity Effects on Ice Recrystallization Inhibition Activity. *ACS Macro Lett.* **6**, 1001–1004 (2017).

160. Stubbs, C., Bailey, T. L., Murray, K. & Gibson, M. I. Polyampholytes as Emerging Macromolecular Cryoprotectants. *Biomacromolecules* **21**, 7–17 (2020).

161. Stubbs, C., Murray, K. A., Ishibe, T., Mathers, R. T. & Gibson, M. I. Combinatorial Biomaterials Discovery Strategy to Identify New Macromolecular Cryoprotectants. *ACS Macro Lett.* 290–294 (2020). doi:10.1021/acsmacrolett.0c00044

162. Congdon, T. R., Notman, R. & Gibson, M. I. Synthesis of star-branched poly(vinyl

alcohol) and ice recrystallization inhibition activity. *Eur. Polym. J.* **88**, 320–327 (2017).

163. Congdon, T. R., Notman, R. & Gibson, M. I. Influence of Block Copolymerization on the Antifreeze Protein Mimetic Ice Recrystallization Inhibition Activity of Poly(vinyl alcohol). *Biomacromolecules* **17**, 3033–3039 (2016).

164. Phillips, D. J., Congdon, T. R. & Gibson, M. I. Activation of ice recrystallization inhibition activity of poly(vinyl alcohol) using a supramolecular trigger. *Polym. Chem.* (2016). doi:10.1039/C5PY01948F

165. MacDonald, M. J., Cornejo, N. R. & Gellman, S. H. Inhibition of Ice Recrystallization by Nylon-3 Polymers. *ACS Macro Lett.* (2017). doi:10.1021/acsmacrolett.7b00396

166. Inada, T. & Lu, S. S. Inhibition of recrystallization of ice grains by adsorption of poly(vinyl alcohol) onto ice surfaces. *Cryst. Growth Des.* **3**, 747–752 (2003).

167. Congdon, T., Notman, R. & Gibson, M. I. Antifreeze (Glyco)protein mimetic behavior of poly(vinyl alcohol): Detailed structure ice recrystallization inhibition activity study. *Biomacromolecules* **14**, 1578–1586 (2013).

168. Jin, S. *et al.* Spreading fully at the ice-water interface is required for high ice recrystallization inhibition activity. *Sci. China Chem.* **62**, 909–915 (2019).

169. Mousazadehkasin, M. & Tsavalas, J. G. Insights into Design of Biomimetic Glycerol-Grafted Polyol-Based Polymers for Ice Nucleation/Recrystallization Inhibition and Thermal Hysteresis Activity. *Biomacromolecules* (2020). doi:10.1021/acs.biomac.0c00907

170. Graham, B. *et al.* Polyproline as a Minimal Antifreeze Protein Mimic That Enhances the Cryopreservation of Cell Monolayers. *Angew. Chemie - Int. Ed.* **56**, 15941–15944 (2017).

171. Xue, B. *et al.* Bioinspired Ice Growth Inhibitors Based on Self-Assembling Peptides. *ACS Macro Lett.* **8**, 1383–1390 (2019).

172. Wu, L. K. *et al.* Carbohydrate-mediated inhibition of ice recrystallization in cryopreserved human umbilical cord blood. *Carbohydr. Res.* **346**, 86–93 (2011).

173. Capicciotti, C. J. *et al.* Potent inhibition of ice recrystallization by low molecular weight carbohydrate-based surfactants and hydrogelators. *Chem. Sci.* **3**, 1408–1416 (2012).

174. Qin, Q. *et al.* Bioinspired l-Proline Oligomers for the Cryopreservation of Oocytes via Controlling Ice Growth. *ACS Appl. Mater. Interfaces* **12**, 18352–18362 (2020).

175. Fan, Q. *et al.* Unraveling Molecular Mechanism on Dilute Surfactant Solution Controlled Ice Recrystallization. *Langmuir* **36**, 1691–1698 (2020).

176. Hua, W. *et al.* Ice Recrystallization Inhibition Activity of Protein Mimetic Peptoids. *J. Inorg. Organomet. Polym. Mater.* (2020). doi:10.1007/s10904-020-01673-9

177. Li, T. *et al.* Effect of surface charge density on the ice recrystallization inhibition activity of nanocelluloses. *Carbohydr. Polym.* **234**, 115863 (2020).

178. Li, T., Li, M., Zhong, Q. & Wu, T. Effect of Fibril Length on the Ice Recrystallization

Inhibition Activity of Nanocelluloses. *Carbohydr. Polym.* **240**, 116275 (2020).

179. Geng, H. *et al.* Graphene Oxide Restricts Growth and Recrystallization of Ice Crystals. *Angew. Chemie - Int. Ed.* **56**, 997–1001 (2017).

180. Georgiou, P. G., Kontopoulou, I., Congdon, T. R. & Gibson, M. I. Ice recrystallisation inhibiting polymer nano-objects: Via saline-tolerant polymerisation-induced self-assembly. *Mater. Horizons* **7**, 1883–1887 (2020).

181. Lee, J., Lee, S. Y., Lim, D. K., Ahn, D. J. & Lee, S. Antifreezing Gold Colloids. *J. Am. Chem. Soc.* **141**, 18682–18693 (2019).

182. Kiran-Yildirim, B., Hale, J., Wefers, D. & Gaukel, V. Ice recrystallization inhibition of commercial κ-, ι-, and λ-carrageenans. *J. Food Eng.* **290**, 1–7 (2021).

183. Gaukel, V., Leiter, A. & Spieß, W. E. L. Synergism of different fish antifreeze proteins and hydrocolloids on recrystallization inhibition of ice in sucrose solutions. *J. Food Eng.* **141**, 44–50 (2014).

184. Mitchell, D. E. & Gibson, M. I. Latent Ice Recrystallization Inhibition Activity in Nonantifreeze Proteins: Ca 2+ -Activated Plant Lectins and Cation-Activated Antimicrobial Peptides. *Biomacromolecules* (2015). doi:10.1021/acs.biomac.5b01118

185. Graham, B., Fayter, A. E. R. & Gibson, M. I. Synthesis of Anthracene Conjugates of Truncated Antifreeze Protein Sequences: Effect of the End Group and Photocontrolled Dimerization on Ice Recrystallization Inhibition Activity. *Biomacromolecules* **20**, 4611–4621 (2019).

186. Suris-Valls, R. & Voets, I. K. The Impact of Salts on the Ice Recrystallization Inhibition Activity of Antifreeze (Glyco) Proteins. (2019).

187. C Olijve, L. L. *et al.* Influence of Polymer Chain Architecture of Poly(vinyl alcohol) on the Inhibition of Ice Recrystallization. *Macromol. Chem. Phys.* **217**, 951–958 (2016).

188. Biggs, C. I. *et al.* Impact of sequential surface-modification of graphene oxide on ice nucleation. *Phys. Chem. Chem. Phys.* **19**, 21929–21932 (2017).

189. Mitchell, D. E., Congdon, T., Rodger, A. & Gibson, M. I. Gold Nanoparticle Aggregation as a Probe of Antifreeze (Glyco) Protein-Inspired Ice Recrystallization Inhibition and Identification of New IRI Active Macromolecules. *Sci. Rep.* **5**, 15716 (2015).

190. Whale, T. F., Rosillo-Lopez, M., Murray, B. J. & Salzmann, C. G. Ice Nucleation Properties of Oxidized Carbon Nanomaterials. *J. Phys. Chem. Lett.* **6**, 3012–3016 (2015).

191. Zhang, M., Gao, C., Ye, B., Tang, J. & Jiang, B. Effects of four disaccharides on nucleation and growth of ice crystals in concentrated glycerol aqueous solution. *Cryobiology* **86**, 47–51 (2019).

192. Leiter, A. *et al.* Influence of heating temperature, pressure and pH on recrystallization inhibition activity of antifreeze protein type III. *J. Food Eng.* **187**, 53–61 (2016).

193. Ren, R. *et al.* HSP70 improves the viability of cryopreserved Paeonia lactiflora pollen by regulating oxidative stress and apoptosis-like programmed cell death events. *Plant Cell,*

Tissue Organ Cult. (2019). doi:10.1007/s11240-019-01661-z

194. Leiter, A., Emmer, P. & Gaukel, V. Influence of gelation on ice recrystallization inhibition activity of κ-carrageenan in sucrose solution. (2016). doi:10.1016/j.foodhyd.2016.11.028

195. Evans, R. P., Hobbs, R. S., Goddard, S. V. & Fletcher, G. L. The importance of dissolved salts to the in vivo efficacy of antifreeze proteins. *Comp. Biochem. Physiol. - A Mol. Integr. Physiol.* **148**, 556–561 (2007).

196. Li, N., Andorfer, C. A. & Duman, J. G. Enhancement of Insect Antifreeze Protein Activity by Solutes of Low Molar Mass. *J. Exp. Biol.* **201**, 2243–2251 (1998).

197. Liu, Z., Li, H., Pang, H., Ma, J. & Mao, X. Enhancement effect of solutes of low molecular mass on the insect antifreeze protein ApAFP752 from Anatolica polita. *J. Therm. Anal. Calorim.* **120**, 307–315 (2015).

198. Balcerzak, A. K., Febbraro, M. & Ben, R. N. The importance of hydrophobic moieties in ice recrystallization inhibitors. *RSC Adv.* **3**, 3232–3236 (2013).

199. Amornwittawat, N. *et al.* Effects of polyhydroxy compounds on beetle antifreeze protein activity. *Biochim. Biophys. Acta - Proteins Proteomics* **1794**, 341–346 (2009).

200. Funakoshi, K., Inada, T., Kawabata, H. & Tomita, T. Cooperative function of ammonium polyacrylate with antifreeze protein type I. *Biomacromolecules* **9**, 3150–3156 (2008).

201. Berger, T. *et al.* Synergy between Antifreeze Proteins Is Driven by Complementary Ice-Binding. *J. Am. Chem. Soc.* **141**, 19144–19150 (2019).

202. Wu, D. W. & Duman, J. G. Activation of antifreeze proteins from larvae of the beetle Dendroides canadensis. *J. Comp. Physiol. B* **161**, 279–283 (1991).

203. Ishibe, T. *et al.* Enhancement of Macromolecular Ice Recrystallization Inhibition Activity by Exploiting Depletion Forces. *ACS Macro Lett.* **8**, 1063–1067 (2019).

204. Davies, P. L. *et al.* Structure and function of antifreeze proteins. *Philos. Trans. R. Soc. B Biol. Sci.* **357**, 927–935 (2002).

205. Wu, D. W., Duman, J. G. & Xu, L. Enhancement of insect antifreeze protein activity by antibodies. *Biochim. Biophys. Acta (BBA)/Protein Struct. Mol.* **1076**, 416–420 (1991).

206. Martino, M. N. & Zaritzky, N. E. Ice recrystallization in a model system and in frozen muscle tissue. *Cryobiology* **26**, 138–148 (1989).

207. Kurtz, S. K. & Carpay, F. M. A. Microstructure and normal grain growth in metals and ceramics. Part II. Experiment. *J. Appl. Phys.* **51**, 5745–5754 (1980).

208. Liou, Y.-C. Y.-C., Tocilj, A., DAvies, P. L. & Jia, Z. Mimicry of ice structure by surface hydroxyls and water of ab -helix antifreeze protein. *Nature* **406**, (2000).

209. Graether, S. P. *et al.* b-Helix structure and ice-binding properties of a hyperactive antifreeze protein from an insect. *Nat. www.nature.com* **406**, (2000).

210. Knight, C. A., Cheng, C. C. & DeVries, A. L. Adsorption of alpha-helical antifreeze

peptides on specific ice crystal surface planes. *Biophys. J.* **59**, 409–418 (1991).

211. Czechura, P., Tam, R. Y., Dimitrijevic, E., Murphy, A. V. & Ben, R. N. The importance of hydration for inhibiting ice recrystallization with C-linked antifreeze glycoproteins. *J. Am. Chem. Soc.* **130**, 2928–2929 (2008).

212. Budke, C. *et al.* Quantitative efficacy classification of ice recrystallization inhibition agents. *Cryst. Growth Des.* **14**, 4285–4294 (2014).

213. Kelly, S. M., Jess, T. J. & Price, N. C. How to study proteins by circular dichroism. *Biochim. Biophys. Acta - Proteins Proteomics* **1751**, 119–139 (2005).

214. Micsonai, A. *et al.* Accurate secondary structure prediction and fold recognition for circular dichroism spectroscopy. *Proc. Natl. Acad. Sci.* **112**, E3095–E3103 (2015).

215. Song, B., Cho, J. H. & Raleigh, D. P. Ionic-strength-dependent effects in protein folding: Analysis of rate equilibrium free-energy relationships and their interpretation. *Biochemistry* **46**, 14206–14214 (2007).

216. Dill, K. A. Dominant Forces in Protein Folding. *Biochemistry* **29**, 7133–7155 (1990).

217. Barth, H. G., Boyes, B. E. & Jackson, C. Size Exclusion Chromatography and Related Separation Techniques. *Anal. Chem.* **70**, 251–278 (1998).

218. Radzicka, A. & Wolfenden, R. Rates of uncatalyzed peptide bond hydrolysis in neutral solution and the transition state affinities of proteases. *J. Am. Chem. Soc.* **118**, 6105–6109 (1996).

219. Lawrence, L. & Moore, W. J. Kinetics of the Hydrolysis of Simple Glycine Peptides. *J. Am. Chem. Soc.* **73**, 3973–3977 (1951).

220. Feeney, E. P., Guinee, T. P. & Fox, P. F. Effect of pH and calcium concentration on proteolysis in Mozzarella cheese. *J. Dairy Sci.* **85**, 1646–1654 (2002).

221. Bar, M., Bar-Ziv, R., Scherf, T. & Fass, D. Effcient production of a folded and functional, highly disulfide-bonded -helix antifreeze protein in bacteria. *Protein Expr. PuriWcation* **48**, 243–252 (2006).

222. Garnham, C. P. *et al.* A Ca2+-dependent bacterial antifreeze protein domain has a novel beta-helical ice-binding fold. *Biochem. J.* **411**, 171–80 (2008).

223. Liang, S. *et al.* Effect of antifreeze glycoprotein 8 supplementation during vitrification on the developmental competence of bovine oocytes. *Theriogenology* **86**, 485-494.e1 (2015).

224. Powers, T. C. Freezing effects in concrete. *Spec. Publ.* **47**, 1–12 (1975).

225. Chao, H., Sönnichsen, F. D., DeLuca, C. I., Sykes, B. D. & Davies, P. L. Structure-function relationship in the globular type III antifreeze protein: identification of a cluster of surface residues required for binding to ice. *Protein Sci.* **3**, 1760–9 (1994).

226. Gauthier, S. Y., Kay, C. M., Sykes, B. D., Walker, V. K. & Davies, P. L. Disulfide bond mapping and structural characterization of spruce budworm antifreeze protein. *Eur. J. Biochem.* (1998). doi:10.1046/j.1432-1327.1998.2580445.x

227. Kristiansen, E. & Zachariassen, K. E. The mechanism by which fish antifreeze proteins cause thermal hysteresis. (2005). doi:10.1016/j.cryobiol.2005.07.007

228. Middleton, A. J., Brown, A. M., Davies, P. L. & Walker, V. K. Identification of the ice-binding face of a plant antifreeze protein. *FEBS Lett.* **583**, 815–819 (2009).

229. Hoshino, T. *et al.* Antifreeze proteins from snow mold fungi. *Can. J. Bot.* **81**, 1175–1181 (2003).

230. Liou, Y.-C. *et al.* Folding and Structural Characterization of Highly Disulfide-bonded Beetle Antifreeze Protein Produced in Bacteria. *Protein Expr. Purif.* **19**, 148–157 (2000).

231. Braslavsky, I., Dolev, M. B., Bernheim, R., Guo, S. & Davies, P. L. Putting life on ice: bacteria that bind to frozen water. doi:10.1098/rsif.2016.0210

232. Vance, T. D. R. *et al.* Ca2+-stabilized adhesin helps an Antarctic bacterium reach out and bind ice. *Biosci. Rep.* **34**, e00121 (2014).

233. Fiala, G. J., Schamel, W. W. A. & Blumenthal, B. Blue native polyacrylamide gel electrophoresis (BN-PAGE) for analysis of multiprotein complexes from cellular lysates. *J. Vis. Exp.* 1–8 (2010). doi:10.3791/2164

234. Krause, F. & Seelert, H. *Detection and Analysis of Protein-Protein Interactions of Organellar and Prokaryotic Proteomes by Blue Native and Colorless Native Gel Electrophoresis*. *Current Protocols in Protein Science* (2008). doi:10.1002/0471140864.ps1411s51

235. Buck, R. P., Singhadeja, S. & Rogers, L. B. Ultraviolet Absorption Spectra of Some Inorganic Ions in Aqueous Solutions. *Anal. Chem.* **26**, 1240–1242 (1954).

236. Bar-Dolev, M., Celik, Y., Wettlaufer, J. S., Davies, P. L. & Braslavsky, I. New insights into Ice growth and melting modifications by antifreeze proteins. *J. R. Soc. Interface* **9**, 3249–3259 (2012).

237. Williams, A. P. Amino Acids | Determination. in *Encyclopedia of Food Sciences and Nutrition* 192–197 (Academic, 2003).

238. Guo, S., Garnham, C. P., Whitney, J. C., Graham, L. A. & Davies, P. L. Re-evaluation of a bacterial antifreeze protein as an adhesin with ice-binding activity. *PLoS One* **7**, e48805 (2012).

239. Duignan, T. T., Parsons, D. F. & Ninham, B. W. Collins's rule, Hofmeister effects and ionic dispersion interactions. *Chem. Phys. Lett.* **608**, 55–59 (2014).

240. Surís-Valls, R. & Voets, I. K. Peptidic antifreeze materials: Prospects and challenges. *Int. J. Mol. Sci.* **20**, (2019).

241. Pettersen, E. F. *et al.* UCSF Chimera - A visualization system for exploratory research and analysis. *J. Comput. Chem.* **25**, 1605–1612 (2004).

242. Xu, H. *et al.* Interfacial Adsorption of Antifreeze Proteins: A Neutron Reflection Study. *Biophys. J.* **94**, 4405–4413 (2008).

243. Xia, X. Protein isoelectric point. *Bioinforma. Cell* 207–219 (2007). doi:10.1007/978-0-387-71337-3_10

244. Margesin, R. *Psychrophiles: From Biodiversity to Biotechnology: Second Edition. Psychrophiles: From Biodiversity to Biotechnology: Second Edition* (2017). doi:10.1007/978-3-319-57057-0

245. Frazier, S. D. *et al.* Inhibiting Freeze-Thaw Damage in Cement Paste and Concrete by Mimicking Nature's Antifreeze. *Cell Reports Phys. Sci.* **1**, 100060 (2020).

246. Qu, Z. *et al.* Enhancing the Freeze-Thaw Durability of Concrete through Ice Recrystallization Inhibition by Poly(vinyl alcohol). *ACS Omega* **5**, 12825–12831 (2020).

247. Alegre-Cebollada, J., Badilla, C. L. & Fernández, J. M. Isopeptide bonds block the mechanical extension of pili in pathogenic Streptococcus pyogenes. *J. Biol. Chem.* **285**, 11235–11242 (2010).

248. Bonds, S. I. *et al.* Revealed in Gram-Positive. *Science (80-.).* **318**, 1625–1628 (2007).

249. Kang, H. J. & Baker, E. N. Intramolecular isopeptide bonds give thermodynamic and proteolytic stability to the major Pilin protein of Streptococcus pyogenes. *J. Biol. Chem.* **284**, 20729–20737 (2009).

250. Zakeri, B. Synthetic Biology: A New Tool for the Trade. *ChemBioChem* **16**, 2277–2282 (2015).

251. Stubbs, C., Bailey, T. L., Murray, K. & Gibson, M. I. Polyampholytes as Emerging Macromolecular Cryoprotectants Polyampholytes as Emerging Macromolecular Cryoprotectants. (2019). doi:10.1021/acs.biomac.9b01053

252. Monteiro, P. J. M., Miller, S. A. & Horvath, A. Towards sustainable concrete. *Nat. Mater.* **16**, 698–699 (2017).

253. Miller, S. A., Horvath, A. & Monteiro, P. J. M. Impacts of booming concrete production on water resources worldwide. *Nat. Sustain.* **1**, 69–76 (2018).

254. Valenza, J. J. & Scherer, G. W. A review of salt scaling: II. Mechanisms. *Cem. Concr. Res.* **37**, 1022–1034 (2007).

255. Jones, P. & Jaffray, B. A. Chapter 3: Effects of deicing materials on natural resources, vehicles, and highway infrastructure. *use Sel. deicing Mater. Michigan roads Environ. Econ. impacts* 26–32 (1982). doi:10.1007/s13398-014-0173-7.2

256. Wong, H. S., Pappas, A. M., Zimmerman, R. W. & Buenfeld, N. R. Effect of entrained air voids on the microstructure and mass transport properties of concrete. *Cem. Concr. Res.* **41**, 1067–1077 (2011).

257. Hudait, A., Odendahl, N., Qiu, Y., Paesani, F. & Molinero, V. Ice-Nucleating and Antifreeze Proteins Recognize Ice through a Diversity of Anchored Clathrate and Ice-like Motifs. *J. Am. Chem. Soc.* **140**, jacs.8b01246 (2018).

258. Chang, J. . *et al. Biopolymers - PVA hydrogels, Anionic Polymerisation, Nanocomposites*. (springer, 2000).

259. Peppas, N. A. & Stauffer, S. R. Reinforced uncrosslinked poly (vinyl alcohol) gels produced by cyclic freezing-thawing processes: a short review. *J. Control. Release* **16**, 305–310 (1991).

260. Lozinsky, V. I. Cryotropic gelation of poly(vinyl alcohol) solutions. *Usp. Khim.* **67**, 651–655 (1998).

261. Lide, D. R. *Handbook of Chemistry and Physics*. (CRC Press, 1991).

262. Ebbesen, M. F., Schaffert, D. H., Crowley, M. L., Oupický, D. & Howard, K. A. Synthesis of click-reactive HPMA copolymers using RAFT polymerization for drug delivery applications. *J. Polym. Sci. Part A Polym. Chem.* **51**, 5091–5099 (2013).

263. Fitzkee, N. C. & Rose, G. D. Reassessing random-coil statistics in unfolded proteins. *Proc. Natl. Acad. Sci. U. S. A.* **101**, 12497–12502 (2004).

264. Smith, L. J., Fiebig, K. M., Schwalbe, H. & Dobson, C. M. The concept of a random coil : Residual structure in peptides and denatured proteins. *Fold. Des.* **1**, 95–106 (1996).

265. Flory, P. J. *Principles of polymer chemistry*. (Cornell University Press, 1953).

266. OBrien, J. T. & Williams, E. R. Effects of ions on hydrogen-bonding water networks in large aqueous nanodrops. *J. Am. Chem. Soc.* **134**, 10228–10236 (2012).

267. Marcus, Y. & Hefter, G. Ion pairing. *Chem. Rev.* **106**, 4585–4621 (2006).

268. Bailey, T. L. *et al.* A Synthetically Scalable Poly(ampholyte) which Dramatically Enhances Cellular Cryopreservation. *Biomacromolecules* acs.biomac.9b00681 (2019). doi:10.1021/acs.biomac.9b00681

269. Matsumura, K. *et al.* Cryopreservation of a Two-Dimensional Monolayer Using a Slow Vitrification Method with Polyampholyte to Inhibit Ice Crystal Formation. *ACS Biomater. Sci. Eng.* **2**, 1023–1029 (2016).

270. Matsumura, S. *et al.* Ionomers for proton exchange membrane fuel cells with sulfonic acid groups on the end-groups: Novel branched poly(ether-ketone)s. *Am. Chem. Soc. Polym. Prepr. Div. Polym. Chem.* **49**, 511–512 (2008).

271. Matsumura, K., Bae, J. Y., Kim, H. H. & Hyon, S. H. Effective vitrification of human induced pluripotent stem cells using carboxylated ε-poly-l-lysine. *Cryobiology* **63**, 76–83 (2011).

272. Zavitsas, A. A. The nature of aqueous solutions: Insights into multiple facets of chemistry and biochemistry from freezing-point depressions. *Chem. - A Eur. J.* **16**, 5942–5960 (2010).

273. Celik, Y. *et al.* Freezing and Melting Hysteresis Measurements in Solutions of Hyperactive Antifreeze Protein from an Antarctic Bacteria.

274. Knight, C. A., DeVries, A. L. Melting Inhibition and Superheating of Ice by an Antifreeze Glycopeptide. *Science (80-.).* **245**, 505–507 (1989).

275. Carignano, M. A., Baskaran, E., Shepson, P. B. & Szleifer, I. Molecular dynamics

simulation of ice growth from supercooled pure water and from salt solution. *Ann. Glaciol.* **44**, 113–117 (2006).

276. Adams, G., Fahy, G. M. & Wowk, B. *Cryopreservation and Freeze-Drying Protocols; Principles of Cryopreservation by Vitrification*. **1257**, (2015).

277. Jang, T. H. *et al.* Cryopreservation and its clinical applications | Elsevier Enhanced Reader. *Integr. Med. Res.* **6**, 12–18 (2017).

278. Tavukcuoglu, S., Al-Azawi, T., Khaki, A. A. & Al-Hasani, S. Is vitrification standard method of cryopreservation. *Middle East Fertil. Soc. J.* **17**, 152–156 (2012).

279. Cheng, Y., Zeng, Q., Han, Q. & Xia, W. Effect of pH, temperature and freezing-thawing on quantity changes and cellular uptake of exosomes. *Protein Cell* **10**, 295–299 (2019).

280. Mochida, K. *et al.* High Osmolality Vitrification: A New Method for the Simple and Temperature-Permissive Cryopreservation of Mouse Embryos. *PLoS One* **8**, 2–9 (2013).

281. Graham, B., Fayter, A. E. R. R., Houston, J. E., Evans, R. C. & Gibson, M. I. Facially Amphipathic Glycopolymers Inhibit Ice Recrystallization. *J. Am. Chem. Soc.* **140**, 5682–5685 (2018).

282. Kelting, D. L. & Laxson, C. L. Review of Effects and Costs of Road De-icing with Recommendations for Winter Road Management in the Adirondack Park. *ADKaction.org* 76 (2010).

283. Destarac, M. Industrial development of reversible-deactivation radical polymerization: Is the induction period over? *Polym. Chem.* **9**, 4947–4967 (2018).

APPENDIX A

Raw Differential Scanning Calorimetry Data for Determining the Melting Point and Enthalpy of Crystallization

Figure A1. Raw DSC melting curves for blank PBS.

Figure A2. Raw DSC melting curves for threonine in PBS at concentrations of (a) 0.001 mg/ml, (b) 0.01 mg/ml, (c) 0.1 mg/ml, (d) 1 mg/ml, and (e) 10 mg/ml.
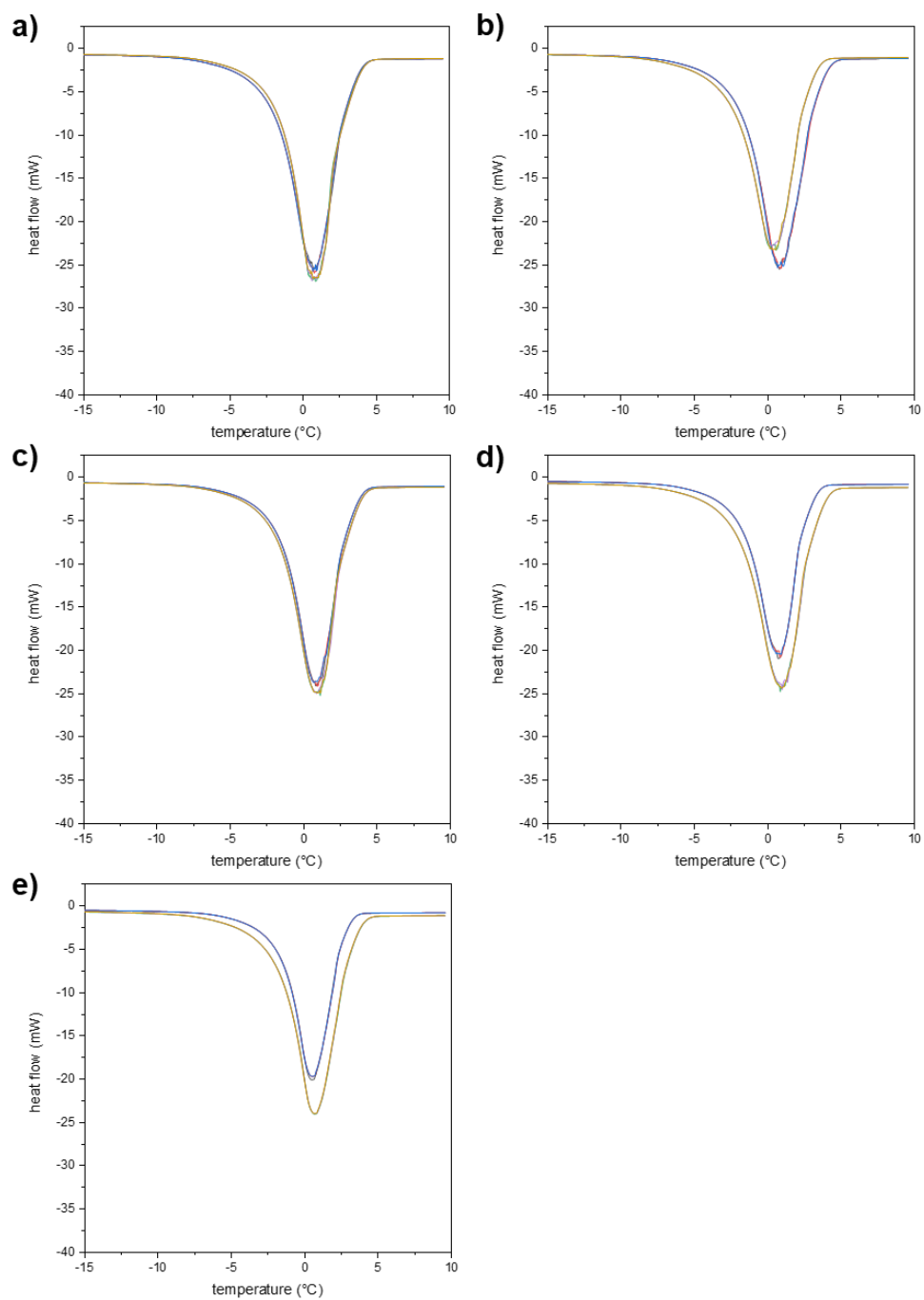
Figure A3. Raw DSC melting curves for poly(threonine) in PBS at concentrations of (a) 0.001 mg/ml, (b) 0.01 mg/ml, (c) 0.1 mg/ml, (d) 1 mg/ml, and (e) 10 mg/ml.
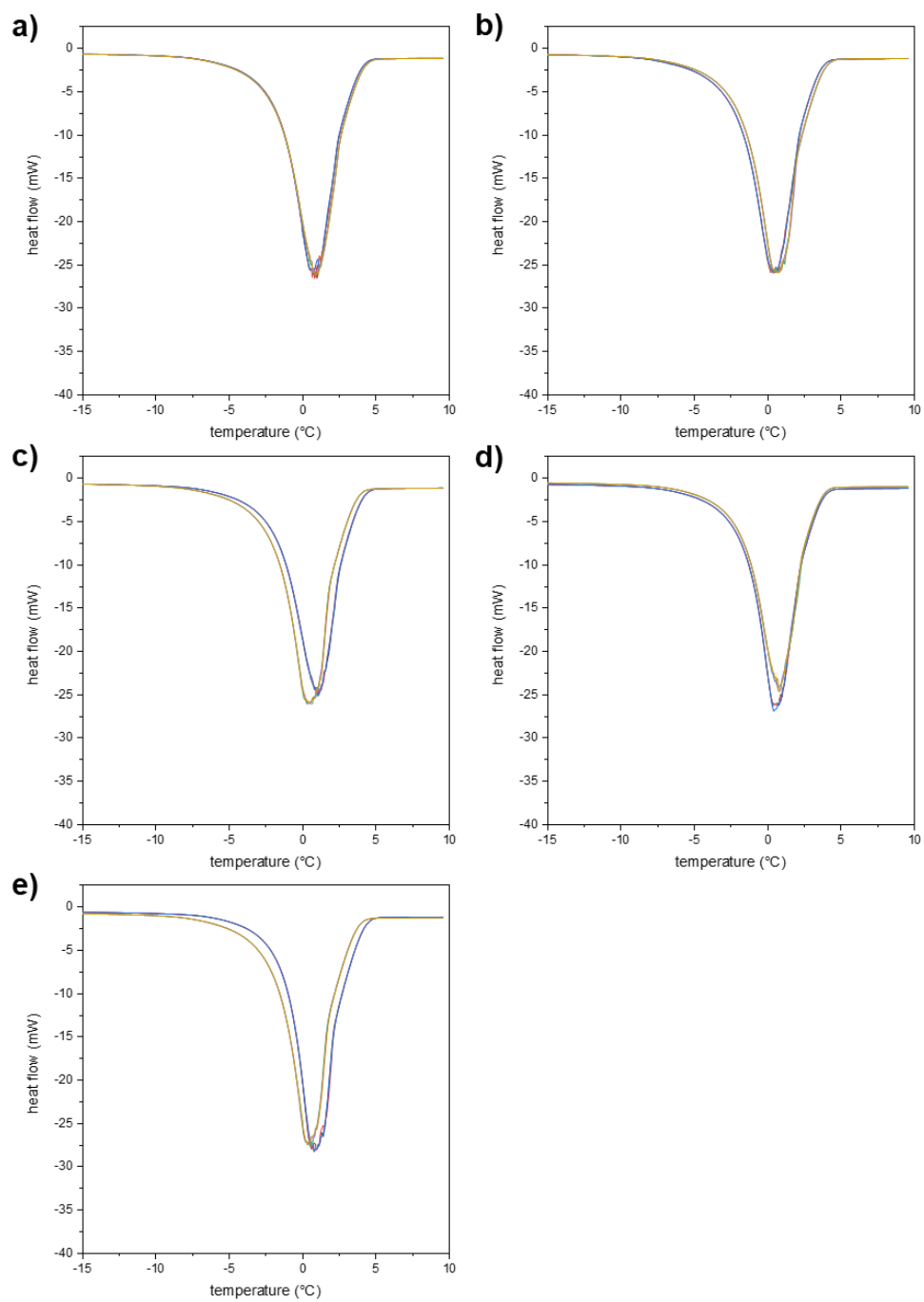
Figure A4. Raw DSC melting curves arginine in PBS at concentrations of (a) 0.001 mg/ml, (b) 0.01 mg/ml, (c) 0.1 mg/ml, (d) 1 mg/ml, and (e) 10 mg/ml.
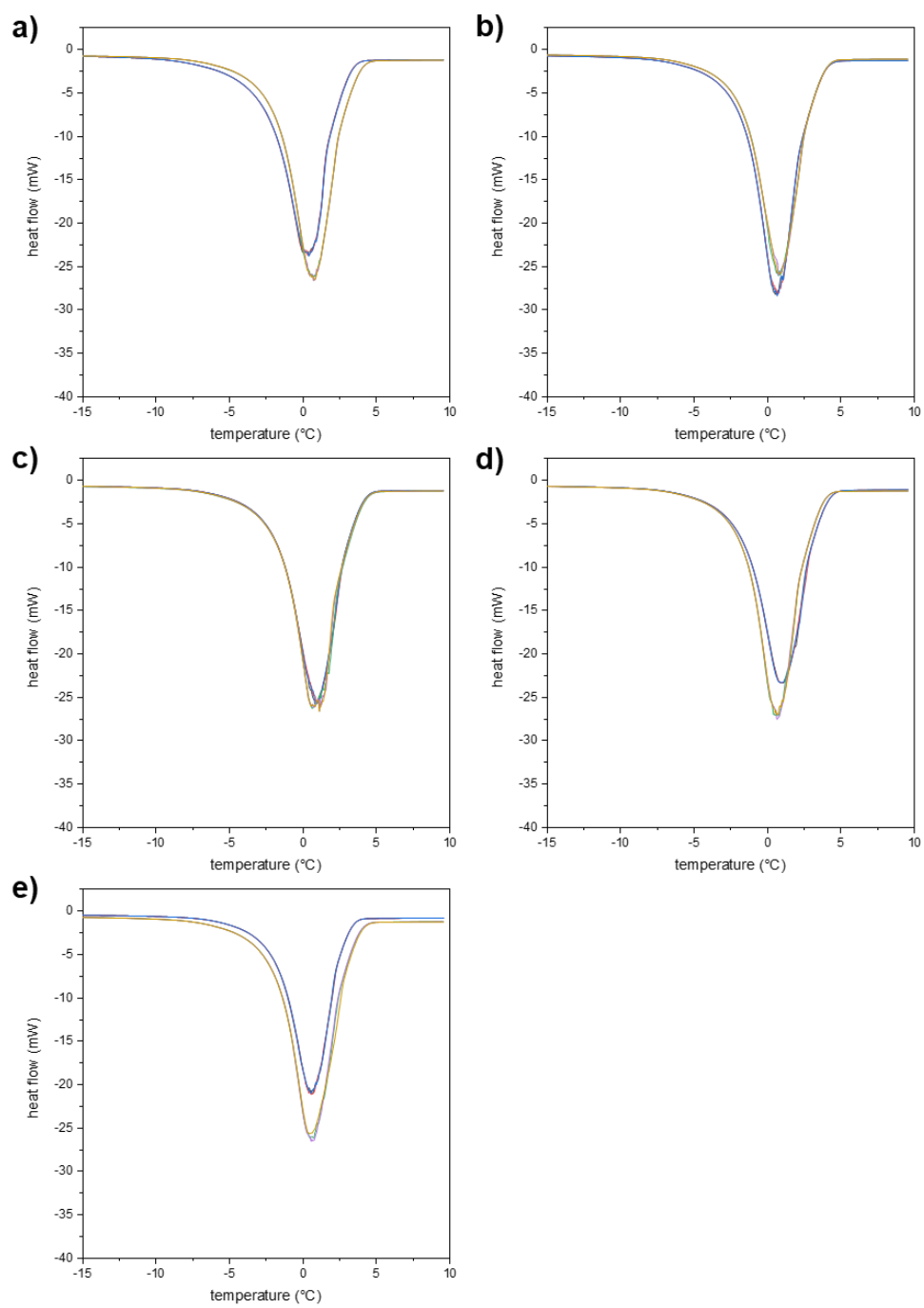
Figure A5. Raw DSC melting curves for poly(arginine) in PBS at concentrations of (a) 0.001 mg/ml, (b) 0.01 mg/ml, (c) 0.1 mg/ml, (d) 1 mg/ml, and (e) 10 mg/ml.
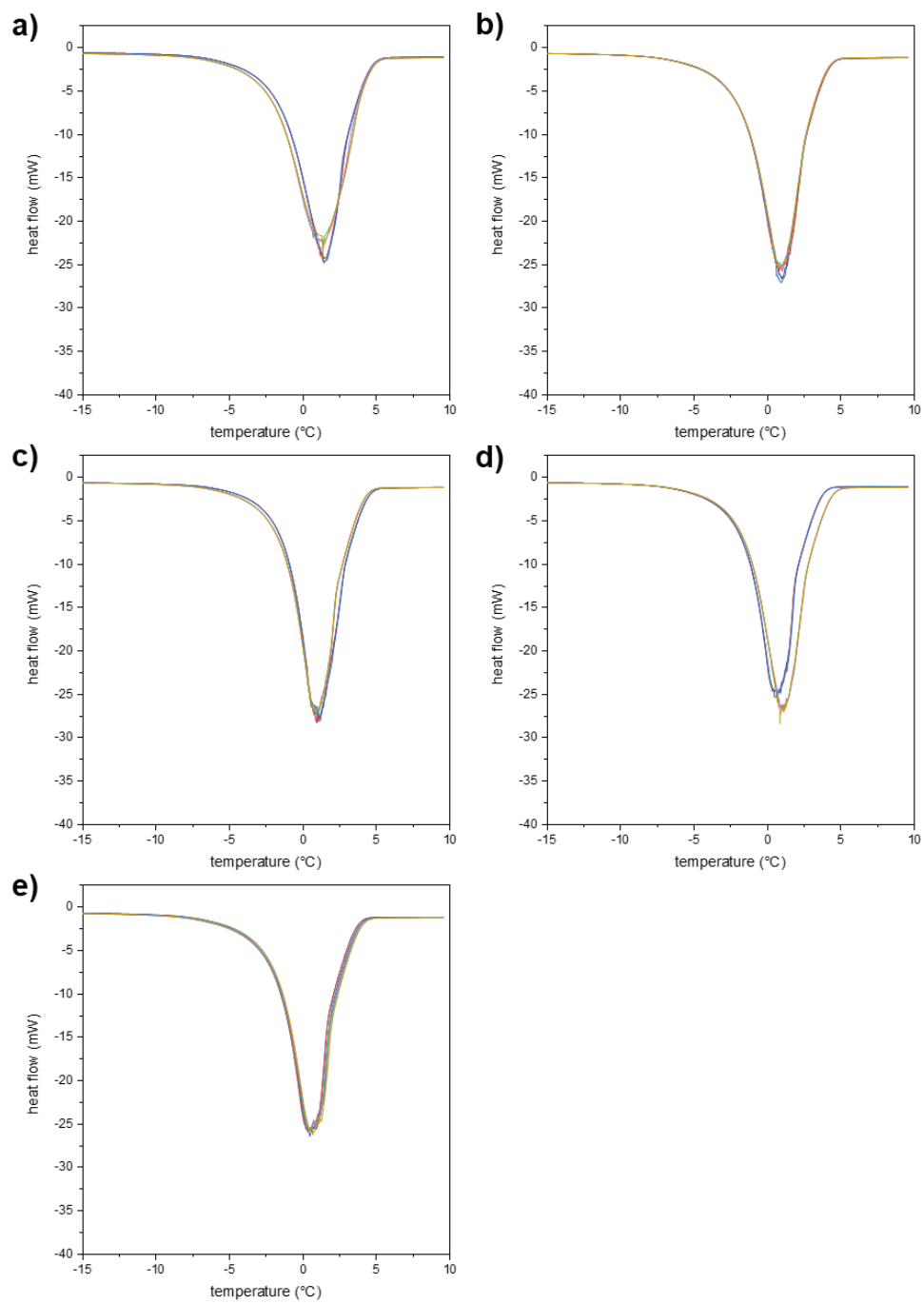
Figure A6. Raw DSC melting curves for glutamic acid in PBS at concentrations of (a) 0.001 mg/ml, (b) 0.01 mg/ml, (c) 0.1 mg/ml, (d) 1 mg/ml, and (e) 8.6 mg/ml.
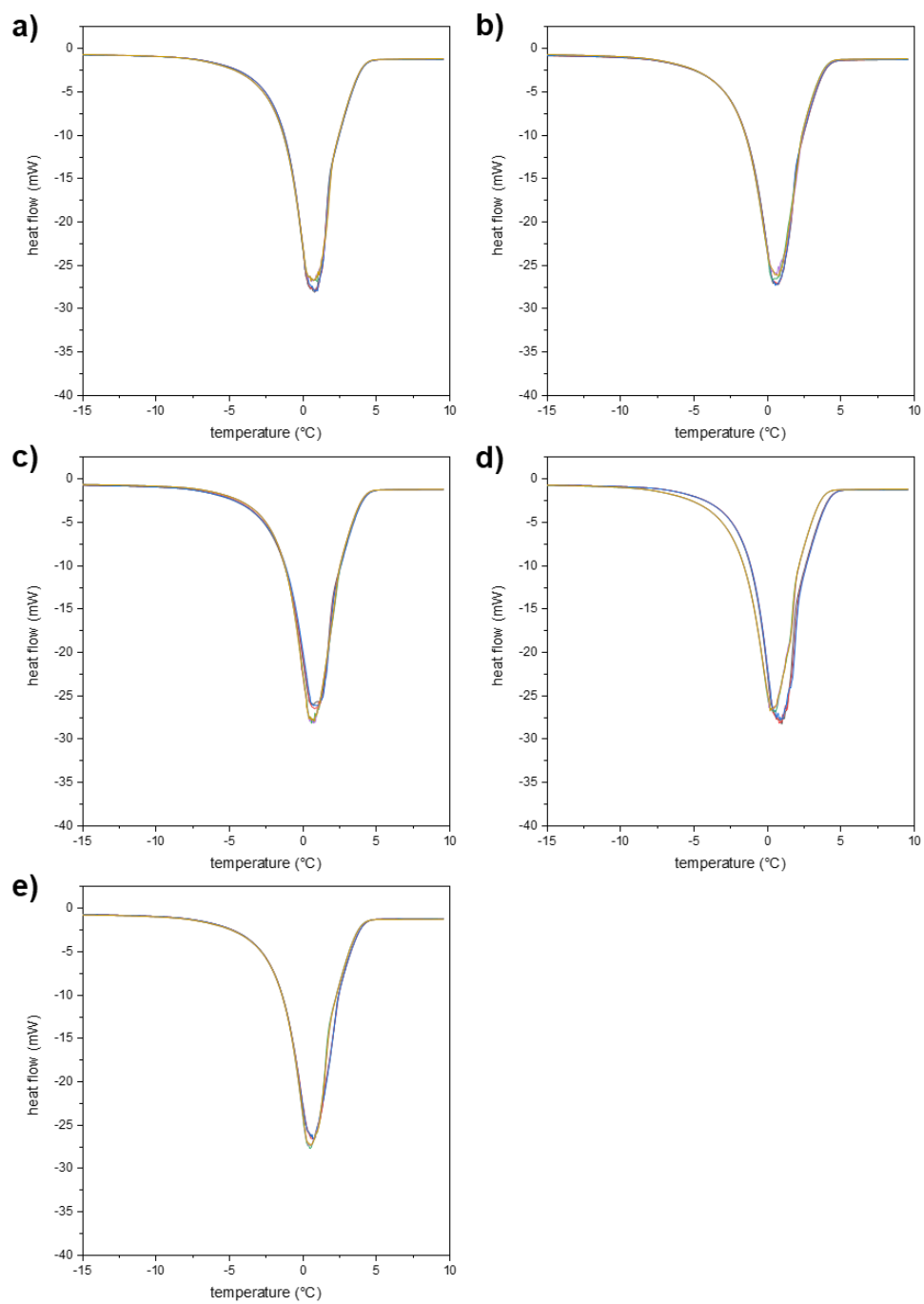
Figure A7. Raw DSC melting curves for poly(glutamic acid) in PBS at concentrations of (a) 0.001 mg/ml, (b) 0.01 mg/ml, (c) 0.1 mg/ml, (d) 1 mg/ml, and (e) 10 mg/ml.
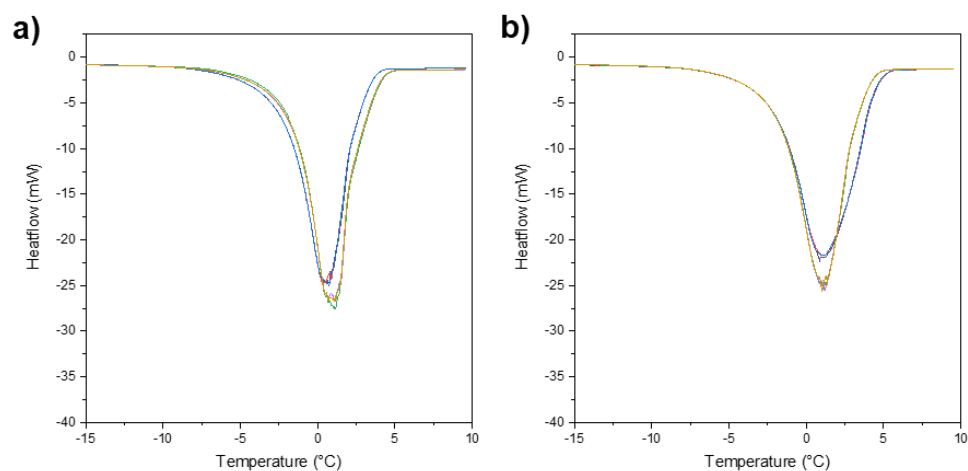
Figure A8. Raw DSC melting curves for (a) HPMA and (b) pHPMA at 10 mg/ml in PBS.
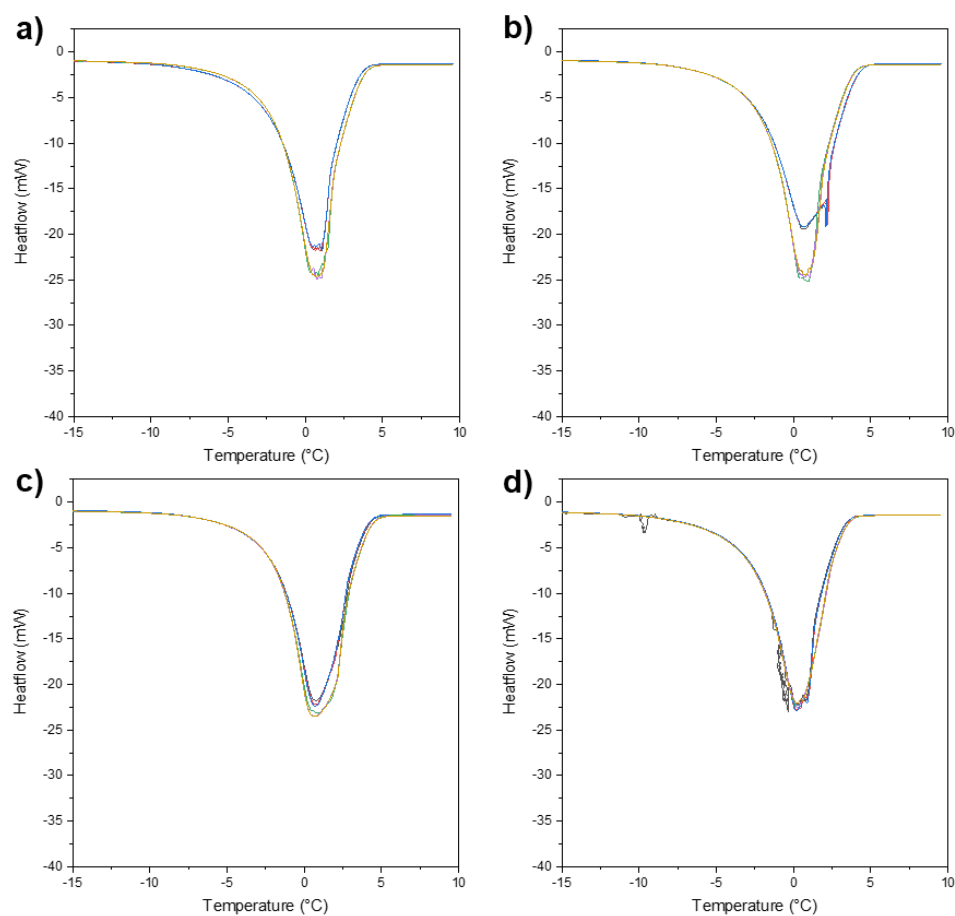
Figure A9. Raw DSC melting curves for blank (a) 151.5 mM $CaCl_2$, (b) 151.5 mM $MgCl_2$, (c) 151.5 mM $CuCl_2$, and (d) 151.5 mM $AlCl_3$.
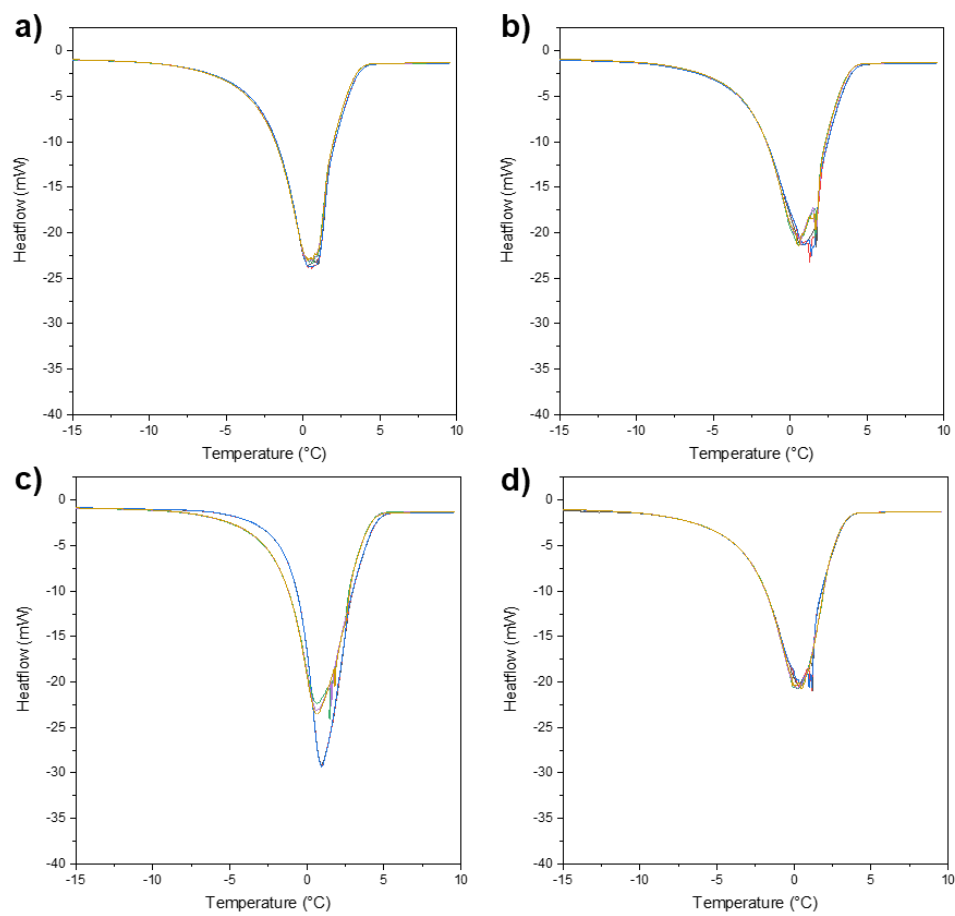
Figure A10. Raw DSC melting curves for threonine at 10 mg/ml (a) 151.5 mM $CaCl_2$, (b) 151.5 mM $MgCl_2$, (c) 151.5 mM $CuCl_2$, and (d) 151.5 mM $AlCl_3$.
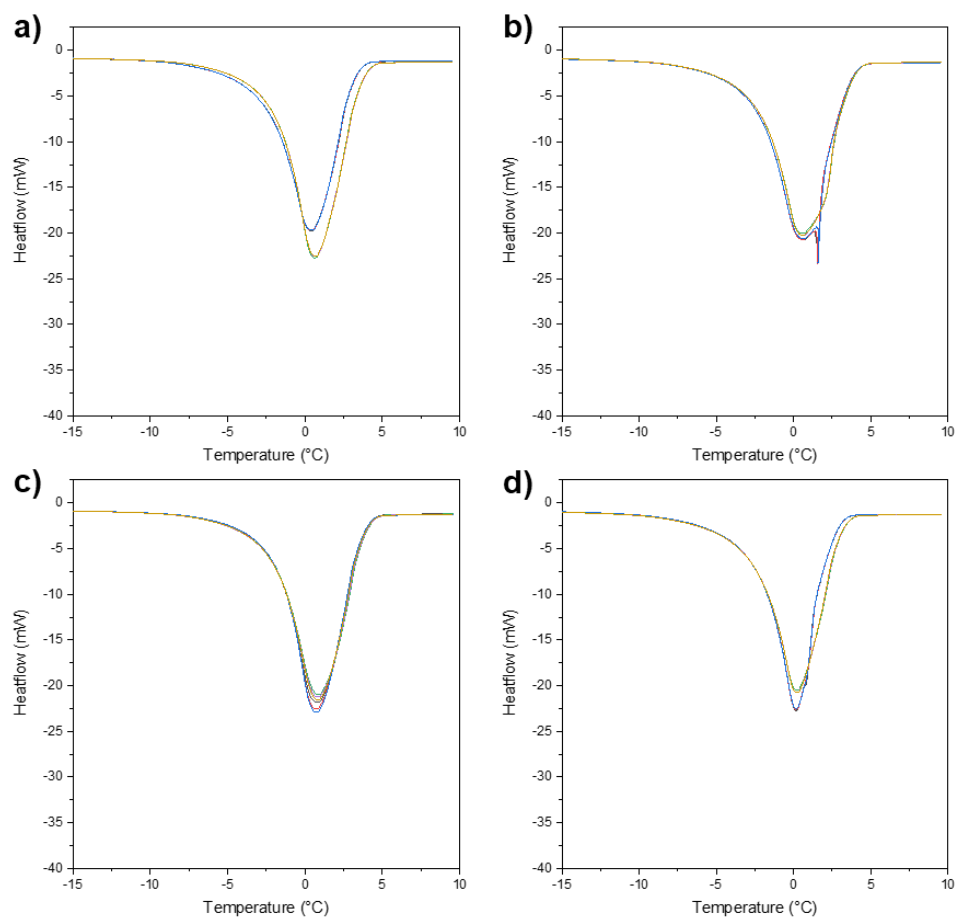
Figure A11. Raw DSC melting curves for poly(threonine) at 10 mg/ml in (a) 151.5 mM CaCl$_2$, (b) 151.5 mM MgCl$_2$, (c) 151.5 mM CuCl$_2$, and (d) 151.5 mM AlCl$_3$.
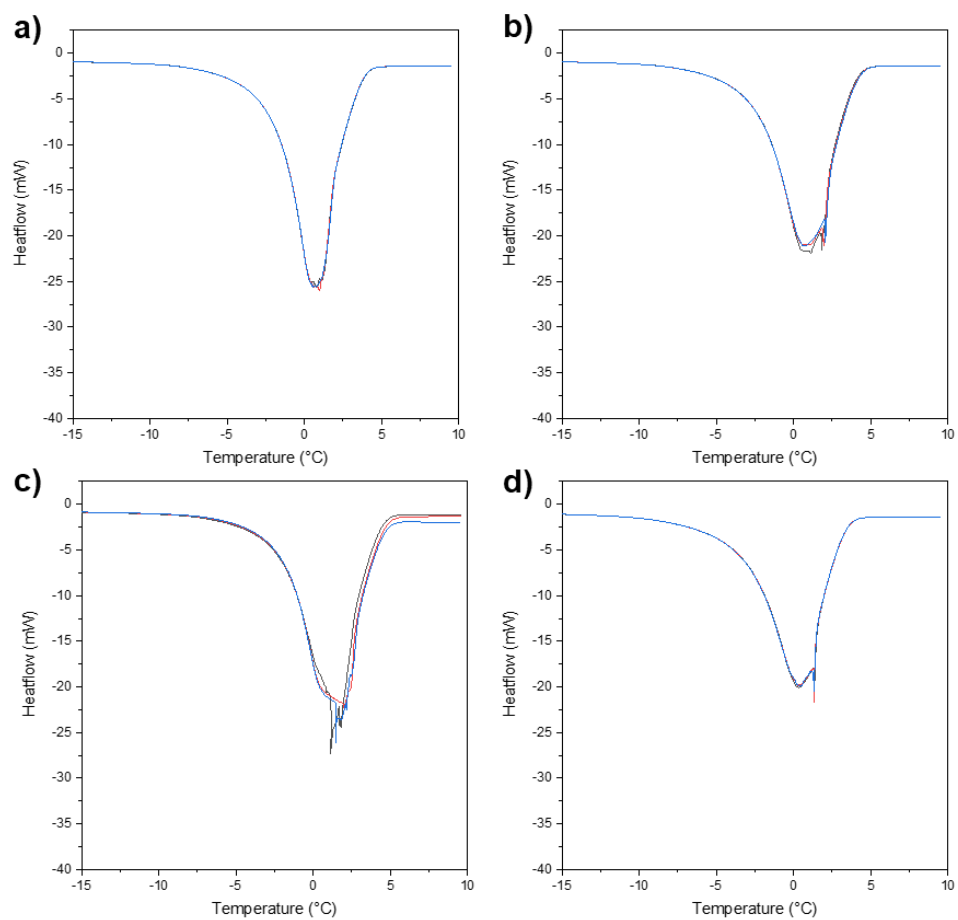
Figure A12. Raw DSC melting curves for arginine at 10 mg/ml (a) 151.5 mM $CaCl_2$, (b) 151.5 mM $MgCl_2$, (c) 151.5 mM $CuCl_2$, and (d) 151.5 mM $AlCl_3$.
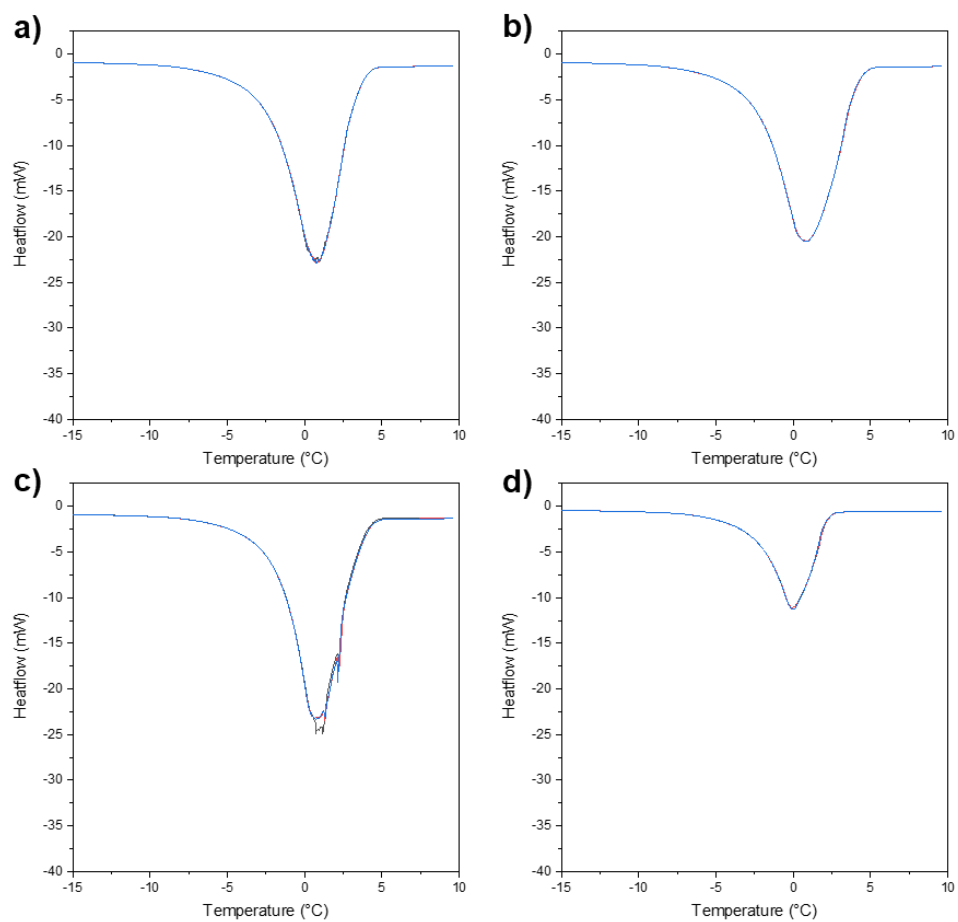
Figure A13. Raw DSC melting curves for poly(arginine) at 10 mg/ml (a) 151.5 mM $CaCl_2$, (b) 151.5 mM $MgCl_2$, (c) 151.5 mM $CuCl_2$, and (d) 151.5 mM $AlCl_3$.
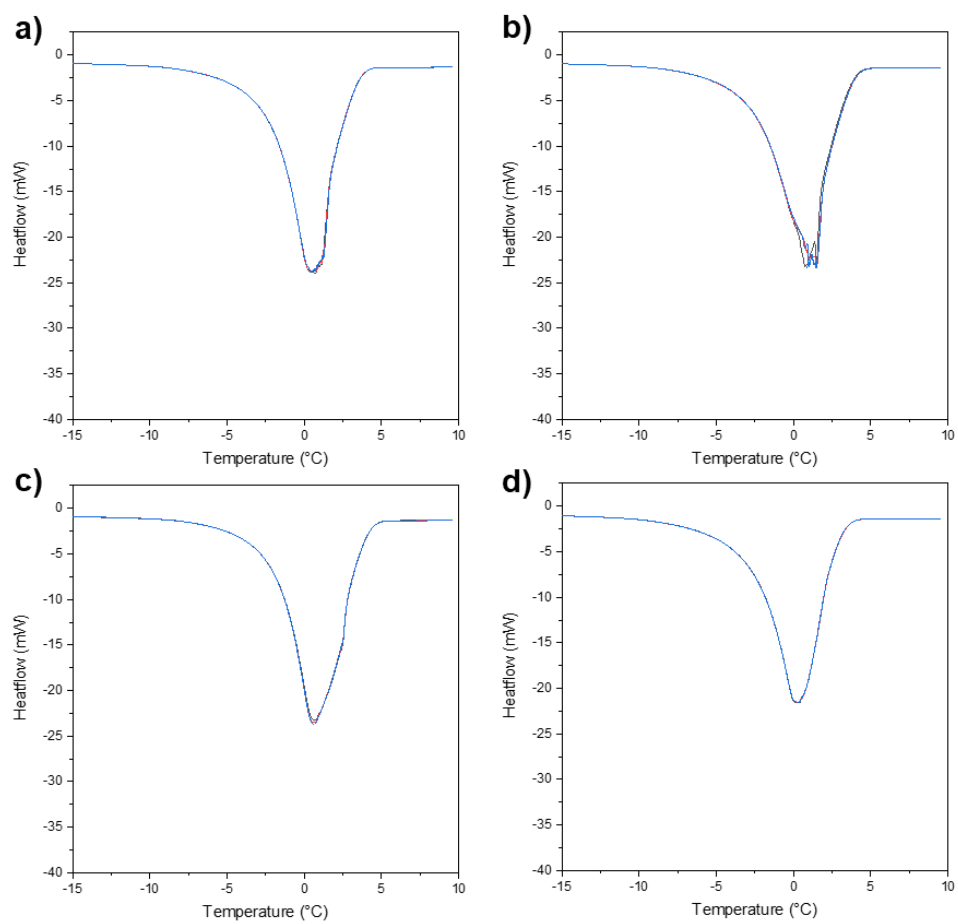
Figure A14. Raw DSC melting curves for glutamic acid at 10 mg/ml (a) 151.5 mM $CaCl_2$, (b) 151.5 mM $MgCl_2$, (c) 151.5 mM $CuCl_2$, and (d) 151.5 mM $AlCl_3$.
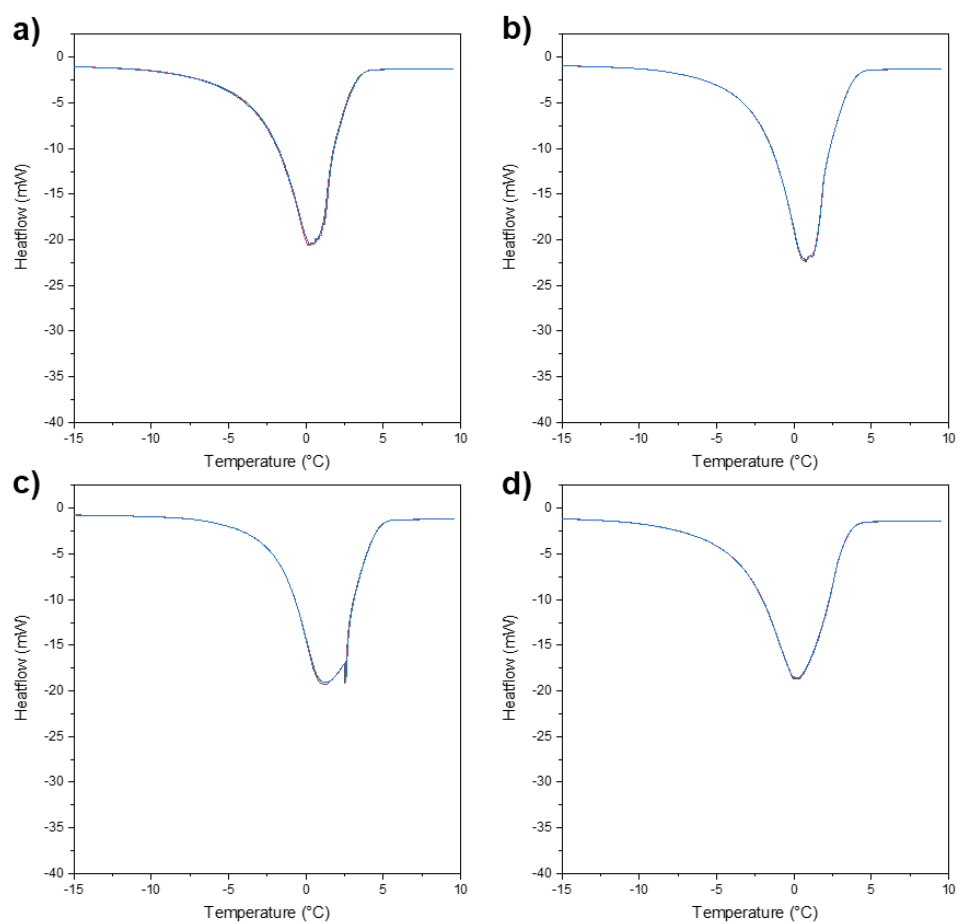
Figure A15. Raw DSC melting curves for poly(glutamic acid) at 10 mg/ml (a) 151.5 mM $CaCl_2$, (b) 151.5 mM $MgCl_2$, (c) 151.5 mM $CuCl_2$, and (d) 151.5 mM $AlCl_3$.
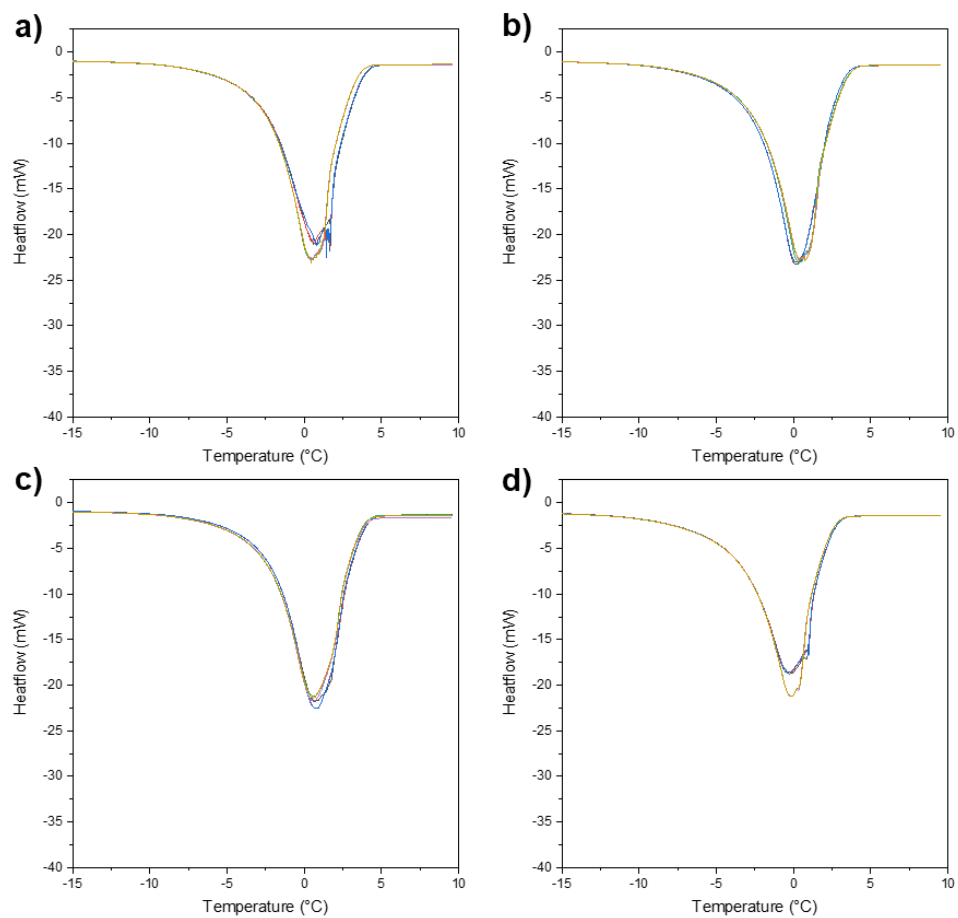
Figure A16. Raw DSC melting curves for HPMA at 10 mg/ml (a) 151.5 mM $CaCl_2$, (b) 151.5 mM $MgCl_2$, (c) 151.5 mM $CuCl_2$, and (d) 151.5 mM $AlCl_3$.
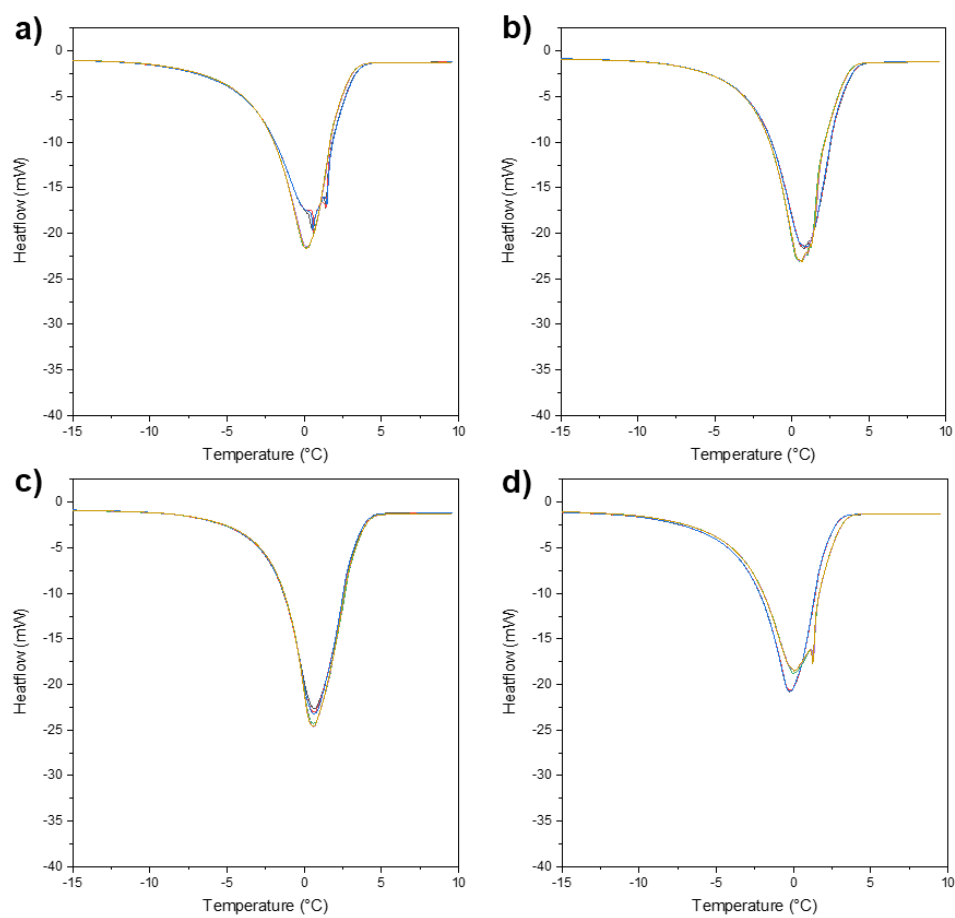
Figure A17. Raw DSC melting curves for pHPMA at 10 mg/ml (a) 151.5 mM CaCl$_2$, (b) 151.5 mM MgCl$_2$, (c) 151.5 mM CuCl$_2$, and (d) 151.5 mM AlCl$_3$.
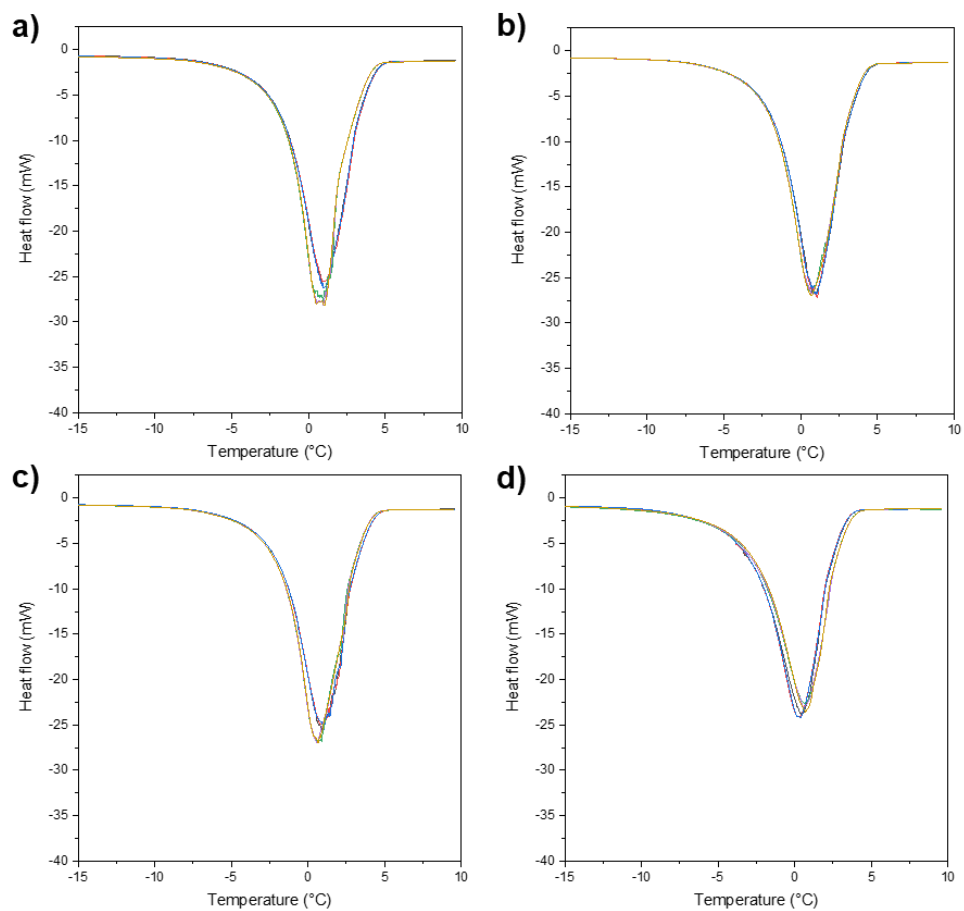
Figure A18. Raw DSC melting curves for blank (a) PBS pH 8, (b) PBS pH 10, (c) PBS pH 12, and (d) PBS pH 13.
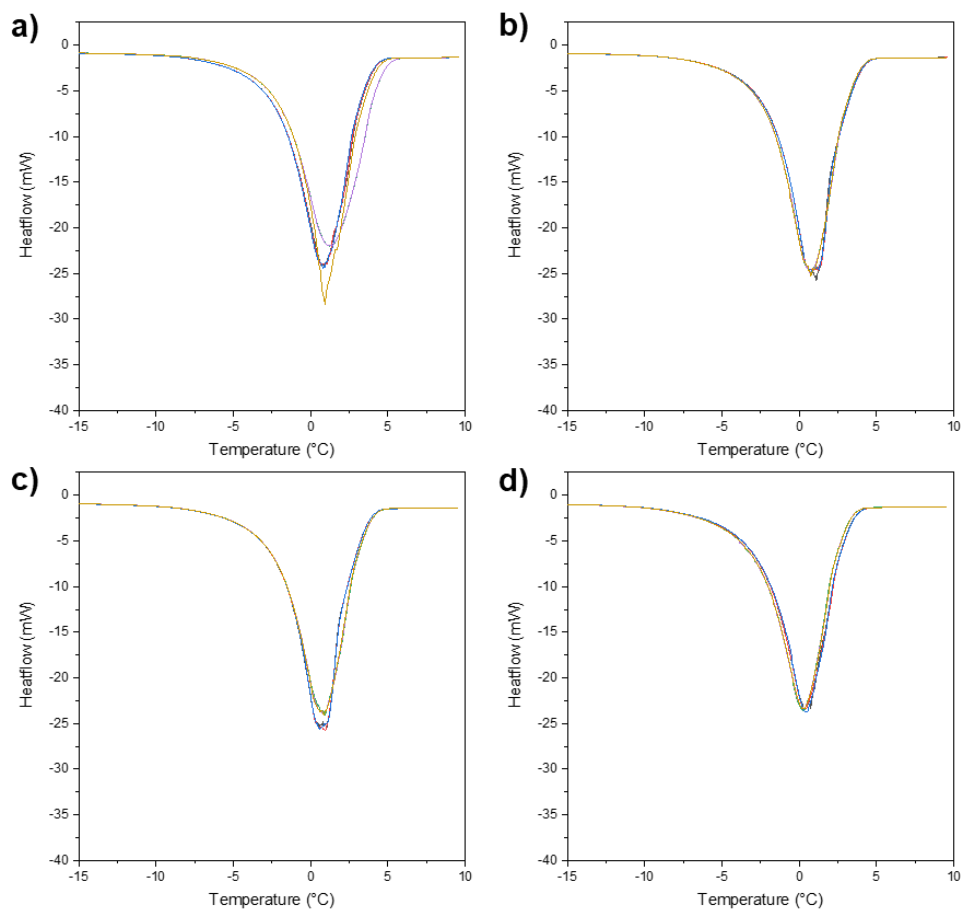
Figure A19. Raw DSC melting curves for threonine at 10 mg/ml in (a) PBS pH 8, (b) PBS pH 10, (c) PBS pH 12, and (d) PBS pH 13.
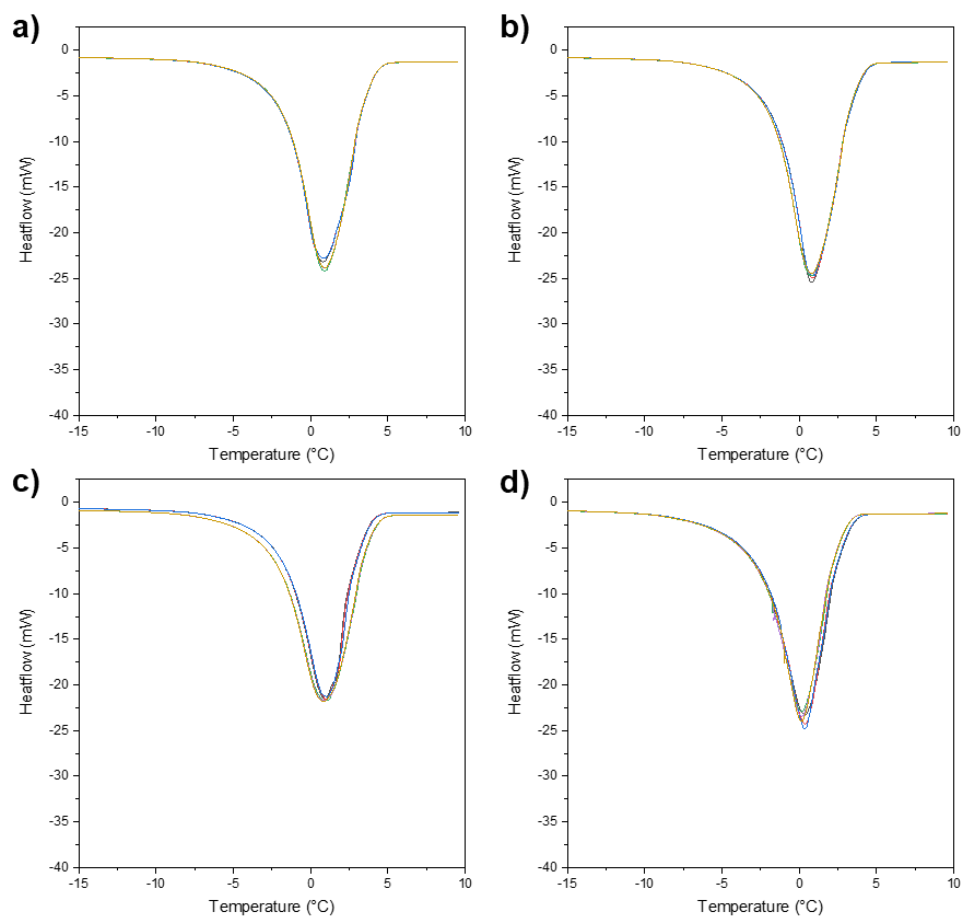
Figure A20. Raw DSC melting curves for poly(threonine) at 10 mg/ml in (a) PBS pH 8, (b) PBS pH 10, (c) PBS pH 12, and (d) PBS pH 13.
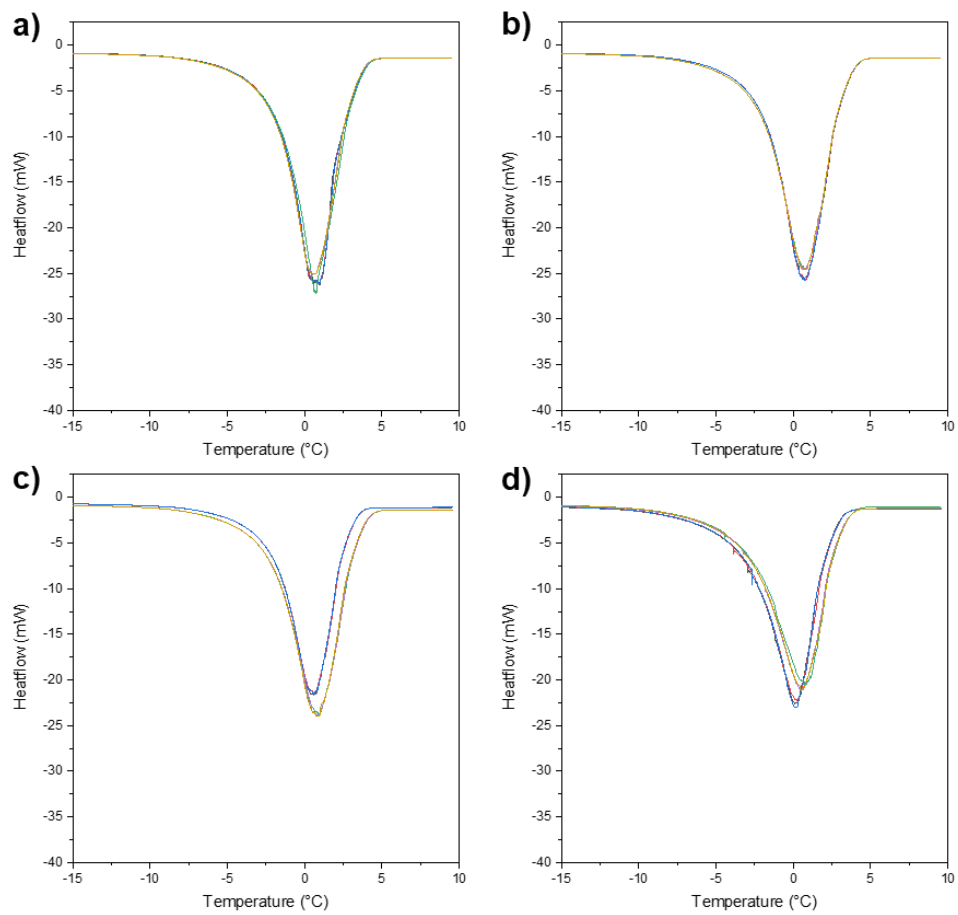
Figure A21. Raw DSC melting curves for HPMA at 10 mg/ml in (a) PBS pH 8, (b) PBS pH 10, (c) PBS pH 12, and (d) PBS pH 13.
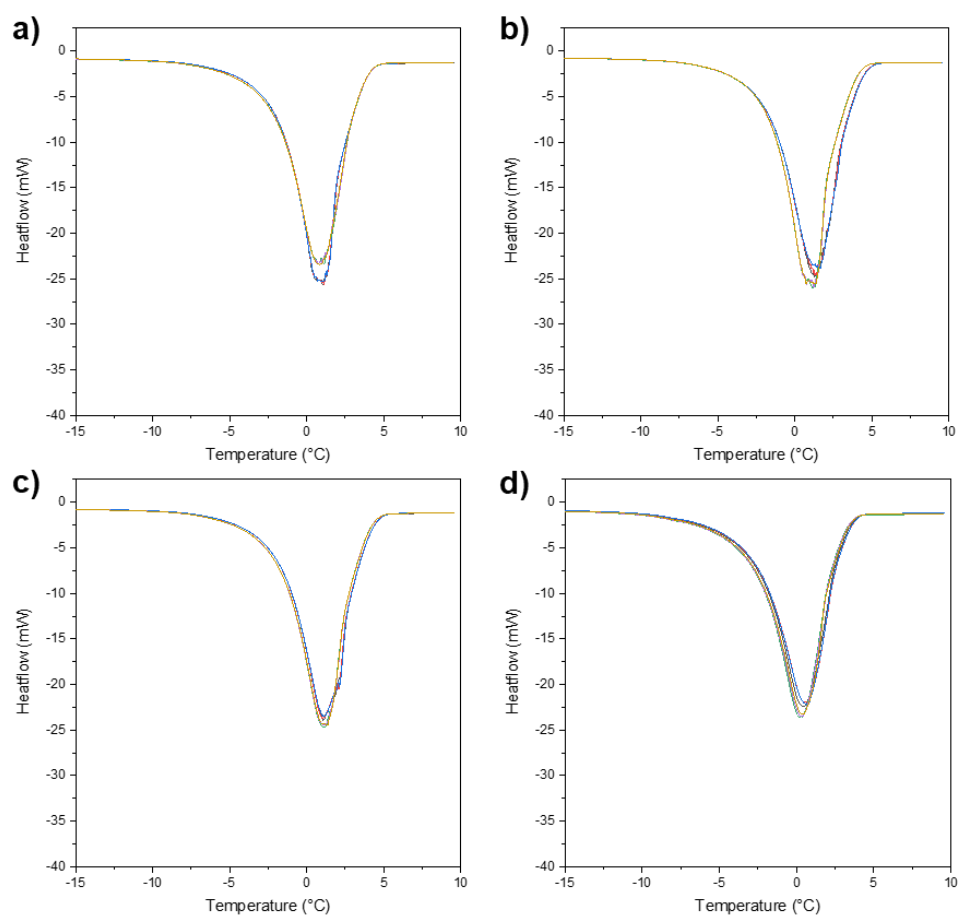
Figure A22. Raw DSC melting curves for pHPMA at 10 mg/ml in (a) PBS pH 8, (b) PBS pH 10, (c) PBS pH 12, and (d) PBS pH 13.

Figure B1. Representative splat images of neat solution ice recrystallization activity for PBS. Scale bar is 100 µm.
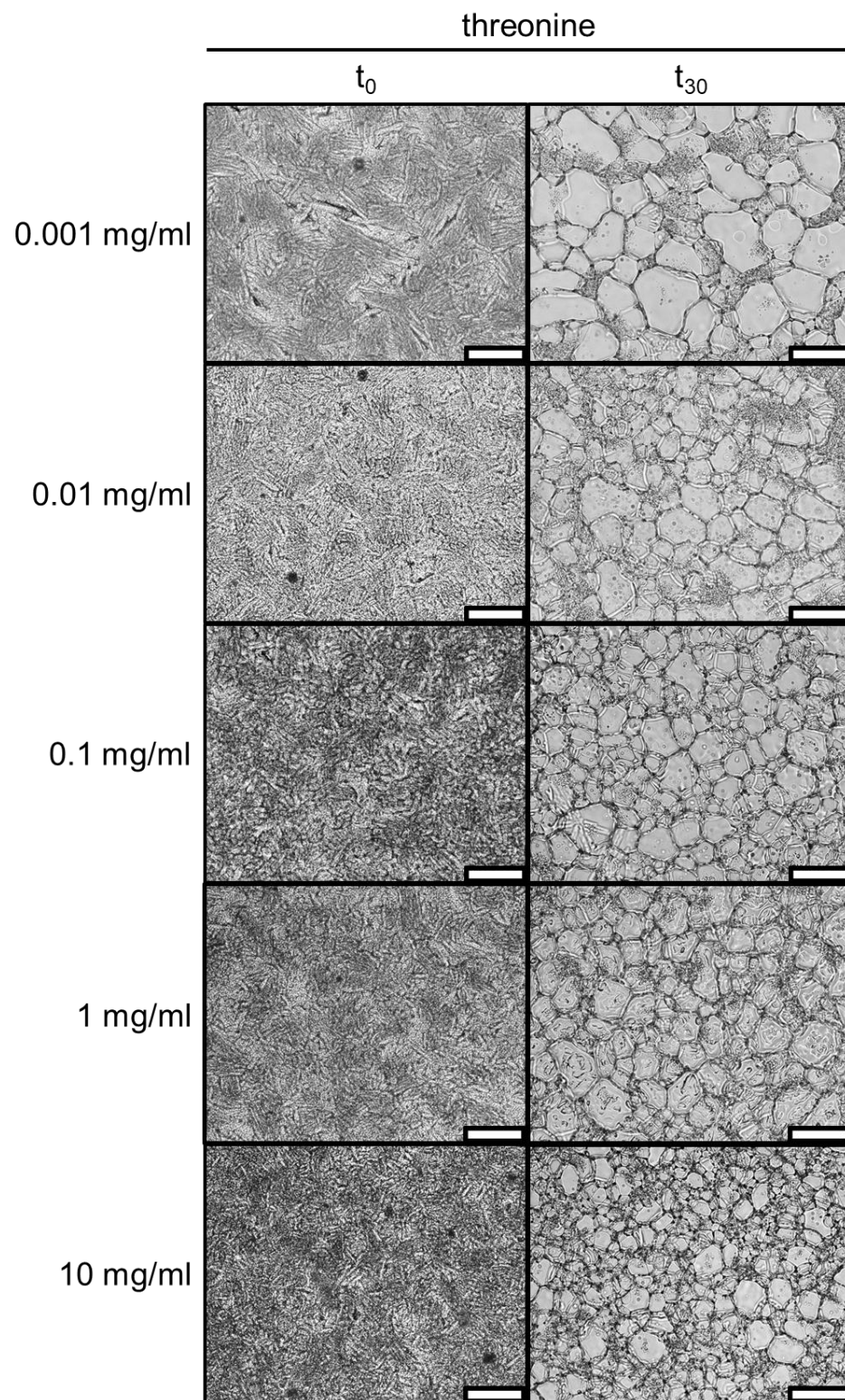
Figure B2. Threonine ice recrystallization activity in PBS at concentrations (top to bottom) of 0.001, 0.01, 0.1, 1, 10 mg/ml. Scale bar is 100 µm.
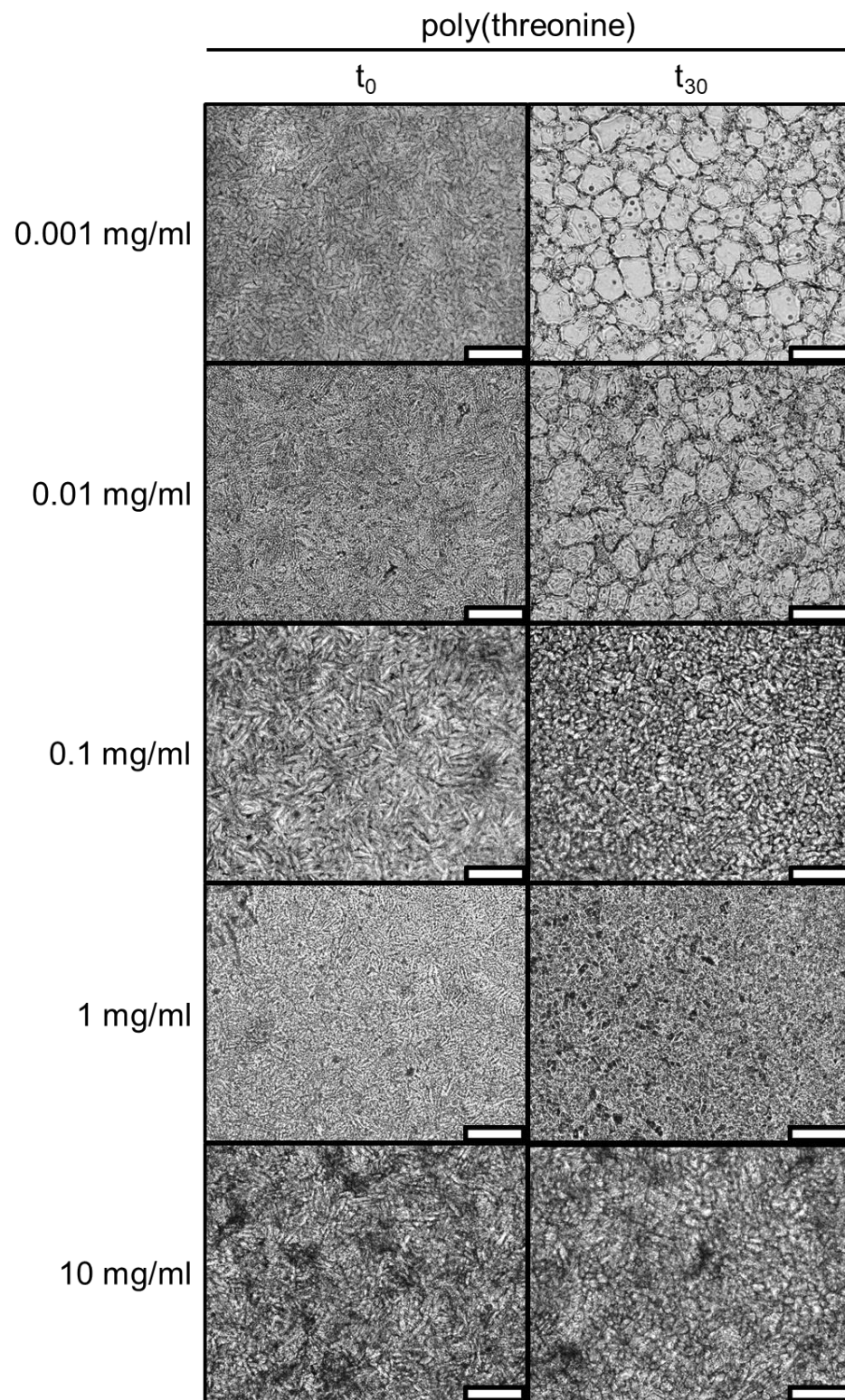
Figure B3. Poly(threonine) ice recrystallization activity in PBS at concentrations (top to bottom) of 0.001, 0.01, 0.1, 1, 10 mg/ml. Scale bar is 100 μm.
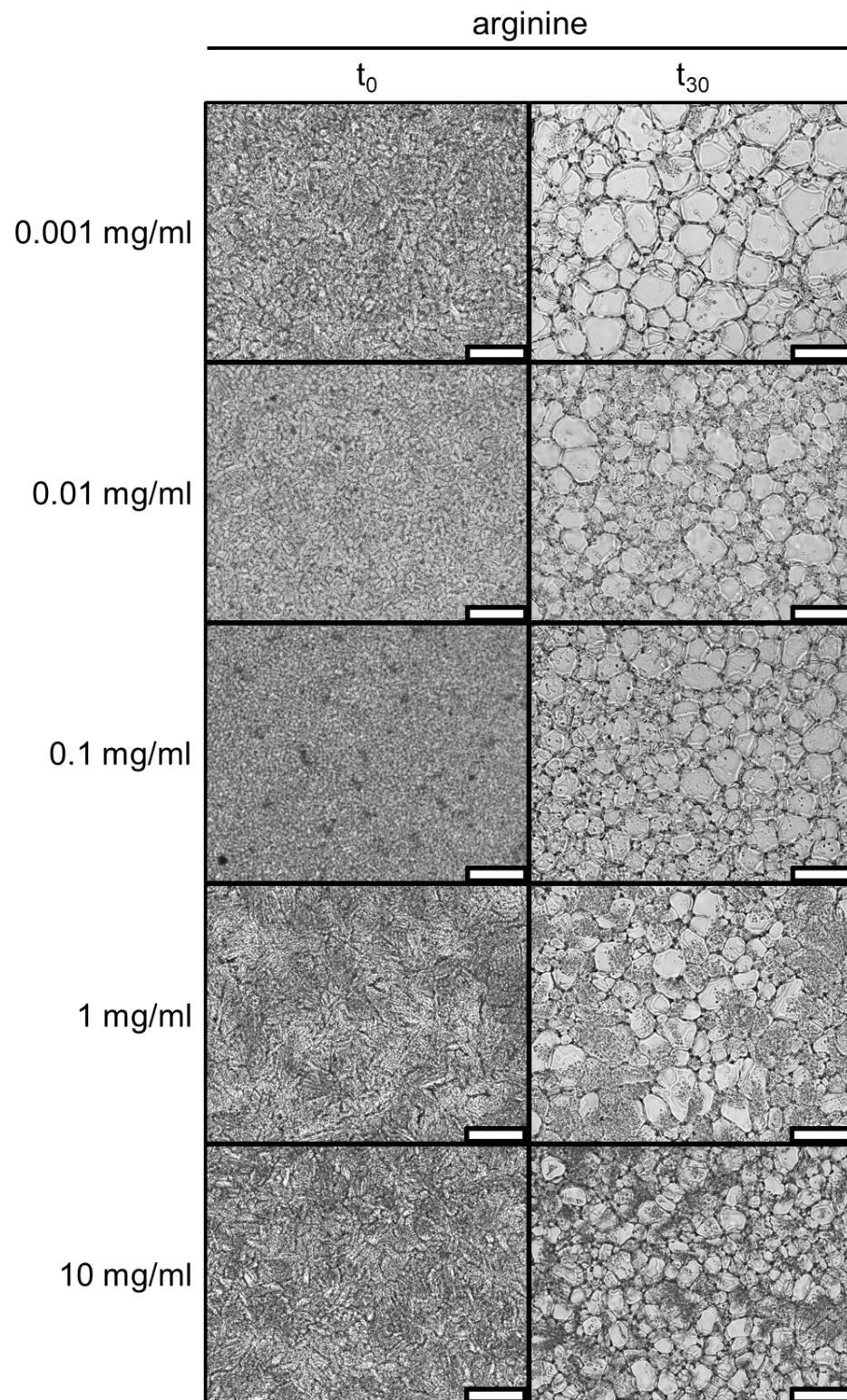
Figure B4. Arginine ice recrystallization activity in PBS at concentrations (top to bottom) of 0.001, 0.01, 0.1, 1, 10 mg/ml. Scale bar is 100 μm.
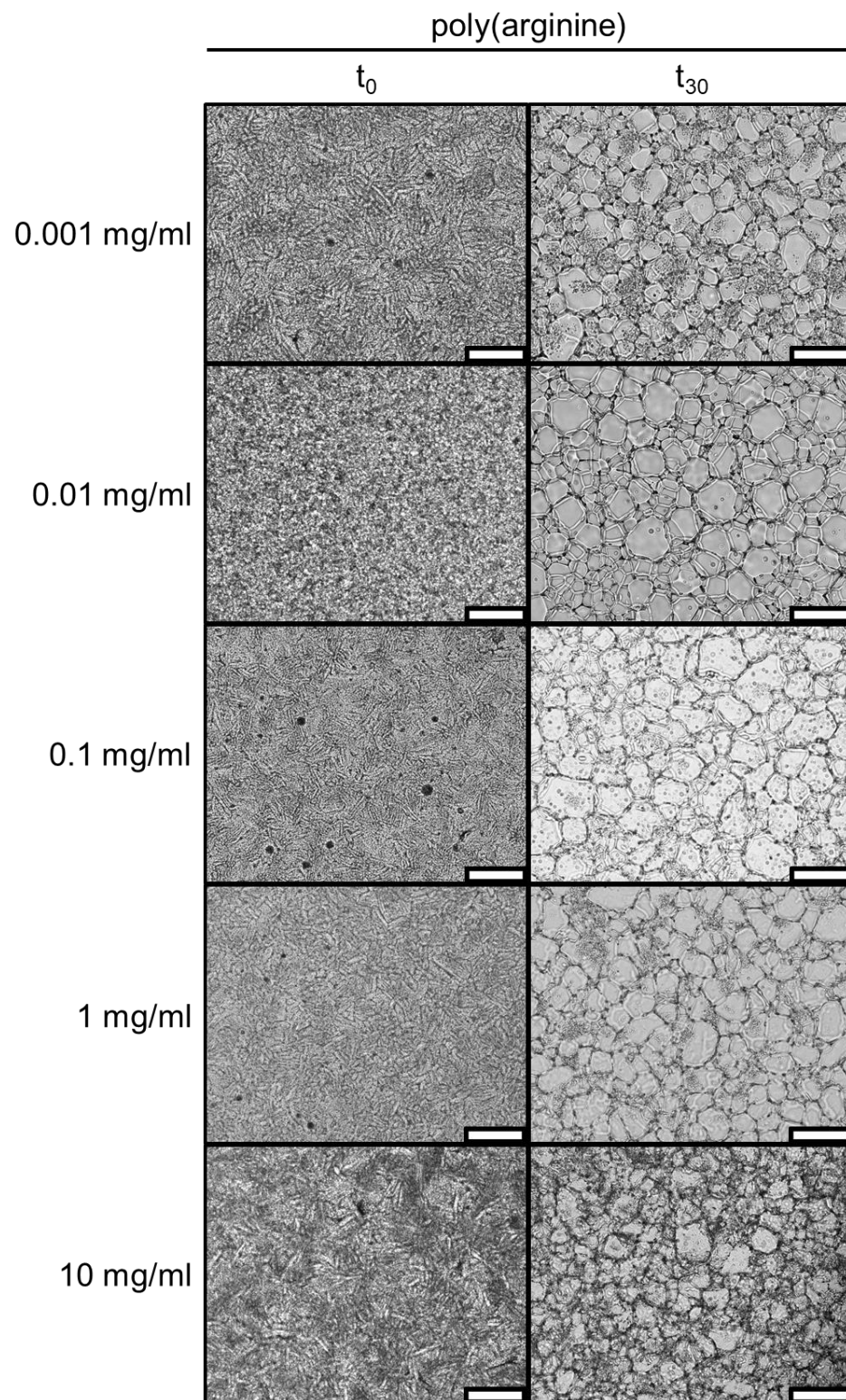
Figure B5. Poly(arginine) ice recrystallization activity in PBS at concentrations (top to bottom) of 0.001, 0.01, 0.1, 1, 10 mg/ml. Scale bar is 100 µm.
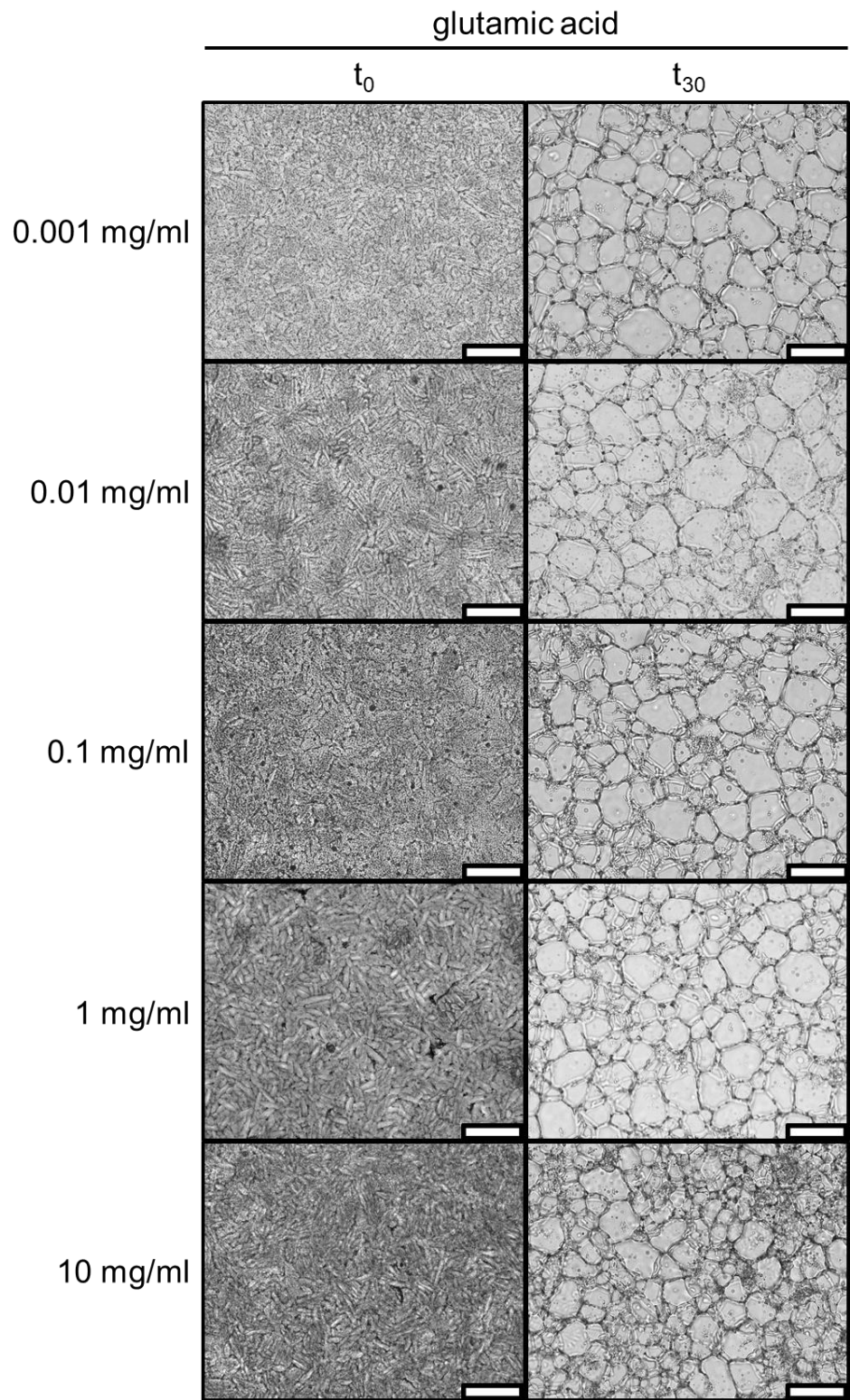
Figure B6. Glutamic acid ice recrystallization activity in PBS at concentrations (top to bottom) of 0.001, 0.01, 0.1, 1, 8.6 mg/ml. Scale bar is 100 µm.
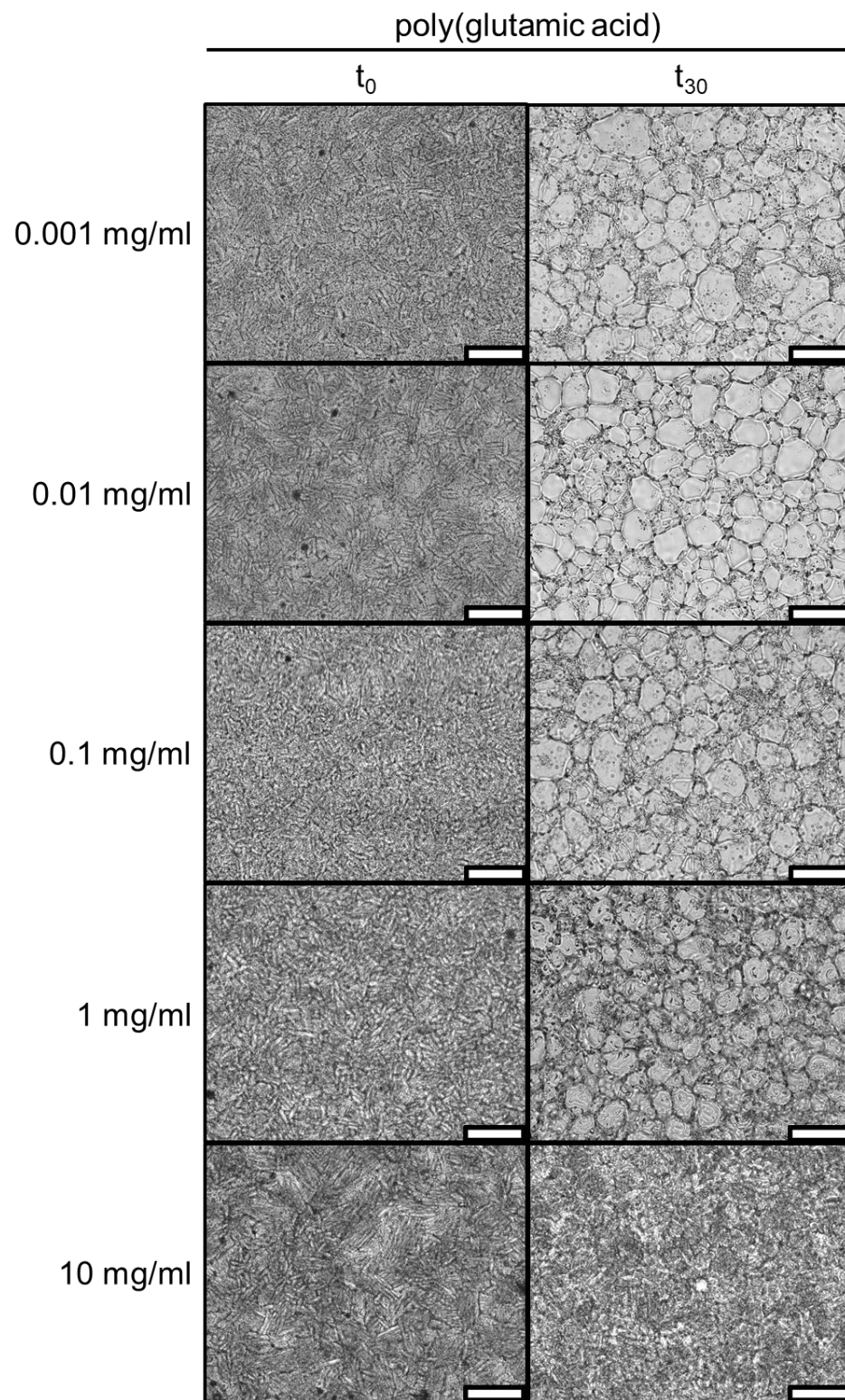
Figure B7. Poly(glutamic acid) ice recrystallization activity in PBS at concentrations (top to bottom) of 0.001, 0.01, 0.1, 1, 10 mg/ml. Scale bar is 100 µm.
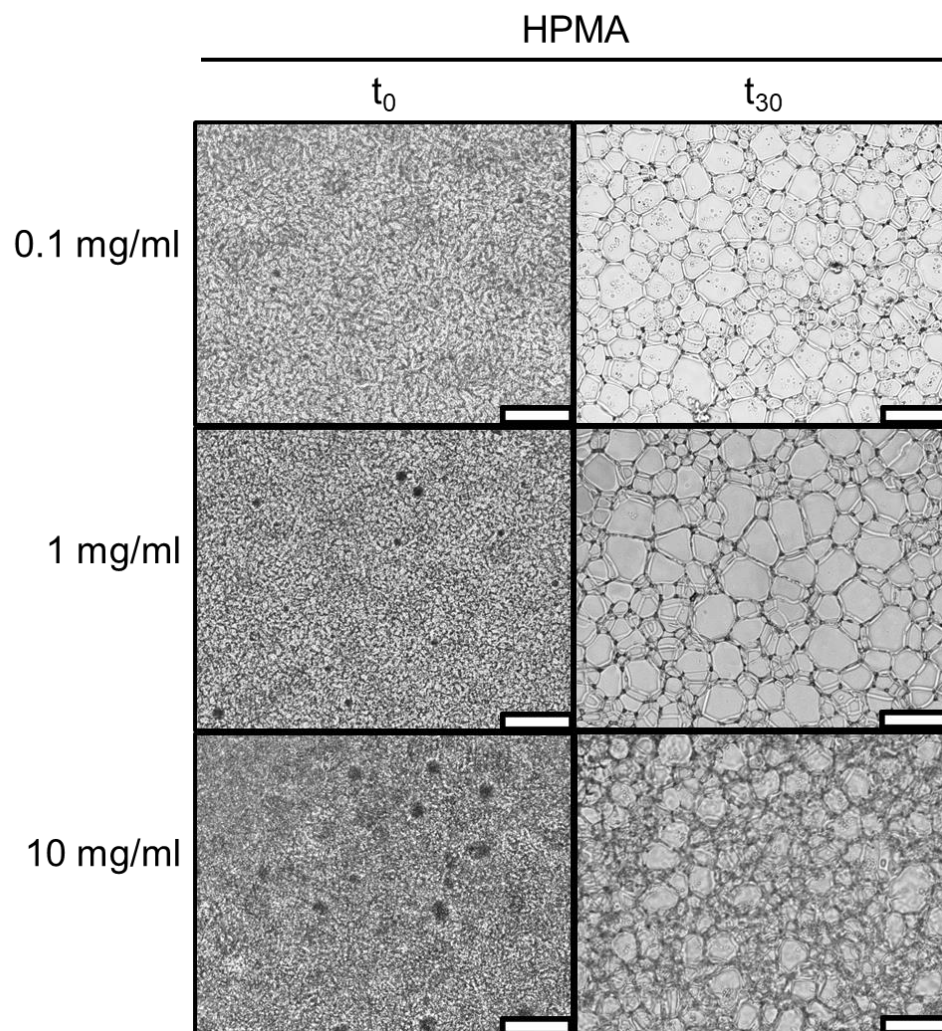
Figure B8. Ice recrystallization activity of HPMA in PBS at concentrations of (top to bottom) 0.1 mg/ml, 1 mg/ml, 10 mg/ml. Scale bar is 100 µm.
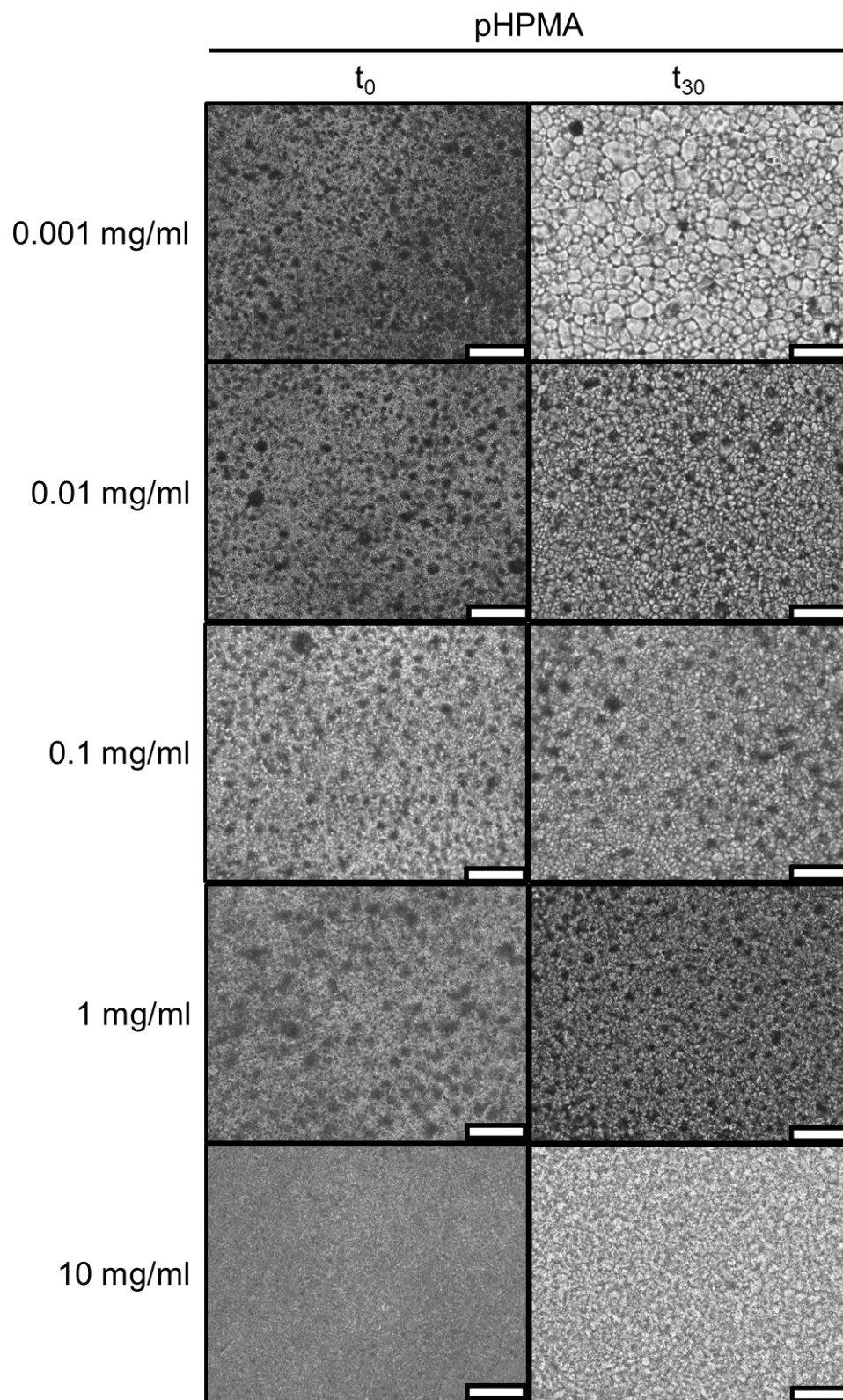
Figure B9. Ice recrystallization activity of pHPMA in PBS at concentrations of (top to bottom) 0.001 mg/ml, 0.01 mg/ml, 0.1 mg/ml, 1 mg/ml, 10 mg/ml. Scale bar is 100 µm.
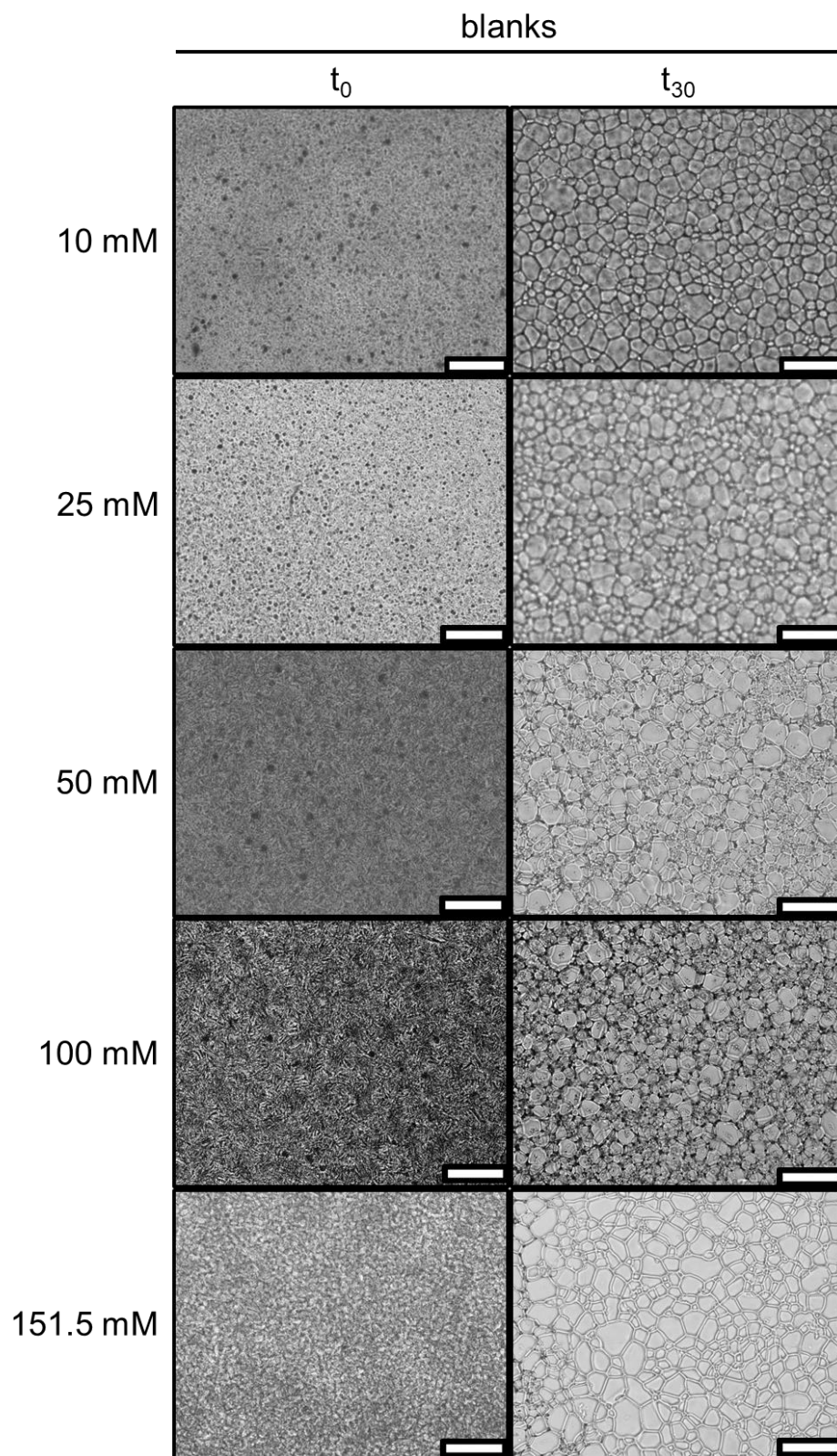
Figure B10. Ice recrystallization activity of blank $CaCl_2$ solutions at (top to bottom) 10 mM, 25 mM, 50 mM, 100 mM, 151.5 mM. Scale bar is 100 µm.
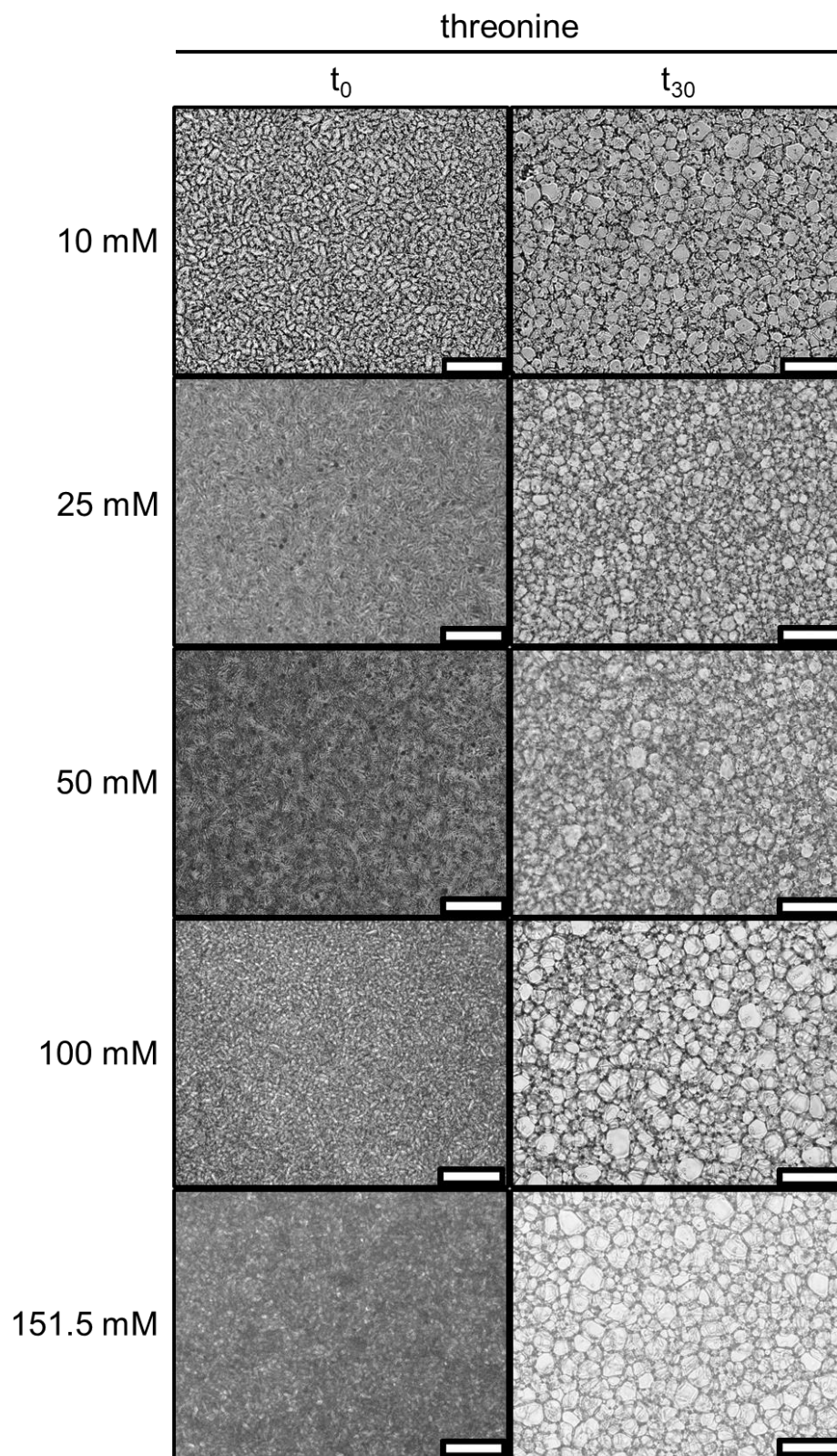
Figure B11. Ice recrystallization activity of 10 mg/ml threonine in (top to bottom) 10 mM CaCl$_2$, 25 mM CaCl$_2$, 50 mM CaCl$_2$, 100 mM CaCl$_2$, 151.5 mM CaCl$_2$. Scale bar is 100 µm.
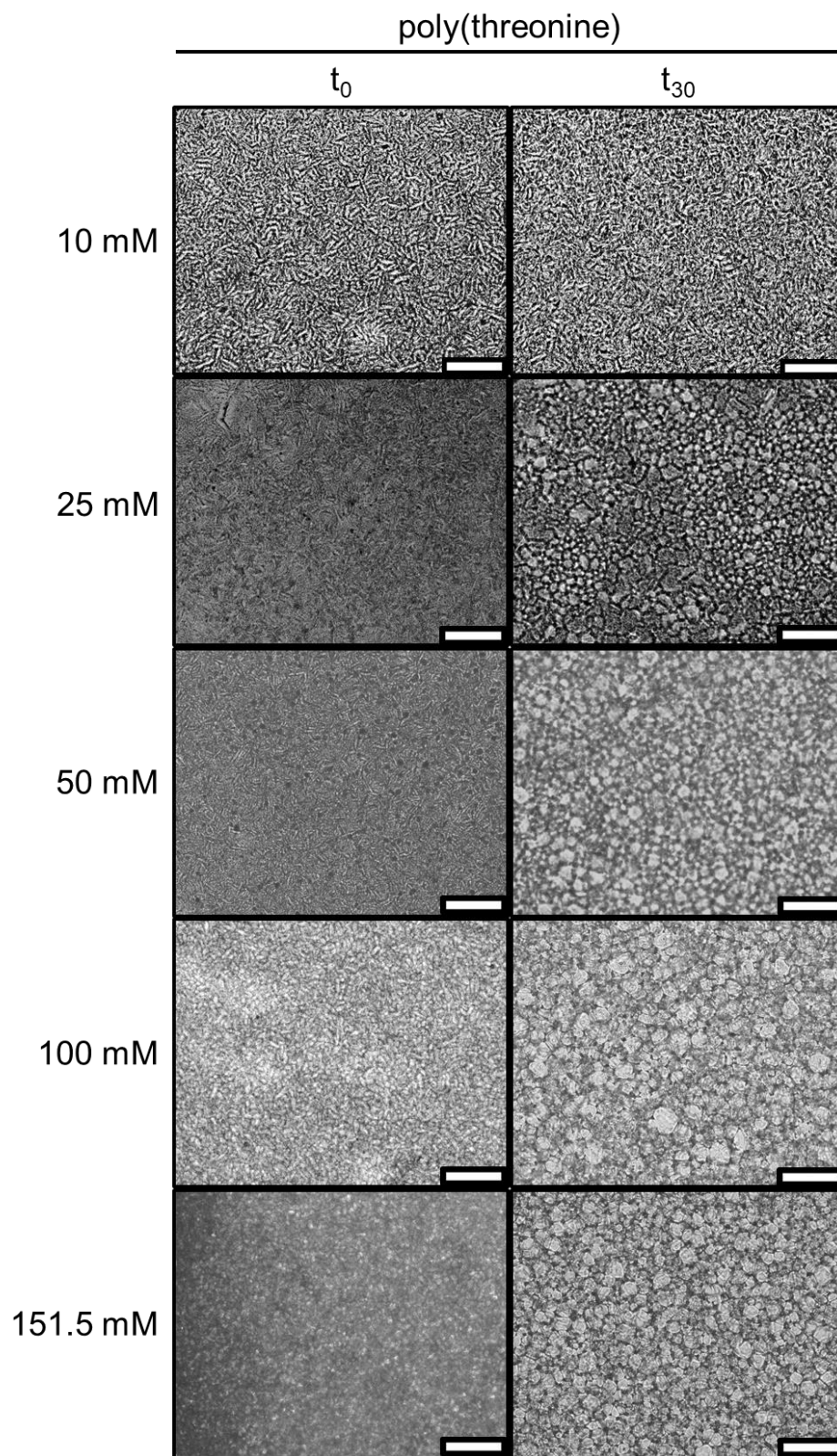
Figure B12. Ice recrystallization activity of 10 mg/ml poly(threonine) in (top to bottom) 10 mM CaCl$_2$, 25 mM CaCl$_2$, 50 mM CaCl$_2$, 100 mM CaCl$_2$, 151.5 mM CaCl$_2$. Scale bar is 100 µm.
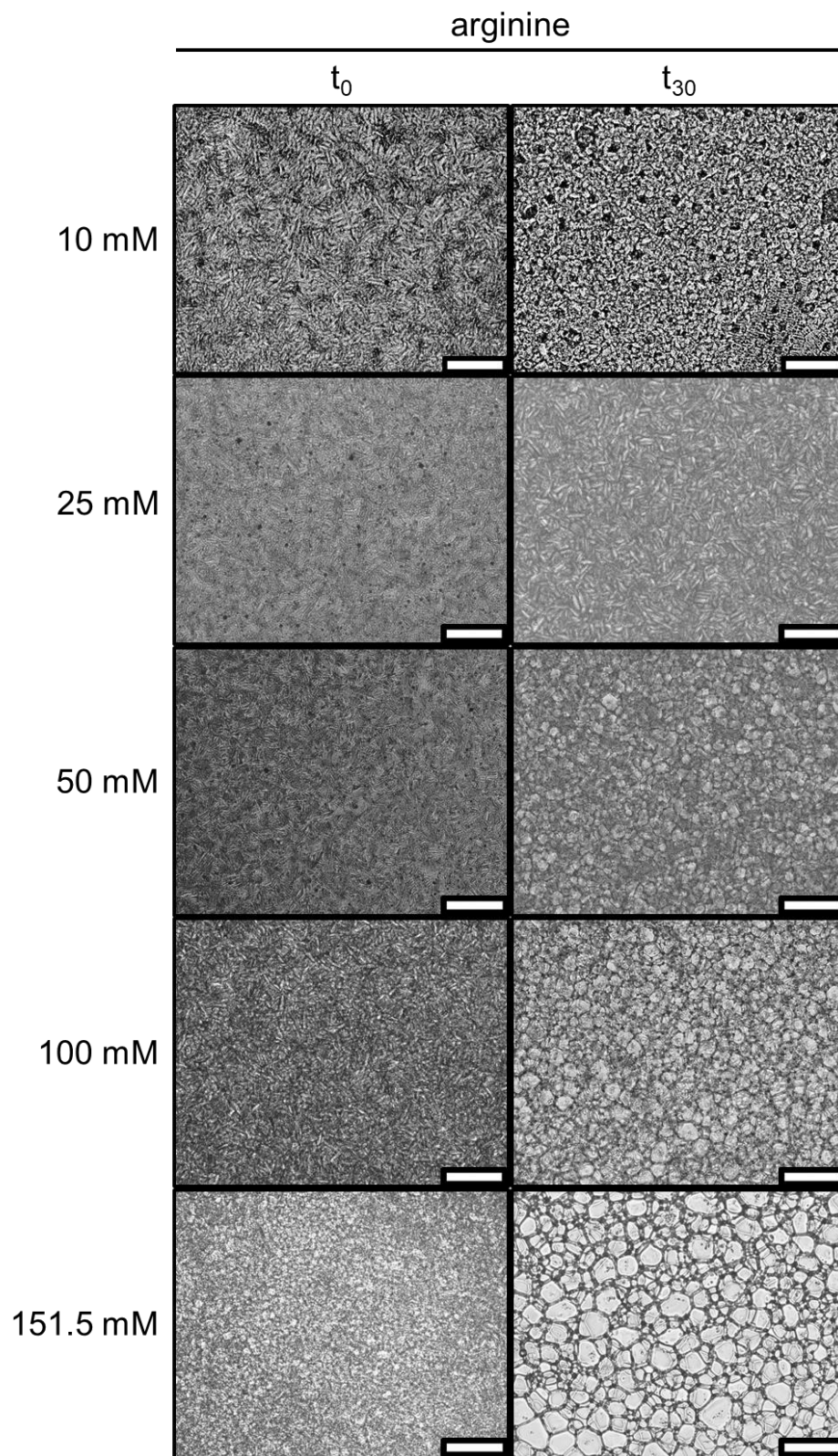
Figure B13. Ice recrystallization activity of 10 mg/ml arginine in (top to bottom) 10 mM CaCl$_2$, 25 mM CaCl$_2$, 50 mM CaCl$_2$, 100 mM CaCl$_2$, 151.5 mM CaCl$_2$. Scale bar is 100 µm.
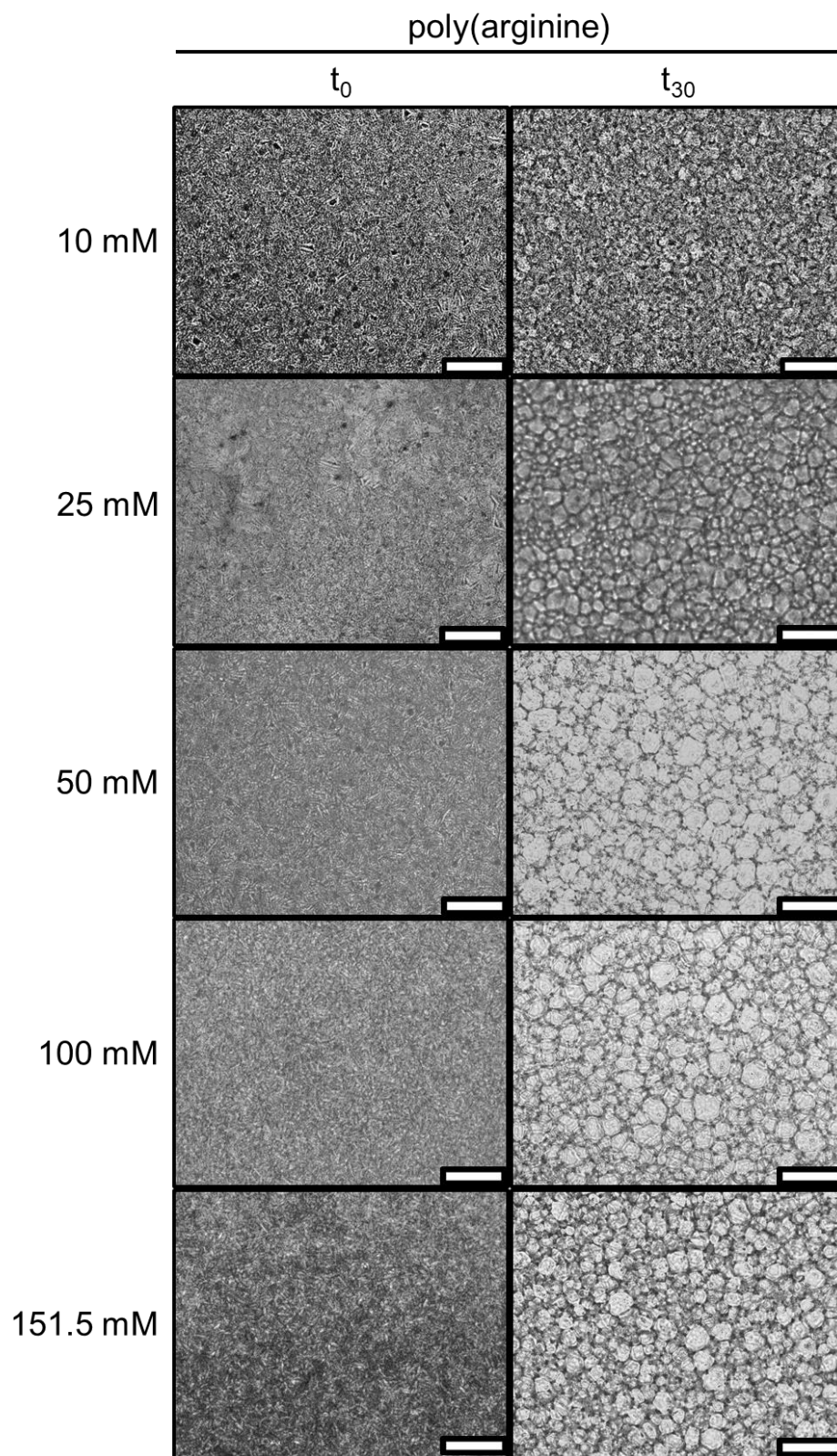
Figure B14. Ice recrystallization activity of 10 mg/ml poly(arginine) in (top to bottom) 10 mM CaCl$_2$, 25 mM CaCl$_2$, 50 mM CaCl$_2$, 100 mM CaCl$_2$, 151.5 mM CaCl$_2$. Scale bar is 100 µm.
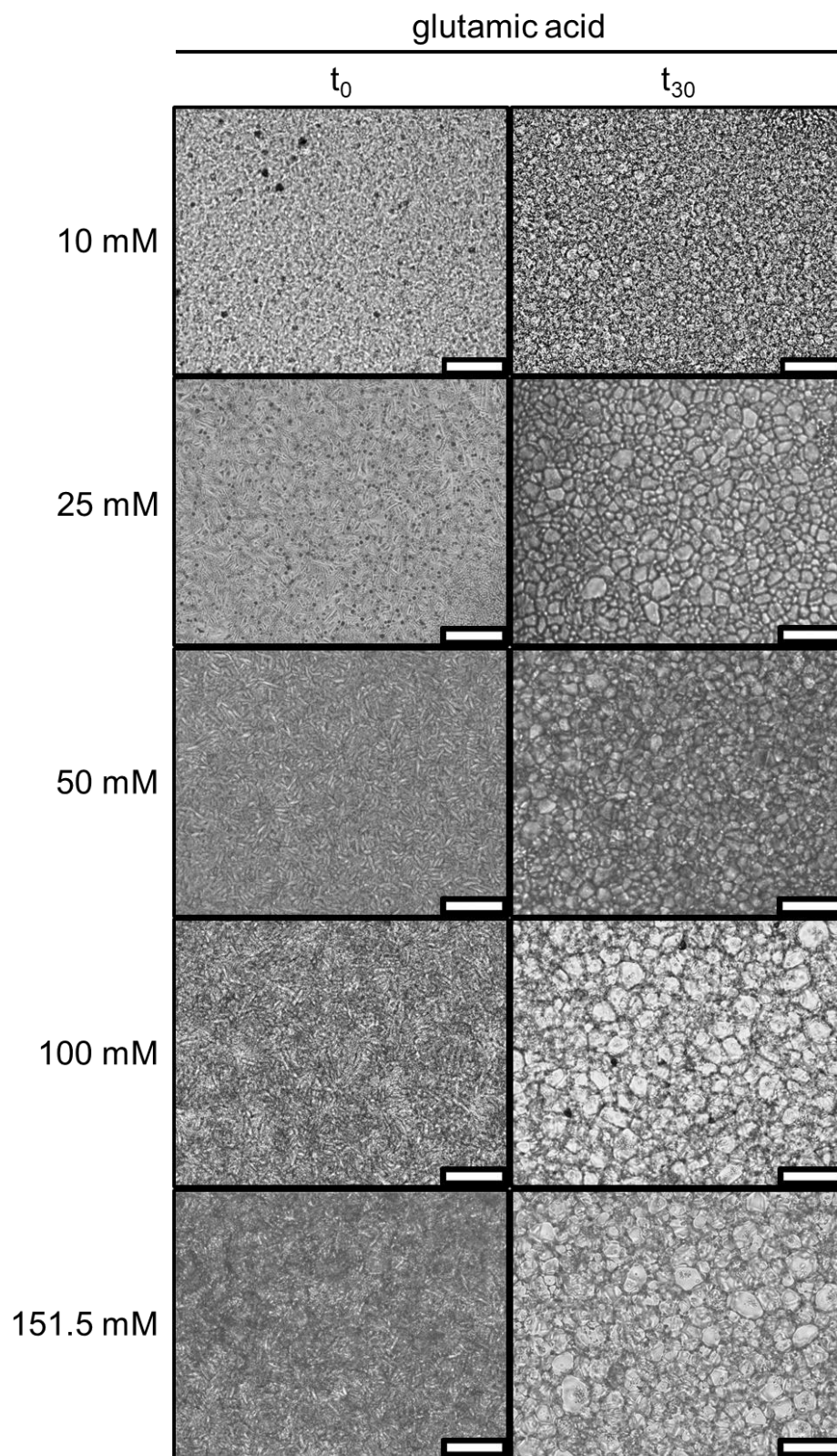
Figure B15. Ice recrystallization activity of 10 mg/ml glutamic acid in (top to bottom) 10 mM CaCl₂, 25 mM CaCl₂, 50 mM CaCl₂, 100 mM CaCl₂, 151.5 mM CaCl₂. Scale bar is 100 µm.
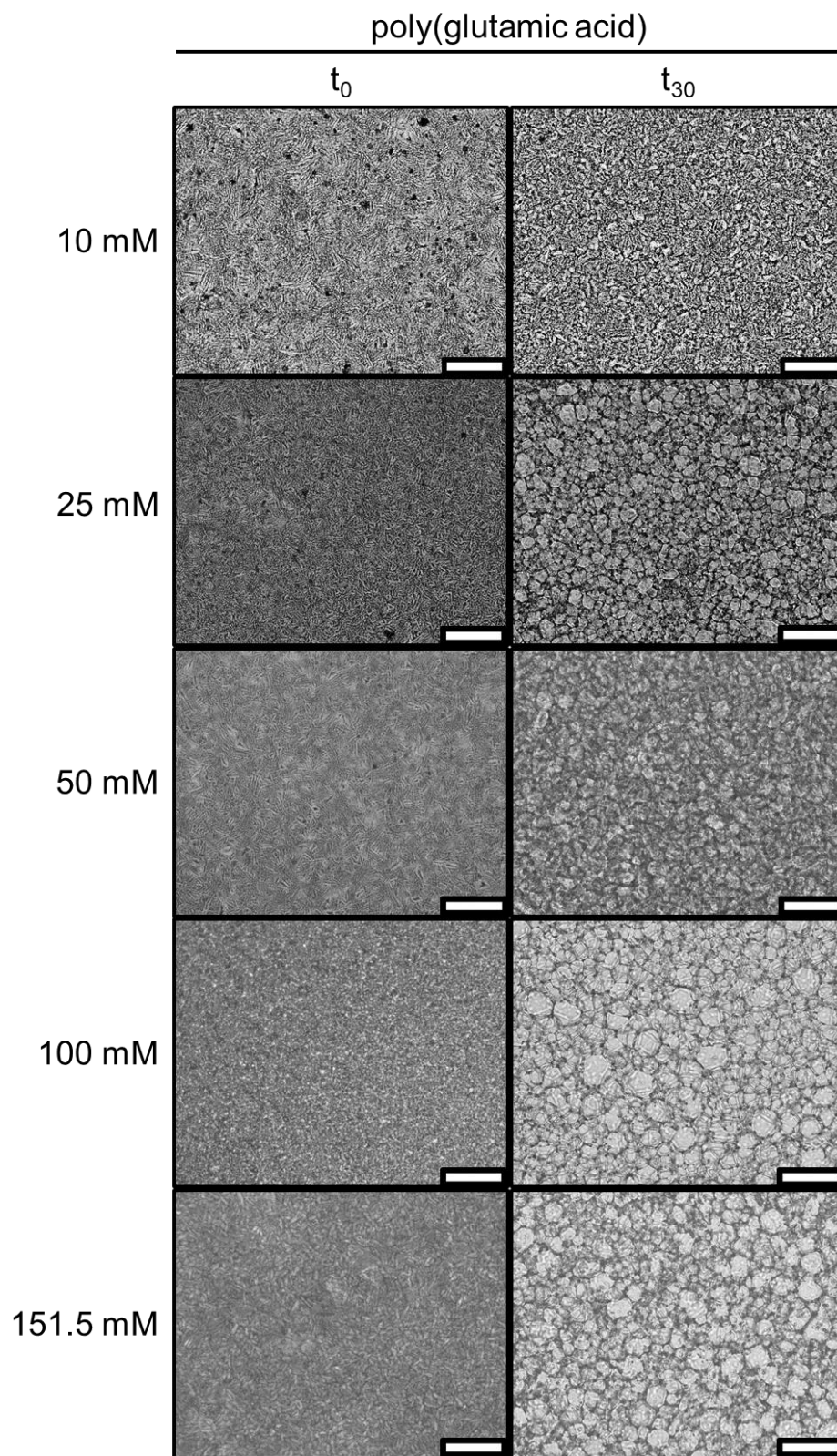
Figure B16. Ice recrystallization activity of 10 mg/ml poly(glutamic acid) in (top to bottom) 10 mM CaCl$_2$, 25 mM CaCl$_2$, 50 mM CaCl$_2$, 100 mM CaCl$_2$, 151.5 mM CaCl$_2$. Scale bar is 100 µm.
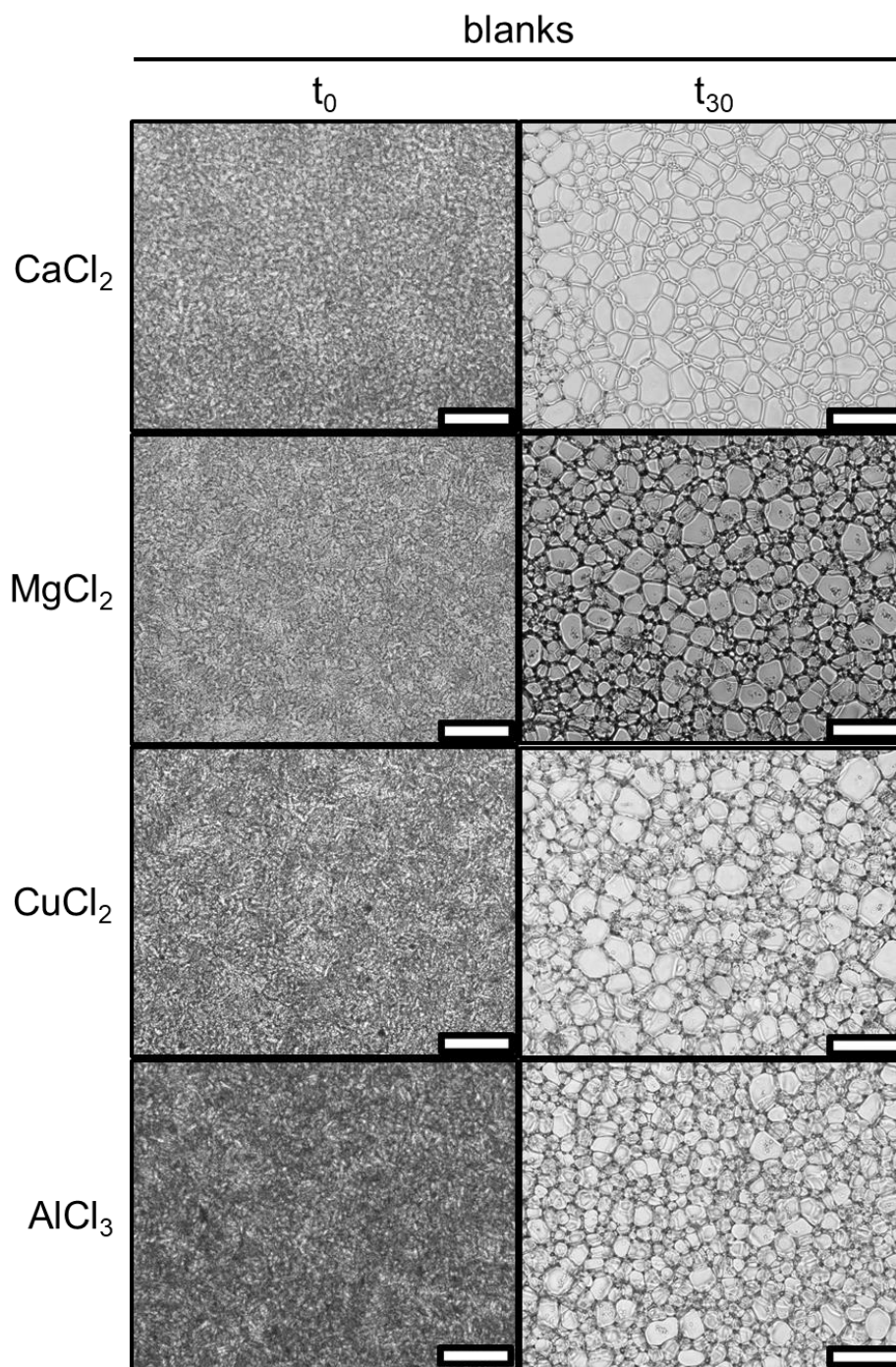
Figure B17. Ice recrystallization activity of blank chloride salt solutions. Top to bottom: 151.5 mM $CaCl_2$, 151.5 mM $MgCl_2$, 151.5 mM $CuCl_2$, 151.5 mM $AlCl_3$. Scale bar is 100 µm.
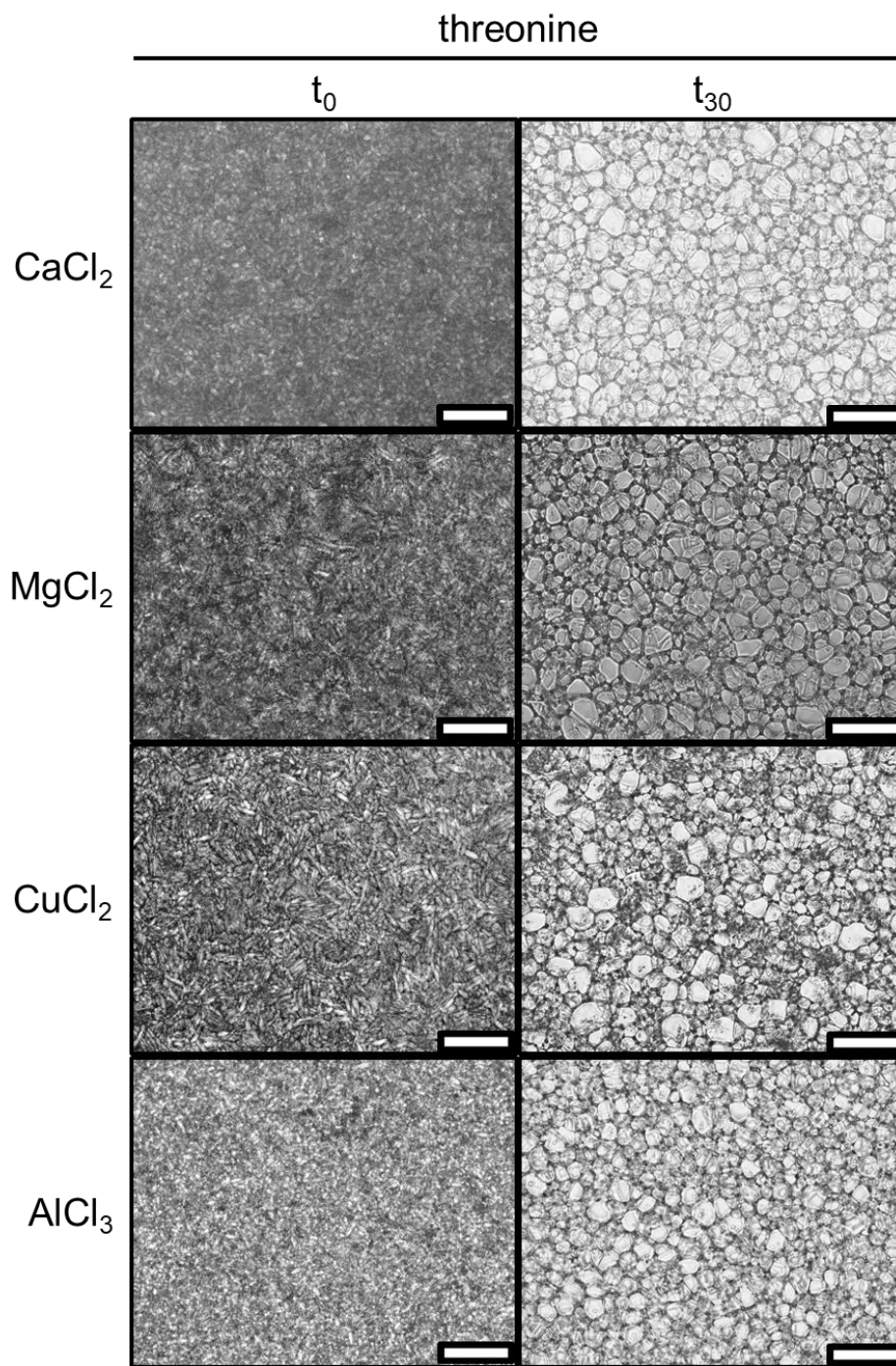
Figure B18. Ice recrystallization activity of 10 mg/ml threonine in chloride salt solutions. Top to bottom: 151.5 mM $CaCl_2$, 151.5 mM $MgCl_2$, 151.5 mM $CuCl_2$, 151.5 mM $AlCl_3$. Scale bar is 100 µm.
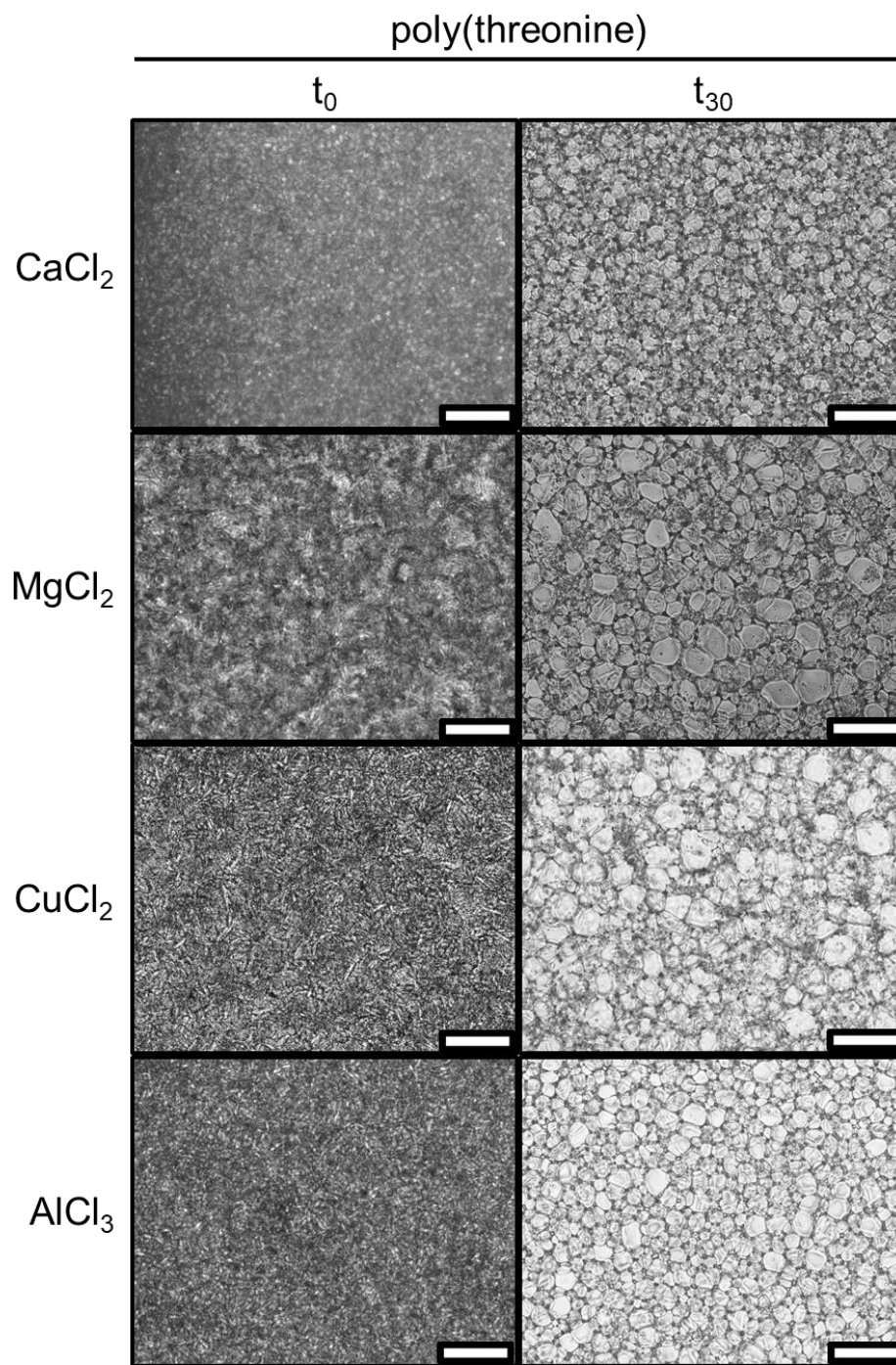
Figure B19. Ice recrystallization activity of 10 mg/ml poly(threonine) in chloride salt solutions. Top to bottom: 151.5 mM $CaCl_2$, 151.5 mM $MgCl_2$, 151.5 mM $CuCl_2$, 151.5 mM $AlCl_3$. Scale bar is 100 µm.
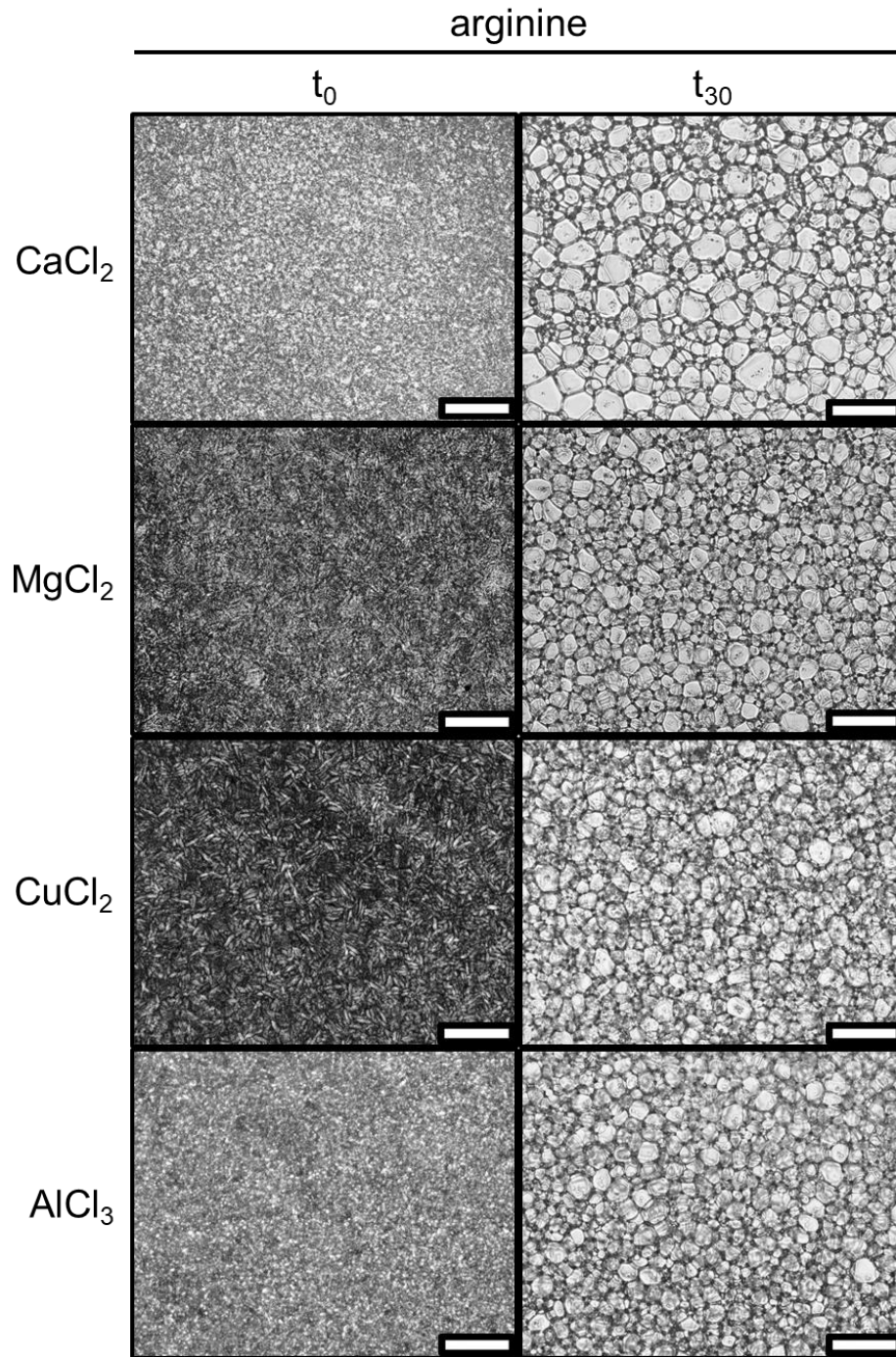
Figure B20. Ice recrystallization activity of 10 mg/ml arginine in chloride salt solutions. Top to bottom: 151.5 mM $CaCl_2$, 151.5 mM $MgCl_2$, 151.5 mM $CuCl_2$, 151.5 mM $AlCl_3$. Scale bar is 100 µm.
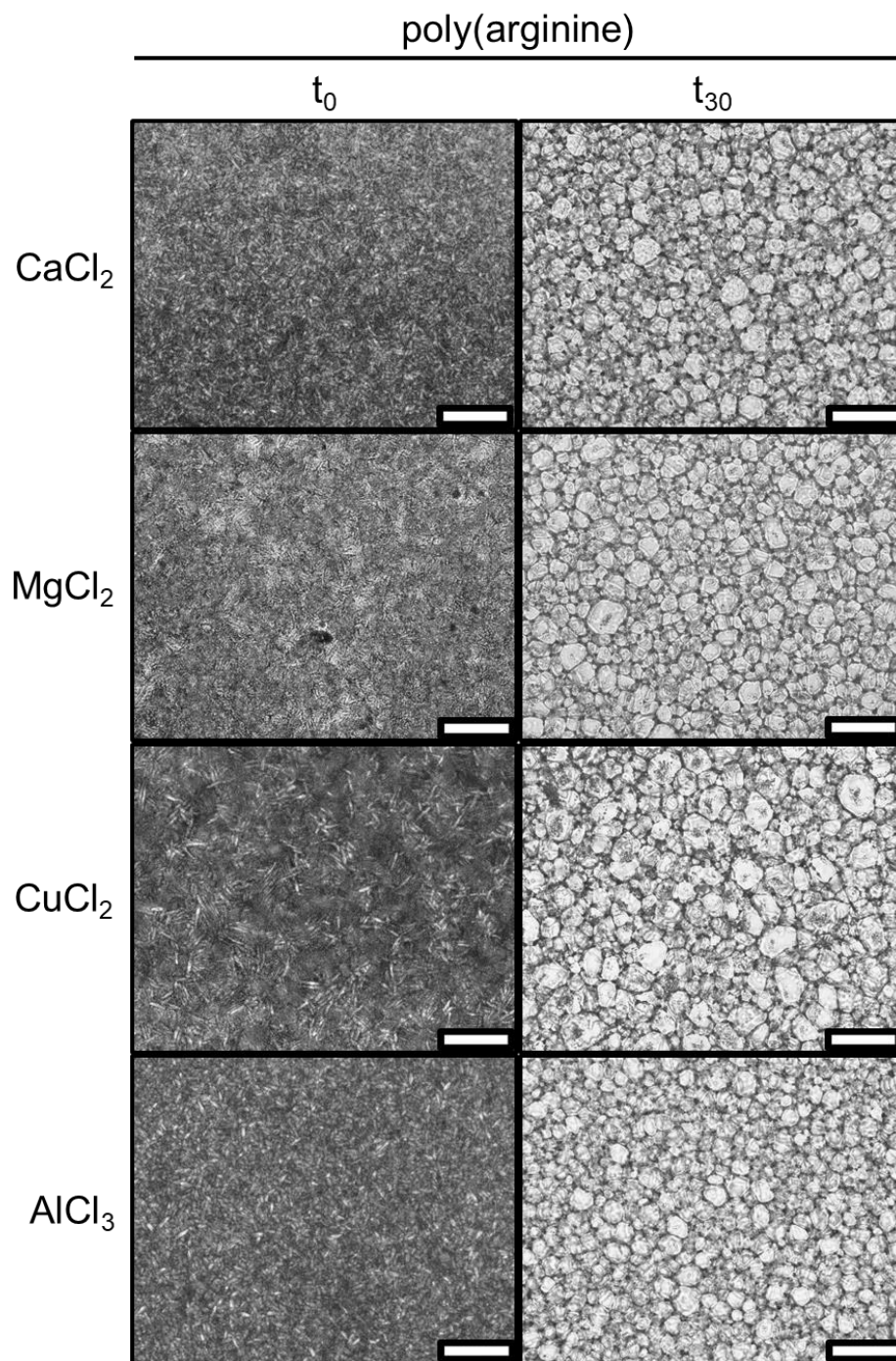
Figure B21. Ice recrystallization activity of 10 mg/ml poly(arginine) in chloride salt solutions. Top to bottom: 151.5 mM $CaCl_2$, 151.5 mM $MgCl_2$, 151.5 mM $CuCl_2$, 151.5 mM $AlCl_3$. Scale bar is 100 µm.
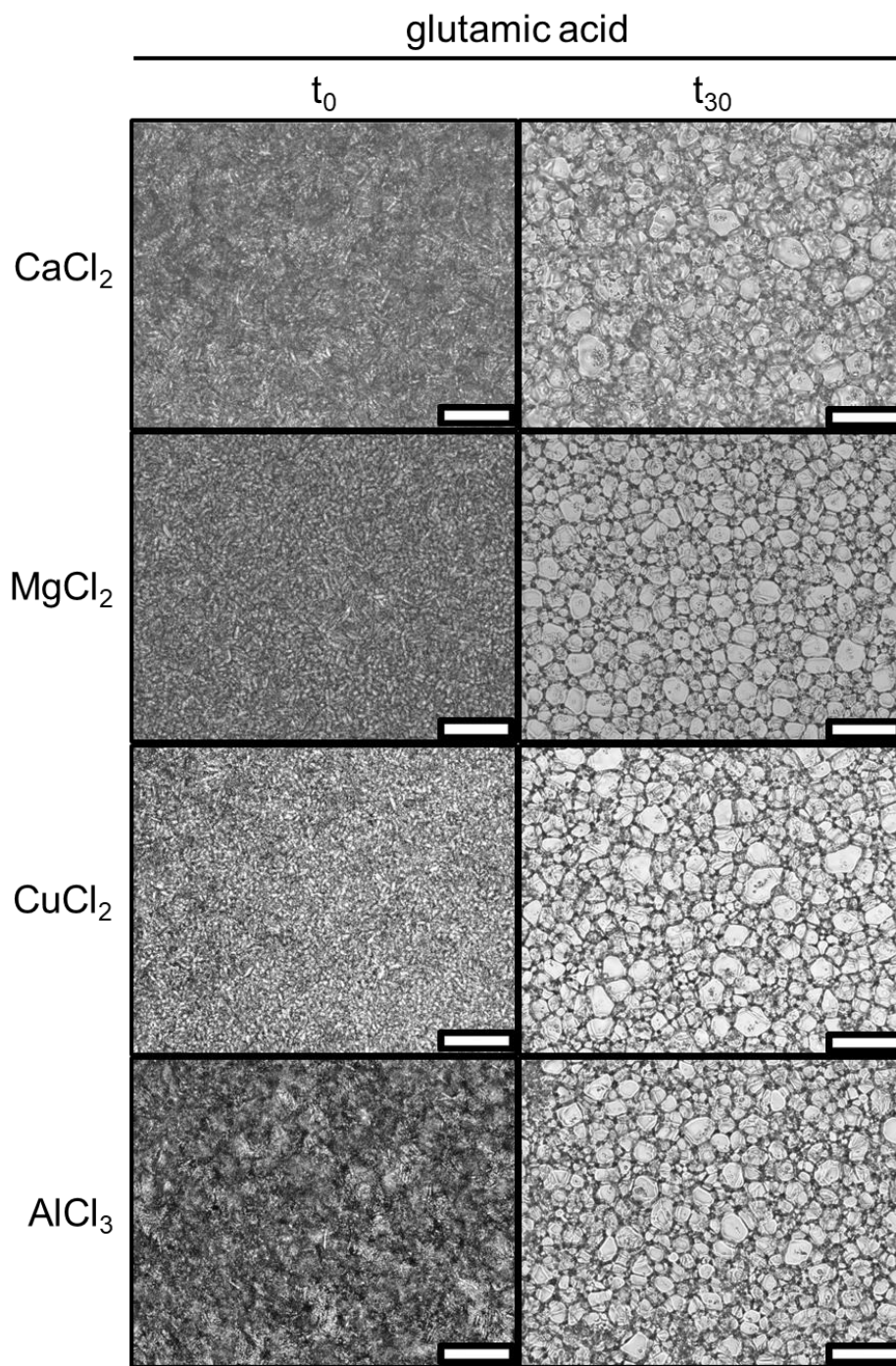
Figure B22. Ice recrystallization activity of 10 mg/ml glutamic acid in chloride salt solutions. Top to bottom: 151.5 mM $CaCl_2$, 151.5 mM $MgCl_2$, 151.5 mM $CuCl_2$, 151.5 mM $AlCl_3$. Scale bar is 100 µm.
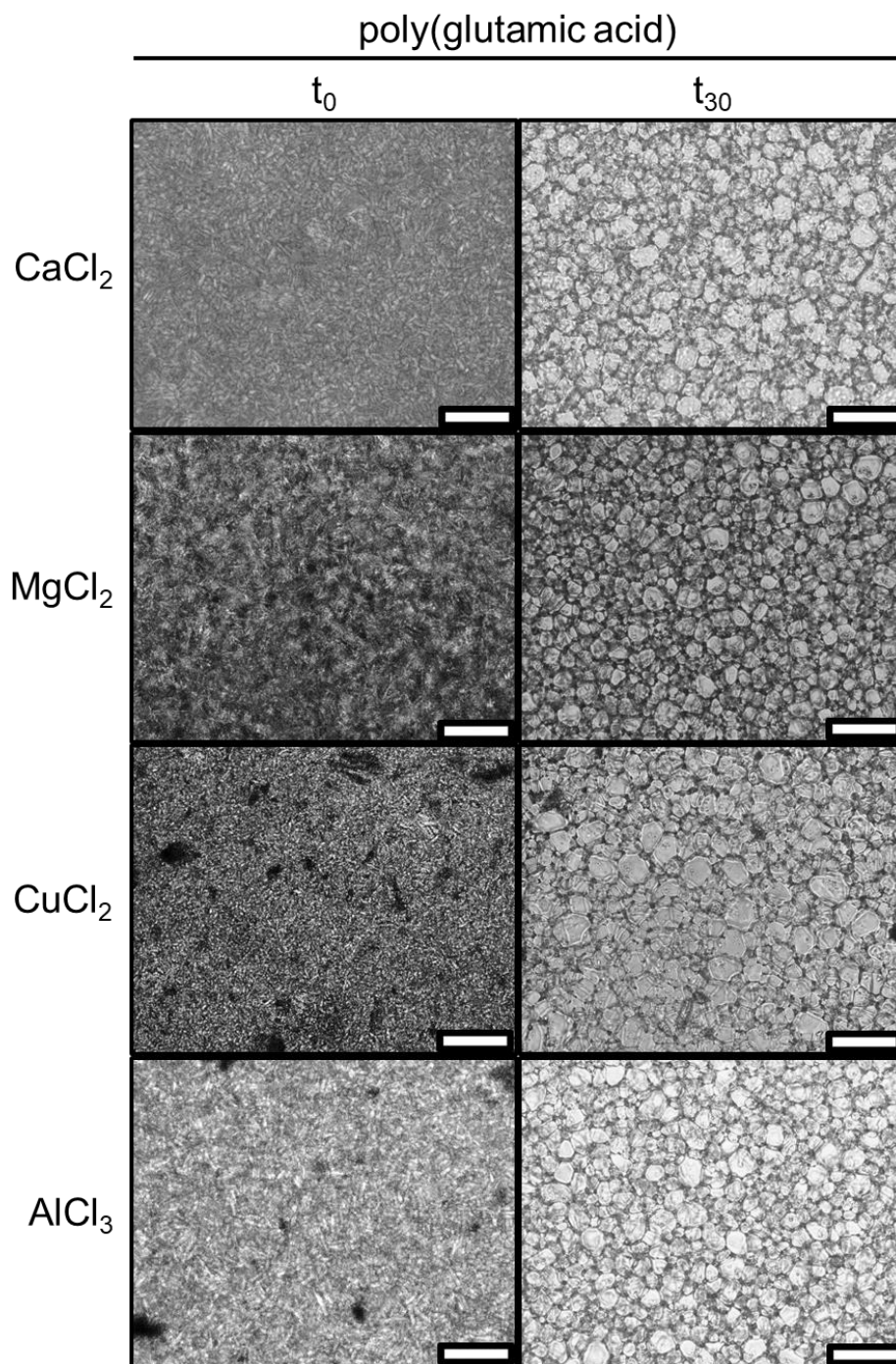
Figure B23. Ice recrystallization activity of 10 mg/ml poly(glutamic acid) in chloride salt solutions. Top to bottom: 151.5 mM $CaCl_2$, 151.5 mM $MgCl_2$, 151.5 mM $CuCl_2$, 151.5 mM $AlCl_3$. Scale bar is 100 µm.
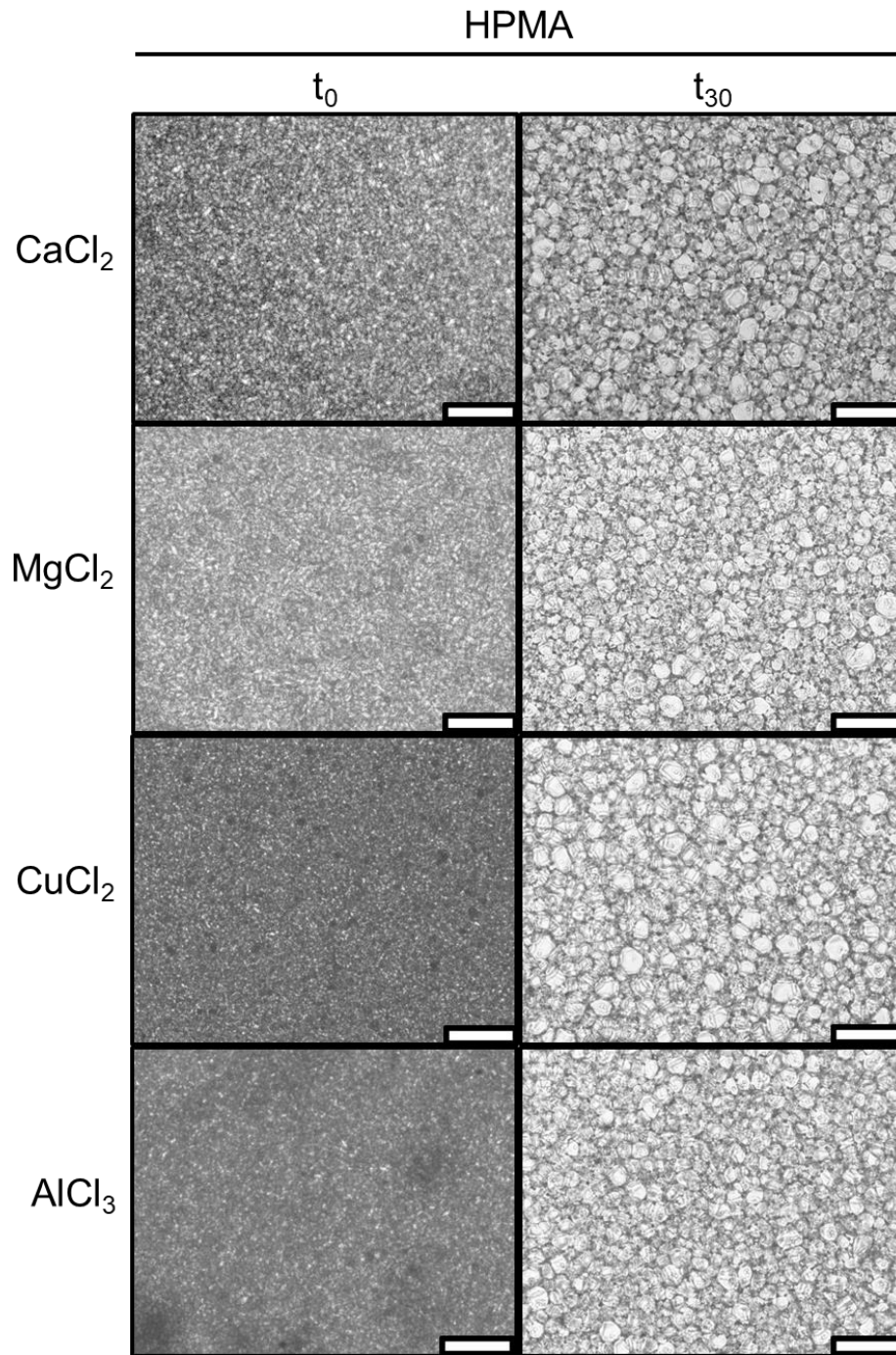
Figure B24. Ice recrystallization activity of 10 mg/ml HPMA in chloride salt solutions. Top to bottom: 151.5 mM $CaCl_2$, 151.5 mM $MgCl_2$, 151.5 mM $CuCl_2$, 151.5 mM $AlCl_3$. Scale bar is 100 µm.
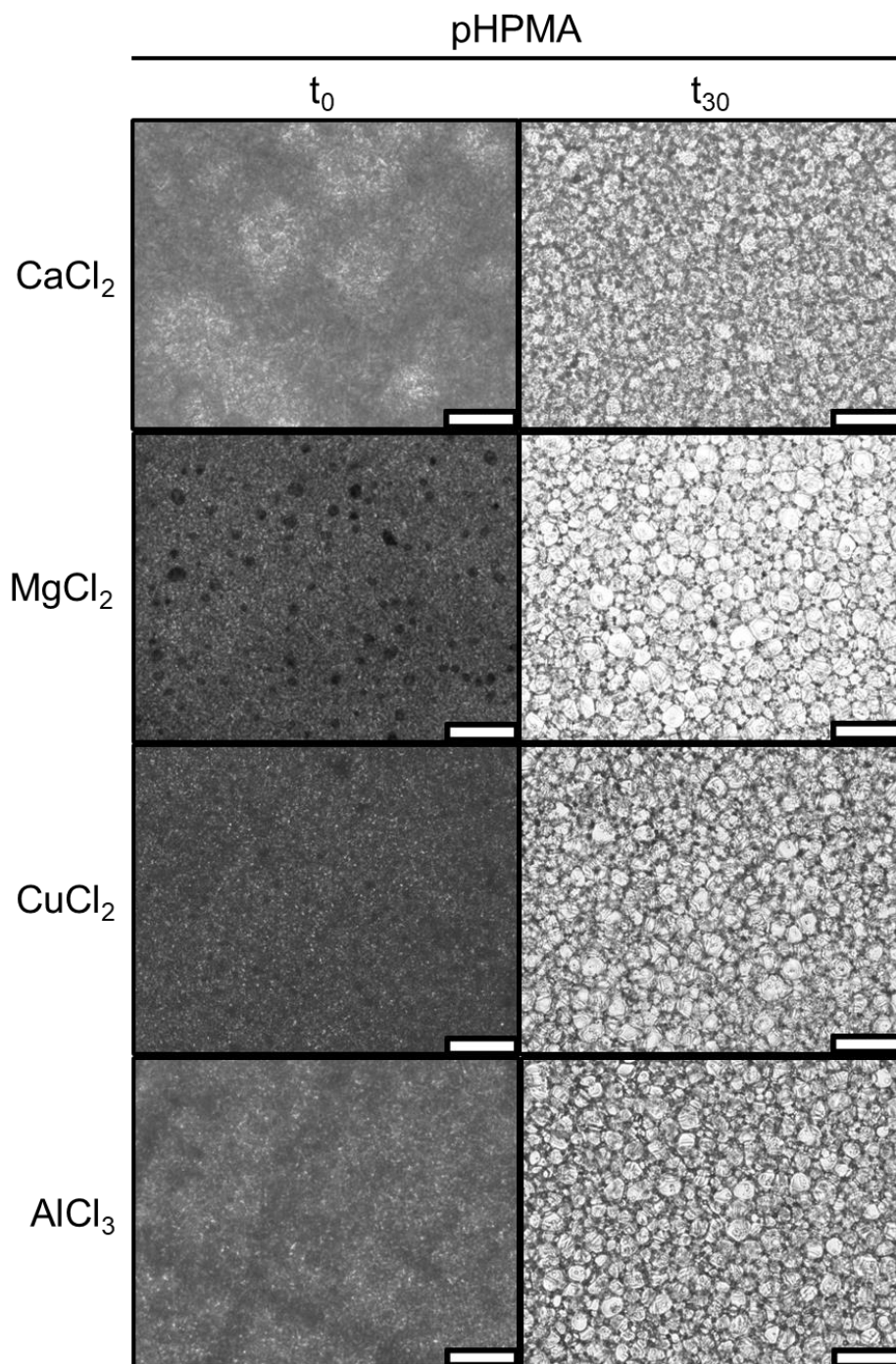
Figure B25. Ice recrystallization activity of 10 mg/ml pHPMA in chloride salt solutions. Top to bottom: 151.5 mM CaCl$_2$, 151.5 mM MgCl$_2$, 151.5 mM CuCl$_2$, 151.5 mM AlCl$_3$. Scale bar is 100 µm.
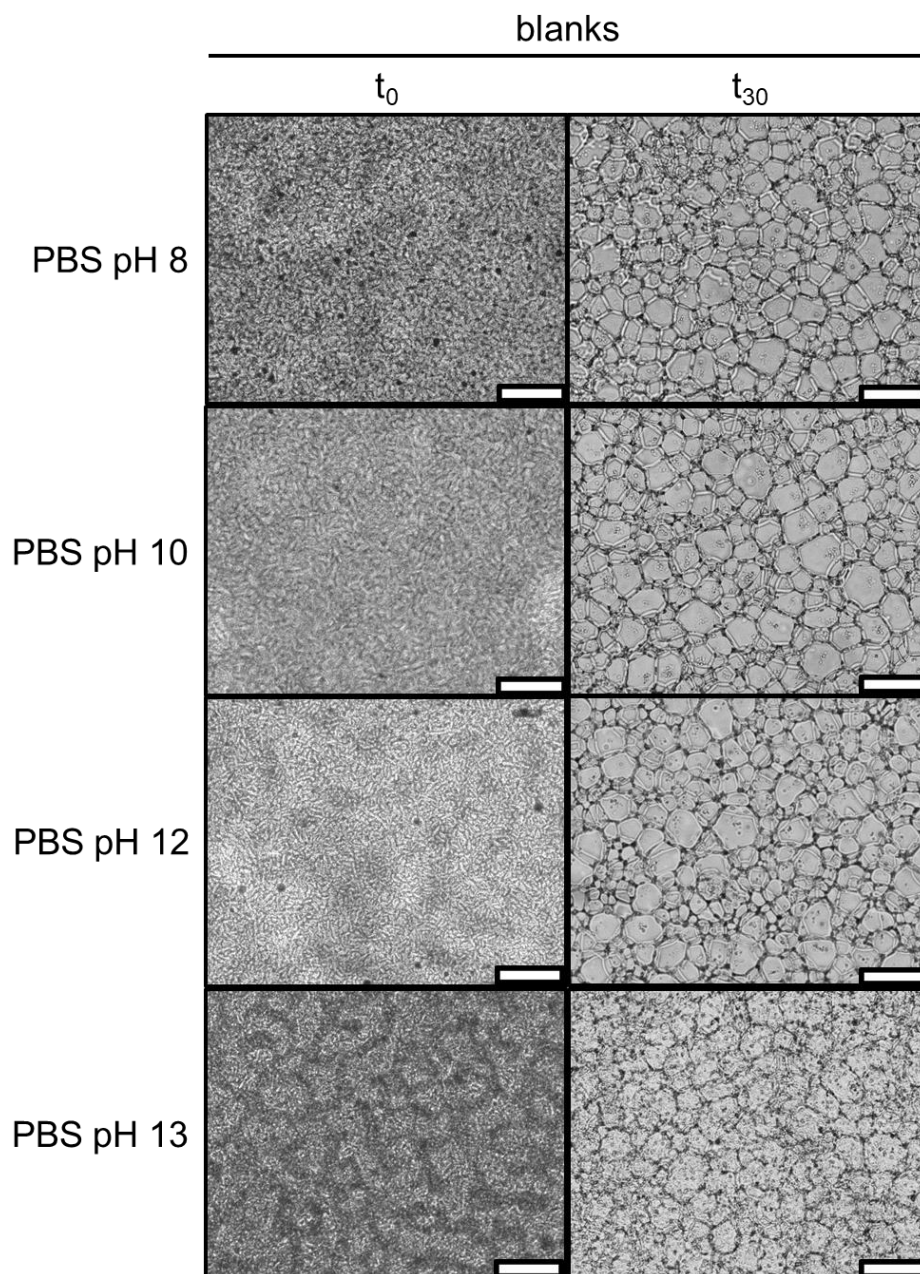
Figure B26. Ice recrystallization activity of blank PBS pH solutions. Top to bottom: PBS pH 8, PBS pH 10, PBS pH 12, PBS pH 13. Scale bar is 100 μm.
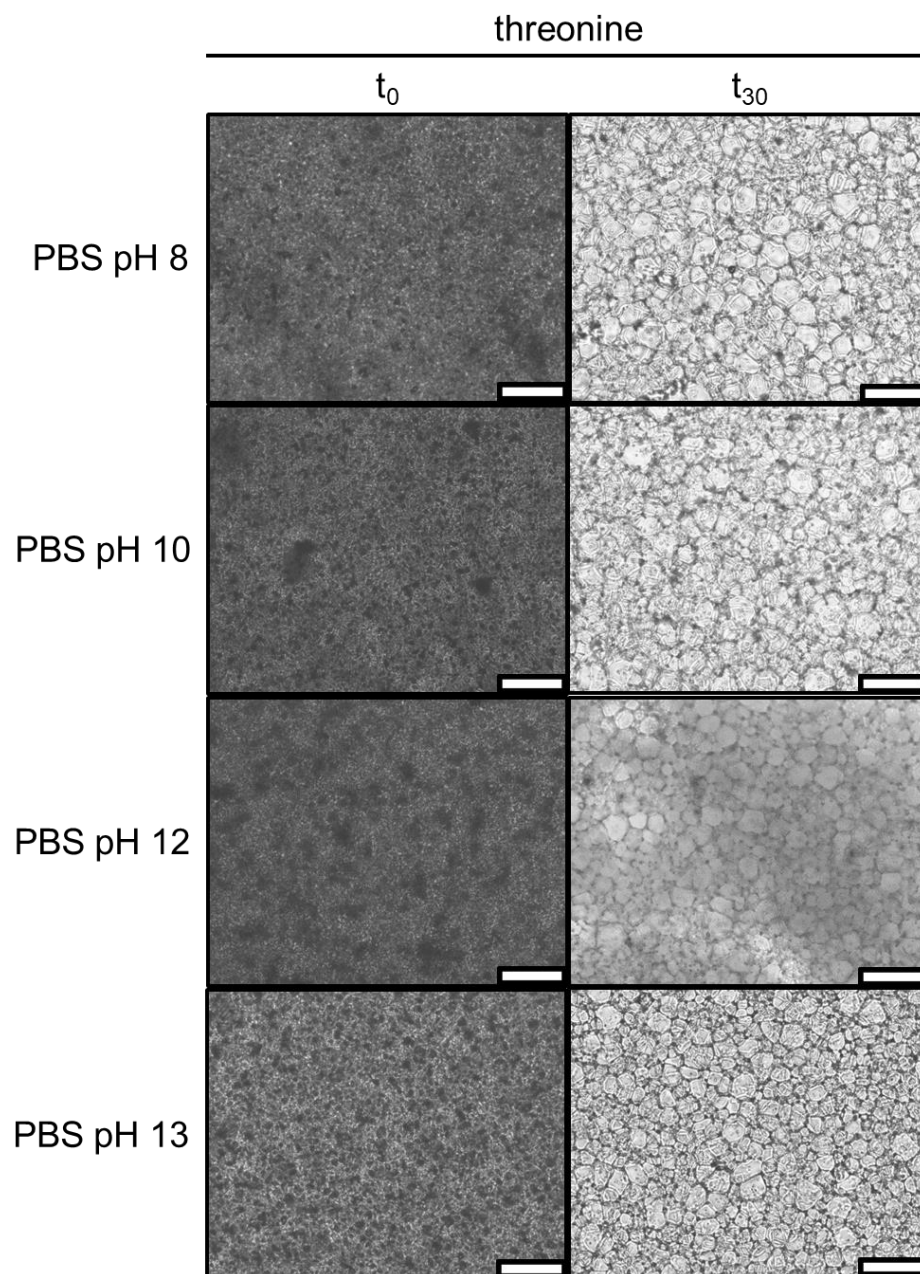
Figure B27. Ice recrystallization activity of 10 mg/ml threonine in PBS pH solutions. Top to bottom: PBS pH 8, PBS pH 10, PBS pH 12, PBS pH 13. Scale bar is 100 μm.
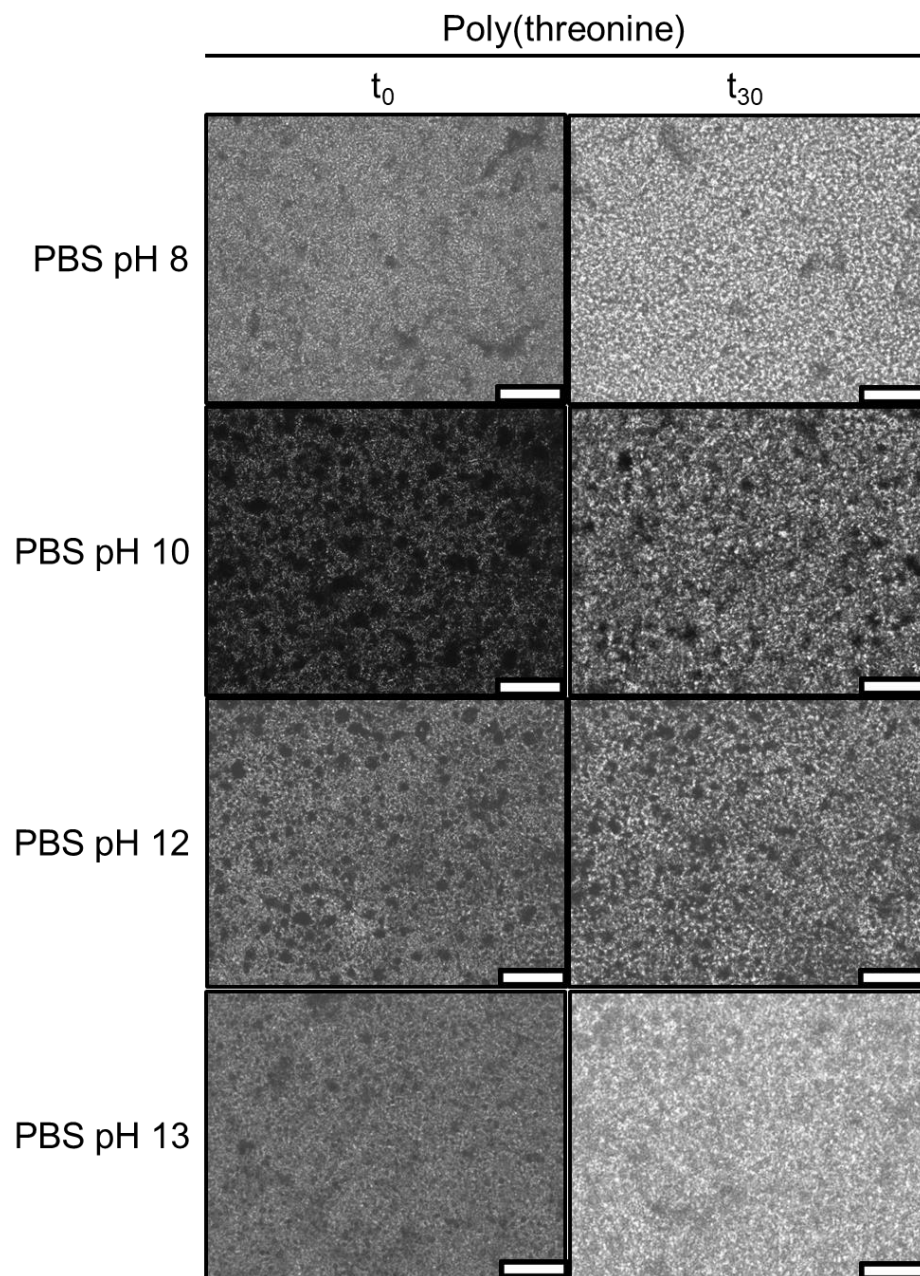
Figure B28. Ice recrystallization activity of 10 mg/ml polythreonine in PBS pH solutions. Top to bottom: PBS pH 8, PBS pH 10, PBS pH 12, PBS pH 13. Scale bar is 100 µm.
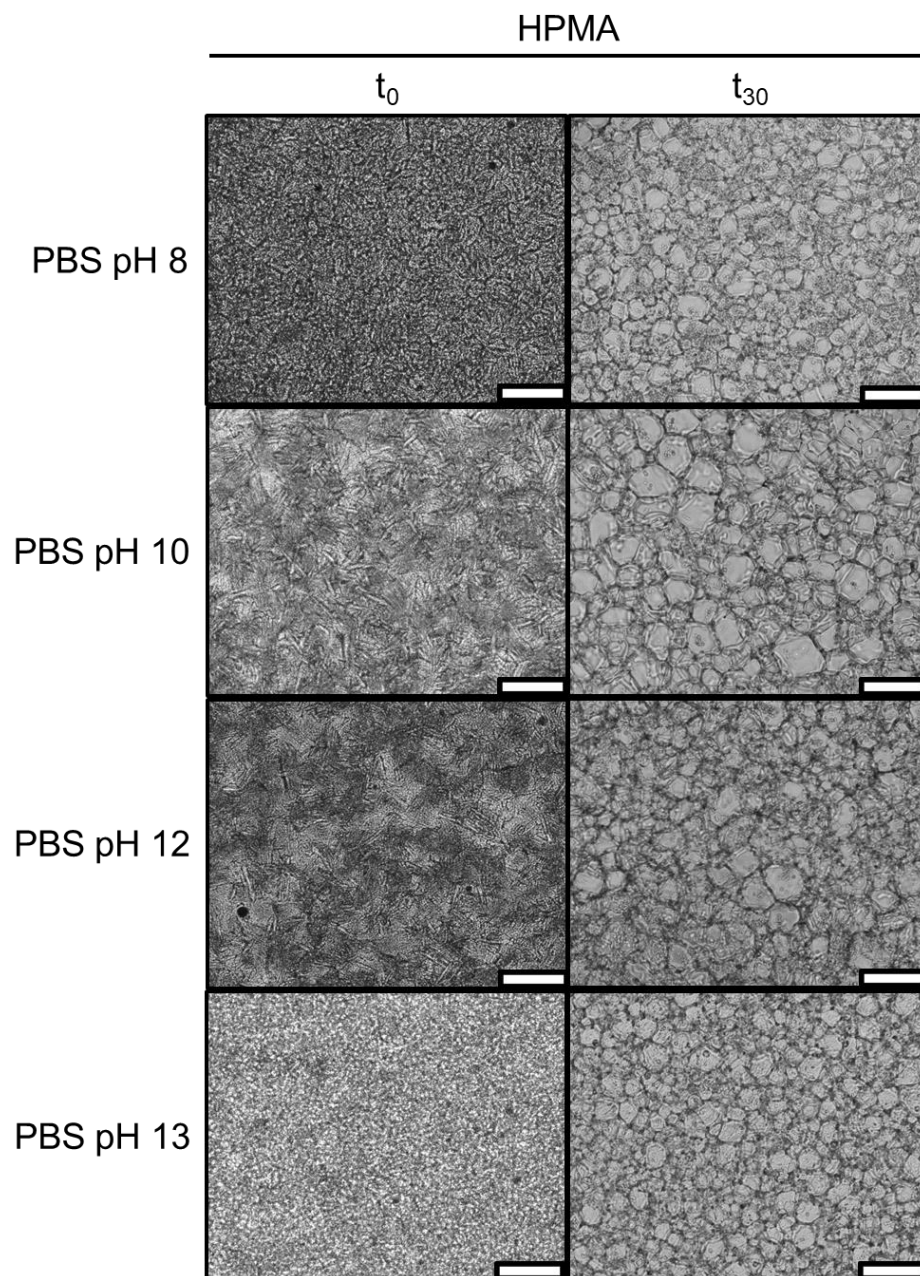
Figure B29. Ice recrystallization activity of 10 mg/ml HPMA in PBS pH solutions. Top to bottom: PBS pH 8, PBS pH 10, PBS pH 12, PBS pH 13. Scale bar is 100 µm.
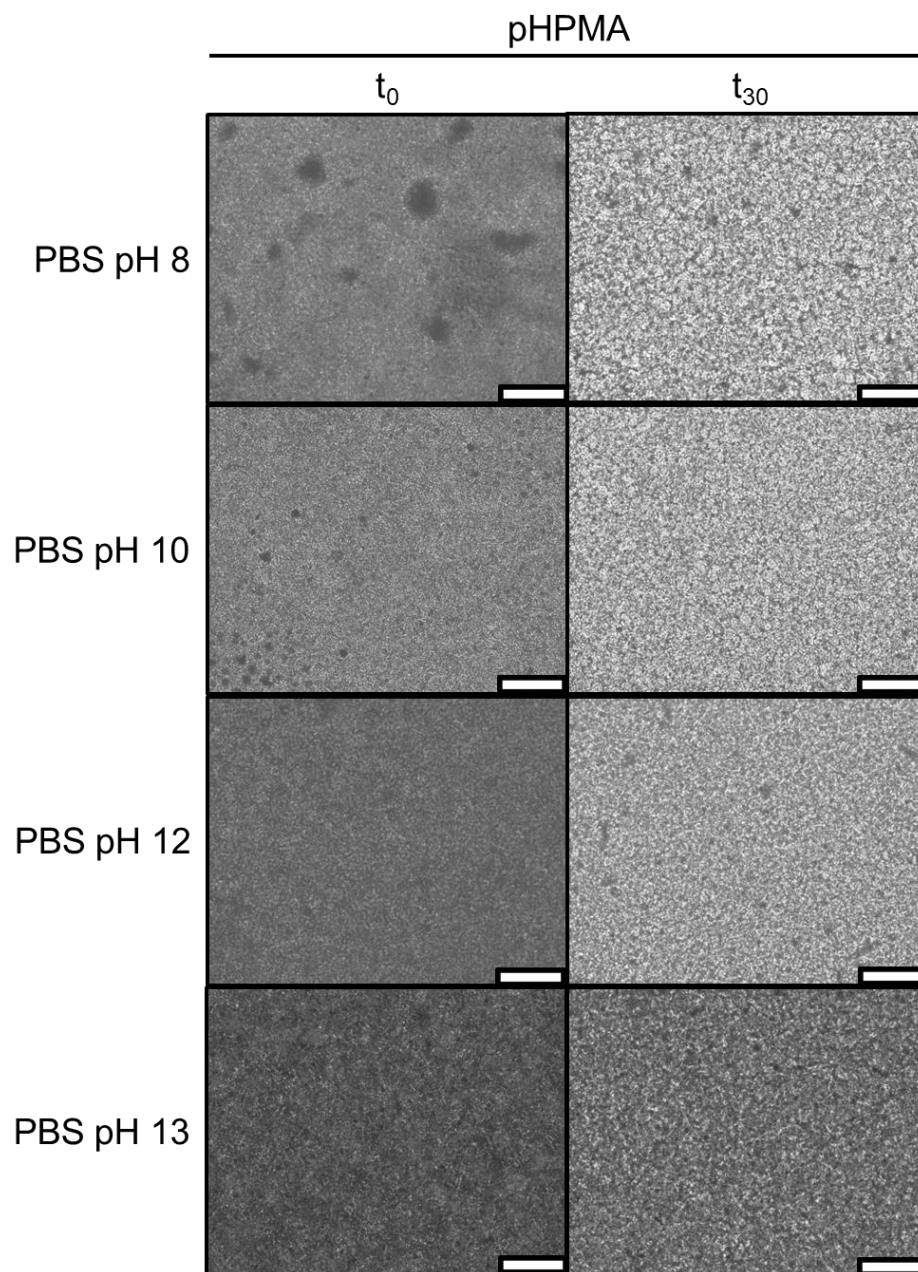
Figure B30. Ice recrystallization activity of 10 mg/ml *pHPMA* in PBS pH solutions. Top to bottom: PBS pH 8, PBS pH 10, PBS pH 12, PBS pH 13. Scale bar is 100 µm.
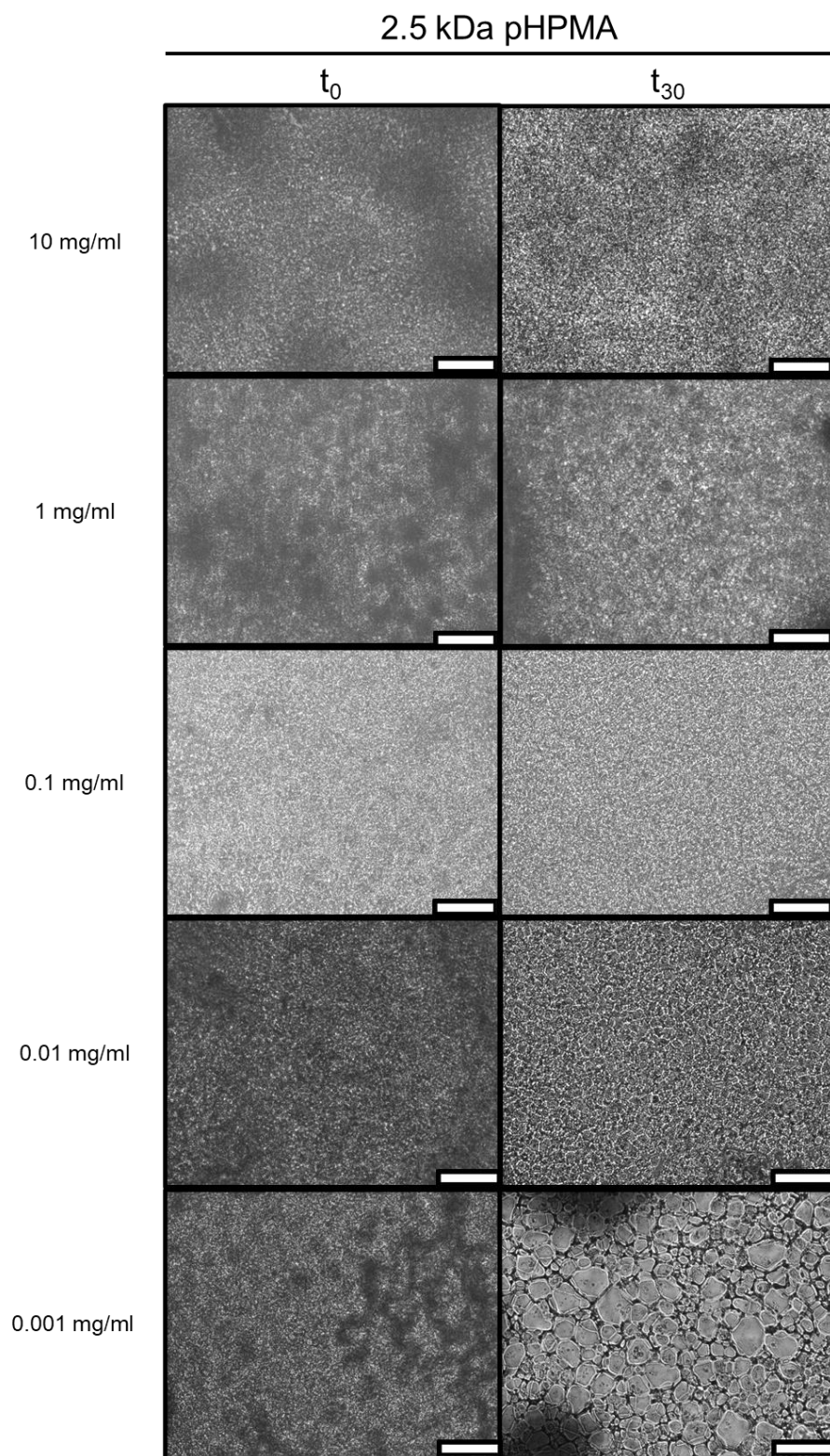
Figure B31. Ice recrystallization activity of 2.5 kDa pHPMA in PBS at concentrations of (top to bottom) 10 mg/ml, 1 mg/ml, 0.1 mg/ml, 0.01 mg/ml, 0.001 mg/ml. Scale bar is 100 μm.
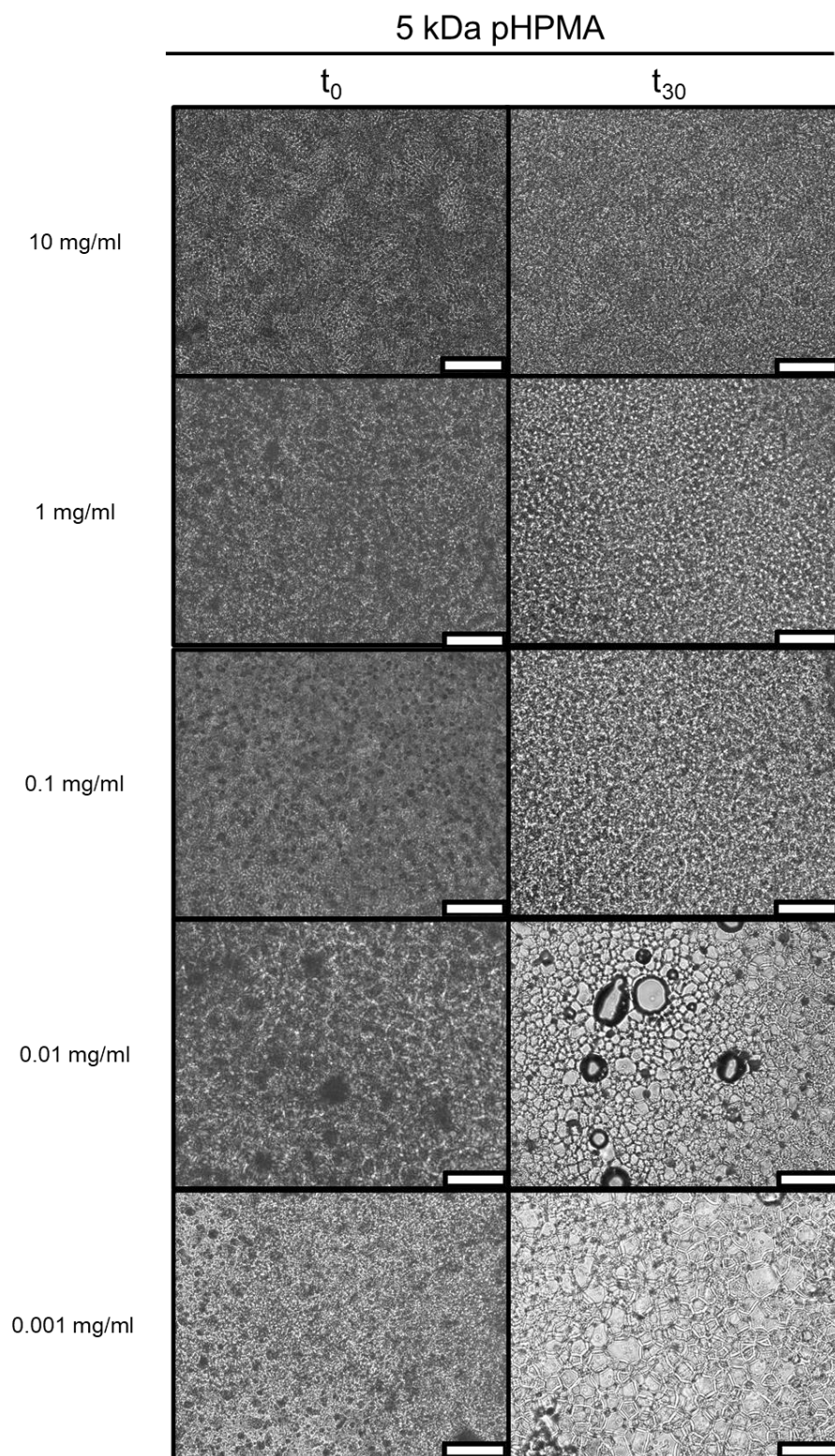
Figure B32. Ice recrystallization activity of 5 kDa *pHPMA* in PBS at concentrations of (top to bottom) 10 mg/ml, 1 mg/ml, 0.1 mg/ml, 0.01 mg/ml, 0.001 mg/ml. Scale bar is 100 µm.
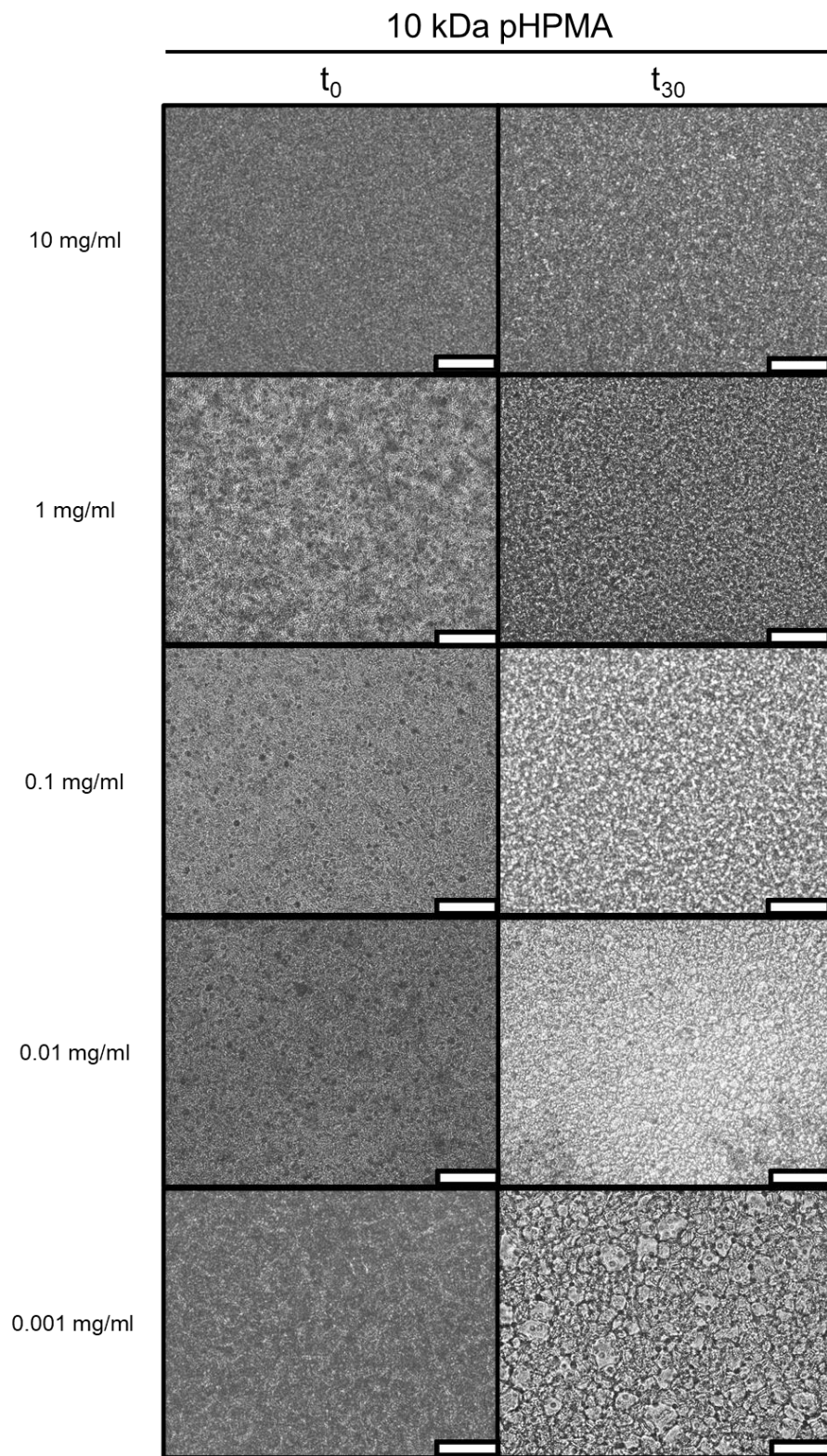
Figure B33. Ice recrystallization activity of 10 kDa *pHPMA* in PBS at concentrations of (top to bottom) 10 mg/ml, 1 mg/ml, 0.1 mg/ml, 0.01 mg/ml, 0.001 mg/ml. Scale bar is 100 µm.
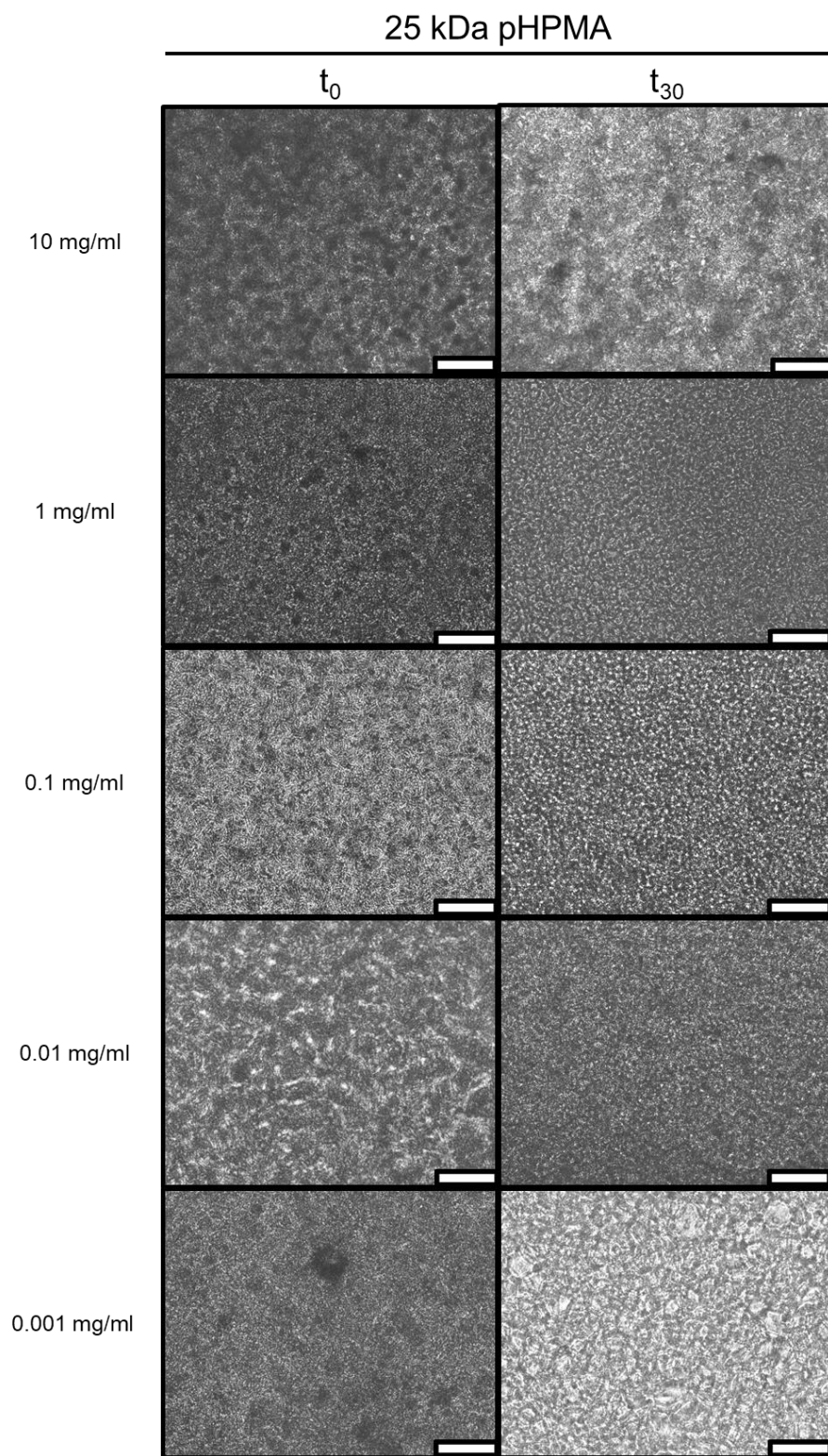
Figure B34. Ice recrystallization activity of 25 kDa *pHPMA* in PBS at concentrations of (top to bottom) 10 mg/ml, 1 mg/ml, 0.1 mg/ml, 0.01 mg/ml, 0.001 mg/ml. Scale bar is 100 µm.